Redox and Mass Transport Phenomena in Resistively Switching Thin Films

Von der Fakultät für Elektrotechnik und Informationstechnik der
Rheinisch-Westfälischen Technischen Hochschule Aachen zur
Erlangung des akademischen Grades eines Doktors der
Ingenieurwissenschaften genehmigte Dissertation

vorgelegt von

Diplom-Ingenieur Elektrotechnik
Stefan Tappertzhofen
aus Düsseldorf

Berichter: Univ.-Prof. Dr.-Ing. R. Waser
apl. Prof. Dr.-Ing. M. Heuken

Tag der mündlichen Prüfung: 20.10.2014

Diese Disseration ist auf den Internetseiten der Hochschulbibliothek online verfügbar.

Bibliografische Information der Deutschen Nationalbibliothek
Die Deutsche Nationalbibliothek verzeichnet diese Publikation in der Deutschen Nationalbibliografie; detaillierte bibliografische Daten sind im Internet über
http://dnb.d-nb.de abrufbar.

ISBN 978-3-8439-1832-9

D 82 (Diss. RWTH Aachen University, 2014)

© Verlag Dr. Hut, München 2014
Sternstr. 18, 80538 München
Tel.: 089/66060798
www.dr.hut-verlag.de

Die Informationen in diesem Buch wurden mit großer Sorgfalt erarbeitet. Dennoch können Fehler nicht vollständig ausgeschlossen werden. Verlag, Autoren und ggf. Übersetzer übernehmen keine juristische Verantwortung oder irgendeine Haftung für eventuell verbliebene fehlerhafte Angaben und deren Folgen.

Alle Rechte, auch die des auszugsweisen Nachdrucks, der Vervielfältigung und Verbreitung in besonderen Verfahren wie fotomechanischer Nachdruck, Fotokopie, Mikrokopie, elektronische Datenaufzeichnung einschließlich Speicherung und Übertragung auf weitere Datenträger sowie Übersetzung in andere Sprachen, behält sich der Autor vor.

1. Auflage 2014

Kurzfassung

Der Einzug moderner Informations- und Kommunikationstechnik in den Alltag während der letzten Jahrzehnte ist direkt mit der Skalierbarkeit von elektronischen Bauteilen und hierbei insbesondere der fortschreitenden Miniaturisierung von Transistoren und Informationsspeichern wie Flash verbunden. Das Skalierungspotentail konventioneller Speichertechnologie ist jedoch auf Grund physikalischer Grenzen weitestgehend ausgeschöpft. Daher sind neuartige Konzepte zur Überwindung dieser Limitierungen Bestandteil aktueller Forschung. Hierbei stellen nichtflüchtige, redoxbasierte resistive Speicher (Redox based Resistive Switching Random Access Memories, ReRAMs) eine herausragende Alternative zu konventionellen ladungsbasierten Speichern wie Flash dar. Die zweipolig ausgeführten Speicherzellen zeichnen sich durch einen einfachen Schichtaufbau aus und kodieren die gespeicherte Information in unterschiedlichen elektrischen Widerstandswerten, die durch Spannungspulse eingeschrieben werden können. Sie zeigen ein Höchstmaß an Skalierbarkeit und ermöglichen einen im Vergleich zu Flash-Speichern deutlich schnelleren Schreibzugriff bei gleichzeitig verbesserten Verlustleistungseigenschaften. Je nach Materialsystem wird resistives Schalten meist auf Grund eines Valenzwechselmechanismus oder des elektrochemischen Metallisierungseffekts beobachtet. Die Effekte, die für den höchst lokalen Schaltprozess eine maßgebliche Rolle spielen, sind bislang jedoch nicht ausreichend erforscht, was für die Optimierung derartiger Speicherzellen einen entscheidenden Nachteil darstellt.

In dieser Dissertation werden elektrochemische und physikalische Effekte, die unmittelbar mit dem resistiven Schaltprozess einhergehen, anhand von ReRAM-Zellen auf der Basis des elektrochemischen Metallisierungseffekts untersucht. Da resistives Schalten in einer Vielzahl unterschiedlicher Materialien beobachtet wird, wurden zwei äußerst gegensätzliche Materialien, Siliziumdioxid (SiO_2) als typischer Vertreter von Isolatoren und Silberjodid (AgI), das ein klassischer Ionenleiter ist, ausgewählt. Hierbei zeigt insbesondere nanoskaliertes Siliziumdioxid eine überraschend hohe Kationen-Mobilität, die bei Bulk-SiO_2 nicht beobachtet wird, aber für den Schaltvorgang unerlässlich ist.

Die vorliegende Arbeit gliedert sich im Wesentlichen in zwei Teile. Im ersten Teil werden elektrochemische Prozesse unmittelbar vor dem Schaltvorgang anhand potentiodynamischer und spektroskopischer Messmethoden analysiert und interpretiert. Es konnte gezeigt werden, dass für den Schaltvorgang in SiO_2 Gegenladungen in Form von OH^--Ionen zwingend erforderlich sind. Bei Silberjodid konnte nachgewiesen werden, dass die Ag/AgI Grenzfläche chemisch inaktiv ist, jedoch Silber in Form kleiner Metallkristallite in AgI eindringt. Zudem werden bei redoxbasierten Speichern Nichtgleichgewichtszustände inhärent aufgebaut, die in den in der Literatur veröffentlichten Modellsystemen bislang unberücksichtigt blieben. Diese Effekte haben einen unmittelbaren Einfluss auf den resistiven Schaltvorgang, der im zweiten Teil der Arbeit untersucht wird. Es konnten sowohl bei SiO_2 als auch bei AgI quantisierte Leitfähigkeitswerte beobachtet werden, die auf ein ultimativ atomares Skalierungspotential von ReRAM-Zellen hinweisen. Darüber hinaus wurde die extrem nichtlineare und für praktische Anwendungen vorteilhafte Schaltkinetik experimentell wie auch theoretisch analysiert.

Abstract

In the last decades, modern information and communication technology have become part of daily life, which is unequivocally linked with the progressive scaling of electronic components and particularly with the ongoing miniaturization of transistors and memory devices such as Flash. As the scaling limit of conventional memory technology is approaching, new concepts are part of current research. In this context, nonvolatile redox based resistive switches (Redox based Resistive Switching Random Access Memories, ReRAMs) are considered as a highly promising alternative to Flash memories. These two-terminal memory cells are based on a simple layer structure and the information is stored as different resistance levels by applying appropriate voltage pulses. In comparison to Flash, ReRAMs offer a high potential of scalability, low power consumption and fast write access. The strongly local resistive switching effect is observed in various material systems and often based on a valance change mechanism or electrochemical metallization effect. However, the processes involved during the resistance transition are not yet studied in detail, which is disadvantageous for device optimization.

In this thesis, ReRAM cells based on the electrochemical metallization effect are analyzed in respect to electrochemical and physical processes, which are contributing to the resistive switching effect. Since resistive switching is observed in various materials, two different materials, i.e. silicon dioxide (SiO_2) and silver iodide (AgI), representing the material class of insulators and ion conductors, respectively, were selected. In particular, nanoscale SiO_2 is characterized by an unexpected high cation mobility, which is essential for the resistive switching effect but not reported in bulk SiO_2.

This work can be divided into two parts. In the first part, electrochemical processes prior to the switching event are analyzed by potentiodynamic and spectroscopic measurement methods. It has been observed that in SiO_2 OH^--ions act as counter charges, which are required for resistive switching. In case of silver iodide the Ag/AgI-interface was found to be chemically inactive, but silver can penetrate as small metal-crystallites in AgI. Moreover, in redox based resistive switches nonequilibrium states are inherently induced, which have been neglected in device models reported in literature. These effects are directly affecting the resistive switching process itself, which is studied in the second part of this thesis. Quantized conductance values have been observed both in silicon dioxide and silver iodide giving the prospect of the ultimate atomic scaling potential of ReRAMs. Additionally, the strongly nonlinear, and from an application point of view beneficial, switching kinetic is analyzed experimentally and is theoretically discussed.

Acknowledgment

This thesis was written during my doctoral research at the Institut für Werkstoffe der Elektrotechnik II (IWE 2) at the RWTH Aachen University. First of all I would like to thank Prof. Dr. Rainer Waser for giving me the opportunity to do research at the IWE 2 on the resistive switching effect. I appreciate the freedom of research at the institute in this highly interdisciplinary field. Moreover, I would like to thank apl. Prof. Dr. Michael Heuken for being the co-examiner of my doctoral thesis.

I am indebted to Dr. Ilia Valov for supervising my work and countless discussions. I appreciate his advices which had a great impact on the successful completion of this thesis. I am also very grateful to Dr. Ulrich Böttger for his support and fruitful discussions during my research. I would like to thank Dr. Stephan Menzel for the excellent collaboration and valuable discussions on the switching kinetics. I thank Dr. Eike Linn and Lutz Nielen for the collaboration which led to many fascinating applications based on resistive switches.

I express my gratitude to all the members of the Nanoarchitecture Laboratory and Peter Grünberg Institut 7 of the Forschungszentrum Jülich for their support and good collaboration. I am very grateful to Florian Lentz, Bernd Rösgen and René Borowski who spend endless hours on fabricating nano crossbar devices. Special thanks to Dr. Roland Rosezin, Dr. Christoph Hermes, Dr. Uwe Breuer, Dr. Bernd Holländer and Dr. Astrid Besmehn.

I thank Peter Roegels for fabrication of silver iodide thin films. To Daliborka Erdoglija, Petra Grewe, Gisela Wasse and René Thelen I owe thanks to their support during my thesis. I would like to thank the staff of the electronics lab (Jochen Heiss and Hartmut Pütz) and the team of the mechanical workshop for assembling processing and measurement equipment I used in this work.

I thank all my student research assistants who spend many hours in the lab and contributed to this work. Special thanks to Hans Mündelein, Marek Hempel, Filip Petri, Katharina Saxe and Jens Paulussen. I am very grateful to Dr. Omid Kavehi, Dr. Tohru Tsuruoka and Dr. Deok-Yong Cho for their collaboration. Additionally, I am also thankful to Udo Evertz, Martina Heins, Maria Gracia, Dagmar Leisten, Katharina Utens, Sebastian Schmelzer, Inka Müller, Mark Röscher, Carsten Dehoff, Priv. Doz. Dr. Georgi Staikov, Jan van den Hurk, David Griesche, Rebacca Hung and Dr. Theo Schneller. I thank all my co-workers at the Institut für Werkstoffe der Elektrotechnik II and Peter Grünberg Institut 7 for the support and inspiring working atmosphere.

Finally, I wholeheartedly thank Nadine Ladkau for her unyielding support and proof-reading. I would like thank my parents, my family and all my friends for encouragement and support in so many years.

Contents

1. Introduction **1**

1.1. State of the Art 1

1.2. Scope of this Work 2

2. Fundamentals **5**

2.1. Nonvolatile Resistive Switching Memories 5

2.1.1. Categories of Resistive Switches 6

2.1.2. Electrochemical Metallization Effect 8

2.2. Mass and Charge Transport in Solid Electrolytes 9

2.3. Electrochemical Oxidation and Reduction 11

2.3.1. Reversible System 13

2.3.2. Irreversible System 15

2.3.3. Quasi Reversible System 16

2.3.4. Multistep and Multielectron Charge Transfer Reactions 16

2.4. Nonequilibrium States 17

2.4.1. Nernst Potential 19

2.4.2. Diffusion Potential 21

3. Experimental **23**

3.1. Fabrication Processes 23

3.1.1. Physical Vapor Deposition (PVD) 23

3.1.2. Pattern Transfer 26

3.2. Characterization Methods 26

3.2.1. Morphology and Stoichiometry Analysis 26

3.2.2. Electrical Characterization 29

3.3. Material Characterization and Sample Preparation 32

3.3.1. Silicon Dioxide 32

3.3.2. Silver Iodide 34

4. Redox Processes in Thin Films **39**

4.1. Cations in Insulators: Silicon Dioxide 39

4.1.1. Anodic Oxidation and Cation Diffusion Behavior 39
4.1.2. Bond Nature of Mobile Cations in Silicon Dioxide 48
4.1.3. Impact of Moisture during Anodic Oxidation 52
4.1.4. Impact of Counter Electrode 54
4.2. Cations in Solid Electrolytes: Silver Iodide 59
4.2.1. Electronic and Ionic Partial Conductivity 59
4.2.2. Chemical Stability of the Ag/AgI Interface 62
4.3. Nonequilibrium States 66
4.3.1. Electromotive Force (emf) Measurements 66
4.3.2. Impact of Water Partial Pressure 69

5. Resistive Switching Effect and Applications 73
5.1. Switching Behavior in Silicon Dioxide and Silver Iodide 73
5.1.1. Current/Voltage Sweep Experiments 73
5.1.2. Impact of Water Partial Pressure on Silicon Dioxide based Cells 81
5.1.3. Quantum Conductance Experiments 82
5.1.4. Pulse Measurements and Switching Kinetics 87
5.2. Nanobatteries in Redox Based Resistive Switches 96
5.2.1. Electromotive Force Measurements under Open Circuit and Short Circuit Conditions 97
5.2.2. Influence on Device Endurance and Retention 101
5.3. Resistive Switching Applications 104
5.3.1. Electrochemical Metallization Cells for Memory Applications . . 104
5.3.2. Nondestructive Readout of Complementary Resistive Switches . 106
5.3.3. Logic and Neuromorphic Applications 110

6. Conclusions 115
6.1. Summary 115
6.2. Outlook 117

List of Figures 119

List of Tables 131

Bibliography 133

A. Appendix 147

Abbreviations

AC	Alternating Current
AFM	Atomic Force Microscopy
CC	Current Compliance
CRS	Complementary Resistive Switch
CV	Cyclic Voltammetry
DC	Direct Current
E-Beam	Electron-Beam
ECM	Electrochemical Metallization Mechanism
EDX	Energy Dispersive X-ray Spectroscopy
HRS	High Resistive State
LRS	Low Resistive State
NDRO	Nondestructive Readout
RBS	Rutherford Backscattering Spectroscopy
ReRAM	Redox based Resistive Switching Random Access Memory
RF	Radio Frequency
RFI	Radio Frequency Interference
RRAM	Resistive Switching Random Access Memory
SEM	Scanning Electron Microscopy
STM	Scanning Tunneling Microscopy
UV	Ultraviolet
VCM	Valence Change Mechanism
XAS	X-ray Absorption Spectroscopy
XPS	X-ray Photo Electron Spectroscopy
XRD	X-ray Diffraction

1. Introduction

In the last decade, modern information and communication technology have exceptionally changed the way people live, communicate and work. Flash transistors became an integral part of daily life and led to a striking increase of mobility, and economic innovation and productivity. The ongoing development of information technology is inextricably linked with the miniaturization of electronic devices. According to Moore's law [1], the number of components on integrated circuits increased exponentially in the last decades. As more electronic elements were integrated on a semiconductor chip, the fabrication cost for each individual component decreased exponentially likewise. However, the integration limit of conventional semiconductor devices is approaching [2]. Among various challenges, substantial problems arise from localized heat generation on integrated circuits, as transistors continue to become smaller. Nowadays, sophisticated semiconductor fabrication techniques are required for device scaling and further miniaturization becomes economically more and more unobtainable.

Nanotechnology has the potential to overcome these issues and research on new materials, revolutionary new logic architectures and neuromorphic concepts may lead to a paradigm shift in information and communication technology. In this context, Resistive Switching Random Access Memories (RRAMs) represent a particularly promising future memory technology [3].

1.1. State of the Art

Advanced Flash memories are currently fabricated using lithography technology beyond the 20 nm node [4]. Vertical Flash [5] and even complete three-dimensional (3D) Flash structures [6] were proposed to negotiate scaling limitations. However, regardless of high effort in research, 3D structures are not yet commercially available due to high fabrication cost and low yield [4]. Among other memory concepts such as Spin-torque-transfer Magnetoresistive Random Access Memories (MRAM) [7] or Ferroelectric Random Access Memories (FeRAM) [3], RRAMs have a high potential to replace Flash memory technology [8].

In this regard, the redox based resistive switching effect (Redox based Resistive Switching Random Access Memories, ReRAM) attracted high attention and can be observed in various material systems [4; 9]. The essential processes for the operation of these resistive switches are redox reactions at the electrode-electrolyte interfaces and the ionic transport within a nanoscale solid film. Depending on the mobile ions and processes involved during resistive switching, devices based on the thermochemical mechanism (TCM) [10] as well as anion based (Valence Change Mechanism, VCM) [11] and cation based (Electrochemical Metallization Mechanism, ECM) [12] memory devices can be distinguished. ReRAMs are in focus of current research due to their ease of fabrication, high scalability, fast read and write access, and low power consumption [13–15]. At first glance, the resistive switching effect seems to be rather simple but detailed microscopic understanding of the processes involved during resistance transition, including the redox reactions on the nanoscale and the switching kinetics, is still missing.

Besides fundamental investigation on the electrochemical and physical effects, and mechanisms underlying the resistive switching effect, the nonlinear characteristics of ReRAMs offer the prospect of new memory architectures and applications. Concepts of fully passive and highly scalable memory crossbar arrays [16] as well as logic-in-memory [17; 18] and neuromorphic applications [19; 20] are discussed in literature, which further intensified the research in the field of ReRAMs.

1.2. Scope of this Work

This work is focused on ReRAMs based on the electrochemical metallization effect (ECM cells). Fundamental questions regarding quantum-size effects, charge and mass transport, nonequilibrium states and redox reactions, and nucleation effects at the electrode-electrolyte interfaces are considered at both experimental and theoretical level.

In respect to various classes of materials showing the resistive switching effect, silicon dioxide (SiO_2) and silver iodide (AgI) have been selected as model materials in this work. Here, silicon dioxide represents the class of conventional insulators and silver iodide is a well-known ion conductor. Despite their antithetic characteristics in the macroscopic bulk phase, both materials are termed as ionic or mixed ionic–electronic electrolytes at room temperature on the nanoscale [12; 21; 22].

This work is divided into six chapters. In the following chapter the resistive switching effect as well as electrochemical fundamentals are introduced. Fabrication and characterization methods are summarized in chapter three. In this context, generic material properties are presented. In chapter four results on redox and transport phenomena of cations in silicon dioxide and silver iodide thin films as well as the origin of nonequilibrium states are discussed and analyzed. Chapter five is concerned with resistive switching experiments in SiO_2 and AgI, and applications based on ReRAMs. The results of this thesis and an outlook are given in chapter six.

2. Fundamentals

The investigation of nanoionic phenomena playing an essential role within the context of the resistive switching effect requires a deep insight into electrochemical fundamentals. Although the basic principle of the resistive switching effect itself is rather descriptive, the processes which are responsible for resistance transition are of complex nature when studied in detail. In this respect, electrochemical fundamentals are outlined in this chapter. Primarily, an overview of resistive switching memories being one example of a promising application of nanoionic redox phenomena is given. Furthermore, special attention is paid to oxidation and reduction (redox) processes of metal cations within solids and the kinetics of these redox reactions.

2.1. Nonvolatile Resistive Switching Memories

The ultimate memory device features high scalability, fast read and write access, high endurance, long (nonvolatile) retention, and low cost fabrication. Nowadays, memory devices can be classified in four major categories in regard to their application requirements [9]. Static Random Access Memories (SRAMs) based on bistable latching circuits offer fast read and write access. Although the stored data does not need to be periodically refreshed, SRAMs are considered as volatile memory devices loosing their stored information when the memory is not powered. Since SRAMs consist of six MOSFETs (Metal Semiconductor Fieldeffect Transistors), highly scalable devices cannot be achieved. In contrast to SRAMs, the information in volatile but highly scalable Dynamic Random Access Memories (DRAMs) is periodically refreshed. For longtime mass storage hard disk drives made of rotating magnetic discs are primarily used. Both write and read access are sequential, and these devices are in such a way not referred as random access memories. State of the art technology of nonvolatile random access memories are Flash devices. They basically consist of floating gate MOSFETs, where the threshold voltage can be modulated by high voltage programming modes. However, reaching its ultimate downscaling limit within the next years, new emerging memory devices are indispensable to replace conventional Flash memory technology [3; 23]. In this context, Resistive Switching Random Access Memory (RRAM) cells are a promising alternative to standard Flash based memory devices due to the prospect of high scalability and low power consumption. Of particular interest among other emerging RRAM technologies are redox based resistive switching memory cells (ReRAMs), which are in the focus of this work.

2.1.1. Categories of Resistive Switches

Different categories of RRAMs based on their physical working principle can be classified as depicted in figure 2.1 [24]. Redox based RRAMs (i.e. ReRAM devices) are highlighted by red color. Regardless of the individual physical working principle, all ReRAM devices have in common that their resistance can be modulated by an appropriate voltage or current pulse. Thus, information is stored in a low resistive state (LRS) and high resistive state (HRS). Moreover, intermediate resistance states can be also programmed in some ReRAM devices giving the prospect of storing multiple bit in one single device [25].

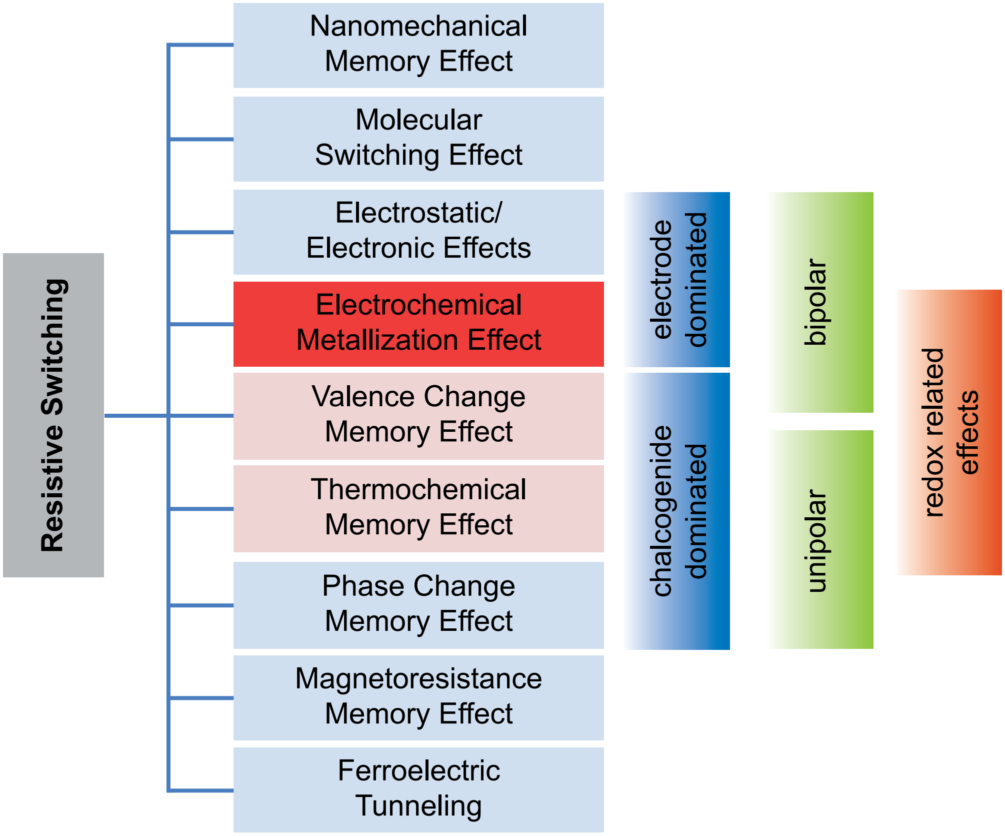
Resistive Switching
Nanomechanical Memory Effect
Molecular Switching Effect
Electrostatic/ Electronic Effects
Electrochemical Metallization Effect
Valence Change Memory Effect
Thermochemical Memory Effect
Phase Change Memory Effect
Magnetoresistance Memory Effect
Ferroelectric Tunneling
electrode dominated
chalcogenide dominated
bipolar
unipolar
redox related effects

Figure 2.1. Categories of resistive switches (based on [11]). Special attention is paid to two-terminal redox related electrochemical metallization cells.

In some ReRAM devices the functional principle is mainly dominated by the working electrode (e.g. Cu or Ag), while for other devices the actual switching layer (typically transition metal oxides or higher chalcogenides) plays the fundamental role [24]. Despite the physical working principle one can also classify ReRAM devices depending on the operating voltage regimes. For unipolar working devices a single voltage polarity is used for both write (SET) and erase (RESET) of the information as shown in figure 2.2a. In some devices unipolar switching in both voltage polarities can be observed. All unipolar switching devices have in common that the current compliance I_{CC} needs to be lower than the current for RESET. In general, a current compliance is needed to prevent damage of the device in the low resistive state. In contrast to unipolar switches, bipolar devices require voltages of opposite polarity for SET and RESET of the cell as depicted in figure 2.2b.

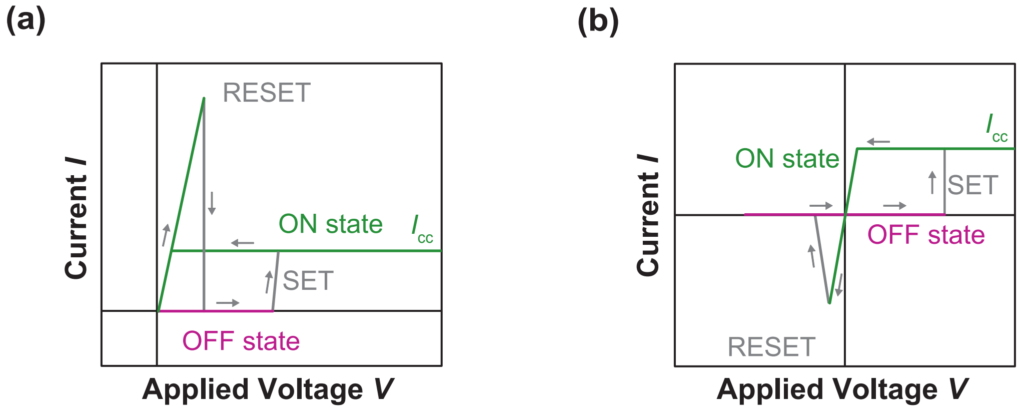

Figure 2.2. Categories of resistive switches classified by the operating voltage regime. Blue and red color indicate the current/voltage characteristic in the HRS and LRS, respectively. The RESET process is highlighted by green colored lines (redrawn from [26]). (a) Unipolar switching (only one voltage polarity is shown for simplification) and (b) bipolar switching.

There are several ways to achieve a significant resistance transition. This work is focused on ReRAM devices, which are based on bipolar electrochemical effects where the active electrode is playing the fundamental role for the switching effect. These two-terminal devices highlighted in figure 2.1 are called Electrochemical Metallization (ECM) cells and are based on redox related effects such as the anodic oxidation of the active electrode [27; 28]. They are typically characterized by ease of fabrication and high scalability.

Besides ECM cells high attention has been also paid to memory devices based on the valence change mechanism (VCM) and thermochemical mechanism (TCM) in literature [3; 8]. VCM and TCM cells both typically consist of transition metal oxides (such as $SrTiO_3$ or TiO_2) as insulating layers. While VCM cells show bipolar switching characteristics, unipolar switching is observed in TCM cells. The valence change mechanism is contributed to migration of oxygen ions leading to different resistance states [11]. In contrast, thermally controlled redox processes leading to the formation of conductive filaments are believed to be responsible for the thermochemical mechanism [29; 30]. Among other material systems NiO is widely used for TCM cells [10].

2.1.2. Electrochemical Metallization Effect

This work is mainly focused on ReRAM devices based on the electrochemical metallization effect. In general, the simple structure of ECM cells consists of a metal/insulator/metal layer stack. Several higher chalcogenides (e.g. $GeSe_x$ [31]) and oxide insulating thin films (such as SiO_2 [21; 32] and TiO_2 [33]) show resistive switching behavior. It is assumed that the transition between the high resistive state and low resistive state of the memory cell is caused by the electrochemical formation and rupture of a nanoscale metallic filament [28].

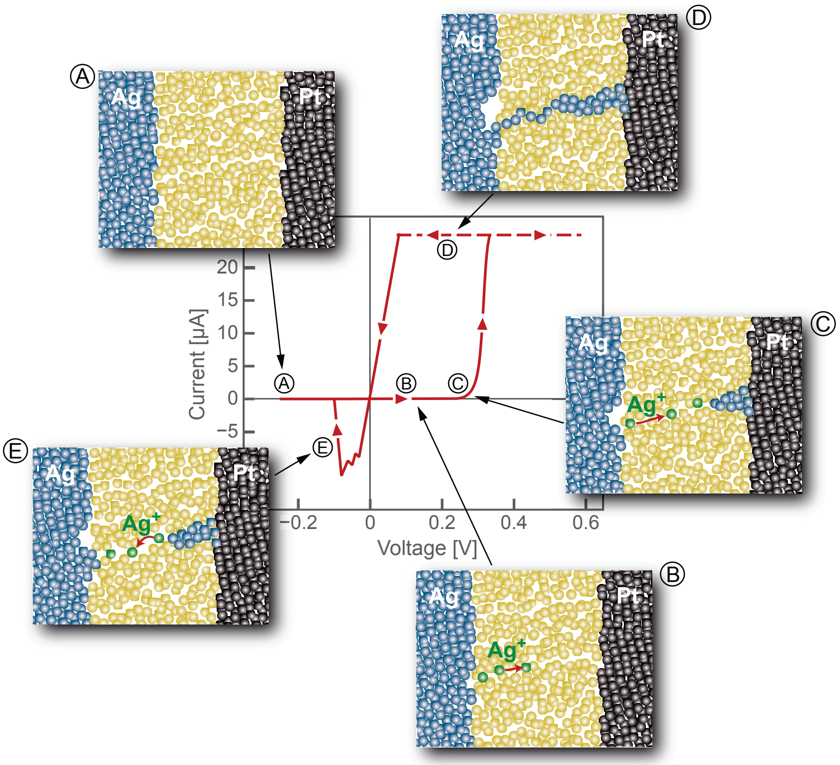

Figure 2.3. Basic principle of the resistive switching effect during a current-voltage (I/V) sweep in electrochemical metallization cells [28].

The basic working principle of an ECM cell becomes clear in figure 2.3. In general, an ECM cell is made of a working electrode (WE) such as Ag or Cu and an electrochemically inert counter electrode (CE) such as Pt or Au. Starting from an initial HRS (A), the cell current is more or less slightly increased by increase of the applied voltage. In the HRS no conductive channel can be found in the insulating layer. Here, the current is dominated by the leakage current and the anodic oxidation of the working electrode metal M to a metal cation M^{z+}:

$$\mathrm{M} \longrightarrow \mathrm{M}^{z+} + z\mathrm{e}^{-}, \tag{2.1}$$

whereas z is the charge number of the metal cation. The metal ions injected into the insulator drift under the applied electric field (B) and are reduced on the surface of the inert counter electrode (C):

$$\mathrm{M}^{z+} + z\mathrm{e}^{-} \longrightarrow \mathrm{M} \tag{2.2}$$

Subsequently, the cation diffusion processes is enhanced by the electric field resulting in the formation of a nanoscale metal filament [34]. The SET voltage V_{SET} is defined as the voltage where the ECM cell switches from the HRS to the LRS (SET process) due to the filament short circuiting both electrodes (figure 2.3 (D)). A current compliance I_{CC} is needed to prevent damage of the cell in the LRS. The current compliance is controlling the effectively applied voltage to regulate a constant cell current (see chapter 3.2.2).

As soon as the voltage is decreased, a linear slope of the current versus voltage is observed when the current is again below the current compliance level. By further decrease of the applied voltage (E) the absolute cell current is increased until the cell switches back from the LRS to the HRS (RESET process). The above described resistance transition is reproducible. In this regard, the filament rupture is contributed to electrochemical oxidation and reduction processes of the filament according to equation 2.1 and 2.2. The existence of one or more nanoscale filaments is motivated by the observation that most ReRAMs show resistances in the LRS, which are independent on the electrode diameter [35].

2.2. Mass and Charge Transport in Solid Electrolytes

When the potential $E = -E_{\mathrm{r}}$ (rest potential E_{r}) is applied, the anodic and cathodic current densities are compensated resulting in a zero net current density of the electrochemical cell. In this case the cathodic and anodic current densities have the same magnitude of the exchange current density j_0 [36]. The exchange current density is determined by the concentration of the active ionic species and the kinetics, and free energies of the electrochemical reaction. As soon as the electrode potential is $E = -E_{\mathrm{r}} + \eta$, where η is the overpotential, a current density j is measured, which can be described by the Butler-Volmer equation consisting of both the cathodic as well as anodic current density [36; 37]:

$$j = \underbrace{j_0 \cdot \exp\left(\frac{(1-\alpha)zF\eta}{RT}\right)}_{\text{anodic current density}} \underbrace{-j_0 \cdot \exp\left(\frac{-\alpha zF\eta}{RT}\right)}_{\text{cathodic current density}} \tag{2.3}$$

Here, z is the number of electrons involved in the transfer process, R the universal gas constant, F the Faraday constant and T the absolute temperature. A graphical representation of the net current density, and the anodic and cathodic fraction is illustrated in figure 2.4a as a function of the overpotential η. The charge transfer coefficient α is in between zero and unity. The current density curve is apparently symmetric solely for $\alpha = 0.5$ as shown in figure 2.4b.

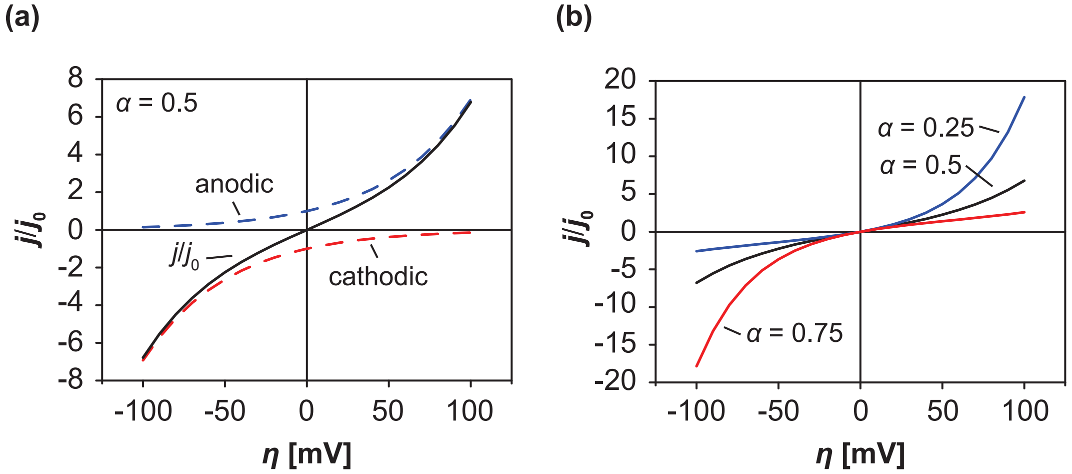

Figure 2.4. Graphical representation of the current density j described by the Butler-Volmer equation. (a) Anodic and cathodic fraction to the net current density, (b) net current density depending on the asymmetry parameter α.

It is noteworthy that the current density can be only thoroughly expressed by the Butler-Volmer equation when the current density depends solely on the interfacial dynamics. In general, this does not hold for thin film insulators such as SiO_2, which initially do not contain mobile ions. Thus, the ion concentration close to the electrode and in the bulk are not self-evidently equal. In this case the current density can be also determined by the mass transport from or to the active electrode. This situation has to be also considered for electrochemical systems at high overpotentials even if the concentration of ions *near* the electrode is equal to the bulk concentration at moderate overpotentials. In this case the current density approaches a limit determined by the mass transport of the ionic species to or from the electrode.

2.3. Electrochemical Oxidation and Reduction

Among other new emerging systems such as solid thin film fuel cells or thin film batteries, resistive switches are one potential application for devices based on nanoionic redox effects. As already outlined above in equation 2.1 and 2.2, these devices are essentially based on electrochemically assisted oxidation and reduction processes. Thus, for a deep insight into the processes involved during the device operation fundamental knowledge of electrochemical oxidation and reduction (redox) processes is indispensable. Oxidation and reduction processes can be studied by linear voltage sweeps and simultaneously measuring the current response of the electrochemical system. In this context, a widely used method in electro chemistry is *cyclic voltammetry* (CV) [38], which is also an integral part of the measurement techniques utilized in this thesis. Cyclic voltammetry is not allowing very precise quantitative analysis. However, CV perfectly affords analyzing trends as well as qualitative analysis, and is furthermore adequate to estimate material parameters such as concentration or diffusion coefficients of mobile ions.

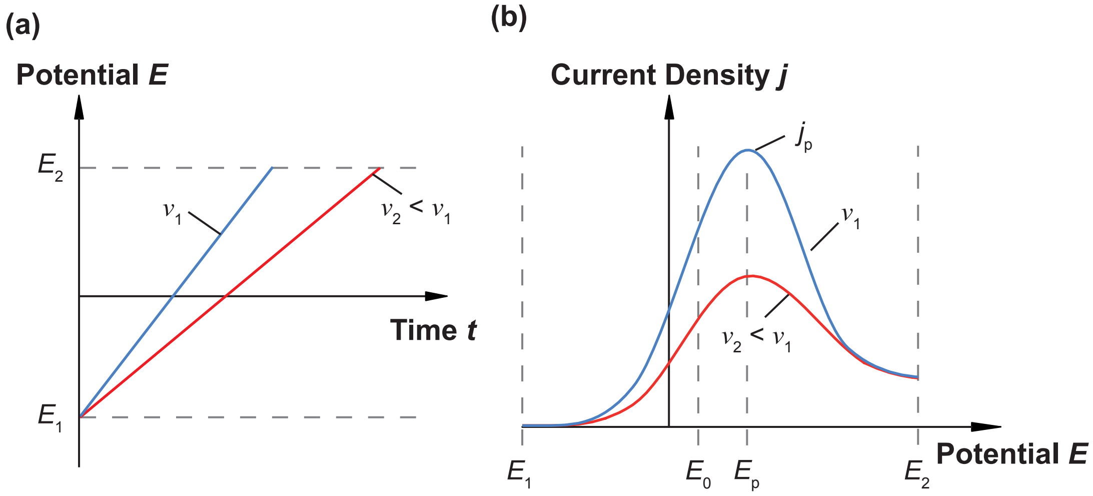

Figure 2.5. Linear voltage sweep while simultaneously measuring the current density response. (a) Transient voltage signals for two different sweep rates $\nu_1 > \nu_2$. (b) Current density response of the electrochemical system.

Considering a single electron transfer for simplification, the oxidation of a species S to S^+ can be written as:

$$S \longrightarrow S^+ + e^- \tag{2.4}$$

A linear voltage sweep from a potential $E = E_1$ to $E = E_2$ at a specific sweep rate $\nu = dE/dt$ (cf. 2.5a) can result in a current response as depicted in figure 2.5b. E_0

is the formal potential denoted by the working electrode. Assuming a virgin cell no significant electrochemical reaction is observed and only non Faradaic currents flow by increase of the potential below E_0. Beyond E_0 the oxidation of S to S^+ begins, resulting in a significant increase of the current density. By further increase of the potential, and thereupon of the driving force for oxidation, the concentration of S close to the electrode drops and mass transfer of S from or into the electrolyte is limited by the diffusion. The concentration depletion of S and the diffusion limitation results in an anodic (oxidation) current density peak j_p at the peak potential E_p. By further increase of the potential the concentration of S stays depleted and the diffusion layer growths at a constant mass transfer of the oxidizable species.

For cyclic voltammetry triangular potential pulses are now applied. The influence of the vertex potential on the subsequent current response is negligible when E_2 lies far enough beyond the anodic current density peak. After the vertex potential is reached, the driving force for oxidation is diminished and the previously oxidized S^+ ions will be reduced by decrease of the potential. Again, a diffusion limitation of the reducible species results in a cathodic (reduction) current density peak. However, for quantitative evaluation of cyclic voltammograms a new baseline for the current density is needed, since the decaying anodic current density is superimposing the current for the cathodic peak. Figure 2.6a depicts transient current responses during oxidation and reduction for two sweep rates $\nu_1 > \nu_2$. In figure 2.6b complete cyclic voltammograms for $\nu_1 > \nu_2$ and a single electron transfer are illustrated. The blue dotted line in figure 2.6b indicates the current response of a virgin cell.

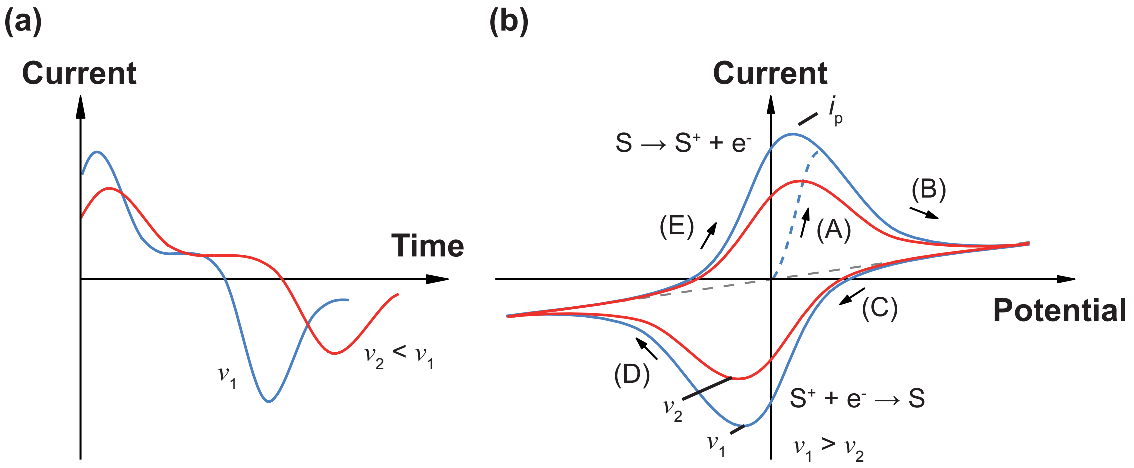

Figure 2.6. Oxidation and reduction measured by applying triangular voltage sweeps. (a) Transient measurement of the current during oxidation, (b) cyclic voltammetry (adapted from [36]).

The specific behavior of the electrochemical system depends instantly on the individual kinetic of the electron transfer during the redox reaction and sweep rate. In general, electrochemical redox systems can be classified in three different categories: (I) reversible systems, (II) irreversible systems, and (III) quasi reversible systems [38]. The nomenclature relates to the kinetic of the electron transfer in comparison to the sweep rate. In this way, the term *irreversible system* does not imply that the oxidation or reduction of a specific species is *generally* not reversible.

2.3.1. Reversible System

In case of a reversible system, also called Nernstian system, the kinetic of the electron transfer compared to the diffusion rate is fast and the concentration of active species close to the electrode follows immediately the ratio given by the Nernst equation (chapter 2.4) [36]:

$$E(x=0,t) = E_0 + \frac{RT}{zF} \ln \frac{c_{\mathrm{S}^+}(x=0,t)}{c_{\mathrm{S}}(x=0,t)} \tag{2.5}$$

Here, $E(x=0,t) = E_1 + \nu t$ is the transient working electrode potential at any time t, R the universal gas constant, z the number of electrons transfered, T the absolute temperature, F the Faraday constant, as well as $c_{\mathrm{S}^+}(x=0,t)$ and $c_{\mathrm{S}}(x=0,t)$ the concentration of oxidized and reduced species at the electrode, respectively. x is the distance from the working electrode. The boundary condition for $x=0$ and $t>0$ can be written as:

$$\frac{c_{\mathrm{S}^+}(x=0,t)}{c_{\mathrm{S}}(x=0,t)} = \exp\left(\frac{zF}{RT}\left(E_1 + \nu t - E_0\right)\right) \tag{2.6}$$

With Fick's second law and the diffusion coefficients D_{S^+} and D_{S} of the oxidized and reduced species, respectively, the diffusion of S^+ and S can be obtained:

$$\frac{\mathrm{d}c_{\mathrm{S}^+}}{\mathrm{d}t} = D_{\mathrm{S}^+}\left(\frac{\mathrm{d}^2 c_{\mathrm{S}^+}}{\mathrm{d}x^2}\right) \tag{2.7}$$

$$\frac{\mathrm{d}c_{\mathrm{S}}}{\mathrm{d}t} = D_{\mathrm{S}}\left(\frac{\mathrm{d}^2 c_{\mathrm{S}}}{\mathrm{d}x^2}\right) \tag{2.8}$$

Using Fick's first law the current density j holds:

$$j = -zFD_{\mathrm{S}^+}\left(\frac{\mathrm{d}c_{\mathrm{S}^+}}{\mathrm{d}t}\right) = zFD_{\mathrm{S}}\left(\frac{\mathrm{d}c_{\mathrm{S}}}{\mathrm{d}t}\right) \tag{2.9}$$

In the special case of an ideally reversible system a semi-infinite linear diffusion and no electrochemical reaction at the potential E_1 is assumed. A reversible system requires that the concentration of oxidized ions S^+ at the working electrode ($x = 0$) tends to zero, while the concentration of S^+ within the electrolyte ($x \rightarrow \infty$) approaches the constant (bulk) concentration $c_{\mathrm{S},0}$. At any time t the boundary conditions for the concentration of S^+ and S for $x = 0$ and $x \rightarrow \infty$ can be written as:

$$c_{\mathrm{S}^+}(x = 0, t) = 0 \tag{2.10}$$

$$c_{\mathrm{S}}(x \rightarrow \infty, t) = c_{\mathrm{S},0} \tag{2.11}$$

Now, the transient current density is given by:

$$j(t) = zFD_{\mathrm{S}} \left.\frac{\mathrm{d}c_{\mathrm{S}}}{\mathrm{d}x}\right|_{x=0} \tag{2.12}$$

Based on the boundary conditions discussed above equation 2.12 can be solved, which leads to the expression [39]:

$$j(t) = zFc_{\mathrm{S},0}\sqrt{\pi D_{\mathrm{S}}\frac{zF}{RT}\nu} \cdot \chi\left(\frac{zF}{RT}\nu t\right) \tag{2.13}$$

χ is a dimensionless current density function, which can be solved numerically [37]. The graphical representation of χ is depicted in figure 2.7. A maximum of $\chi \approx 0.4463$ is found at the peak potential $E_{\mathrm{p}} \approx \pm 28.5/z\,\mathrm{mV}$ (at room temperature).

Figure 2.7 Graphical representation of the dimensionless current density function χ (adapted from [36; 37]).

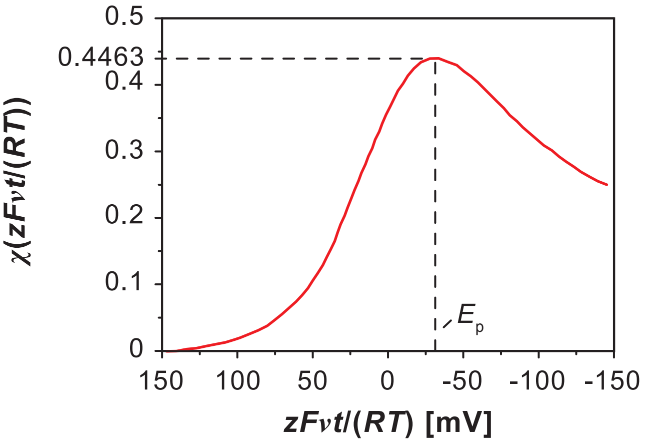

This leads to the Randles-Sevcik equation for reversible systems, which describes the current density peak as a function of the sweep rate ν:

$$j_{\mathrm{p}} = 0.4463 \cdot zF \cdot c_{\mathrm{S},0} \cdot \sqrt{\frac{zFD_{\mathrm{S}}}{RT}\nu}, \tag{2.14}$$

where j_p is in A/cm^2, $c_{\mathrm{S},0}$ in mol/cm^3, D_S in cm^2/s and the sweep rate ν is in V/s. The Randles-Sevcik equation predicts a linear increase of the peak current density j_p with $\sqrt{\nu}$. At room temperature equation 2.14 can be simplified:

$$j_\mathrm{p} = 2.69 \cdot 10^5 \cdot z^{\frac{3}{2}} \cdot c_{\mathrm{S},0} \cdot \sqrt{D_\mathrm{S}\nu} \tag{2.15}$$

For reversible systems the peak potentials $E_\mathrm{p} \approx \pm 28.5/z\,\mathrm{mV}$ for reduction and oxidation are independent on the sweep rate [36]. The Randles-Sevcik equation is valid for both reduction and oxidation. Nonetheless, the boundary conditions may not hold for thin film electrolytes in general. However, in this case the Randles-Sevcik equation can be used as a first approximation of electrolytic characteristics of thin films.

2.3.2. Irreversible System

In case of an irreversible system the electron transfer is slow in comparison to the diffusion rate, so that the ion concentration at the electrode cannot follow the Nernst equation. Thus, equation 2.6 is not valid anymore. To obtain notable Faradaic currents, a potential far beyond E_0 is needed. The current density can be written as:

$$j = zFD_\mathrm{S} \cdot \left[\frac{\mathrm{d}c_\mathrm{S}(x,t)}{\mathrm{d}x}\right]_{x=0} \tag{2.16}$$

The solution of equation 2.16 follows in analogous manner to that described in section 2.3.1. Again, a closed solution for the current density cannot be given. However, based on numerical integration the current density peak for irreversible systems at room temperature can be written as [37]:

$$j_\mathrm{p} = 2.99 \cdot 10^5 \cdot z^{\frac{3}{2}} \cdot c_{\mathrm{S},0} \cdot \sqrt{\alpha D_\mathrm{S}\nu}, \tag{2.17}$$

where $\alpha \approx 0.1...0.9$ (typical values) is the dimensionless charge transfer coefficient. It is remarkable that although the boundary conditions for reversible and irreversible systems are not comparable, a similar equation for the current density peak j_p in equation 2.16 and 2.17 can be found, respectively. However, in contrast to reversible systems the peak potential E_p in irreversible systems shifts to the vertex potential by increase of the sweep rate ν.

2.3.3. Quasi Reversible System

A system is called *quasi reversible* when the current density depends both on the charge transfer as well as diffusion limitation. This implies that depending on the sweep rate the system is either dominated by the diffusion limitation (making the system more or less reversible) or charge transfer (making the system more or less irreversible). However, besides the kinetic of the electrochemical system itself high sweep rates resulting in higher current densities may also result in a shift of the peak potential due to significant ohmic loss effects in the electrolyte.

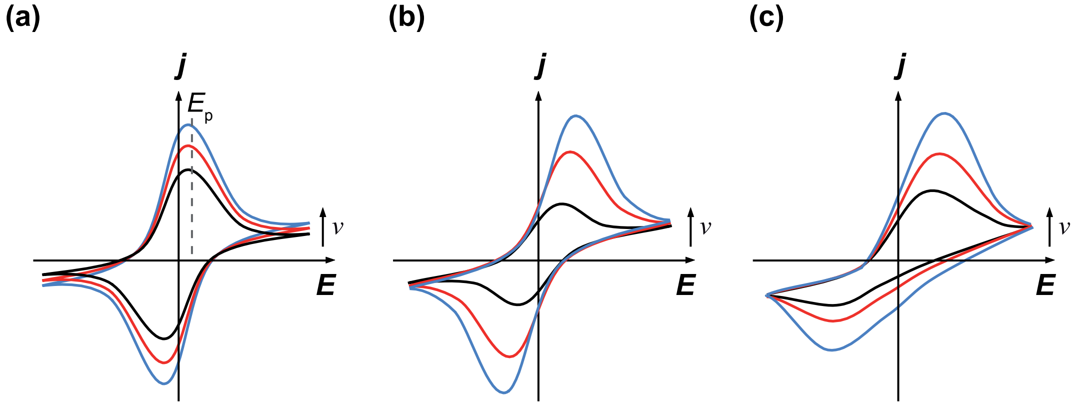

Figure 2.8. Cyclic voltammograms for different sweep rates $\nu_1 < \nu_2 < \nu_3$ in case of (a) a reversible redox reaction, (b) a quasi reversible reaction and (c) an irreversible redox reaction (adapted from [38]).

Figure 2.8 depicts exemplarily cyclic voltammograms of (a) a reversible system, (b) a quasi reversible system, and (c) an irreversible system by variation of the sweep rate. It is noteworthy that intercepts with the j-axis cannot directly be related to electrode potentials in thermodynamic equilibrium. A general trend can be observed that an electrochemical system may only yield reversible characteristics at small sweep rates [37]. In contrast, at high sweep rates irreversible characteristics are observed. The quasi reversible behavior is an intermediate state.

2.3.4. Multistep and Multielectron Charge Transfer Reactions

In chapter 2.3.1 to 2.3.3 a single electron transfer reaction is considered for simplification. Physical systems typically show multistep and/or multielectron charge transfer reactions. For example, in aqueous solutions dissociation of water can be observed resulting in hydrogen or oxygen formation dominating the current density at higher potentials. Additionally, the electrochemical active species itself can undergo multistep charge transfer reactions. For example, copper can be oxidized to Cu^+ or Cu^{2+} during one linear voltage sweep. Thus, for the case of multistep/multielectron charge transfer reactions the current densities of each reaction are superimposed as illustrated in figure 2.9. For a quantitative analysis two baselines have to be obtained in order to measure the precise current density peaks $j_{\mathrm{p},1}$ and $j_{\mathrm{p},2}$.

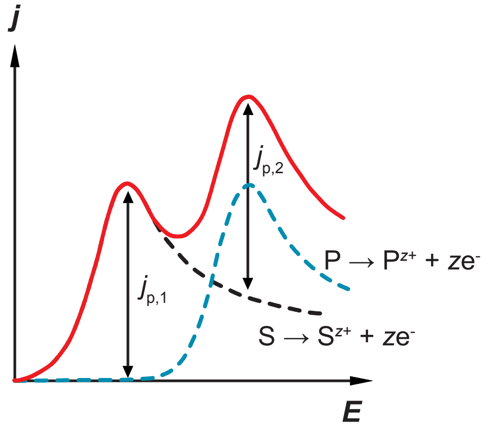

Figure 2.9 Multistep charge transfer reaction of an oxidation process $\mathrm{S} \longrightarrow \mathrm{S}^{z+} + ze^-$ and $\mathrm{P} \longrightarrow \mathrm{P}^{z+} + ze^-$. The blue curve is the current density j response of the electrochemical system consisting of the superimposition of both partial reactions (adapted from [37]).

2.4. Nonequilibrium States

Three origins of nonequilibrium states can be found, which are depicted in figure 2.10 [40]. A Nernst potential (see figure 2.10a) is formed due to a gradient of the chemical potential of a certain species (e.g. neutral silver atoms) [37]:

$$V_{\mathrm{N}} = V^0 + \frac{RT}{zF} \ln\left(\frac{a_{\mathrm{O}}}{a_{\mathrm{R}}}\right) \tag{2.18}$$

Here, V^0 is the standard potential, R the universal gas constant, T the absolute temperature, z the charge number, F the Faraday constant, and a_{O} and a_{R} the activity of the oxidized and reduced species, respectively. The Nernst potential is further discussed in section 2.4.1. In case of a concentration gradient of e.g. Ag^+ and OH^- ions a diffusion potential (cf. 2.10b) is generated, which will be discussed in section 2.4.2. Since the metallic filament in a ReRAM is considered as a nanosized phase an additional surface energy term must be added to the chemical potential, resulting in the Gibbs-Thomson potential as illustrated in figure 2.10c. The evidence of the Gibbs-Thomson potential has been reported for Ag/$\mathrm{GeS}_{2.2}$/Pt cells [28]. In this case the emf corresponds to the previously programmed metallic ON resistance R_{ON} after transition from an (unstable) ON to OFF state, and thus, it depends on the geometry of the nanosized filament. It should be noted that the contribution of the Gibbs-Thomson potential cannot be clearly distinguished from the contribution of the diffusion potential in the systems discussed in this work.

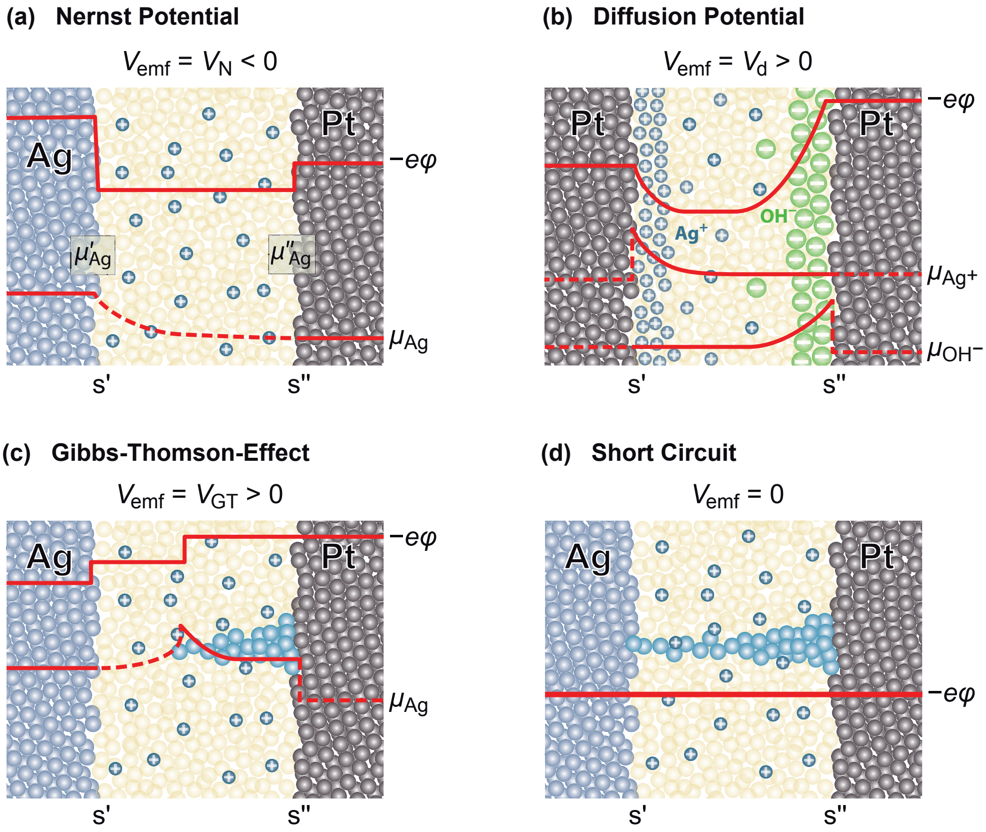
(a) Nernst Potential
$V_{emf} = V_N < 0$
Ag
Pt
$-e\varphi$
μ'_{Ag}
μ''_{Ag}
μ_{Ag}
s'
s"
(b) Diffusion Potential
$V_{emf} = V_d > 0$
Pt
Pt
$-e\varphi$
Ag^+
OH^-
μ_{Ag^+}
μ_{OH^-}
s'
s"
(c) Gibbs-Thomson-Effect
$V_{emf} = V_{GT} > 0$
Ag
Pt
$-e\varphi$
μ_{Ag}
s'
s"
(d) Short Circuit
$V_{emf} = 0$
Ag
Pt
$-e\varphi$
s'
s"

Figure 2.10. Origins of nonequilibrium states in redox based resistive switches resulting in an electromotive force voltage V_{emf} (redrawn from [40]). $e\varphi$ describes the electrostatic potential. (a) Nernst potential V_{N} given by electrochemical activity gradient of atomic silver μ_{Ag}, (b) concentration gradient of Ag^+ and OH^- ions resulting in a diffusion potential voltage V_{d}, (c) the chemical potential of silver must be extended by an additional surface energy term in case of a nanosized filament, resulting in the Gibbs-Thomson potential V_{GT}, and (d) the emf voltage cannot be measured in case of a metallic short circuit. The interfaces electrode/electrolyte (insulator) and electrolyte (insulator)/electrode are labeled by s' and s".

Depending on the operation nonequilibrium states are induced in ReRAMs based on at least one of these three effects. These nonequilibrium states result in a measurable cell voltage V_{Cell}, whose value depends both on the device operation and material properties. In particular, the ionic and electronic transference number t_{ion} and t_e (defined by the ionic and electronic partial conductivity σ_{ion} and σ_e) strongly influence the measurable cell voltage V_{Cell} (with $t_{\mathrm{ion}} + t_e = 1$):

$$V_{\mathrm{Cell}} = t_{\mathrm{ion}} V_{\mathrm{emf}} = \frac{\sigma_{\mathrm{ion}}}{\sigma_{\mathrm{ion}} + \sigma_e} V_{\mathrm{emf}} \qquad (2.19)$$

Here, $t_i = \sigma_i / \sum_j \sigma_j$ is the transference number of species i given by the quotient of the conductivity σ_i and the total conductivity $\sum_j \sigma_j$. In this regard, t_{ion} is the ionic transference number, which is a sum of the transference numbers of all ionic species participating to the emf. In case of a metallic short circuit (e.g. low resistive ON state in ReRAMs, cf. 2.10d) $t_e \rightarrow 1$ holds. Thus, in this case no emf voltage can be measured according to equation 2.19.

2.4.1. Nernst Potential

A simple H_2 partial pressure concentration cell, as depicted in figure 2.11, is a typical example of an electrochemical system, where a Nernst potential can be observed. A H^+ conductor with electrode grids on both sides separates two half cells with different hydrogen partial pressures $p{H_2}^{\mathrm{I}} > p{H_2}^{\mathrm{II}}$. The chemical potential gradient is a driving force for H_2 diffusion from half cell I to II. However, only protons are mobile within the H^+ conductor. Hence, molecular hydrogen will be oxidized at the left electrode and protons will be reduced to molecular hydrogen at the right electrode. The electrons involved in this redox reaction are charging the electrode grids resulting in an electric field, which will counter act the chemical potential difference, and as follows, an electrochemical equilibrium is reached.

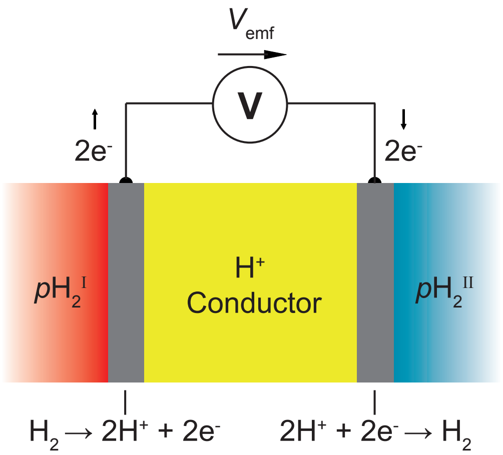

Figure 2.11 Schematic of a H_2 partial pressure concentration cell with a concentration gradient determined by the hydrogen partial pressure in both half cells $p{H_2}^{\mathrm{I}} > p{H_2}^{\mathrm{II}}$.

It is sufficient to describe the redox reaction on each side $i \in \{\mathrm{I,II}\}$ of the concentration cell by the chemical potential $\mu_{\mathrm{H}_2,i}$ since H_2 is neutral [36]:

$$\mu_{\mathrm{H}_2,i} = \mu^0_{\mathrm{H}_2,i} + kT \ln a_{\mathrm{H}_2,i} = 2\bar{\mu}_{\mathrm{H}^+,i} + 2\bar{\mu}_{e,i}, \tag{2.20}$$

where k is the Boltzmann constant, T the absolute temperature, $a_{\mathrm{H}_2,i}$ the chemical activity and $\mu^0_{\mathrm{H}_2,i}$ the standard chemical potential of H_2 on side i, respectively. The charge number is $z = 2$ for H_2.

For gaseous reactants the chemical activity can be expressed by the partial pressure of the reactant p_x, the standard pressure p^0 and a dimensionless fugacity coefficient ϕ_x:

$$a_x = \phi_x \frac{p_x}{p^0} \tag{2.21}$$

The fugacity coefficient depends on the active species, and is thus, equal for both half cells. The local electrostatic potential is the potential at the electrode E, i, respectively, and can be expressed by the electrochemical potential of the electrons:

$$\bar{\mu}_{e,i} = \mu_{e,i} - e\varphi_{\mathrm{E},i} \tag{2.22}$$

Evidentiality, $\mu_{e,\mathrm{I}} = \mu_{e,\mathrm{II}}$ when both electrodes are of the same material. Hence, the potential difference is given by:

$$\varphi_{\mathrm{E,I}} - \varphi_{\mathrm{E,II}} = \frac{\bar{\mu}_{e,\mathrm{II}} - \bar{\mu}_{e,\mathrm{I}}}{e} \tag{2.23}$$

With equation 2.20 it follows:

$$\varphi_{\mathrm{E,I}} - \varphi_{\mathrm{E,II}} = \frac{1}{2e} \cdot \left(\mu_{\mathrm{H_2,II}} - \mu_{\mathrm{H_2,I}}\right) + \frac{1}{e} \cdot \left(\bar{\mu}_{\mathrm{H^+,II}} - \bar{\mu}_{\mathrm{H^+,I}}\right) \tag{2.24}$$

The concentration gradient of $\mathrm{H^+}$ ions and the electrical potential gradient within the electrolyte is zero, and thus, $\bar{\mu}_{\mathrm{H^+,I}} - \bar{\mu}_{\mathrm{H^+,II}} \to 0$. With $V_{\mathrm{emf}} = V_{\mathrm{N}} = \varphi_{\mathrm{E,I}} - \varphi_{\mathrm{E,II}}$, and equation 2.20 and 2.24 the electromotive force may be written as ($z = 2$):

$$V_{\mathrm{emf}} = V^0 + \frac{kT}{ze} \ln\left(\frac{p\mathrm{H_2}^{\mathrm{II}}}{p\mathrm{H_2}^{\mathrm{I}}}\right) \tag{2.25}$$

Here, the standard potential is $V^0 = 1/(2e) \cdot \left(\mu^0_{\mathrm{H_2,II}} - \mu^0_{\mathrm{H_2,I}}\right)$. In the case of a $\mathrm{H_2}$ partial pressure concentration cell $V^0 = 0$ due to the same reaction on both sides of the electrolyte. Equation 2.25 is the Nernst equation, where the partial pressures can be also replaced in a more general form by chemical activities. The hydrogen concentration cell example can be applied for other electrochemical systems as well, where a gradient of the electrochemical activity of a certain species is observed. For example, in case of a Ag/AgI/Pt cell the electrochemical activity of silver at the Ag/AgI interface (s') is different from the AgI/Pt interface (s"). In this way, a Nernst potential is induced in the cell.

2.4.2. Diffusion Potential

Besides the Nernst potential a diffusion potential contribution to the emf voltage is observed in case of excess concentrations of charged species [40]. In general, the diffusion potential voltage V_d is given by [41]:

$$V_\mathrm{d} = -\frac{kT}{e} \sum_i \int_{\mathrm{II}}^{\mathrm{I}} \frac{t_i}{z_i}\, d\ \ln a_i \tag{2.26}$$

Here, k is the Boltzmann constant, T the absolute temperature, e the elementary charge, z_i the charge number, t_i the transference number and a_i the activity of species i (including ions and electrons), respectively. For the derivation of the diffusion potential equ. 2.26 is integrated along the concentration gradients (e.g. I: high concentration, II: low concentration). Figure 2.12 depicts two examples where the concentration gradient of two species is in the same and opposite direction, respectively.

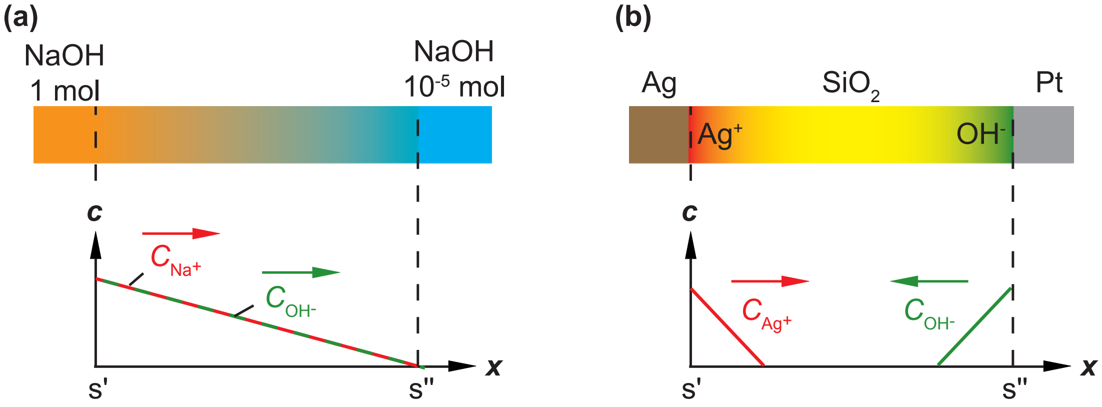

Figure 2.12. Example of the origin of a diffusion potential for two theoretical systems. (a) Concentration profile for Na^+ and OH^- ions in case of a 1 mol:NaOH/10^{-5} mol:NaOH solution system. The concentration of both ions is equal. The red and green arrows indicate the diffusion direction of each species. Both anions and cations diffuse in the same direction. (b) Concentration profile for Ag^+ and OH^- in case of a Ag/$\mathrm{SiO_2}$/Pt ReRAM cell. Now, the concentration profiles are not in the same direction, and thus, the directions of diffusion are opposed.

The situation of a 1 mol:NaOH/10^{-5} mol:NaOH solution system is illustrated in figure 2.12a. Here, the concentration profile of Na^+ and OH^- ions is equal and the diffusion for both species is in the same direction. Thus, the integration limits in equation 2.26 are equal for both anions and cations. In this case, the contribution of Na^+ and OH^- would be compensated. However, a small diffusion potential voltage is measured due to the different mobility of each ion species.

A different situation is given in figure 2.12b. As discussed in chapter 4.1, OH^- acts as a counter charge for the anodic oxidation of the silver electrode. Here, Ag^+ and OH^- show opposite diffusion directions due to their concentration gradients. In this case the integration limits I and II in equation 2.26 are different for each species. This inhomogeneous charge distribution results in a diffusion potential voltage accounted for Ag^+, OH^- and e^- (not shown in fig. 2.12b). In case of a $\mathrm{Ag/SiO_2/Pt}$ ECM cell the average of the total ionic transference number is given by $\bar{t}_{\mathrm{ion}} = \bar{t}_{\mathrm{Ag}^+} + \bar{t}_{\mathrm{OH}^-}$ with $z_{\mathrm{Ag}^+} = +1$, $z_{\mathrm{OH}^-} = -1$ and $z_{e^-} = -1$ [28]. Thus, the diffusion potential voltage may be written as:

$$V_{\mathrm{d}} = V_{\mathrm{d,Ag}^+} + V_{\mathrm{d,OH}^-} + V_{\mathrm{d},e^-} \tag{2.27}$$

$$\Rightarrow V_{\mathrm{d}} = \frac{kT}{e} \cdot \left(-\bar{t}_{\mathrm{Ag}^+} \ln \frac{\left(a_{\mathrm{Ag}^+}\right)_{\mathrm{s'}}}{\left(a_{\mathrm{Ag}^+}\right)_{\mathrm{s''}}} - \bar{t}_{\mathrm{OH}^-} \ln \frac{\left(a_{\mathrm{OH}^-}\right)_{\mathrm{s'}}}{\left(a_{\mathrm{OH}^-}\right)_{\mathrm{s''}}} - \bar{t}_{\mathrm{e}^-} \ln \frac{\left(a_{e^-}\right)_{\mathrm{s'}}}{\left(a_{e^-}\right)_{\mathrm{s''}}} \right) \tag{2.28}$$

Experimental results on nonequilibrium states are given in chapter 4.3. Furthermore, the impact of the Nernst potential (equation 2.25) and the diffusion potential (equation 2.28) on ReRAMs are discussed in chapter 5.2.

3. Experimental

In this chapter the experimental methods used within this work are outlined. This includes the fabrication processes covering thin film deposition, and pattern transfer using UV lithography and reactive ion etching. Special attention is paid to the analytical methods, which were primarily used in the context of this work. Nondestructive measurement techniques such as X-ray Diffraction (XRD) are used to investigate the structure and crystallographic properties of the deposited thin films. Furthermore, the electrical characterization of the fabricated samples is certainly of major importance. Besides the experimental techniques introduced in this chapter, additional methods such as Rutherford Backscattering Spectroscopy (RBS), X-ray Photo Electron Spectroscopy (XPS) and Atomic Force Microscopy (AFM) were also used. Detailed information on these techniques can be found in the corresponding literature (e.g. [42–45])

3.1. Fabrication Processes

3.1.1. Physical Vapor Deposition (PVD)

For thin film fabrication Physical Vapor Deposition (PVD) was used within this work covering direct current (DC) and radio frequency (RF) sputtering, electron-beam (e-beam) evaporation and thermal evaporation. While Chemical Vapor Deposition (CVD) methods (and in particular Atomic Layer Deposition, ALD) are commonly used in semiconductor industry, PVD is typically used in ReRAM research due to ease of sample fabrication. Nevertheless, sputtering and evaporation are state of the art technologies for thin film deposition, and are thus, only briefly introduced. For sputtering and e-beam evaporation a Cluster Tool 500 ES by *von Ardenne* was used as depicted in figure 3.1. The tool is equipped with an e-beam evaporation chamber, a sputter chamber and a transfer chamber, which allows to fabricate *in situ* SiO_2 and Pt thin film stacks without breaking the vacuum. The process tool offers four positions to store substrates in vacuum (P1 to P4), four sputter positions (DC1, DC2, RF and ISE) and one e-beam evaporation position (EB). Wafers can be transfered from each position using a robotic arm.

Sputtering

The term sputtering denotes ejecting material from a *sputter target*, which is subsequently deposited onto a *substrate*. Depending on the material used as target two categories of sputter deposition can be distinguished: direct current sputtering (used for metals) and radio frequency sputtering (used for any material but mainly for semiconductors and insulators). During DC sputtering a sputter gas (e.g. argon) is injected into a high vacuum chamber. By applying an electric field between the cathode (target) and anode (substrate) the sputter gas is ionized and the positively charged ions are accelerated towards the target under the electric field, and ballistically eject target material. Subsequently, the ejected material condenses onto the substrate. The deposition rate can be increased by increase of the sputter power and decrease of the chamber pressure. At high pressure, target material will collide with gas atoms more easily resulting in a lower deposition rate. However, at high deposition rates the thin film quality (e.g. surface roughness) degrades. Therefore, high pressure DC sputtering (about 10^{-3} hPa to 10^{-2} hPa) was used within this work.

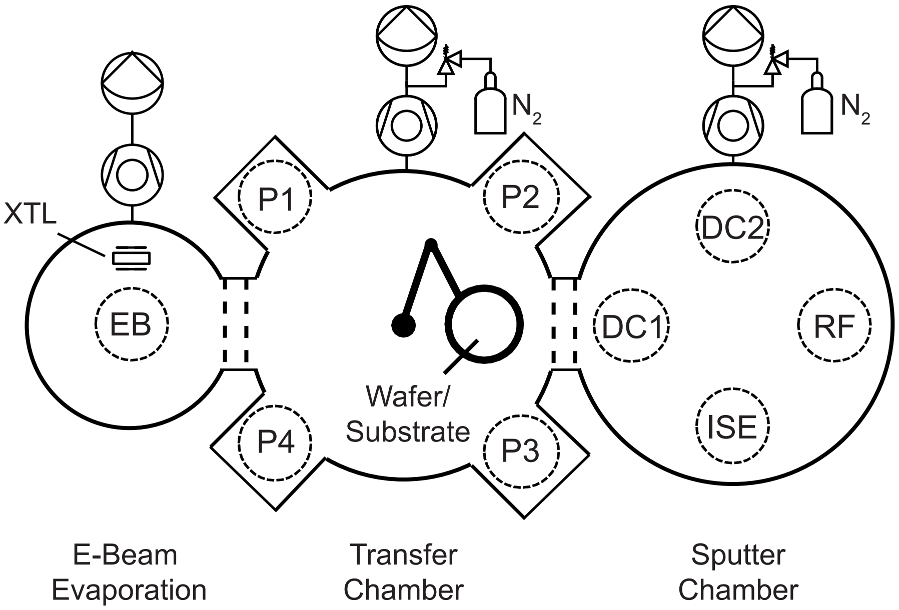

Figure 3.1. Schematic of the Cluster Tool 500 ES by *von Ardenne*. The 6” high vacuum process tool is equipped with an e-beam evaporation chamber, a sputter chamber and a transfer chamber. The Inverse Sputter Etching (ISE) position is not used in this work.

The above described sputter process can be only utilized for conducting materials such as platinum. When semiconductors or insulators are sputtered the target being collided by sputter gas ions cannot be discharged. Thus, charging of the target results in an electric field counter acting the applied electric field, which suppresses the sputter deposition. In this case, radio frequency sputtering is used for materials such as SiO_2. The alternating electric field avoids charging up of the target material. When the frequency of the electric field is high enough, the ions in the gas phase cannot follow the electric field due to their mass inertia. By applying a bias voltage the gas ions can be accelerated towards the target and eject material without charging up the target. The subsequent sputter deposition is similar to the DC sputter process.

In addition to the electric field a magnetic field is applied in case of *magnetron sputtering*. The magnetic field results in circuitous path carved by electrons enhancing the probability of ionizing sputter gas atoms by several orders of magnitude. This increases the deposition rate significantly. Sputtering can be also used for plasma etching. In this work a Reactive Ion Etching (RIE) tool (by *Roth und Rau*) was used for plasma etching. Details on this technique and process parameters can be found in [46].

Electron-Beam and Thermal Evaporation

Electron-beam and thermal evaporation have in common that in high vacuum (typically between 10^{-7} hPa to 10^{-5} hPa) a source material within a crucible is vaporized (by either a focused electron-beam or a heating coil). Atoms or molecules from the source material are evaporated and subsequently precipitate on the substrate. The thickness and deposition rate is typically controlled by a quartz oscillator (XTL). E-beam evaporation and thermal evaporation can be used both for metals, and semiconducting and insulating materials. In the particular case of silver iodide (chapter 4.2) thermal evaporation is used since AgI can be reduced by the electron-beam. Based on the vapor pressure the evaporation temperature T_B can be estimated by a fit function (cf. 3.2). For AgI the temperature for thermal evaporation is below 300 °C. The current for evaporation of AgI is in this case close to the lower limitation of the equipment. Therefore, the

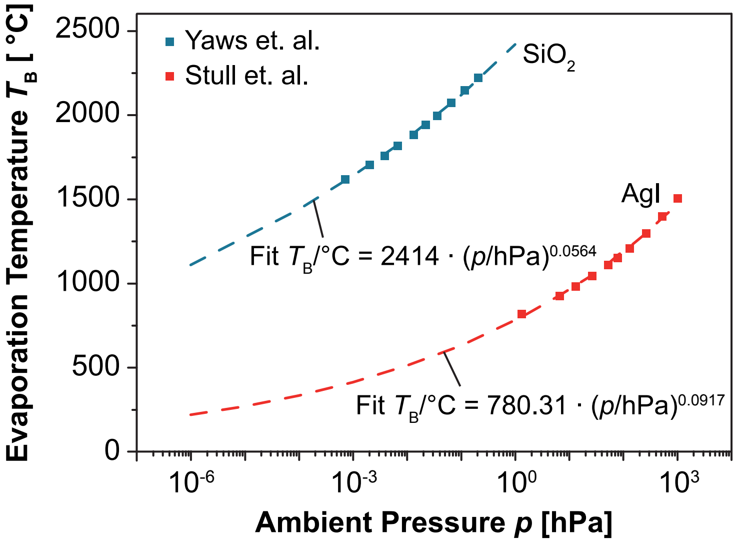

Figure 3.2 Vapor pressure results for SiO$_2$ (Yaws et. al. [47]) and AgI (Stull et. al. [48]). The evaporation temperature T_B is plotted versus the absolute ambient pressure p.

control of the evaporation speed is sophisticated. However, an advantage of e-beam and thermal evaporation is that the kinetic energy of the source material precipitating on the substrate is much lower in comparison to sputtering methods.

3.1.2. Pattern Transfer

Primarily, conventional (optical) UV lithography is used for pattern transfer. Thereby, a UV light sensitive photo resist polymer is deposited by spin-coating onto the substrate (with a thickness of $\approx 1.4\,\mu$m) and exposed to UV light after heating and drying. A photo-mask is in contact to the photo resist during UV light exposure. Depending on the process flow the resist in the illuminated areas will be either removed (positive lithography), or remains (negative lithography) after exposure and development. Finally, pattern transfer is done either by a subtractive pattern transfer process (e.g. using a Reaction Ion Etching tool) or a simple lift-off (e.g. in acetone), depending whether a positive or negative lithography process is used, respectively. For UV lithography a *Suss Microtech* Maskalinger MA 6 (UV wavelength 365 nm) is used. More details on the UV lithography process steps used within this work can be found in [35; 46; 49], and on UV lithography in general in [50]. The fabrication processes for nano crossbar devices is described in [51].

3.2. Characterization Methods

3.2.1. Morphology and Stoichiometry Analysis

Thin film morphology was mainly analyzed using a *Veeco* CP-2 Atomic Force Microscope (AFM) in noncontact mode and a *Zeiss* 982 Gemini digital Scanning Electron Microscope (SEM). In case of silver iodide thin films, the electron-beam of the SEM affects the morphology and stoichiometry of the thin films and therefore, an AFM is more suitable for morphology analysis.

Analysis of stoichiometry requires various methods including Rutherford Backscattering Spectroscopy (RBS) and X-ray Absorption Spectroscopy (XAS). XAS measurements were performed at the A1 beam line at DORIS III (Deutsches Elektronen-Synchrotron, DESY, Hamburg) and at the 11A1 beamline at Taiwan Light Source. Additionally, impurities were analyzed using Energy Dispersive X-ray Spectroscopy (EDX) using the *Zeiss* 982 Gemini digital Scanning Electron Microscope. Moreover, injected Cu ions in SiO_2 were analyzed by X-ray Photo Electron Spectroscopy.

X-ray Diffraction (XRD)

The crystallographic structures of thin films were investigated by X-ray Diffraction, which utilizes the interference spectrum of a X-ray beam. When X-ray waves are reflected at the crystal lattice planes, the different path lengths of reflected waves lead to constructive and destructive interferences. This interference spectrum depends on the crystallographic structure and orientation of the thin film, the distance of lattice planes in the crystals, and the angle of incidence. A simple schematic of a XRD measurement is depicted in figure 3.3a.

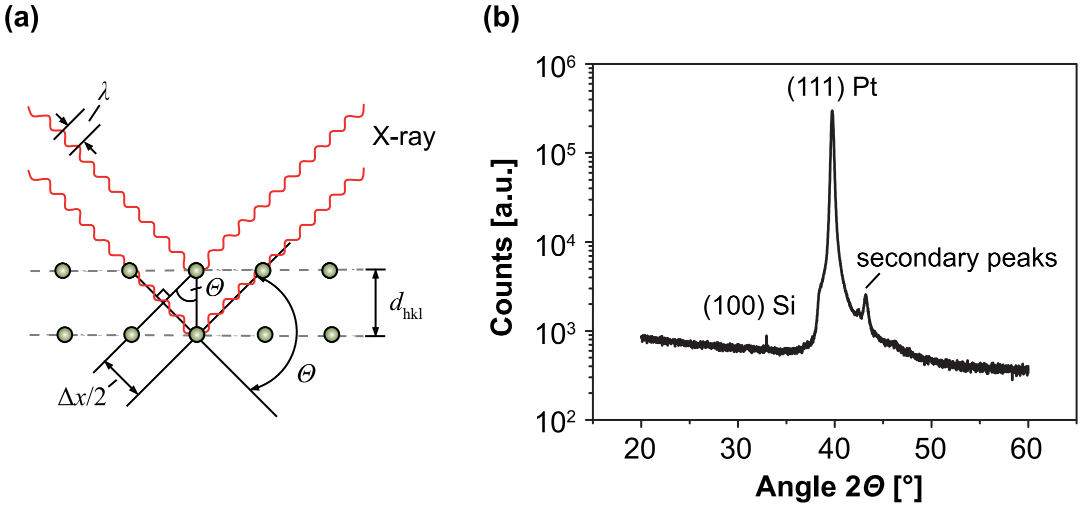

Figure 3.3. (a) Principle of X-ray Diffraction. The interference spectrum depends on the crystallographic characteristic of the thin film and the incident angle Θ. (b) Crystalline response of a platinum thin film on (100) orientated silicon.

A relation between the X-ray wave lengths, the crystal lattice plane distance d_{hkl} (where hkl are the Miller indices), the incident angle Θ and the order n of constructive interference is given by *Bragg's Law* [52]:

$$n \cdot \lambda = 2d_{\text{hkl}} \cdot \sin \Theta \tag{3.1}$$

By comparing the resulting XRD peaks with reference data, different crystalline stoichiometric phases can be distinguished. XRD spectra are measured using a X'Pert Pro diffractometer (by *PANalytical*) in Θ–2–Θ geometry. Since the XRD tool is not equipped with a monochromator, a nickel filter is used to suppress the X-ray tube characteristics. However, crystalline responses with high intensity can lead to secondary peaks being a measurement artifact. Figure 3.3b shows exemplarily the crystalline response of a 100 nm thick platinum film on (100) orientated silicon. The X-ray diffractometer is furthermore equipped with an *Anton Paar* XRK 900 thermal processing chamber allowing to heat the sample at a constant rate of 4 K/min, while simultaneously monitoring crystalline responses in ambient atmosphere. The peak positions of the XRD diffractograms are evaluated using the *PANalytical* High-Score software.

X-ray Reflectivity (XRR)

X-ray Reflectivity is a powerful measurement technique to analyze thin film thicknesses between 2 nm and 100 nm with an accuracy of typically down to 0.1 nm. Moreover, thin film roughness as well as density with a precision of up to 1 % can be measured. A schematic of a XRR measurement is illustrated in figure 3.4a. For XRR, a grazing incident angle is used. At $\Theta = \Theta_c$ total reflection is observed, whereas Θ_c corresponds to the thin film density. For $\Theta > \Theta_c$ oscillations can be detected. These oscillations can be attributed to reflections of X-rays at interfaces and at underlying layers resulting in constructive and destructive interferences. Thus, the period of oscillations $\Delta\Theta$ allows calculating the thin film thickness. By further increase of the reflection angle the intensity of the oscillations is decreasing due to the interface roughness.

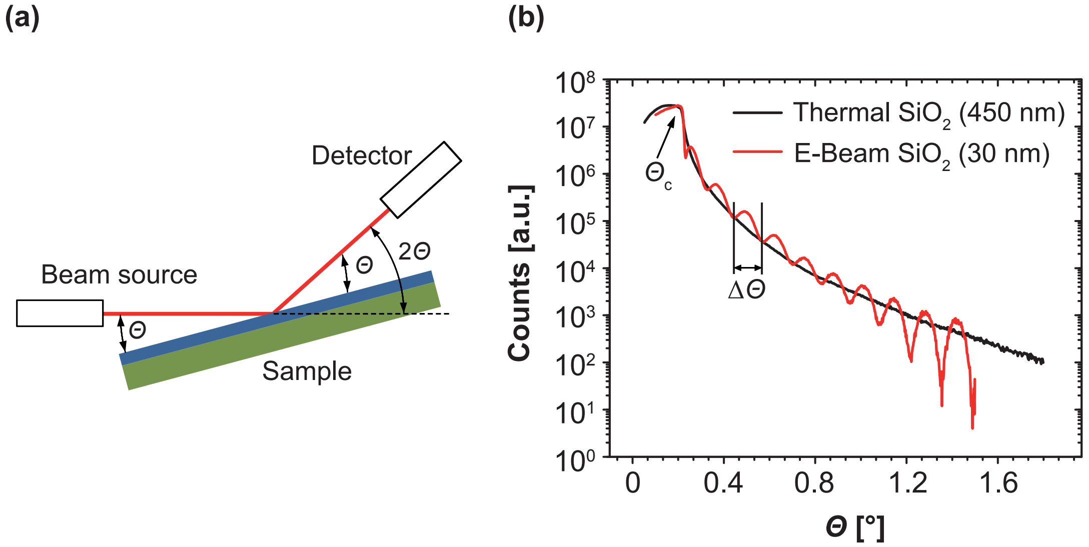

Figure 3.4. (a) Schematic of a X-ray Reflectivity measurement setup and (b) XRR scans of wet-thermally oxidized SiO_2 and e-beam evaporated SiO_2.

Typical XRR scans for wet-thermal oxidized SiO_2 (thickness 450 nm) and e-beam evaporated SiO_2 (thickness 30 nm) are shown in figure 3.4b. The thickness of the wet-thermal oxidized SiO_2 film is too high for XRR and oscillations are suppressed. However, the critical angle Θ_c can be used to calculate the film density. In contrast, the e-beam evaporated SiO_2 film shows pronounced oscillations.

XRR allows to analyze multilayer thin film stacks as well. Nonetheless, interpretation of XRR scans is usually sophisticated. Software tools such as *PANalytical* X'Pert Reflectivity are used to simulate the sample stack.

3.2.2. Electrical Characterization

Electrical characterization covers measurement techniques such as leakage current measurement, current-voltage sweeps (I/V switching curves and cyclic voltammetry, CV) and AC impedance spectroscopy. Leakage current measurements and potentiodynamic current-voltage sweeps are typically performed using a *Keithley* 6430 Subfemto Remote Source Meter, which allows to apply triangular voltage sweeps. Details on the waveform and background on the measurement technique can be found in [35; 49; 53; 54].

Using a triaxial measurement setup currents between $< 0.01\,\mathrm{pA}$ and $105\,\mathrm{mA}$ can be measured with a sweep rate from $1\,\mathrm{mV/s}$ to $4\,\mathrm{V/s}$ (depending on the integration time of the specific current range). The triaxial setup allows to decrease the effective cable capacity by a factor of 10^{-4} to 10^{-5}. Although the source meter can automatically adjust the measurement range, a preset current and voltage range is recommended to avoid switching between different ranges and to adjust a constant sweep rate. The specifications of the *Keithley* source meter can be found in [55]. In case of resistive switching experiments a current compliance is needed to avoid damage of the memory cell in the low resistive state. To suppress thermal effects [25], low current compliances between $1\,\mathrm{nA}$ and $10\,\mu\mathrm{A}$ were mainly used. In addition to the trixial measurement setup, all measurements have been performed in a radio frequency shielded setup.

Resistive Switching

Figure 3.5 shows the resistive switching characteristics of a Ag/AgI/Pt micro crossbar cell (see chapter 5). The current response is given by the black curve, while the cell voltage V_{Cell} during I/V sweeping is depicted by a red curve. Arrows indicate the sweeping direction. The *applied voltage* V_{Appl} is the voltage sent to the source meter by a computer. $V_{\mathrm{Cell}} = V_{\mathrm{Appl}}$ holds as long as the current is below the current compliance I_{CC} (a). When the cell switches from the high resistive state to the low resistive state, the effectively applied cell voltage is regulated to adjust the preset current compliance (b) to (d) despite V_{Appl}. For low cell voltages, a linear slope of the current versus cell voltage is observed when the current is below the current compliance level. In this case and during RESET the applied voltage and cell voltage are equal again ((e) and (f)).

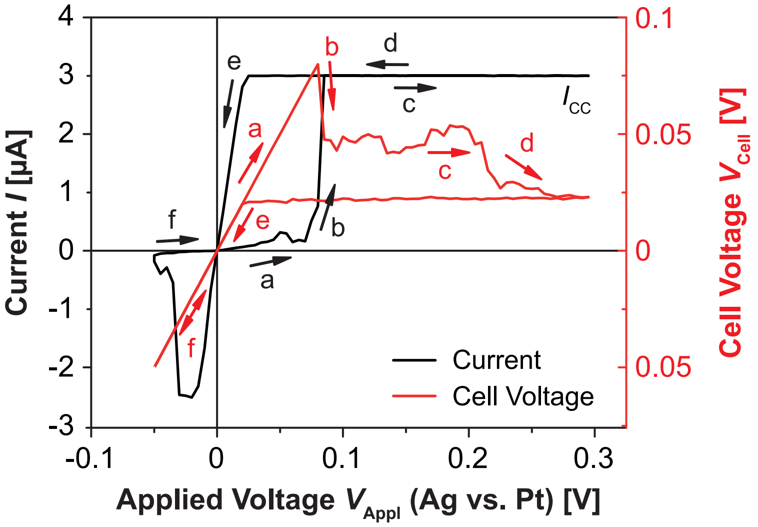

Figure 3.5. Resistive switching of a Ag/AgI/Pt micro crossbar cell. The current is given as black curve, while the effectively applied voltage to the cell is shown as red curve. As soon as the cell switches to the ON state, the source meter switches from voltage to current driven mode.

A current compliance measurement is depicted in figure 3.6. Here, a voltage pulse of 2 V is applied. Within a few hundred microseconds the current is regulated to the current compliance $I_{CC} = 50$ nA. However, a significant current overshoot of up to 105 nA is detected. This current overshoot can drastically affect the switching behavior of the cell and is a potential reason for device degradation.

Figure 3.6 Current compliance overshoot experiment. A current compliance of $I_{CC} = 50$ nA is applied and a current overshoot of up to 105 nA is recorded.

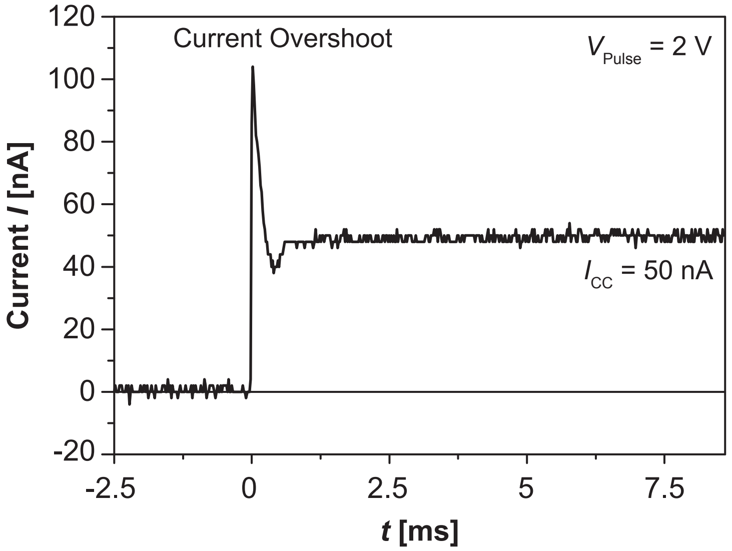

Cyclic Voltammetry

For cyclic voltammetry of SiO_2 based cells, sweep rates between 1 mV/s and 4 V/s and current ranges of 0.1 nA to 1 μA were used. The vertex potentials were set to ±2 V in case of Cu, and ±1.2 V...1.5 V in case of Ag to avoid resistive switching at higher voltages. The voltage and current transients and the corresponding cyclic voltammograms are shown in figure 3.7a,b using a Cu/SiO_2/Pt cell with sputtered silicon dioxide (see chapter 4.1). A current compliance is not needed since the current is limited by the electrochemical behavior of the cell and the cell remains in the high resistive state.

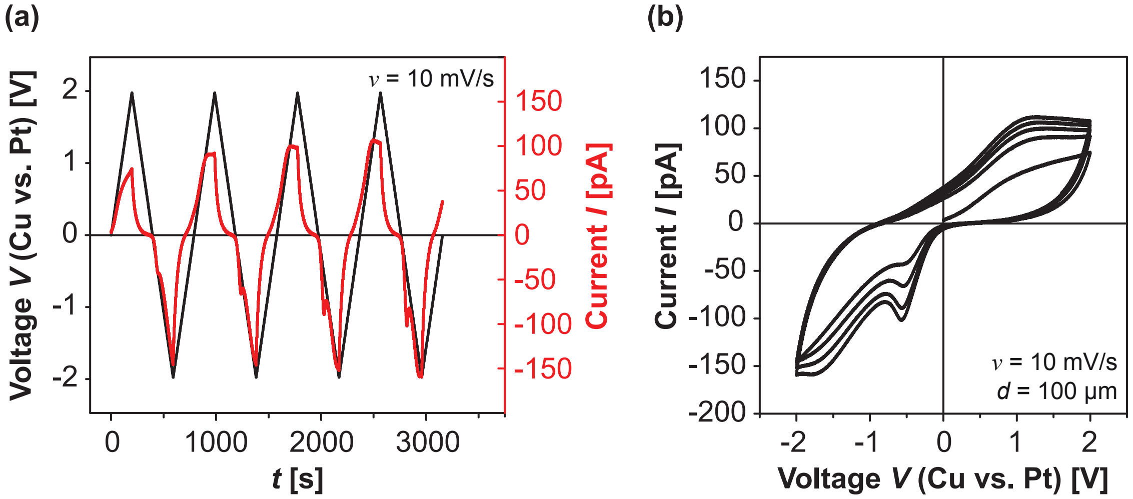

Figure 3.7. Cyclic voltammetry of a Cu/SiO_2/Pt cell using sputtered silicon dioxide (Cu electrode diameter $d = 100\,\mu m$). The sweep rate is set to 10 mV/s. (a) Voltage and current transients during cycling. (b) Corresponding cyclo voltammogram.

For cyclic voltammetry non polarizable reference electrodes are typically used and the electrode potentials are related to reference potentials. For example, a common reference electrode for liquid electrolytes is the standard hydrogen electrode (SHE). The reversible hydrogen electrode (RHE) or more practically the silver chloride electrode (Ag/AgCl/KCl) [36; 37] are often used as well. However, due to the sample geometry the placement of a reference electrode is not as simple as for liquid electrolytes in case of solid thin films [56; 57], and in particular even more complicated for high resistive thin films such as SiO_2. Despite that several approaches for solid thin film reference electrodes have been reported (e.g. [58; 59]), an approved and standardized reference electrode technique is still missing. Thus, in the context of this work a two-electrode setup is used, where the potential of the counter electrode (e.g. Pt) has been used as a quasi-reference electrode. Therefore, the impact of ohmic losses in the electrolyte has to be considered [56] when interpreting measurement results and identifying peak potentials to specific electrochemical reactions. Alternatively, additional experimental verifications (such as XAS or XPS) can be used to overcome this drawback.

Short Voltage Pulse Measurements

For short pulse measurements, with pulse lengths between 50 ns and 1 s, a Wavetek 100 MHz Synthesized Arbitrary Waveform Generator (model 395) was used. Pulse voltages between 70 mV to 2 V were applied. Transient current and voltage signals were recored by a Tektronix TSD 684A digital oscilloscope (1 GHz bandwidth). The voltage signal was measured by a 50 Ω coupled input in parallel to the sample (DUT, device under test) to suppress RF reflections. The input impedance (1 MΩ coupled input) for the current signals acts as a simple current/voltage converter and series resistor to limit the current in the low resistive ON state.

3.3. Material Characterization and Sample Preparation

3.3.1. Silicon Dioxide

Silicon dioxide is deposited by physical vapor deposition using either radio frequency sputtering or electron-beam evaporation. In both cases amorphous SiO_2 thin films are prepared. Nevertheless, morphology, film density and roughness depend on the deposition technique and parameters. Both sputtered and evaporated SiO_2 show similar electrical and electrochemical characteristics, respectively, and resistive switching can be observed in all fabricated Ag(Cu)/SiO_2/Pt devices. However, e-beam evaporation offers some benefits compared to RF sputtering, such as ease of thickness control using a quartz micro balance during evaporation and lower kinetic energy for deposition. Therefore, SiO_2 was mainly deposited by e-beam evaporation.

Thin Film Stoichiometry

The chemical composition of the deposited thin films was analyzed using Rutherford Backscattering Spectroscopy as depicted in figure 3.8a for e-beam evaporated and 3.8b sputtered silicon dioxide. In both cases the simulations of stoichiometric SiO_2 fit well to the measured spectra. Impurities of copper or silver have not been found.

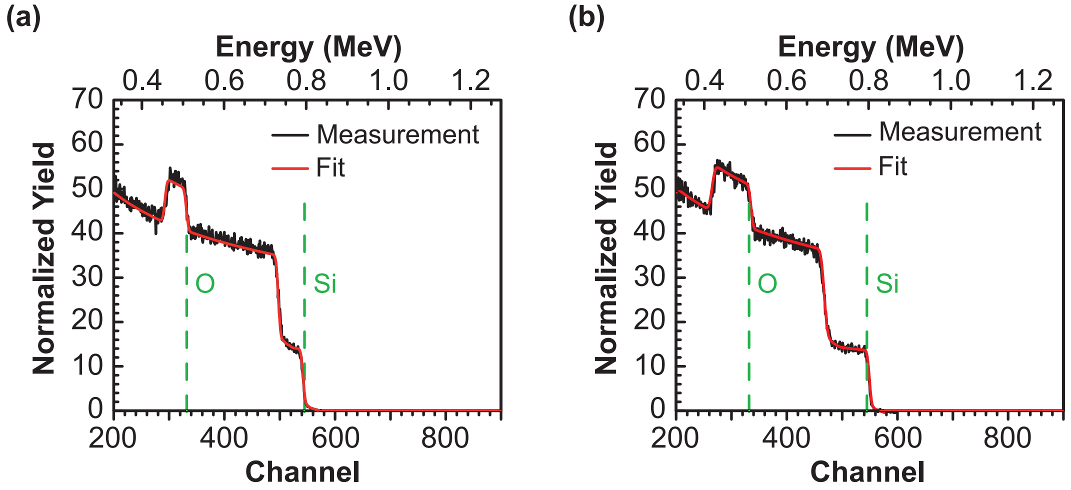

Figure 3.8. Rutherford Backscattering Spectroscopy of (a) 120 nm e-beam evaporated silicon dioxide and (b) 215 nm rf sputtered SiO_2. In both cases the measurements fit to simulations of stoichiometric SiO_2.

Thin Film Density and Morphology

X-ray Reflectivity scans of e-beam evaporated and sputtered SiO_2 are shown in figure 3.9a. For comparison the XRR signal of a silicon wafer after wet-thermal oxidation is depicted as well. The film density ρ is of particular interest since the amorphous structure on the nanoscale is believed to have an impact on the cation mobility. ρ can be calculated by the critical angle Θ_c. Based on a XRR simulation (not shown) the thin film density of both e-beam evaporated and sputtered SiO_2 equals $\rho = 2.2\,\mathrm{g/cm^3}$,

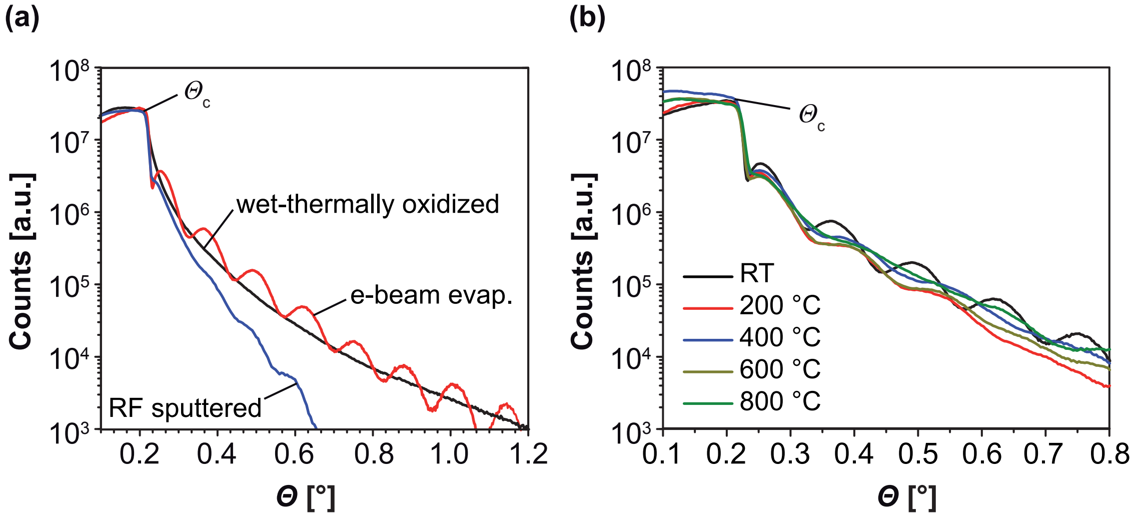

Figure 3.9. X-ray Reflectivity of (a) wet-thermal oxidized, e-beam evaporated and sputtered SiO_2, and (b) e-beam evaporated SiO_2 after temperature annealing. The thickness of the wet-thermal oxidized SiO_2 layer is 450 nm and of the e-beam and sputtered thin films between 15 nm and 30 nm, respectively.

which fits to the literature value of amorphous SiO_2 ($\rho_{\mathrm{Ref}} = 2.23\,\mathrm{g/cm^3}$, [60]) and to the density of wet-thermally oxidized silicon dioxide.

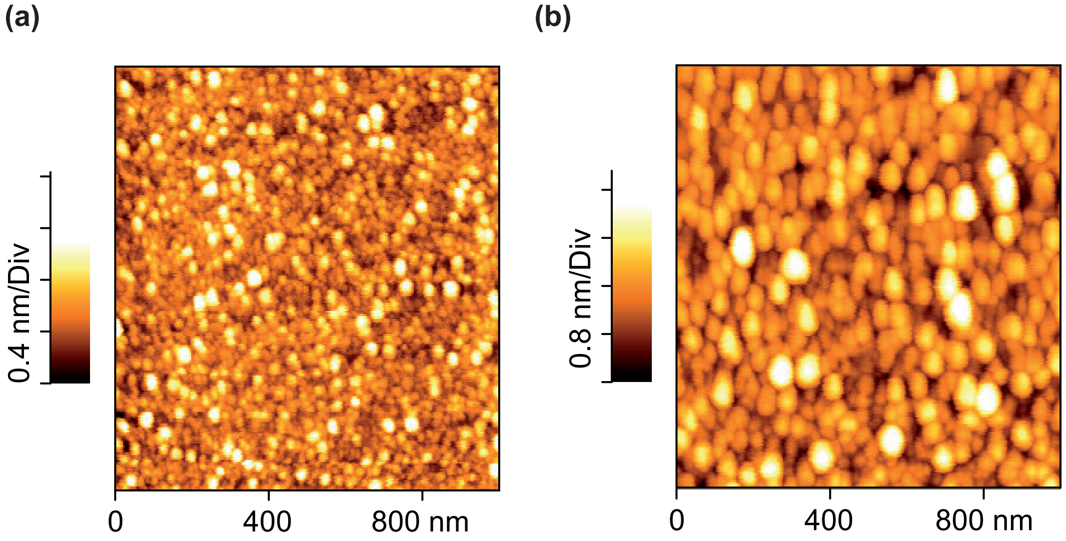

Figure 3.10. Atomic Force Microscopy of a 30 nm thick e-beam evaporated SiO_2 thin film on (a) a SiO_2/Si substrate and (b) a Pt/TiO_2/SiO_2/Si substrate.

Figure 3.9b shows XRR scans of e-beam evaporated SiO_2 after thermal annealing for 1 h in air at different temperatures (30 nm SiO_2 at RT = room temperature, 15 nm SiO_2 at 200 °C to 800 °C). In contrast to a previous work on resistively switching silicon dioxide [35], the critical angle does not shift to higher values, and as follows, an increase of the thin film density cannot be observed. Notwithstanding, a change of the density for a temperature range between 20 °C and 800 °C is questionable, because the as-deposit density is $\rho = 2.2\,\mathrm{g/cm^3}$, which is already close to ρ_{Ref} of amorphous silica. The thin film roughness of e-beam evaporated SiO_2 was analyzed using Atomic Force Microscopy. A roughness of $r_{\mathrm{RMS}} \approx 0.9\,\mathrm{nm}$ has been estimated on a SiO_2/Si substrate (figure 3.10a) and $r_{\mathrm{RMS}} \approx 2.4\,\mathrm{nm}$ on a Pt/TiO_2/SiO_2/Si substrate (figure 3.10b), respectively. This roughness fits to XRR measurements for e-beam evaporated SiO_2.

3.3.2. Silver Iodide

Silver iodide is a crystalline silver cation conductor offering a high ion conductivity. At room temperature the β- and γ-AgI phase are thermodynamically stable. A phase transformation to superionic conducting α-AgI can be observed above 147 °C for bulk silver iodide [61; 62]. Although bulk AgI is a well known Ag^+ ion conductor, in nanoscale dimensions the morphological and electrochemical characteristics (especially the resistive switching properties), and its stoichiometry has not been analyzed in detail yet.

Thin Film Stoichiometry

The crystalline structure of AgI thin films can be easily analyzed by X-ray Diffraction. This technique enables to distinguish between α-AgI, β-AgI and γ-AgI. AgI samples were heated from room temperature up to 600 °C (constant temperature ramp of 4 °C/min), while the crystalline response was simultaneously measured in a Θ-2-Θ geometry, in order to analyze the phase transition between γ-/β- and α-phase AgI thin films deposited on silicon wafers. The corresponding XRD profiles are shown in figure 3.11a.

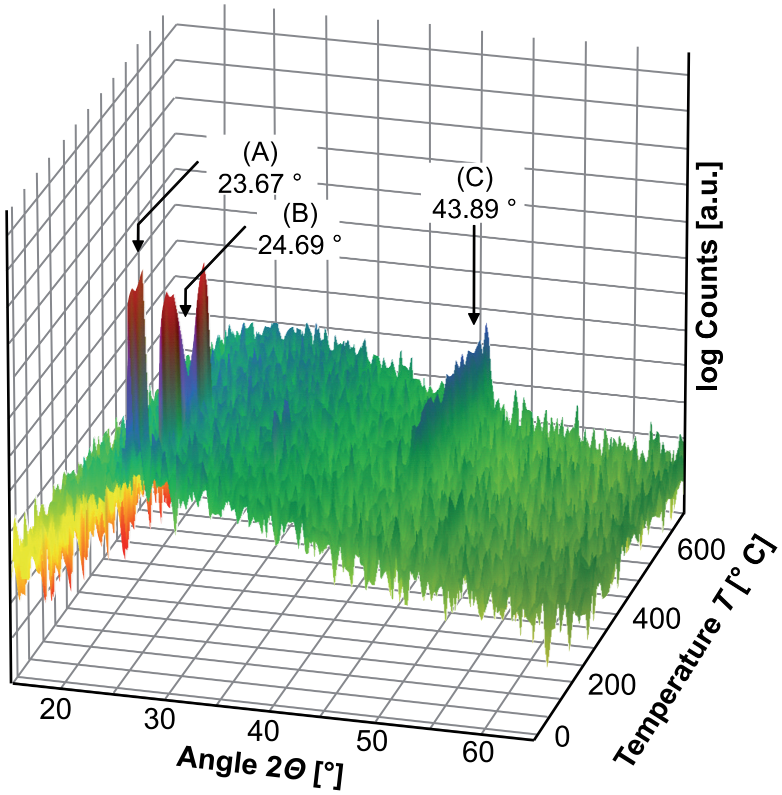

Figure 3.11. XRD profiles of a AgI thin film deposited on a silicon wafer simultaneously measured during increase of the sample temperature indicating a phase transition at $T \approx 145\,°\mathrm{C}$.

At room temperature the observed peak (A) at $2 \cdot \Theta = 23.67°$ corresponds to the (111) γ-AgI phase [63] and a thorough analysis reveals that the β-AgI phase concentration is below 1 % [64] (see chapter 4.2.2). At an ambient temperature above $T > 145\,°\mathrm{C}$ a phase transition to the α-AgI phase is observed, which is revealed by the peak (B) at $2 \cdot \Theta = 24.69°$, and fits well to literature values [61; 62]. Additionally, a high temperature peak for $T > 526\,°\mathrm{C}$ (C) at $2 \cdot \Theta = 43.89°$ is recorded. However, the identification of peak (C) is unclear. It can be attributed both to a β-AgI or more probably to a AgO phase.

In conclusion, (poly-) crystalline stoichiometric AgI thin films have been deposited and the characteristic phase transition to the high temperature phase of AgI is observed at about $T \approx 145\,^{\circ}\mathrm{C}$. Besides a potential decomposition of the thin film at high temperature ($T > 526\,^{\circ}\mathrm{C}$), nonstoichiometric crystalline phases have not been observed. Nonetheless, XRD profiles do not reveal the existence of amorphous nonstoichiometric phases. Therefore, X-ray Absorption Spectroscopy measurements have been performed in a detailed study (see chapter 4.2.2) revealing a high chemical stability of Ag on the deposited AgI thin films. This indicates the absence of nonstoichiometric amorphous phases.

Thin Film Density and Morphology

Besides the chemical composition of the deposited AgI thin films analyzed by XRD, both thin film density and morphology are of high importance for device performance. The morphology of a deposited AgI thin film measured by Atomic Force Microscopy is shown in figure 3.12a. The comparatively high roughness of $r_{\mathrm{RMS}} \approx 5.3\,\mathrm{nm}$ ($r_{\mathrm{RMS}} \approx 4.6\,\mathrm{nm}$ based on the XRR measurement) is contributed to the evaporation method. As the evaporation temperature of AgI is below $300\,^{\circ}\mathrm{C}$ in high vacuum (cf. 3.2), the control of the evaporation speed is difficult. This may result in a temporary high evaporation speed, and thus, a poor thin film roughness. Additionally, the adhesion of AgI especially on Pt,

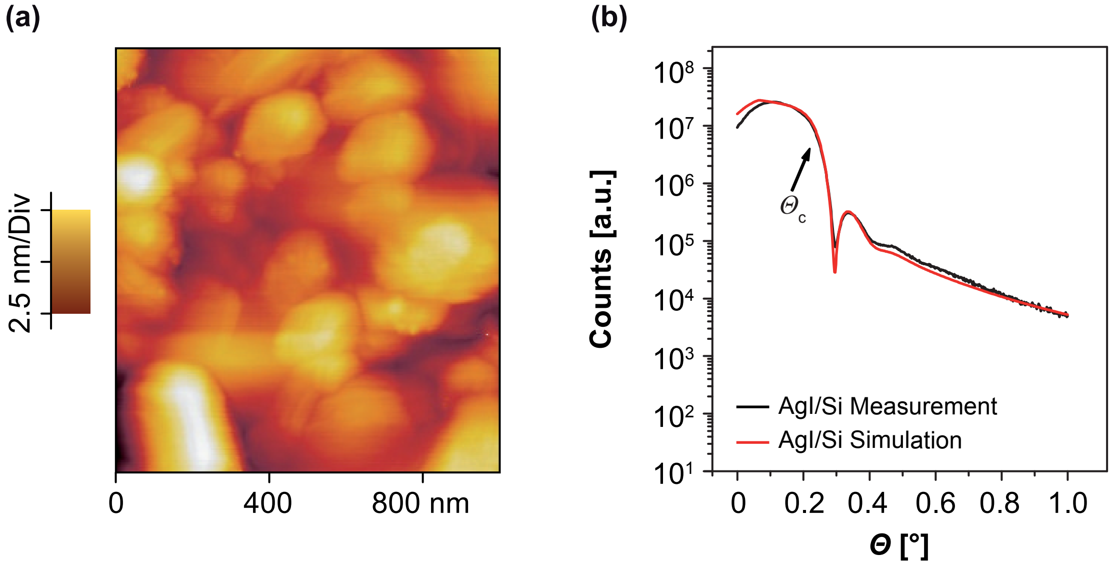

Figure 3.12. AgI thin film morphology and density analysis. (a) Atomic Force Microscopy scan of a deposited AgI thin film on Si revealing a high roughness of $r_{\mathrm{RMS}} \approx 5.3\,\mathrm{nm}$ ($r_{\mathrm{RMS}} \approx 4.6\,\mathrm{nm}$ based on the XRR measurement). (b) XRR measurement of a AgI thin film (intended thickness 20 nm) on a silicon substrate. The measurement is compared to a simulation of a 23.8 nm thick AgI layer. The thin film density ρ_{AgI} can be calculated by measuring the critical angle (see section 3.2.1).

Si, TiO_2 and SiO_2 is rather poor. This could further contribute to the high r_{RMS} value. Further experiments are required to optimize the thin film quality including alternative deposition methods such as Pulsed Laser Deposition (PLD).

The film density ρ_{AgI} has been measured by XRR (see figure 3.12b). Based on the critical angle a density of $\rho_{\mathrm{AgI}} = 4.4\,\mathrm{g/cm^3}$ has been found, which is smaller than the literature value of bulk AgI ($5.667\,\mathrm{g/cm^3}$ [65]). A reason for the deviation of ρ_{AgI} from the literature value could be a porous structure of the AgI thin film due to the evaporation conditions.

Pattern Transfer

Silver iodide is sensitive towards UV light, electron-beams and many chemicals including TMAH (Tetramethylammonium hydroxide), which is required for UV lithography and pattern transfer. Moreover, the adhesion of AgI thin films on SiO_2, Si, TiO_2, and Pt is poor. Though, conventional pattern transfer is unfeasible, pattering of micro crossbars and even nano crossbars can be realized when the AgI/Ag layers are deposited as the last critical process step during device fabrication.

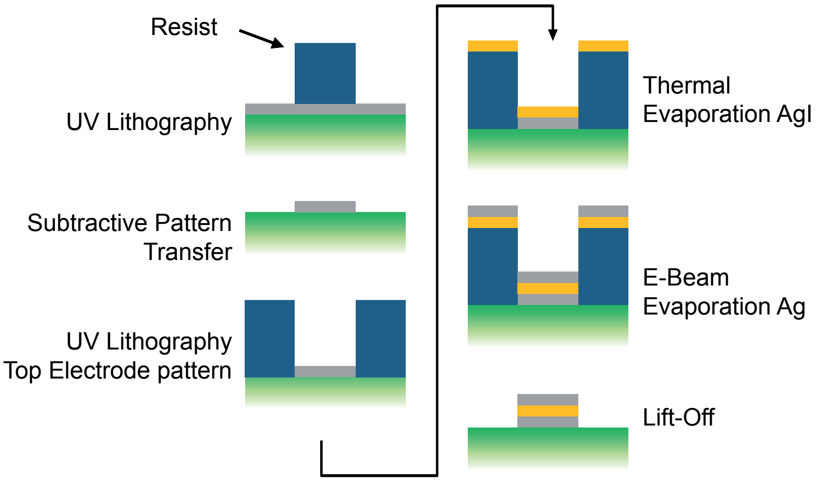

Figure 3.13. Flow chart of the pattern transfer for AgI based micro crossbars [54].

In [54] a fabrication method for micro crossbars is presented, which can be easily adapted for nano crossbars without making use of shadow masks (which typically limits scaling down the lateral dimensions). The process flow chart is shown in figure 3.13 for micro crossbars. At first, the Pt bottom electrodes are fabricated by conventional UV lithography or nano imprint technology, followed by subtractive pattern transfer using a Reactive Ion Etching tool or a Reactive Ion Beam Etching (RIBE) tool. In case of conventional ReRAM device fabrication the subsequent step would be the deposition of the electrolyte, i.e. silver iodide. However, following treatments may result in crucial impact on the AgI thin film. To avoid potential thin film damages the pattern for the top electrode is directly transfered either by UV or e-beam lithography to the etched bottom electrode. Subsequently, the AgI thin film and the actual Ag top electrode metal are deposited by thermal and e-beam evaporation, respectively, making use of the strongly anisotropic deposition characteristics. Finally, the device fabrication is completed by a lift-off in acetone, isopropanol and water. The lift-off step is crucial and needs to be act with caution.

4. Redox Processes in Thin Films

4.1. Cations in Insulators: Silicon Dioxide

Silicon dioxide is an insulating material, and widely used in nanoscale devices and information technology. Despite that SiO_2 is electrically insulating, electrochemical redox reactions of Cu/Cu^{z+} (charge number z) as well as Ag/Ag^+ at the interface with SiO_2 thin films can be observed. These redox reactions are analyzed in the following chapter using cyclic voltammetry and spectroscopic techniques such as XPS and XAS. Special attention is paid to the kinetics of the redox reactions, particular half cell redox reactions and cation diffusion behavior. Of high importance are nonequilibrium states, which are inherently induced during operation of redox based resistive switches. These nonequilibrium states result in a nanobattery effect, which is discussed in section 4.3.

4.1.1. Anodic Oxidation and Cation Diffusion Behavior

By applying a positive voltage between the active electrode (e.g. Cu or Ag) and inert electrode (e.g. Pt), anodic oxidation of the active electrode takes place and cations (e.g. Cu^+) are penetrating into the insulating SiO_2 thin film. Without limitation of the voltage and/or time the injected ions are reduced at the inert electrode and form a filament, and the cell switches to a low resistive state. However, when the voltage amplitude during a voltage sweep is limited to avoid resistive switching, redox processes prior to the switching event can be observed (see also chapter 5.1.1). These sweep experiments are further denominated as *cyclic voltammetry* (CV). A typical cyclic voltammogram for a $Cu/SiO_2/Pt$ cell is shown in figure 4.1. Here, the Cu oxidation appears to be the preceding process enabling the first resistive switching event, which is observed without voltage limitation (not shown). The current during the redox reaction depends on the electrode area and therefore, the current density is plotted in the following figures.

The observed current peaks are associated to redox reactions of the Cu electrode [53]. Despite that current peaks are clearly shown, a major disadvantage here is the missing reference electrode typically used for cyclic voltammetry experiments. This is due to the nanoscale vertical dimensions and comparatively high lateral insulator resistance (see

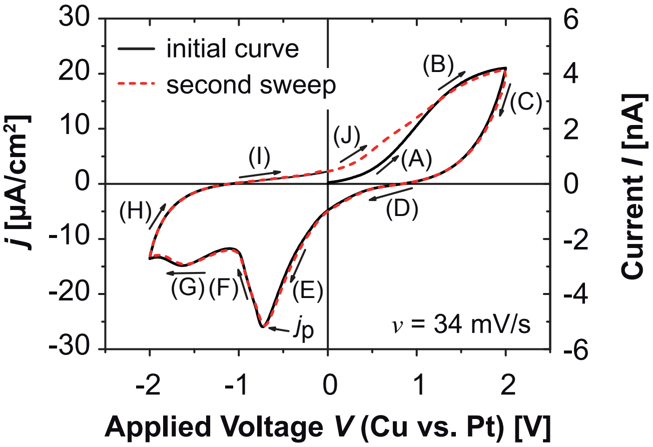

Figure 4.1 Cyclic voltammetry of a Cu/SiO_2/Pt cell (Cu top electrode diameter $d = 150\,\mu$m) [53]. By limitation of the voltage amplitude to avoid resistive switching, redox processes prior to the switching event can be analyzed. Arrows and labels indicate the direction of the sweep.

chapter 3.2.2). Nevertheless, CV curves give qualitative information and trends of the electrochemical system. In this way, the redox reactions depicted in figure 4.1 can be interpreted as follow: Cu is initially oxidized by applying a positive voltage between the Cu and Pt electrode (A). As the voltage further increases more Cu^{z+} ions are formed by anodic oxidation resulting in an increase of the current (B). The oxidized Cu ions are injected into the SiO_2 thin film under the concentration and electrical field gradients. After the vertex potential is reached, the current decreases because the driving force of the oxidation process is reduced (C). At $V \approx 0.85\,\mathrm{V}$ a reduction of the oxidized Cu ions is starting to take place (D). By further decrease of the applied voltage a reduction current density peak j_p at $V_\mathrm{p} \approx -0.72\,\mathrm{V}$ is observed. Here the concentration of Cu ions close to the Cu electrode is strongly decreased and the current is limited by the diffusion of Cu ions (injected into the SiO_2 thin film during oxidation). In this case the reduction cannot take place at the Pt electrode due to the voltage polarity. In contrast, injected Cu ions are reduced at the active electrode. The second peak (G) $V \approx -1.6\,\mathrm{V}$ is associated to a direct Cu^{2+} to Cu reduction or to a partial Cu^{2+} to Cu^{+} reduction. As soon as the driving force of the reduction is diminished, the absolute current decreases (H) while a second current zero crossing is observed at $-1.1\,\mathrm{V}$ (I). During the reverse sweeping anodic oxidation is observed although a voltage of less than 0 V is applied (J). Hence, the initial curve and second curve do not overlap for $V = 0$. Without an initial sweep in the positive direction, a current density peak j_p in the negative voltage regime has not been observed because there are no Cu ions which can be reduced.

Typical CV measurements with variable sweep rates ν are shown in figure 4.2a [53]. The current peaks increase by increase of the sweep rate, and simultaneously, the peak potential V_p shifts to more negative values, indicating an inhibited charge transfer controlled electrode reaction [37]. In case of an inhibited charge transfer, the reduction peak current density j_p can be estimated at room temperature based on the Randles-

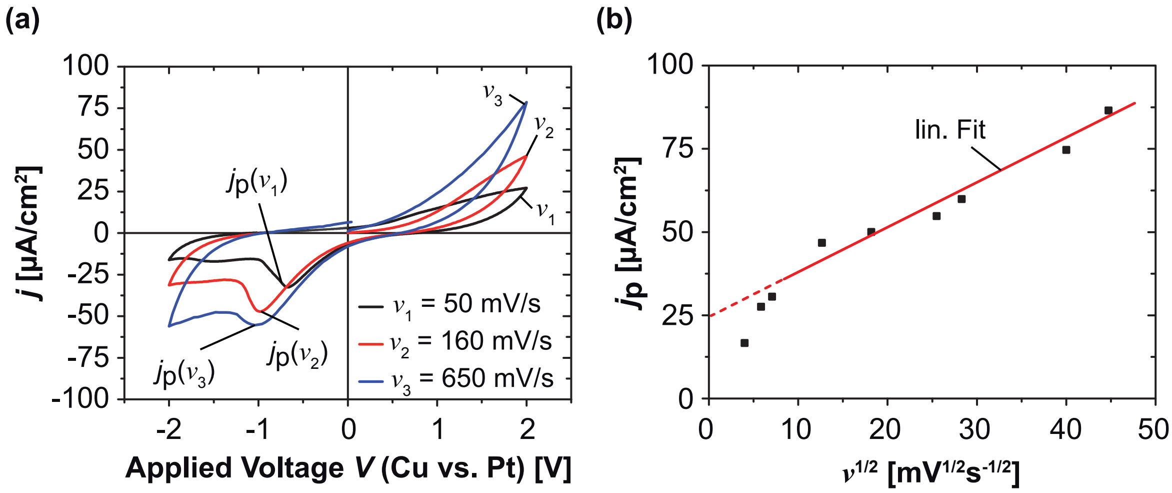

Figure 4.2. Kinetics of anodic Cu oxidation [53]. (a) Cyclic voltammorgrams by variation of the sweep rate ν. (b) Reduction peak j_p vs. $\nu^{1/2}$.

Sevcik equation (see chapter 2.3.1 and 2.3.2). Thus, a linear relation of j_p versus $\nu^{1/2}$ is expected, which is shown in figure 4.2b. At a sweep rate below $\approx 30\,\mathrm{mV/s}$ the interpretation of CV curves becomes difficult as more than one reduction and oxidation peaks are observed, which can be attributed to partial redox reactions of different Cu^{z+} species.

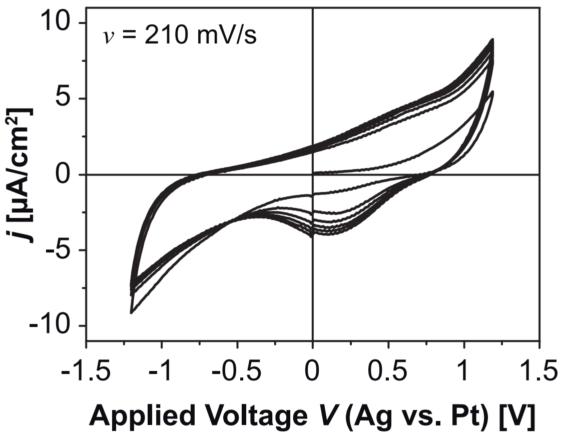

Figure 4.3 Cyclic voltammetry of a Ag/SiO$_2$/Pt cell (Ag top electrode diameter $d = 150\,\mu\mathrm{m}$). Analogous to Cu/SiO$_2$/Pt cells, Ag based cells also show redox reactions during cyclic voltammetry. However, the voltage amplitude is reduced since the electroforming and SET voltages for resistive switching of Ag/SiO$_2$/Pt cells are typically smaller than for Cu/SiO$_2$/Pt cells.

Figure 4.3 depicts a typical cyclic voltammogram for a Ag/SiO$_2$/Pt cell. Though, the voltage amplitude is limited compared to Cu/SiO$_2$/Pt cells, since the electroforming and SET voltages for resistive switching of Ag/SiO$_2$/Pt cells are typically smaller compared to Cu based cells, redox reactions of Ag/Ag$^+$ can be clearly observed. However, the following sections are mainly focused on Cu/SiO$_2$/Pt, since the redox current response is higher compared to Ag based systems and Cu^{z+} ions can be easier detected by further analysis methods such as XPS.

Ion Concentration and Diffusion Coefficient

The ion concentration c_{ion} can be derived by the integration of charge from cyclic voltammograms. Afterwards, the diffusion coefficient D can be calculated based on c_{ion} and the Randles-Sevcik equation (see chapter 2.3.1) for reversible systems

$$j_{\mathrm{p}} = 2.69 \cdot 10^5 \cdot z^{\frac{3}{2}} \cdot c_{\mathrm{ion}} \cdot \sqrt{D\nu}, \tag{4.1}$$

and

$$j_{\mathrm{p}} = 2.99 \cdot 10^5 \cdot z^{\frac{3}{2}} \cdot c_{\mathrm{ion}} \cdot \sqrt{\alpha D\nu} \tag{4.2}$$

for irreversible systems (see chapter 2.3.2) at room temperature for a specific sweep rate ν. In the particular case of a Cu/SiO$_2$/Pt cell, the charge number of Cu^{z+} ions can be $z = 1, 2$ while for Ag/SiO$_2$/Pt cells the charge number of Ag^{z+} ions is $z = 1$. As discussed below, $z = 2$ is assumed for Cu/SiO$_2$/Pt cells as the dominating ion species. The ion concentration is given by the concentration of cations $c_{\mathrm{Cu}^{z+}}$ and counter charge(s) (e.g. c_{OH^-}, see section 4.1.3), i.e. $c_{\mathrm{ion}} = c_{\mathrm{Cu}^{z+}} + c_{\mathrm{OH}^-}$.

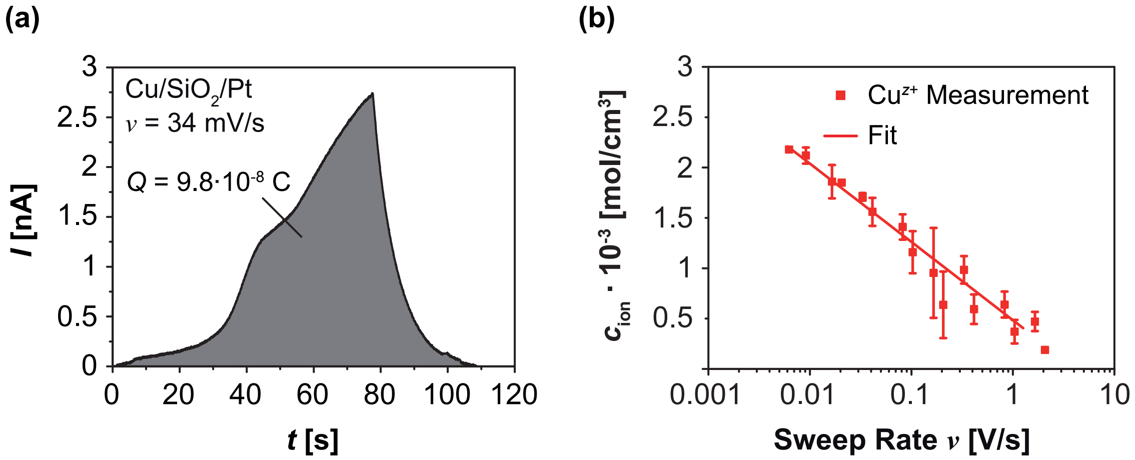

Figure 4.4. Ion concentration for a Cu/SiO$_2$/Pt cell. [66] (a) The ion concentration c_{ion} is calculated by the total charge Q and cell geometry. Q is given by the integration of the current during anodic oxidation. (b) Ion concentration depending on the sweep rate. At high sweep rates less time is available for anodic oxidation resulting in a lower ion concentration.

The ion concentration c_{ion} is estimated by integration of the current during anodic oxidation (assuming the total current is ionic) as shown in figure 4.4a (here for Cu/SiO$_2$/Pt) and $\nu = 34\,\mathrm{mV/s}$. c_{ion} depends on ν as depicted in figure 4.4b for a Cu/SiO$_2$/Pt cell and 4.5a for a Ag/SiO$_2$/Pt cell. The ion concentration decreases by increase of ν, which can be contributed to shorter time for oxidation during the voltage sweep. At low sweep rates sufficient time is available for oxidation of the active electrode, and thus, c_{ion} is high. Based on equation 4.2 the diffusion coefficient D (in cm^2/s) can be calculated (assuming a charge transfer coefficient $\alpha = 0.5$ [53]). The estimation of D is complicated when more than one reduction current density peak is clearly observed (below $\nu \approx 30\,\text{mV/s}$ for Cu/SiO$_2$/Pt cells). In this case the dominating peak is used for a first approximation of D.

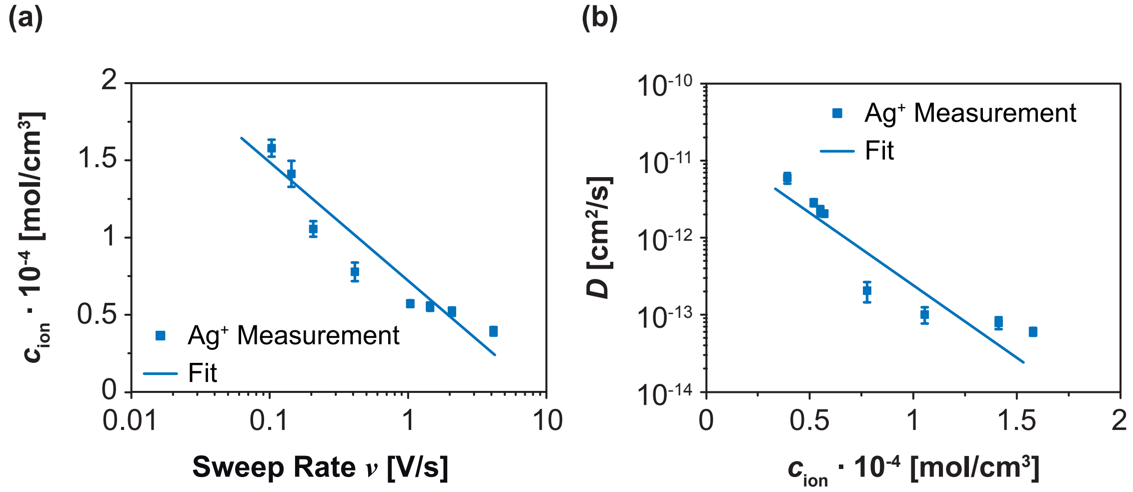

Figure 4.5. (a) Ion concentration c_{ion} for a Ag/SiO$_2$/Pt cell versus sweep rate ν. c_{ion} is smaller for Ag than for Cu based cells. (b) Diffusion coefficient D for Ag$^+$ ions in SiO$_2$. D is significantly smaller compared to Cu based cells (cf. 4.6a).

The ion mobility μ can be further calculated by the Nernst-Einstein relation (with e the elementary charge, k_{B} the Boltzmann constant and T the absolute temperature):

$$\mu = \frac{Dze}{k_{\text{B}}T} \tag{4.3}$$

For most of the ion conducting solids, the ion mobility is expected to be nearly independent on the defect concentration presuming an ideally diluted solution. In contrast, a strong dependence of the cation diffusion coefficient (and thus, ion mobility) on c_{ion} is observed as shown in figure 4.5b for a Ag/SiO$_2$/Pt cell and figure 4.6a for a Cu/SiO$_2$/Pt cell. c_{ion} is smaller for Ag than for Cu based cells. However, this is not only due to the different cation species but also due to the different experimental parameters. Since the forming voltage for resistive switching is smaller in Ag/SiO$_2$/Pt cells compared to Cu based cells, the voltage amplitude for cyclic voltammetry is limited to $\pm 1.2\,\text{V} \ldots 1.5\,\text{V}$ affecting the lower value for c_{ion}.

As the sweep rate deceases, the ion concentration increases, and as follows, D decreases indicating that the SiO$_2$ layer close to the active electrode behaves similar like a concentrated solution. Apparently, ion-ion interactions cannot be neglected, which results in a decrease of the diffusion coefficient. At high sweep rates less time is available for anodic oxidation and c_{ion} is low. The weaker ion-ion interactions result in an increase of D, and as follows, the ion mobility increases. Figure 4.6b shows the cation diffusion coefficient versus sweep rate ν for Cu/SiO$_2$/Pt and Ag/SiO$_2$/Pt cells, respectively. Silver ions seem to be less mobile in SiO$_2$ than Cu ions. Assuming in both cases OH$^-$ as counter charge species (see section 4.1.3), the limiting factor for anodic oxidation seems to be the cation oxidation of the active electrode.

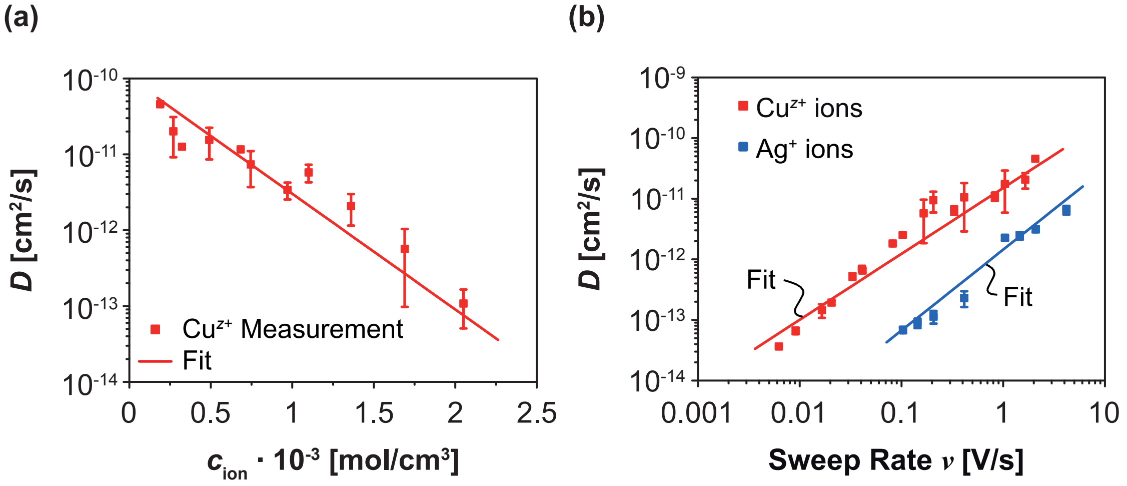

Figure 4.6. Diffusion behavior of cations in SiO$_2$ [66]. (a) Diffusion coefficient D of Cu^{z+} ions depending on the ion concentration c_{ion}. (b) Diffusion coefficient D for both Cu^{z+} and Ag$^+$ ions as a function of the sweep rate ν. The ion concentration, and thus, the diffusion coefficient can be adjusted by variation of ν.

It is noteworthy that the diffusion coefficients and ion concentrations measured in this study are orders of magnitudes higher than the values for Cu and Ag atoms in bulk SiO$_2$ extrapolated to room temperature. However, based on bulk SiO$_2$ diffusion coefficients, resistive switching in a few hundred microseconds or even below cannot be explained at all. McBrayer et. al. [67] measured diffusion coefficients and *solid solubility* for singly ionized Cu and Ag atoms in SiO$_2$ prepared by wet- and dry-oxidation of Si. The quality of the SiO$_2$ layers was reported to be comparable to SiO$_2$ used for integrated devices (and thus, potentially much more insulating as evaporated SiO$_2$ in this study). The thickness of SiO$_2$ was 500 nm and thicker (compared to 50 nm and below used here). The results are shown in figure 4.7 and fit to other reports in literature (e.g. [68]). Both the diffusion coefficients and ion concentrations for Ag and Cu are much higher in this study compared to Ref. [67]. Based on figure 4.7 the diffusion coefficient of Cu extrapolated to room temperature is in the order of 10^{-21} cm^2/s, resulting in an ion

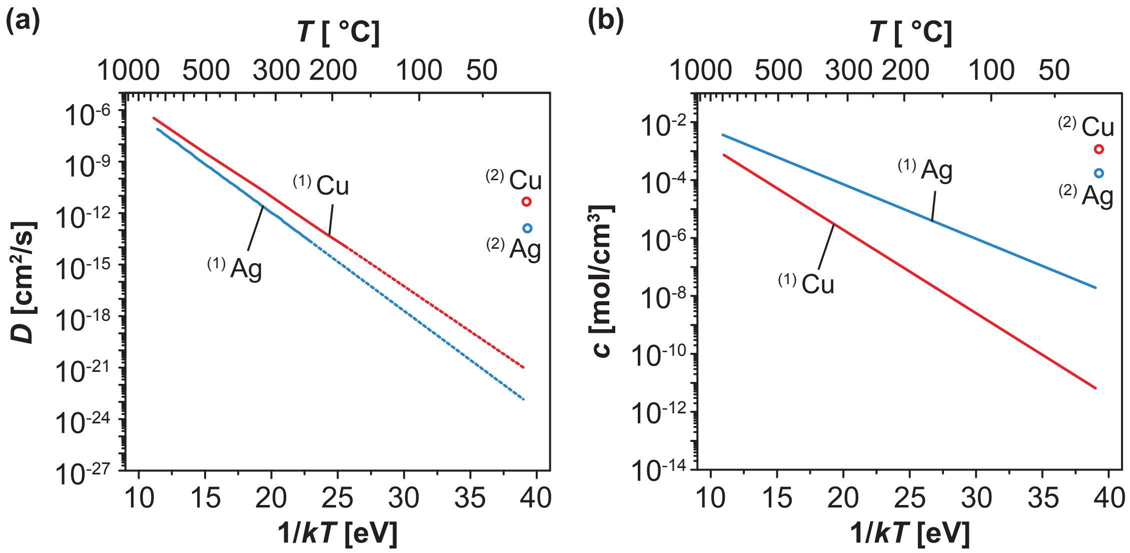

Figure 4.7. Temperature dependence of diffusion coefficient D (a) and *solid solubility* c (b) of singly ionized Ag and Cu atoms in SiO_2 derived from Ref. [67] (labeled by (1)) and compared to values measured in this study (labeled by (2) with $\nu = 0.1\,\mathrm{V/s}$). The extrapolation to room temperature for D is indicated by dotted lines.

mobility of $\mu \approx 10^{-20}\,\mathrm{cm^2/Vs}$. The average drift velocity v_D of ions can be described by the formula for high-field ionic drift [69]:

$$v_\mathrm{D} = \mu \cdot E_0 \cdot \exp\left(\frac{E}{E_0}\right) \tag{4.4}$$

Here, $E = V/d$ is the electric field (applied voltage V and oxide thickness d) and E_0 the characteristic field for a specific mobile ion in the solid. E_0 is typically in the order of $1\,\mathrm{MV/cm}$ for $T = 300\,\mathrm{K}$ [69]. Additional acceleration of ions due to Joule heating can be excluded in case of ECM cells, as switching with low currents (below $1\,\mu\mathrm{A}$) has been reported in literature [70; 71] (see also e.g. figure 5.2). The minimum time for resistive switching can be roughly approximated by the drift time of the ions across the insulating solid (see chapter 5.1.4). Based on diffusion coefficients reported by McBrayer et. al., the time for resistive switching of a $Cu/SiO_2/Pt$ cell would be in the order of $10^8\,\mathrm{s} \approx 76$ years. Thus, these low diffusion coefficients cannot explain properly the resistive switching effect. In contrast, the high diffusion coefficients measured here can explain switching within milli seconds down to tens of micro seconds, and are contributed to a nano porous thin film structure [35] and due to rest moisture (see section 4.1.3).

Ion Distribution

The formation of Cu ions during electrode polarization is clearly confirmed by XPS depth profiles of Cu/SiO_2/Pt cells in as-deposited state (Figure 4.8b) and after electrochemical oxidation (Figure 4.8c). The spectra evidently reveal the presence of Cu^{2+} ions underneath the Cu electrode in the case of previously applied electrode polarization. While cyclic voltammograms indicate the presence of a small amount of Cu^{+} ions ($z = 1$, see below) additionally to Cu^{2+} ions, by XPS profiles it is not possible to clearly distinguish the Cu^{+} signal from metallic copper due to the small difference in the binding energies (below 0.1 eV for both species). However, the XPS results confirm the findings discussed below drawn on the basis of the CV analysis indicating the presence of Cu^{2+} ions. As derived in chapter 4.1.2, Cu^{2+}-O^{2-} bonds in SiO_2 are much weaker than Cu^{+}-O^{2-} bonds, suggesting that Cu^{2+} is more mobile in SiO_2 and in this way dominating the switching process. It is worth mentioning that the thickness of the interface layer containing Cu^{2+} ions is in the range of a few nm limited by the Cu^{2+} mobility. This indicates that during the switching event Cu ions must be (further) significantly accelerated by the applied field in order to achieve switching times in the μs regime or below [69].

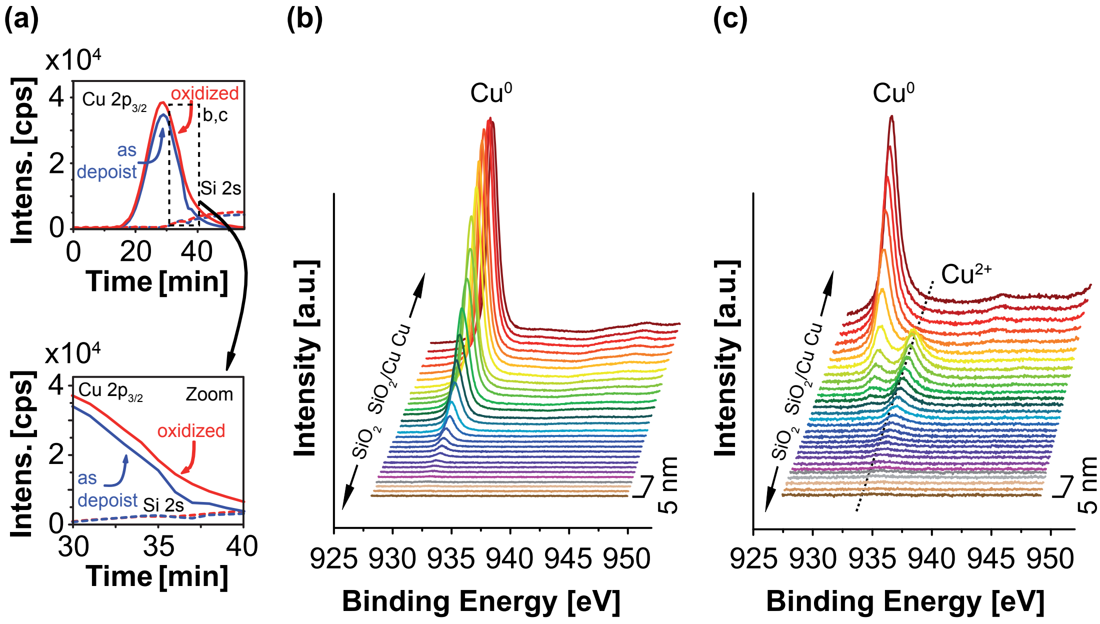

Figure 4.8. Cation distribution in a Cu/SiO_2/Pt cell. (a) For simplification only the signal response around the binding energy of Cu $2p_{3/2}$ at the Cu/SiO_2 interface is shown (see zoom). Depth profile XPS analysis of (b) a pristine Cu/SiO_2/Pt cell and (c) a cell after anodic oxidation. The distribution of Cu^{2+} ions underneath the Cu electrode can be clearly observed. Redrawn from [72].

Partial Redox Reactions

It is generally expected that current peaks during anodic oxidation are observed. However, here the active electrode acts as an endless source for Cu^{z+} ions and is of the same thickness as the SiO_2 insulator. Additionally, oxidation peaks are not observed since diffusion seems to be not significantly limiting the ion generation above $\nu > 35\,\mathrm{mV/s}$. Notwithstanding, as the sweep rate decreases diffusion limitation becomes more dominating both during oxidation and reduction processes.

Figure 4.9 depicts a typical CV sweep for a low sweep rate of $\nu = 15\,\mathrm{mV/s}$. Analogous to the processes described for figure 4.1, anodic oxidation of the Cu electrodes takes place by increase of the applied voltage V resulting in an increase of the current. After reaching the vertex potential at $V = 2\,\mathrm{V}$ the driving force for further oxidation is diminished and the current density decreases. During the following negative voltage sweep the oxidized Cu ions are reduced, whereby diffusion limitations of Cu ions injected into the SiO_2 thin film are responsible for the negative current density peak $j_{\mathrm{p,red(2)}}$. A subsequent reduction peak $j_{\mathrm{p,red(1)}}$ is also observed indicating several partial redox reactions. Additionally, two oxidation peaks $j_{\mathrm{p,ox(1)}}$ and $j_{\mathrm{p,ox(2)}}$ can be distinguished in contrast to figure 4.1. Note, peak $j_{\mathrm{p,ox(2)}}$ is only observed for subsequent cycles but not observed during the first sweep when the cell is in an initial pristine state.

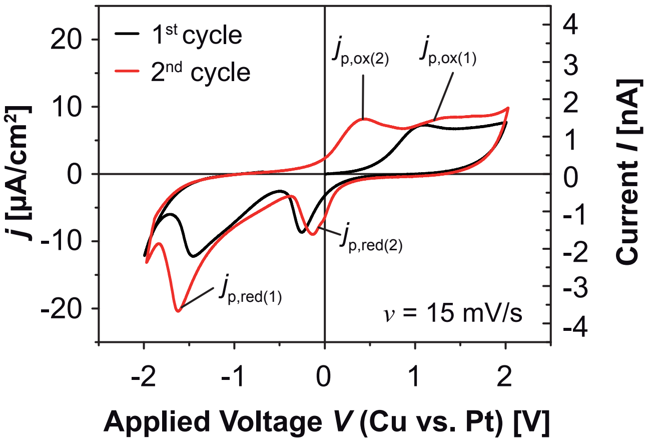

Figure 4.9 Partial redox reactions observed at a low sweep rate $\nu = 15\,\mathrm{mV/s}$ [66]. Various peaks are observed, which are contributed to Cu^+ and Cu^{2+} redox reactions.

The dependence of D on ν depicted in figure 4.6b can explain why current density peaks for anodic oxidation are observed by decrease of the sweep rate. Here, the high ion concentration decreases D and further oxidation is limited by the diffusion of Cu^{z+} into SiO_2. At high sweep rates the fewer oxidized ions can diffuse faster in SiO_2 and the diffusion limitation is less pronounced. The interpretation of $j_{\mathrm{p,ox(1)}}$ and $j_{\mathrm{p,ox(2)}}$ as well as $j_{\mathrm{p,red(1)}}$ and $j_{\mathrm{p,red(2)}}$ can lead to the identification of each electrochemical partial reaction and the dominating ion species (Cu^+ or Cu^{2+}).

In aqueous solutions the standard redox potentials for Cu are given as: Cu^+/Cu $E_{\phi,1} = 0.52\,V$, Cu^{2+}/Cu $E_{\phi,2} = 0.34\,V$ and Cu^{2+}/Cu^+ $E_{\phi,3} = 0.159\,V$. Although Cu ions are dissolved in SiO_2 in this case, the general trend of reduction potentials holds here as well and furthermore, incorporation of water in SiO_2 based ECM cells has been reported [32; 73] (see also chapter 4.1.3). Thus, Cu should be oxidized to Cu^{2+} first since this process is thermodynamically favorable according to the standard redox potentials. The current density peak $j_{\mathrm{p,ox(1)}}$ is contributed to this partial reaction. The Cu to Cu^+ oxidation takes place after $j_{\mathrm{p,ox(1)}}$ and a current density peak may be beyond the vertex potential of 2 V. Hence, both Cu^+ and Cu^{2+} can be found in SiO_2 after the oxidation. When V is decreased the reduction of Cu^+ to Cu is thermodynamically favorable (lower reduction energy) resulting in the current density peak $j_{\mathrm{p,red(2)}}$. The absolute current density increases further close to the vertex potential $-2\,V$, which is an indication for Cu^{2+} to Cu reduction ($j_{\mathrm{p,red(1)}}$), and by further decrease of V Cu^{2+} to Cu^+ reduction may take place as well. When a subsequent cycle is started a new $j_{\mathrm{p,red(2)}}$ oxidation peak is observed. Accounting that only a part of the generated Cu^+ ions were reduced these ions can now undergo an oxidation to Cu^{2+} ions since the standard reduction potential for this process is lower than for Cu to Cu^+ or Cu^{2+}.

In summary, both Cu^+ and Cu^{2+} are observed by CV sweeps in $Cu/SiO_2/Pt$ cells. As discussed above, Cu^{2+} can be also found by XPS. In the following section the bond nature of both Cu^+ and Cu^{2+} are analyzed by X-ray Absorption Spectroscopy to identify the more mobile, and as follows, the dominating ion species during resistive switching in $Cu/SiO_2/Pt$ cells.

4.1.2. Bond Nature of Mobile Cations in Silicon Dioxide

The experimental findings discussed in the last section reveal the existence of mobile Ag^+ and Cu^{z+} cations in SiO_2. The chemical interactions of these cations, and the dominating charge number of mobile ions for resistive switching (in case of $Cu/SiO_2/Pt$ cells), remain however still questionable. Therefore, the bonding characteristics of Ag^+ and Cu^{z+} cations in silicon dioxide based ECM cells have been examined using soft X-ray Absorption Spectroscopy at the 11A1 beam line at Taiwan Light Source [74]. XAS gives complementary (local) geometric and electronic structural information including bond lengths [75].

The XAS experiments were performed with SiO_2 samples (thickness 60 nm) prepared by e-beam evaporation on platinized Si substrates. Cu and Ag electrodes (thickness 5 nm) *in situ* deposited by e-beam evaporation on SiO_2 were used. X-ray Absorption Spectra were measured at the O K-edge ($h\nu \sim 530\,eV$) and Cu $L_{2,3}$-edges ($h\nu \sim 930\,eV$). While the

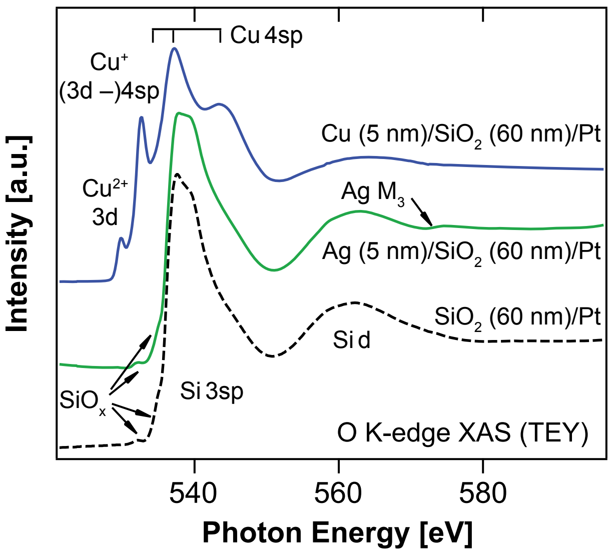

Figure 4.10 O K-edge XAS spectra in TEY mode of pure SiO_2 and SiO_2 thin films, covered by 5 nm Cu or Ag thin films, respectively. The Ag/SiO_2 and pure SiO_2 spectra are similar (except for a small Ag M_3-edge absorption) indicating the absence of any chemical interaction of Ag and SiO_2. Reproduced from Ref. [74].

absorption spectra near the O K-edge were both measured in total electron yield (TEY) and fluorescence yield (FY) modes, absorption spectra near the Cu $L_{2,3}$-edges were measured only in TEY mode. The fluorescence yield reflects most likely bulk properties of the SiO_2 film, while TEY can be utilized to analyze the electronic structures near the surface due to their probing depths, respectively.

Figure 4.10 depicts O K-edge XAS spectra in TEY mode of pure SiO_2, and SiO_2 thin films covered by 5 nm Cu or Ag thin films on Pt, respectively. While the spectra of the Ag/SiO_2/Pt sample is similar to the pure SiO_2 sample, the spectra of the Cu/SiO_2/Pt sample is considerably different. In particular, figure 4.10 reveals that the bonding of oxygen ions of the Ag/SiO_2/Pt sample is the same as for the pure SiO_2 sample, indicating the absence of any chemical interaction of Ag and SiO_2. Thus, Ag is only electrochemically dissolved in SiO_2 prior to the resistive switching event.

The spectra of the Cu/SiO_2/Pt and pure SiO_2/Pt sample are comparatively different. The two low-energy features below $h\nu = 540\,\text{eV}$ are attributed to the Cu^{2+} ($3d^9$) and Cu^+ (4sp) ionized states, respectively. The features at higher energies represent a mixture of Cu^{2+} and Cu^+ (4sp) states. Hence, copper is partially oxidized by the presence of SiO_2 in contrast to silver.

A more detailed insight into the oxidation state of Cu on top of SiO_2 is given by a magnified view of the O K-edge XAS spectra shown in figure 4.11a in TEY mode. The oxidation of Cu is mainly driven by the ambient (moisture and oxygen), and the intensity ratio of the Cu^{2+} and Cu^+ features are proportional to the ion concentration ratio $\left[Cu^{2+}\right]/\left[Cu^{+}\right]$ [74]. Additionally, chemical copper dissolution into SiO_2 seems to further facilitate the $Cu^+ \to Cu^{2+}$ oxidation. In the fluorescence yield mode (figure 4.11b) bulk properties are dominating the spectra. For comparison the signal of a pure

Pt layer is depicted indicating that even bare platinum is partially oxidized. Again, the Cu^{2+} signal is stronger while the Cu^{+} is weaker in case of the Cu/SiO_2 sample, respectively. As follows, Cu^{+} seems to be further oxidized to Cu^{2+} in the presence of SiO_2. This can be clearly observed when the strong contributions of the SiO_2 and Pt signals are subtracted as shown in figure 4.11c. While the Cu/SiO_2/Pt sample shows features of Cu^{2+} (3d) and Cu^{2+} (4sp), similar features are suppressed for the Cu/Pt sample.

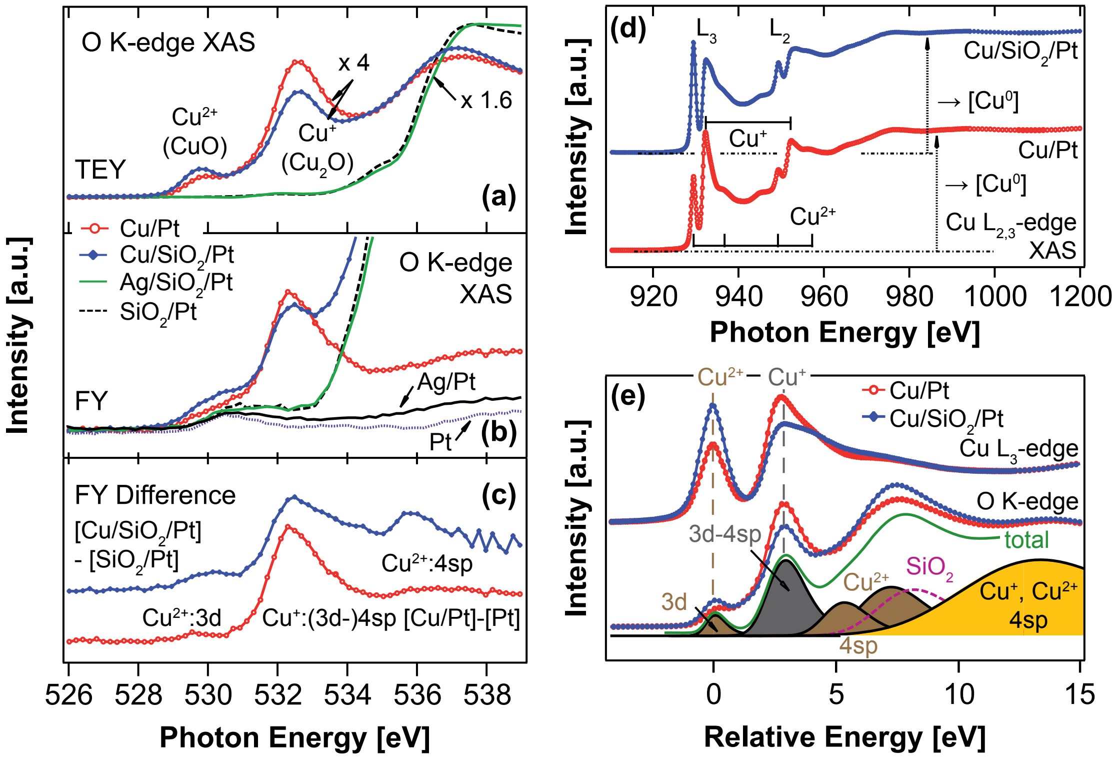

Figure 4.11. Analysis of oxidation state of Cu on top of SiO_2 [74]. Magnified view of the O K-edge XAS spectra in (a) TEY and (b) FY mode. In (c) the contributions from Pt/SiO_2 and Pt are subtracted, respectively. (d) Cu $L_{2,3}$-edge XAS of Cu/SiO_2/Pt and Cu/Pt samples (TEY mode). The spectra look very similar and the sharp features reflect the coexistence of Cu^{2+} and Cu^{+} ions with considerable higher-energy backgrounds for both samples [74]. Additionally, a high Cu^{0} background is observed in both samples indicating that only a few percent of Cu atoms are oxidized. (e) Hybridization strengths of Cu (3d/4sp)-O (2p) orbitals in the Cu^{+} and Cu^{2+} ions. The features for Cu^{2+} (3d) and (4sp) in brown, Cu^{+} (3d-4sp) in gray, and Cu^{2+} and Cu^{+} (4sp) in yellow of O K-edge XAS spectra are decomposed exemplary for clarity, respectively. These signals contribute to the total spectra (green) which is very similar to the measured O K-edge XAS spectra.

The resistive switching effect is based on the drift of mobile cations under the applied electric field, and thus (in case of SiO_2), the bonds of cations to the nearest oxygen ions should be weak for a considerable high diffusion coefficient. Figure 4.11d depicts

Cu $L_{2,3}$-edge XAS of Cu/SiO_2/Pt and Cu/Pt samples. Similar to the O K-edge XAS spectra shown in figure 4.11a, both Cu^{2+} and Cu^{+} features are observed. The high background of metallic Cu^0 (indicating a high Cu^0 concentration) reveals that only a few percent of atoms of the Cu electrode are oxidized and can incorporate into SiO_2. In figure 4.11e both Cu L_3-edge and O K-edge XAS spectra are shifted for comparison. The Cu^{2+} and Cu^{+} signals can be roughly separated for the O K-edge XAS spectra. The

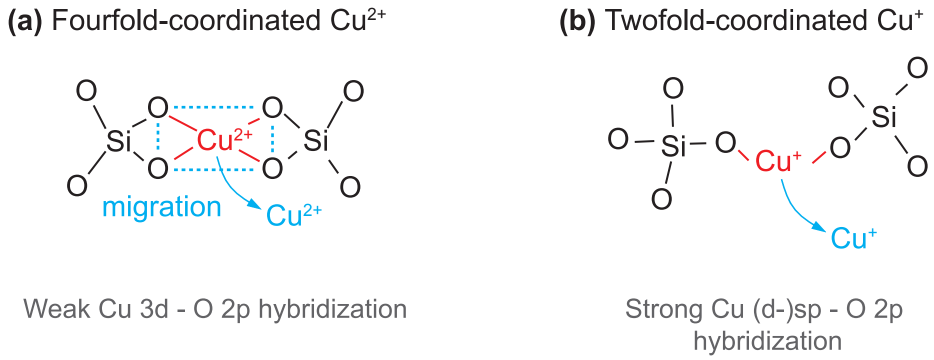
(a) Fourfold-coordinated Cu2+
O
O
O
O
Si
Si
Cu2+
O
O
O
O
migration
Cu2+
Weak Cu 3d - O 2p hybridization
(b) Twofold-coordinated Cu+
O
O
O
O-Si-O
Si
Cu+
O
O
O
Cu+
Strong Cu (d-)sp - O 2p hybridization

Figure 4.12. Schematic of the bond structures of (a) fourfold-coordinated Cu^{2+} and (b) twofold-coordinated Cu^{+} ions in association with SiO_4 networks in the SiO_2 matrix [74].

Cu L_3-edge and O K-edge spectra show similar Cu^{2+} (3d) and Cu^{+} (3d-4sp) features below a relative photon energy of 5 eV. The features above 5 eV (mainly originating from Cu (4sp) states) become weaker for the Cu L_3-edge spectra compared to the O K-edge XAS spectra. While the peak intensities of both species in the Cu L_3-edge spectra are comparatively high indicating a similar concentration of $\left[Cu^{2+}\right]$ to $\left[Cu^{+}\right]$ close to the surface, the Cu^{+} peak is at least 3 times higher than the Cu^{2+} peak in the O K-edge XAS spectra. Therefore, Cu^{+}-O^{2-} bonds are much stronger than Cu^{2+}-O^{2-} bonds. This reveals that the hybridization strengths of Cu^{2+} and Cu^{+} ions are different, as shown in figure 4.12 for (a) fourfold-coordinated Cu^{2+} and (b) twofold-coordinated Cu^{+} ions.

The strength difference of the Cu^{+}-O^{2-} and Cu^{2+}-O^{2-} bonds results in different diffusion coefficients $D_{Cu^{2+}} \approx 10^{-12}\,\mathrm{cm^2/s}$ and $D_{Cu^{+}} \approx 10^{-22}\,\mathrm{cm^2/s}$ calculated for $T = 723\,\mathrm{K}$ [74], respectively. Though the actual energy cost for Cu migration can be larger, because drift of Cu^{z+} ions by a hopping mechanism is reasonable, the tendency that Cu^{2+} are more mobile than Cu^{+} ions may still hold, despite the nature of the migration process.

In summary, XAS measurements support the observation by cyclic voltammetry that both Cu^{+} and Cu^{2+} ions can be found in SiO_2, while Cu^{2+} appears to be more mobile than Cu^{+}. Cu^{2+} ions may therefore play the dominating role during resistive switching of Cu/SiO_2/Pt based ECM cell.

4.1.3. Impact of Moisture during Anodic Oxidation

In contrast to AgI or Ag-GeSe, SiO_2 does not initially contain mobile metal cations, which are responsible for the filament formation during resistive switching. The XAS measurements discussed in section 4.1.2 reveal only the existence of a small amount of Cu^{z+} ions close to the Cu/SiO_2 surface but not within the insulator. Evidently, one needs first to electrochemically dissolve Cu ions into SiO_2 in order to operate the cell. In this case it is not sufficient to simply apply a positive voltage to the electrochemically active electrode. A counter charge(s)/reaction, e.g. electrons or OH^-, must keep electroneutrality during anodic oxidation. OH^- ions can be supplied by reduction of moisture from the surrounding ambient, which is incorporated into SiO_2 because of its nano-porous structure. Hence, during the CV sweeps the half cell reaction at the active electrode is:

$$Cu^{z+} + ze^- \rightleftharpoons Cu \tag{4.5}$$

And at the inert Pt electrode the required counter reaction is given by

$$\frac{1}{2}O_2 + H_2O + 2e^- \rightleftharpoons 2OH^-, \tag{4.6}$$

or alternatively by

$$2H_2O + 2e^- \rightleftharpoons 2OH^- + H_2. \tag{4.7}$$

Different water and oxygen partial pressures (pH_2O and pO_2, respectively) were set up in an enclosed measurement chamber, using two MKS 179B digital mass flow controllers admixing anhydrous N_2 with anhydrous O_2 or hydrated N_2, to study in detail the impact of moisture on Cu redox processes. The total flow rate through the measurement chamber was kept constant to 100 sccm. The absolute pressure within the measurement chamber was also kept constant close to the ambient absolute pressure using a pressure relief valve. During the measurement the oxygen partial pressure was measured by a *Zirox* O2-DF 12.2 oxygen sensor. The water partial pressure was monitored by a *Honeywell* HIH-4000 humidity sensor. The sample temperature (room temperature) was simultaneously measured.

Figure 4.13a depicts the impact of pH_2O in N_2 atmosphere on the redox reactions of Cu at the interface with SiO_2 (Pt used as counter electrode). As pH_2O increases the current during anodic oxidation increases, and thus, the reduction current increases as well. In anhydrous atmosphere anodic oxidation does not take place and as follows, there are no Cu^{z+} ions, which can be reduced. Absence of any redox processes is observed in anhydrous O_2 atmosphere as well. The impact of pH_2O on the anodic oxidation is attributed to counter charges supplied by water. In this case water is most likely penetrating from the lateral into the SiO_2 thin film as schematically illustrated in figure 4.13b.

Based on the cyclic voltammograms shown in figure 4.13a, the ion concentration and the diffusion coefficient can be calculated by the Randles-Sevcik equation (equ. 4.2) and integration of the current during anodic oxidation. The impact of pH_2O on the ion concentration c_{ion} is depicted in figure 4.14a. Note, both Cu^{z+} and the counter charge are contributing to c_{ion}. Increase of pH_2O results in an increase of c_{ion} because the counter charge concentration at the Pt/SiO_2 interface seems to be the limiting process for the cation generation. This relation unequivocally reveals that hydroxide ions are acting as counter charges rather than electrons. At a higher water partial pressure more OH^- can be reduced at the Pt/SiO_2 interface, and in this way, a higher amount of Cu^{z+} can be dissolved. In the following only one cation species $z = 2$ is assumed to be dominating based on XAS measurements (see section 4.1.2). Since the high local concentration of Cu^{2+} ions leads to ion-ion interactions, the thermodynamic factor $\partial \ln a_i / \partial \ln c_i$ (with the activity a_i and the concentration c_i of species i) is reduced. Thereupon, increasing the water partial pressure results in a decrease of the diffusion coefficient D as shown in figure 4.14b. This situation is typically observed for concentrated solution conditions,

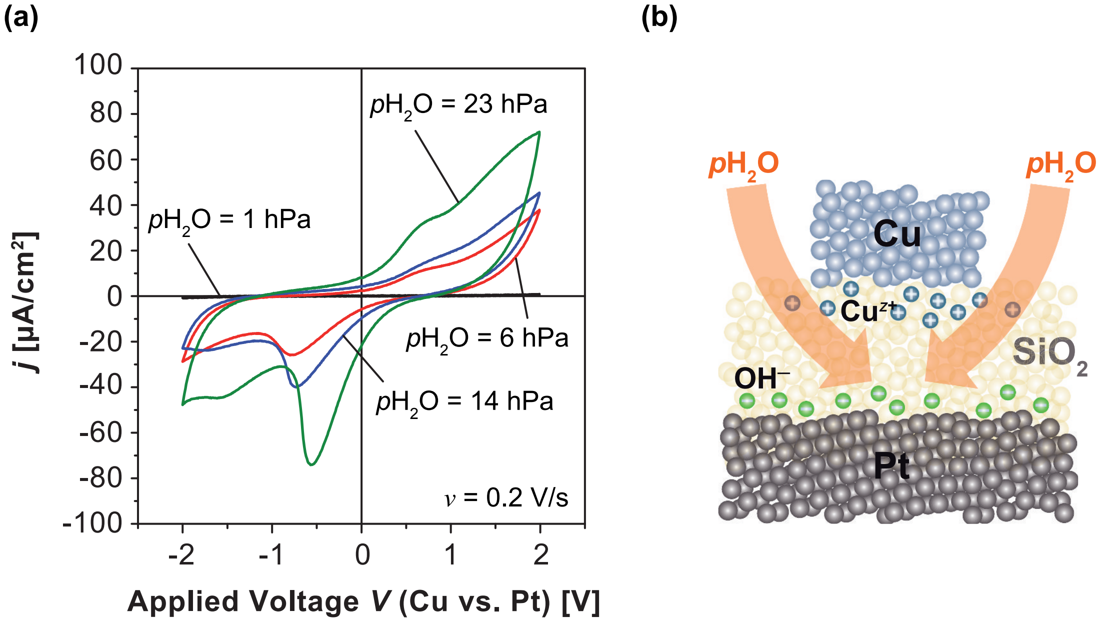

Figure 4.13. Role of water supplying counter charges during anodic oxidation [72]. (a) Impact of water partial pressure pH_2O on redox reactions studied by cyclic voltammetry. (b) Potential water penetration in SiO_2.

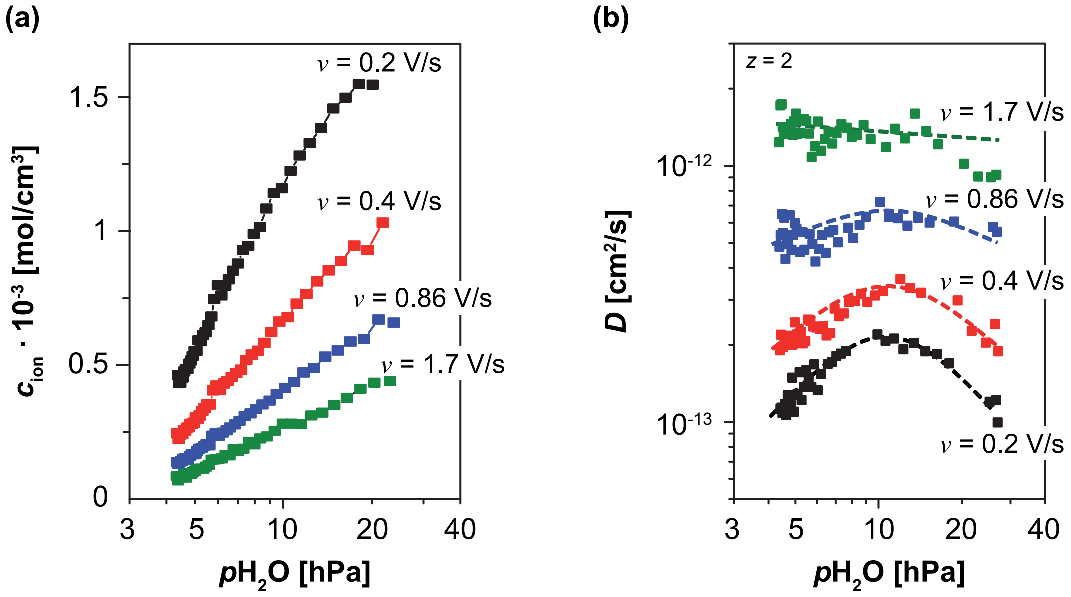

Figure 4.14. (a) Impact of $p\text{H}_2\text{O}$ on the ion concentration c_{ion} for various sweep rates $\nu = 0.2\,\text{V/s}$ to $1.7\,\text{V/s}$. (b) Diffusion coefficient D as a function of the water partial pressure. As $p\text{H}_2\text{O}$ increases the ion concentration increases as well, and ion-ion interactions become dominating. This results in a decrease of D at high water partial pressures. Redrawn from [72].

and is further supported by the observed impact of the sweep rate ν on the diffusion coefficient (cf. 4.6b).

In conclusion, water is supplying the counter charge OH^-, which is necessarily needed for anodic oxidation. In anhydrous atmosphere Cu^{z+} ions cannot be formed, and thus, resistive switching is suppressed. As $p\text{H}_2\text{O}$ increases the ion concentration increases as well. The impact of $p\text{H}_2\text{O}$ on the diffusion coefficient is rather complex, since high ion concentrations result in ion-ion interactions decreasing the effective diffusion coefficient.

4.1.4. Impact of Counter Electrode

Although cations supplied by the active electrode are responsible for filament formation, the material of the counter electrode also affects electrochemical reactions (i.e. the resistive switching processes), due to redox reactions supplying the necessarily needed counter charge. Figure 4.15a depicts cyclic voltammograms of $\text{Cu/SiO}_2\text{/CE}$ cells with various counter electrodes CE = Pt, Ir, Ti and Ru, respectively. The cell geometry and sweep rate was kept constant for all devices. A significant impact of the counter electrode material is observed. Notably, the Ir based cell is characterized by the highest current density amplitude. By integration of the current during anodic oxidation (see section 4.1.1) the ion concentration c_{ion} composed both of cations and the counter charge(s)

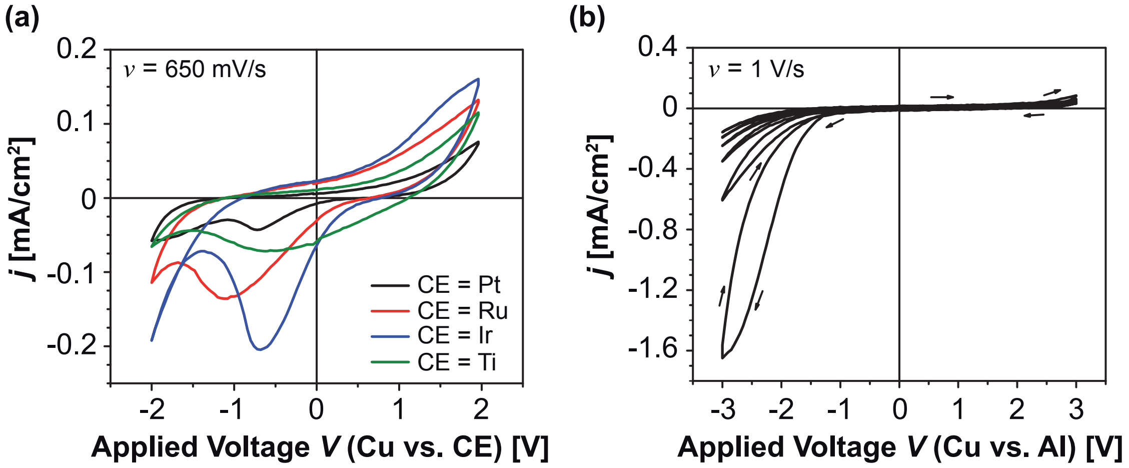

Figure 4.15. Impact of counter electrode material on the redox reactions prior to resistive switching. (a) CV of Cu/SiO_2/CE cells with various counter electrodes CE = Pt, Ir, Ti and Ru, and (b) of a Cu/SiO_2/Al cell. Redrawn from [76].

can be calculated. For some counter electrode materials, e.g. Al, only one significant anodic oxidation sweep can be observed (figure 4.15b). An insulating (or counter charge blocking) aluminum oxide layer could be potentially formed during the first reduction sweep, and may further grow in subsequent sweeps. The potential oxide layer seems to withstand positive voltage sweeps. Thus, only one anodic oxidation sweep is observed.

Figure 4.16a shows c_{ion} in SiO_2 for various counter electrodes, and Cu and Ag as active electrode materials (AE). The ion concentration is calculated from cyclic voltammetry experiments. In principle, a small ion concentration in Ag based cells is observed

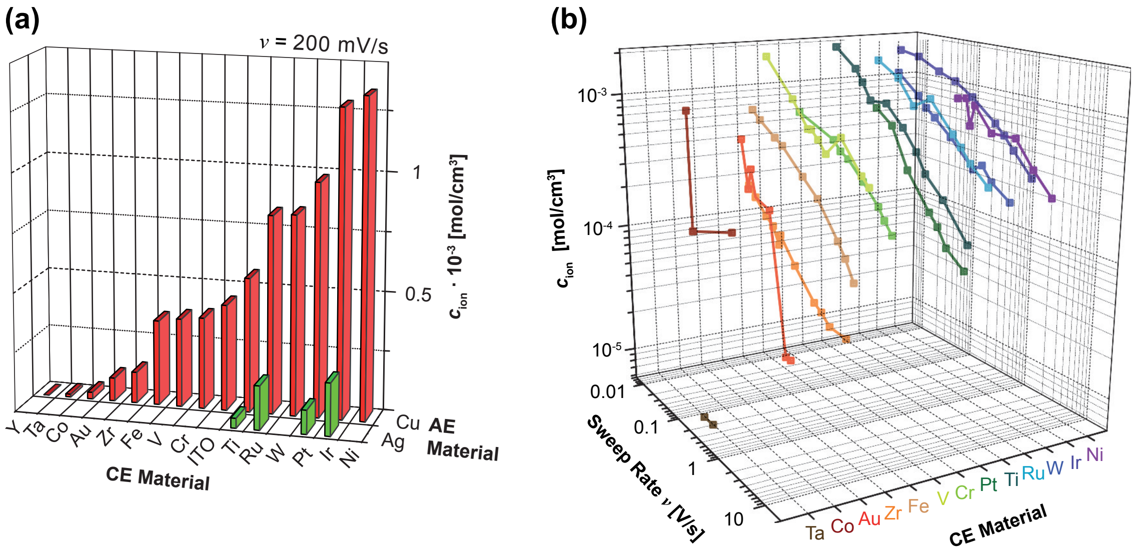

Figure 4.16. (a) c_{ion} depending on the counter and active electrode material. (b) c_{ion} for various CE materials as a function of the sweep rate ν for Cu based cells. Redrawn from [76].

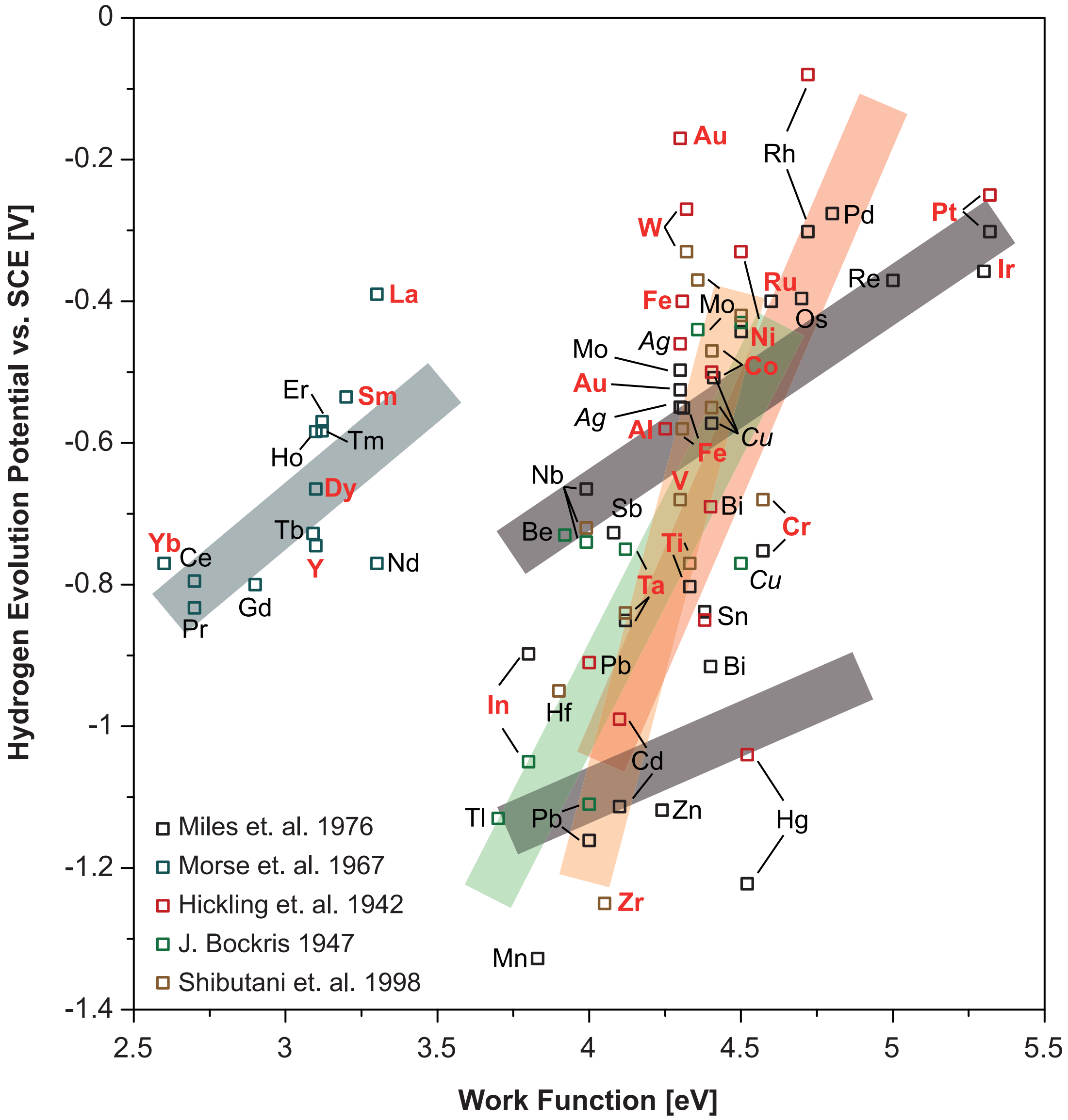

Figure 4.17. Hydrogen evolution potential (vs. SCE) for various electrode materials vs. work function. A general trend can be observed: the hydrogen evolution potential decreases as the work function increases. Small hydrogen evolution potentials are found for noble metals such as Pt and Ir but also Ni. Materials in italic are used as active electrode material, and those in bold red font are used as counter electrode material in this study. Variation of the hydrogen evolution potential can be explained by the measurement conditions such as temperature, current density, and sweep rate. Details are given in Miles et. al 1976 [77], Morse et. al. 1967 [78], Hickling et. al. [79], J. Bockris 1947 [80] and Shibutani et. al. 1998 [81]. The work function is based on measurement data given in [82; 83]. Redrawn from [76].

compared to Cu based cells. However, the voltage amplitude is additionally reduced to ±1.2 V...1.5 V for Ag based cells to avoid resistive switching. The counter electrodes are sorted by the resulting ion concentration during anodic oxidation. A more detailed analysis of c_{ion} for various CE materials is given in figure 4.16b as a function of the sweep rate.

In figure 4.17 hydrogen evolution potential values are shown for various electrode materials (measured versus the potential of the saturated calomel electrode, SCE). The hydrogen evolution potential values vary depending on the measurement conditions. The values by Miles et. al. [77] for example are given at a specific current density $2\,\text{mA/cm}^2$ and sweep rate $\nu = 50\,\text{mV/s}$ in 0.1 M H_2SO_4 solution at 80 °C. In principle, small hydrogen evolution potentials are found for noble metals (including Pt, Pd and Ir).

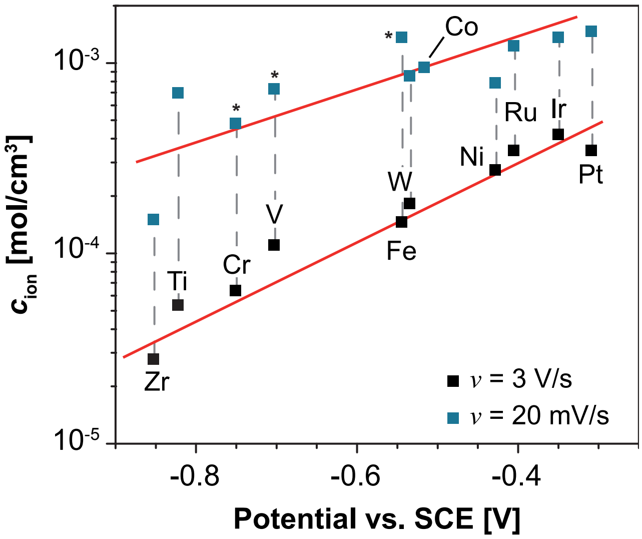

Figure 4.18 c_{ion} from figure 4.16b as a function of the hydrogen evolution potential (measured vs. SCE) [77], exemplary for $\nu = 3\,\text{V/s}$ and $\nu = 20\,\text{mV/s}$ for selected counter electrode materials. Data points labeled with asterisk are extrapolated values from figure 4.16b. Redrawn from [76].

The ion concentrations for $\nu = 3\,\text{V/s}$ and $\nu = 20\,\text{mV/s}$ and selected counter electrode materials for a Cu/SiO_2 based cell as a function of the hydrogen evolution potential (based on [77]) are shown in figure 4.18. c_{ion} tends to increase as the equilibrium potential for hydrogen evolution decreases, i.e. reduction of H_2O (equation 4.7), and therefore, supply of counter charges becomes energetically more favored, and more counter charges are available [76].

Regardless that the hydrogen evolution potential values reported in literature (cf. 4.17) vary on the preparation of the cathode material and experimental conditions, a similar trend of the hydrogen evolution potential values vs. work function as shown in figure 4.17 can be also observed eg. for Fe, Ni, W, Pt in [79] and Zr, Ti, V, Cr, Fe, Co, Ni in [81]. For some CE metals like Y and Ta the ion concentration is close to the measurement limitation. This could be explained by a native oxide of these materials suppressing the anodic oxidation. Similar effects and additional oxygen evolution could also affect the anodic oxidation using counter electrode materials like Zr, Ti or Fe. In case of In as CE material the current density was found to be very high and potentially dominated by electronic current since no redox reactions were observed. Materials such as La, Sa or Yb show ion concentrations similar to Co and Ni (cf. 4.19a,b). The work function of these materials is low and higher hydrogen evolution potentials are expected for lanthanides. However, the hydrogen evolution potentials for lanthanides is comparatively high in figure 4.17. This is potentially due to different measurement conditions in Ref. [78] compared to Ref. [77]. It is noteworthy that resistive switching is not observed when La, Sa or Yb are used. The forming voltages are above 20 V (SiO_2 thickness 50 nm). The reason for this is yet unclear and should be further investigated.

Compared to lanthanides, ITO (indium tin oxide) and TiN are of more practical use. Cyclic voltammograms of these materials as counter electrodes in Cu/SiO_2 based cells

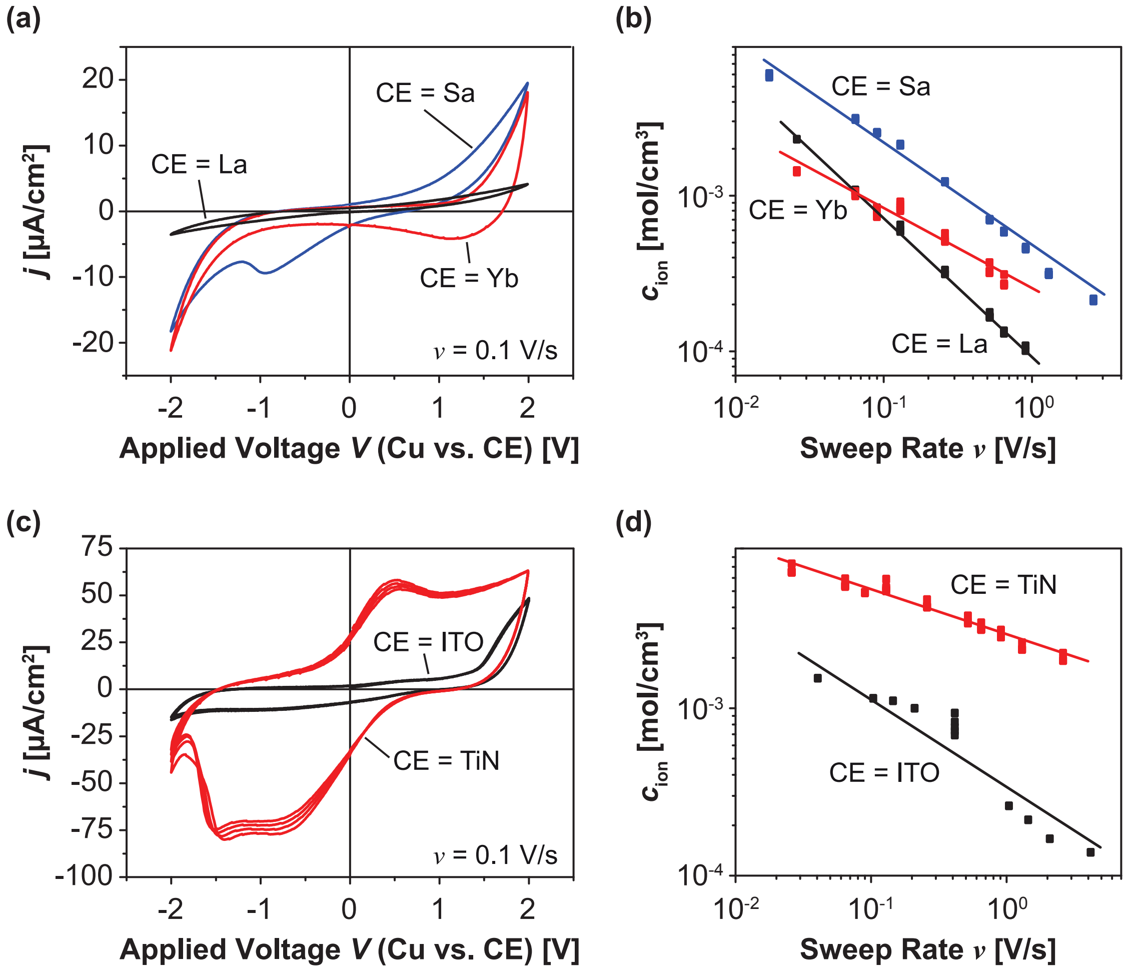

Figure 4.19. Redox reactions and ion concentration for Cu/SiO_2 based cells with various counter electrode materials. (a) Cyclic voltammetry for counter electrode materials CE = Yb, Sa and La. (b) Corresponding ion concentration versus sweep rate. (c) Cyclic voltammetry for counter electrode materials CE = ITO and TiN. (d) Corresponding ion concentration versus sweep rate. Redrawn from [76].

are shown in figure 4.19c. The corresponding ion concentration versus sweep rate is depicted in figure 4.19d. TiN based cells show various redox reaction peaks indicating several multielectron reactions. The ion concentration for ITO and TiN is comparable to Ti or Cr, making these materials interesting for practical devices where noble materials cannot be used.

4.2. Cations in Solid Electrolytes: Silver Iodide

In contrast to SiO_2, which is a typical insulating material, silver iodide AgI is a well-known ion conductor. AgI is chosen as a model system because the concentration of Ag^+ ions in the electrolyte material stays constant during device operation (stoichiometric material). In contrast to SiO_2, silver iodide already consists of mobile Ag^+ cations.

4.2.1. Electronic and Ionic Partial Conductivity

Silver iodide is a well studied Ag^+ ion conductor at room temperature and becomes a solid *superionic* conductor after the γ-AgI/β-AgI to α-AgI phase transition at about $T \approx 150\,^\circ\mathrm{C}$ [84], i.e. α-AgI shows an ion conductance in the order of some liquid electrolytes. The high temperature phase has not been studied in this work since the normal operating temperature for ReRAM devices is below 150 °C. The superionic high temperature phase can be achieved even at room temperature for some AgI based glasses such as the AgI-Ag_2O-V_2O_5-P_2O_5 system [85], $RbAg_4I_5$ [86; 87] and $Ag_6I_4WO_4$ [88; 89]. These materials are however, even more sensitive towards light and moisture (e.g. $RbAg_4I_5$) and the stoichiometry control (in case of $Ag_6I_4WO_4$) by thermal evaporation is difficult to be achieved.

Although AgI has still a high ion conductance at room temperature (compared to other solid electrolytes) the electronic partial conductivity can be also significantly high especially in thin film systems. The electronic partial conductivity can be derived by measuring the emf voltage of a Ag/AgI/C(I_2) layer stack as depicted in figure 4.20a. The reaction at the Ag/AgI interface is:

$$2\mathrm{Ag}^+ + 2\mathrm{e}^- \rightleftharpoons 2\mathrm{Ag} \tag{4.8}$$

and at the AgI/C(I_2) interface:

$$\mathrm{I}_2 + 2\mathrm{e}^- \rightleftharpoons 2\mathrm{I}^- \tag{4.9}$$

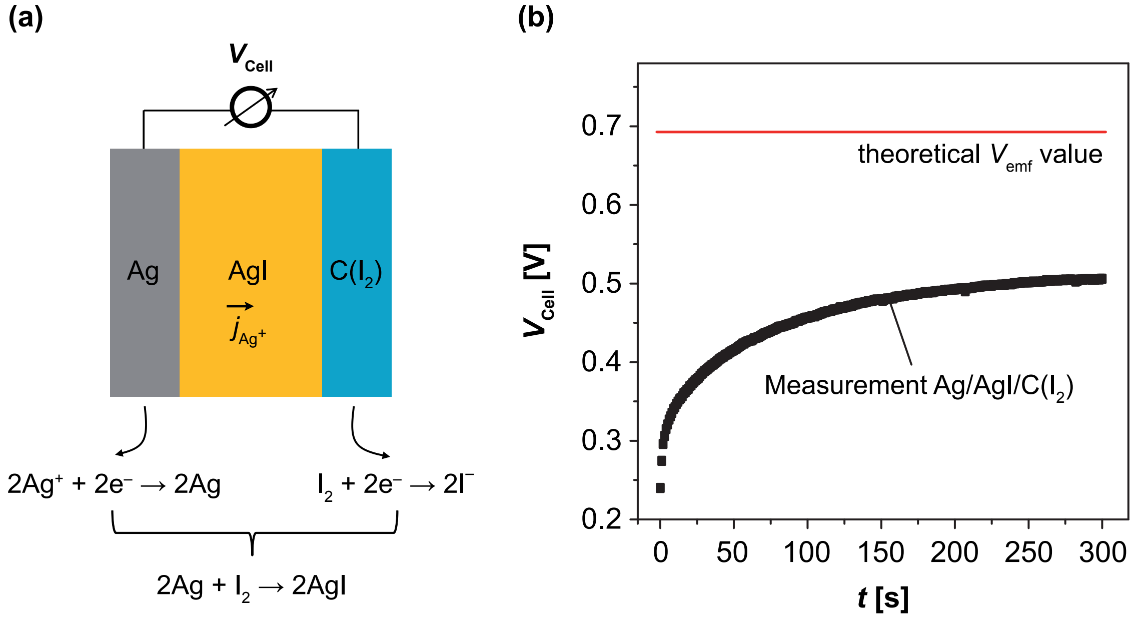

Figure 4.20. (a) Measurement setup for evaluating the electronic and ionic partial conductivity. (b) The ionic transference number is derived from the ratio of measured cell voltage V_{Cell} and theoretically expected emf voltage.

As follows, the overall redox reaction is given by

$$2\mathrm{Ag} + \mathrm{I}_2 \rightleftharpoons 2\mathrm{AgI}, \tag{4.10}$$

and the theoretical value of the emf is $V_{\mathrm{emf}} = 0.69\,\mathrm{V}$. However, the measurable absolute cell voltage V_{Cell} is expressed by the ionic transference number. Therefore, the electronic partial conductivity can be calculated by the ratio of the theoretical value of the emf and the practically measured cell voltage after relaxation of the electrochemical system. The result of the experiment is shown in figure 4.20b. Here, the ionic transference number is $t_{\mathrm{ion}} \approx 0.7$ (thus, the electronic transference number is $t_{\mathrm{el}} = 1 - t_{\mathrm{ion}} \approx 0.3$). Based on impedance spectroscopy of Ag/AgI/Pt (cf. 4.21) a total conductivity of $\sigma \approx 1.9 \cdot 10^{-6}\,\Omega^{-1}\mathrm{cm}^{-1}$ was found. This gives an ion conductivity of $\sigma_{\mathrm{ion}} \approx 10^{-6}\,\Omega^{-1}\mathrm{cm}^{-1}$, which is about three times higher than the ion conductivity of bulk γ-AgI ($3 \cdot 10^{-7}\,\Omega^{-1}\mathrm{cm}^{-1}$, [90]). The higher conductivity differs slightly from cell to cell and could be explained by the morphology of the deposited AgI thin films, since a significant higher ion conductivity of small-grain polycrystals of AgI compared to bulk AgI has been reported [62].

In figure 4.22 the temperature dependence of the ion conductivity of a Ag/AgI/Pt micro crossbar is shown. The activation energy for the hopping transport is about $\Delta H_{\mathrm{hop}(\gamma)\text{-AgI}} \approx 0.34\,\mathrm{eV}$, which is similar to values reported in literature [62; 91; 92]. A phase transition for $T \approx 130\,^{\circ}\mathrm{C} - 150\,^{\circ}\mathrm{C}$ is found, which fits to the phase transition

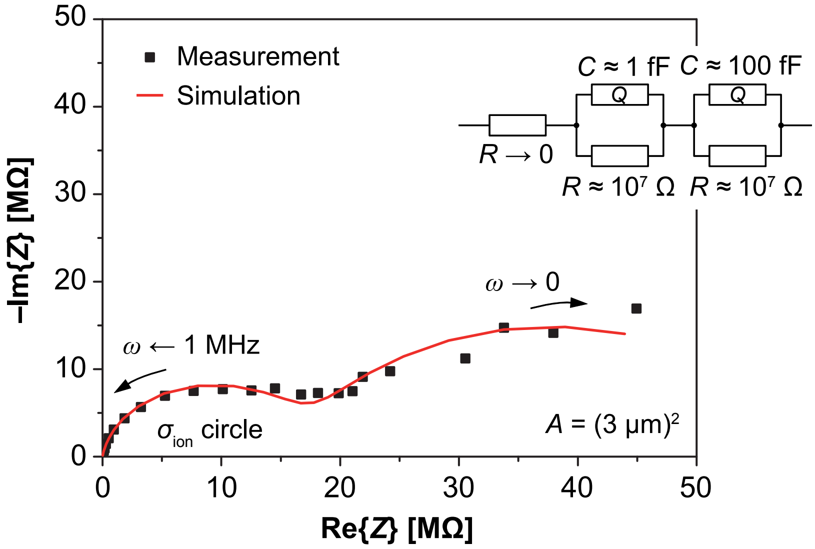

Figure 4.21 Impedance spectroscopy of a Ag/AgI/Pt micro crossbar cell. The measurement of the complex impedance Z fits well to a simulation based on the equivalent circuit shown in the inset. From the fit parameters a total conductivity of $\sigma \approx 1.9 \cdot 10^{-6}\,\Omega^{-1}\mathrm{cm}^{-1}$ was calculated.

to the high conductive α-AgI phase observed by XRD measurements. The activation enthalpy for the ion transport in the α-AgI phase is $\Delta H_{\mathrm{hop}(\alpha)\text{-AgI}} \approx 0.1\,\mathrm{eV}$. This value is in good agreement with literature values [92].

For short pulse experiments (see chapter 5.1.4) the RC time constant is important in case of fast switching. Therefore, the capacity, dielectric constant, and dissipation factor tan δ of a Ag/AgI/Pt micro crossbar cell versus frequency f has been measured as shown in figure 4.23. At low frequencies a high dielectric constant ϵ_{r} and dissipation factor is observed. ϵ_{r} and tan δ decrease as the frequency increases. For $f = 1\,\mathrm{MHz}$ the dissipation factor $\epsilon_{\mathrm{r}} \approx 10$ is similar to values reported for bulk AgI at $f = 18\,\mathrm{GHz}$ [93]. Most analysis of the frequency behavior of AgI has been done in the microwave range to study the ion conduction mechanism [93], and only few results are given for

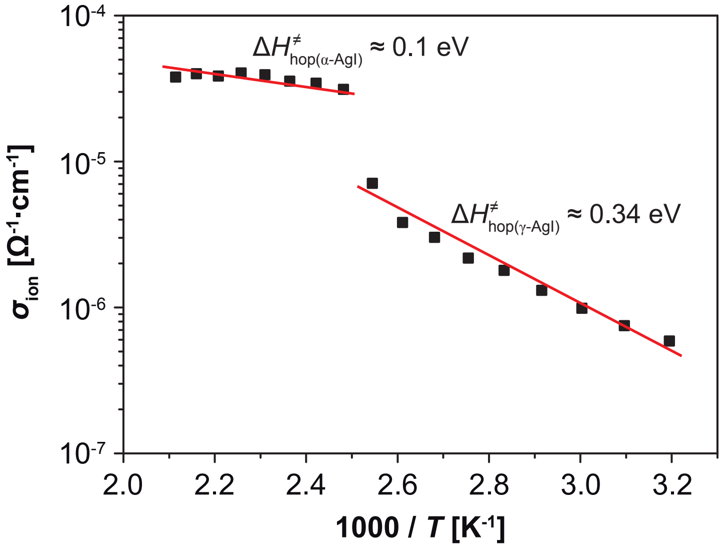

Figure 4.22 Temperature dependence of the ion conductivity σ_{ion} of Ag/AgI/Pt micro crossbars measured by impedance spectroscopy. A phase transition is observed for $T \approx 130\,°\mathrm{C} - 150\,°\mathrm{C}$.

a frequency range below 1 MHz. Nonetheless, it has been reported for AgI that the dielectric constant decreases by increase of f [94]. B. Deb et. al. measured the dielectric constant for the AgI–Ag_2O–SeO_2 material system in a frequency range of $f = 10\,\mathrm{Hz}$ to $f = 2\,\mathrm{MHz}$ [95]. The authors report on a high dielectric constant of up to $\epsilon_r = 2 \cdot 10^3$. Moreover, ϵ_r decreases similar to the measurement performed in this study by increase of f.

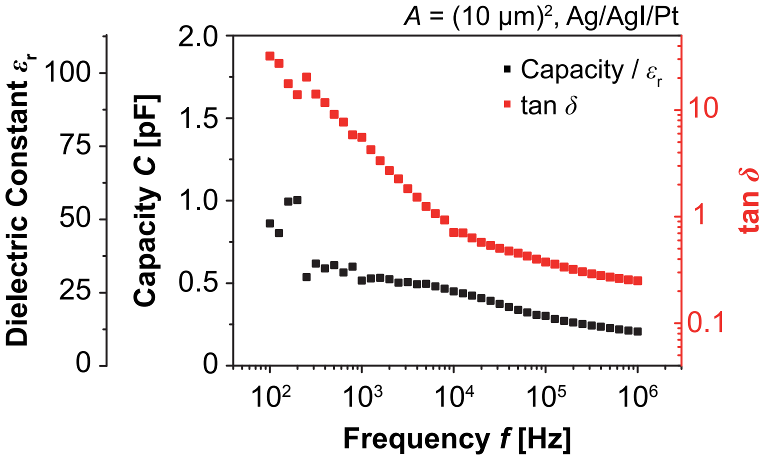

Figure 4.23. Capacity, dielectric constant and dissipation factor tan δ measurement of a Ag/AgI/Pt micro crossbar cell versus frequency f. At small frequencies a high dissipation factor is observed, because AgI is a good ion conductor. This results in a high dielectric constant. At high frequencies the dissipation factor is drastically reduced, and the dielectric constant of about $\epsilon_r \approx 10$ is similar to values reported for bulk AgI in the microwave range [93].

4.2.2. Chemical Stability of the Ag/AgI Interface

In ReRAMs a nanoscale filament is grown within the resistive switching layer and the chemical stability of the (metal) filament at the interface with the electrolyte is crucial for device operation. For example, in GeS or GeSe nanoscale Ag filaments are easily dissolved (e.g. by UV-light) [40; 96]. As discussed in section 4.1.2, Ag seems to be chemically inactive in contact to SiO_2. In contrast, a few at-% of Cu are oxidized to Cu^+ and mainly Cu^{2+}, but the majority of Cu remains inactive in contact with SiO_2. Bulk AgI is a stoichiometric compound, and is therefore, believed not to dissolve Ag chemically. However, in thin film systems the situation can be different compared to bulk materials. Additionally, the ionic transference number differers from the ideal value $t_{\mathrm{ion}} = 1$ (for γ-AgI) indicating some (amorphous) impurities in AgI. Moreover, Ag/AgI/Pt samples with a thin Ag top electrode showed poor device characteristics,

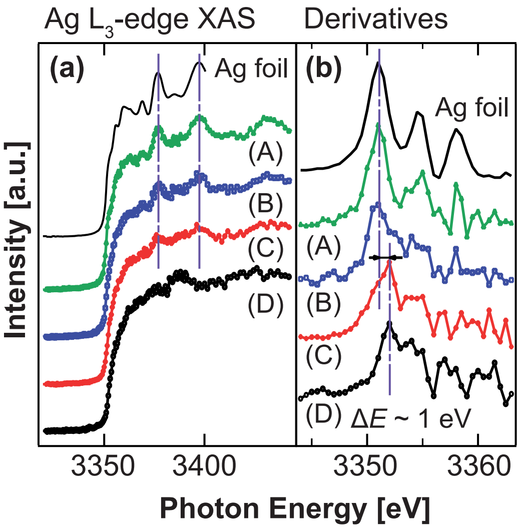

Figure 4.24 XAS of bare AgI thin films and AgI thin films covered by Ag layers (thickness 10 nm, 20 nm and 50 nm) [64]. (a) Ag L_3-edge XAS and (b) their derivative spectra of the AgI films after Ag deposition. For comparison the signal of a Ag foil is added.

such as high switching voltages and high resistance. Therefore, the chemical stability of the Ag/AgI interface was studied by X-ray Absorption Spectroscopy [64].

Normalized Ag L_3-edge XAS of 50 nm thick bare AgI thin films, and AgI thin films covered by 10 nm, 20 nm and 50 nm thick Ag films, respectively, are shown in figure 4.24a. The spectra clearly depend on the amount of Ag deposited on AgI. As the amount of Ag on AgI increases the Ag/AgI signal becomes more similar to the signal of a bare Ag foil. Since the signals can be separated into respective XAFS (X-ray Absorption Fine Structure) features of Ag and AgI (indicated by vertical lines), the absence of a chemical reaction of Ag and AgI is assumed. In principle, the edge energy in the XAS spectra reflects the chemical valence of a photo-excited atom (and thus, chemical interaction of the specific species) [64]. The edge energy can be estimated by the maximal slope of the excited atom's lowest-energy feature. The derivative spectra of the thin films are shown in figure 4.24b. At a photon energy of 3551 eV the peak maxima for Ag^0 ions (Ag metal) is observed. The peak maxima (highlighted by vertical lines) at 3552 eV corresponds to Ag^{1+} ions as in AgI. The Ag^{1+} signal decreases by increase of the Ag thickness deposited on AgI. This implies that no chemical reaction of Ag and AgI is observed.

Despite that no evidence of any chemical interaction of Ag at the interface with AgI was found, thin Ag films (electrodes) on AgI seem to be unstable resulting in bad device performance. Thus, Ag seems to be incorporated as small metallic (but potentially reduced) clusters in AgI. However, the spectra shown in figure 4.24a,b only reflect the averaged electronic structures over all silver atoms, regardless if they are penetrated into AgI or not.

For a more specific analysis of the interaction of Ag at the interface with AgI, Ag difference spectra are depicted in figure 4.25a. Here, several AgI samples (thickness 50 nm) with

Figure 4.25 (a) Difference spectra derived from the XAS spectra in figure 4.24a. (b) Schematic description to account for the difference analysis in (a) [64].

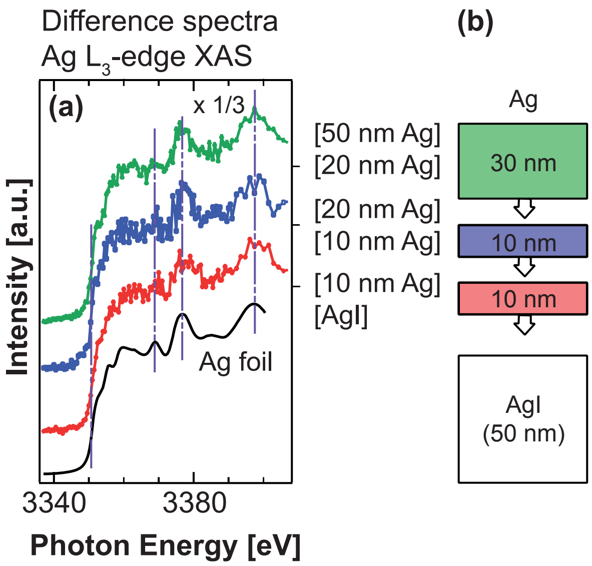

different Ag thickness (0 nm, 10 nm, 20 nm and 50 nm) are analyzed (schematic shown in figure 4.25b). The red line in figure 4.25a corresponds to the AgI sample with 10 nm Ag thickness on top ([10 nm Ag]) subtracted by the spectra of a pure AgI sample ([AgI]). The blue line is the difference spectra of the AgI sample with 20 nm Ag thickness ([20 nm Ag]) subtracted by the spectra of the [10 nm Ag] sample, and the green line corresponds to the spectra of the AgI sample with 50 nm Ag thickness ([50 nm Ag]) subtracted by the [20 nm Ag] sample. While the red spectrum reflects the unoccupied electronic structure of added Ag, separately out of the contribution of AgI (due to the same AgI thickness), the blue and green spectra correspond to further addition of 10 nm Ag and 30 nm Ag to that spectra, respectively. For simplification the edge energies of all signals in figure 4.25a are labeled by vertical lines. The XAS spectrum of a Ag foil is added for comparison. The XAFS features in all difference spectra are very similar and the edge energies fit to the XAS spectrum of the pure Ag foil. AgI has a zinc-blend structure, and hence, any intercalation of added Ag in AgI would change the local structure. However, such a change of the local structure is not observed and added Ag seems to aggregate in a metallic face-centered-cubic (fcc) structure. Thus, the added Ag appears to remain as metallic Ag^0 when diffused in AgI.

The I L_3-edge XAS spectra of the AgI thin films with and without additional Ag evaporation is shown in figure 4.26a, reflecting the chemistry of I^- ions in AgI. The XAS spectra of AgI and AgI with Ag evaporation are very similar. Therefore, no chemical interaction of Ag at the interface with AgI is observed based on both Ag L_3-edge and I L_3-edge XAS spectra.

On the atomic scale a change in the local structure of AgI (i.e. stoichiometry) by evaporation of Ag on AgI is not observed. However, the penetration of Ag in AgI can

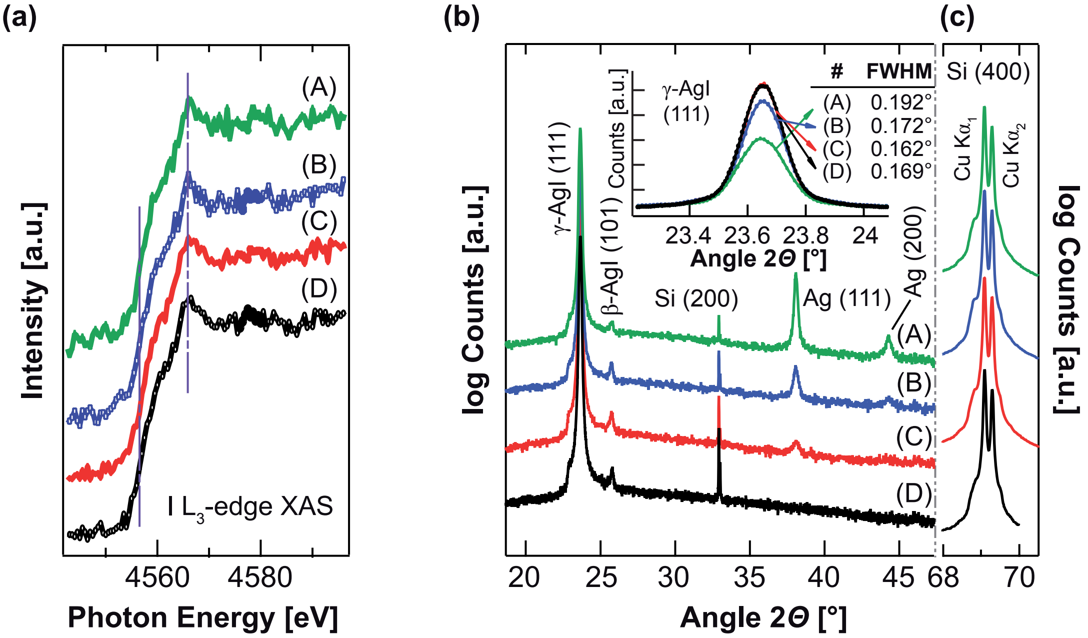

Figure 4.26. (a) I L$_3$-edge XAS spectra and (b) XRD profiles of the AgI thin films with and without additional Ag evaporation [64]. The I L$_3$-edge XAS spectra reveal no change in the local structure of AgI by evaporation of Ag. However, adding Ag can take effect in the scale of some tens of atoms as revealed by the inset in (b). The full-width-at-half-maximum (FWHM) of the (111) γ-AgI peak for each sample is also tabulated. (c) XRD pattern close to the (400) Si peak indicating no decrease of signal intensity as observed for the γ-AgI (111) peak in the inset of (b).

take effect in the scale of some tens of atoms. XRD profiles of AgI thin films with and without additional Ag evaporation are depicted in figure 4.26b. The peak $2\Theta = 23.65\,^\circ$ can be identified as γ-AgI (111), and the peak at $2\Theta = 25.5\,^\circ$ corresponds to a small ($< 1\,$Vol%) amount of β-AgI. Ag (111) features for samples with additional Ag layer are also observed. The γ-AgI (111) peaks are magnified in the inset of figure 4.26b. A systematic decrease of the intensity is observed by increase of the Ag thickness. Figure 4.26c shows the peak intensities of Si (400) diffraction (from the Si substrate), which, in contrast to the γ-AgI peak intensities, do not depend on the amount of added Ag. Thus, the decrease of the γ-AgI (111) intensity by increase of the Ag thickness cannot be attributed to measurement artefacts, which would also affect the Si (400) peak intensities. The full-width-at-half-maximum (FWHM) of the (111) γ-AgI peak for each sample is also shown in figure 4.26b. As the Ag thickness increases the FWHM also increases, indicating a weaken of long-range order in the AgI thin films. The slightly higher FWHM of pure AgI compared to the [10 nm Ag] sample is potentially due to an improvement of the crystallinity, caused by the Ag bombardment during fabrication. Hence, despite no chemical interaction of Ag on/within AgI was found the evaporation of Ag on AgI results in some disorder effect in the AgI thin film. These disorder effects can be explained by the formation of Ag metal crystallites in the AgI thin films in a sub-mesoscopic scale [64]. Thus, Ag can penetrate into AgI thin films without any chemical interaction. This penetration can affect the morphology of thin Ag electrodes on top of AgI, which results in a loss of electric contact. It can also affect the stability of nanoscale Ag filaments in the ON state after resistive switching.

4.3. Nonequilibrium States

Nonequilibrium states are inherently induced during device operation in nanoionic based cells including ReRAMs, which involve the oxidation, reduction and transport of active ions [40; 97]. These nonequilibrium states result in a nanobattery effect and in open circuit conditions an electromotive force (emf) is measured, which depends on the chemistry and the transport properties of the materials system. During device operation nonequilibrium states can be also induced or influenced. The emf is not only useful to further analyze redox reactions (including the nature of counter charges in SiO_2, see section 4.3.2), but has also a strong impact on the dynamic behavior of nanoscale devices. Nonequilibrium states have been observed in various material systems including SiO_2, AgI, GeS_x and $SrTiO_3$ both for ECM and VCM type ReRAMs. The theoretical background for nonequilibrium states is given in chapter 2.4. Special attention to nonequilibrium states introduced during ReRAM operation is paid in chapter 5.2.

4.3.1. Electromotive Force (emf) Measurements

In AgI nonequilibrium states are attributed to a gradient of the (electro-) chemical potential difference μ_{Ag} of atomic silver. Hence, in open circuit conditions the measurable cell voltage is believed to be dominated by a Nernst potential V_{N}. In case of AgI the measurable emf is only slightly affected by device operation, and can thus, only be controlled in a small bandwidth. In contrast, the emf in SiO_2 based devices is believed to be dominated by a concentration gradient of cations and counter charges. Here, the concentration gradient can be easily adjusted during device operating (e.g. by variation of the sweep rate and voltage amplitude). The emf in SiO_2 based devices gives also information about the nature of counter charges (i.e. OH^- ions or electrons, see section 4.3.2). Special attention is thence paid to nonequilibrium states in Ag/SiO_2/Pt and Cu/SiO_2/Pt devices in this section.

Regardless of the cation species, i.e. Ag^+ or Cu^{z+} (with $z = 2$ expected as the dominating species for Cu based devices), the nanobattery effect is influenced by a concentration gradient of cations and counter charges, and can be expressed by the diffusion potential

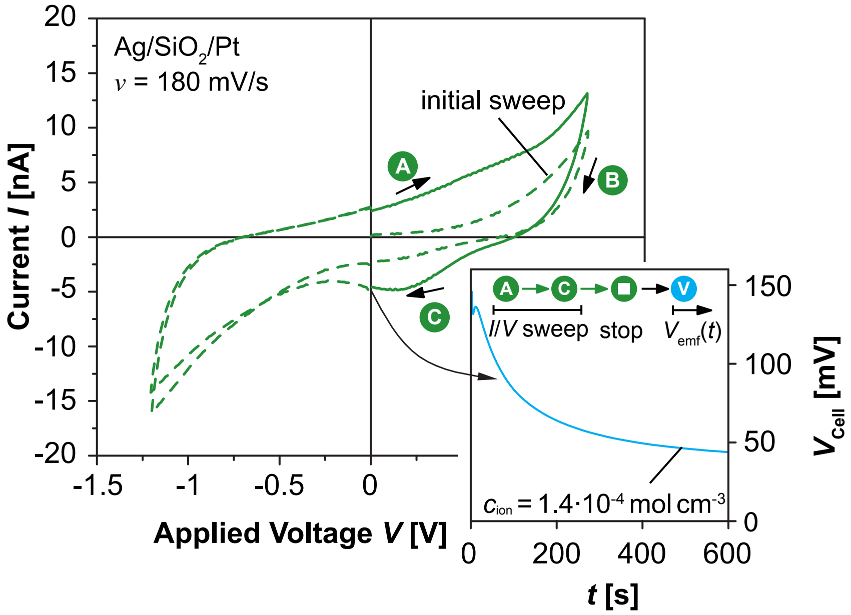

Figure 4.27. Measurement setup for emf measurements of a Ag/SiO$_2$/Pt cell [40]. A similar procedure is used for emf measurements of Cu/SiO$_2$/Pt cells. The cell voltage V_{Cell} was measured (as depicted in the inset) using a high impedance voltage mode of the source meter after anodic oxidation. For Cu based cells the voltage amplitude can be increased due to higher forming voltages.

voltage and Nernst potential voltage $V_{\mathrm{emf}} = V_{\mathrm{d}} + V_{\mathrm{N}}$. For Cu/SiO$_2$/Pt based cells the overall diffusion potential voltage V_{d} is determined by the diffusion potential voltage accounting for the cations $V_{\mathrm{d,Cu^{2+}}}$, and counter charges and electrons $V_{\mathrm{d,OH^-}} + V_{\mathrm{d},e^-}$:

$$V_{\mathrm{d}} \quad = \quad V_{\mathrm{d,Cu^{2+}}} + V_{\mathrm{d,OH^-}} + V_{\mathrm{d},e^-} \tag{4.11}$$

As follows, V_{d} may be written as (see section 2.4.2) [72]:

$$V_{\mathrm{d}} \quad = \quad \frac{kT}{e} \cdot \left(-\frac{\bar{t}_{\mathrm{Cu^{2+}}}}{2} \ln \frac{(a_{\mathrm{Cu^{2+}}})_{\mathrm{s'}}}{(a_{\mathrm{Cu^{2+}}})_{\mathrm{s''}}} - \bar{t}_{\mathrm{OH^-}} \ln \frac{\left(a_{\mathrm{OH^-}}\right)_{\mathrm{s'}}}{\left(a_{\mathrm{OH^-}}\right)_{\mathrm{s''}}} - \bar{t}_{\mathrm{e^-}} \ln \frac{(a_{e^-})_{\mathrm{s'}}}{(a_{e^-})_{\mathrm{s''}}} \right) \tag{4.12}$$

Additionally to the diffusion potential voltage a Nernst potential V_{N} can also contribute to the nanobattery voltage [72]:

$$V_{\mathrm{N}} \quad = \quad V^0 + \frac{kT}{2e} \cdot \ln \frac{(a_{\mathrm{Cu^{2+}}})_{\mathrm{s'}} \cdot (a_{\mathrm{OH^-}})_{\mathrm{s''}}{}^2}{(a_{\mathrm{Cu}})_{\mathrm{s'}} \cdot (a_{\mathrm{O_2}})_{\mathrm{s''}}{}^{\frac{1}{2}} \cdot \left(a_{\mathrm{H_2O}}\right)_{\mathrm{s''}}} \tag{4.13}$$

Equation 4.13 accounts also for the electrochemical activity of oxygen $\left(a_{\mathrm{O_2}}\right)_{\mathrm{s''}}$ (given by $p\mathrm{O_2}$) and the electrochemical activity of water $\left(a_{\mathrm{H_2O}}\right)_{\mathrm{s''}}$ (given by $p\mathrm{H_2O}$) at the interface s” (SiO$_2$/Pt).

Cyclic voltammetry of a Ag/SiO_2/Pt cell is shown in figure 4.27. For emf measurements the voltage was swept from 0 V to the maximum voltage amplitude (here 1.2 V), and subsequently back to 0 V. Afterwards, the source meter was switched to a high impedance voltage measurement mode. The cell voltage V_{Cell} was finally measured as a function of the ion concentration c_{ion} as shown in the inset of figure 4.27. The ion concentration can be adjusted by variation of the sweep rate (as discussed in 4.1.1). Figure 4.28a depicts cell voltage measurements versus time t for various ion concentrations for a Ag/SiO_2/Pt cell.

Relaxation of the cell voltage is observed within several minutes up to a few hours for Ag based cells. The cell voltage strongly depends on the ion concentration (i.e. concentration gradient of cations and counter charges) as shown in figure 4.28b after initial relaxation. The slope of the line provides the pre-exponential term and can be used to determine the average ionic transference number $\bar{t}_{\mathrm{ion}} \approx 0.5$. The c_{ion}-axes intercept corresponds to the condition $\ln(c_{\mathrm{ion}}) = \ln(a_{\mathrm{ion}}) = 0$ and provides the value of $V_0 = 0.17\,\mathrm{V}$.

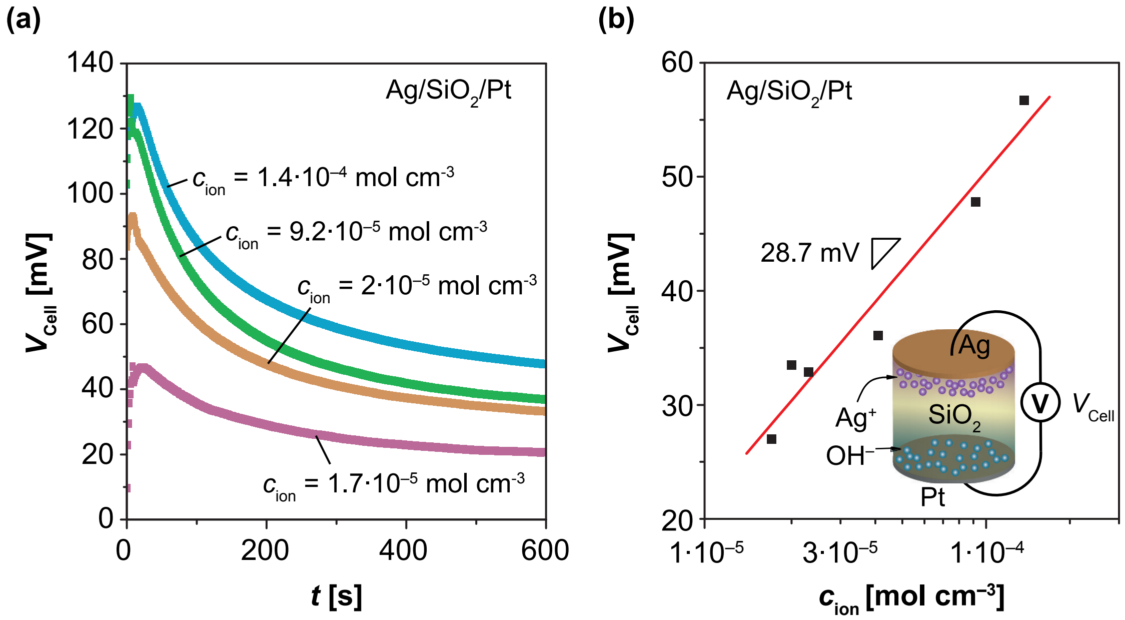

Figure 4.28. Electromotive force measurements for a Ag/SiO_2/Pt cell [40]. (a) Cell voltage V_{Cell} versus time for various ion concentrations c_{ion} adjusted by the sweep rate during anodic oxidation. (b) V_{Cell} versus c_{ion}. The ionic transference number can be determined by the slope of the regression line. The inset depicts a schematic of the concentration gradients of cations and counter charges (e.g. OH^- ions) both contributing to the emf.

An equivalent circuit for Ag/SiO_2/Pt or Cu/SiO_2/Pt cells is shown in figure 4.29a. It consists of the nanobattery (emf voltage V_{emf}), the ionic resistance R_{i} and the electronic resistance R_{el}. The emf cannot be directly measured since the measurable cell voltage V_{Cell} is determined by the voltage divider of R_{i} and R_{el}. For as-deposited cells, R_{i} and

R_{el} depend on the device geometry, and the electronic resistance is determined by the electronic partial conductivity. After forming and resistive switching the situation can be different. Now the device can be dominated by filamentary effects, and R_{i} and R_{el} may not scale compared to as-deposited cells. Additionally, R_{el} comprises also of the (high conducting) filament resistance in the ON state. In case of a metallic ON state $R_{\mathrm{el}} >> R_{\mathrm{i}}$ holds. Thus, the cell voltage is drastically reduced close to zero. However, the nonequilibrium states are still remaining in the ON state and can affect the state retention (see also chapter 5.2.2) [40].

Figure 4.29b shows cell voltages of a Cu/SiO_2/Pt cell versus time for various ion concentrations. The relaxation time for Cu based cells is in the order of several hours up to days, and is therefore, significantly larger than for Ag/SiO_2/Pt cells. Moreover, the cell voltage in Cu cells is up to ten times higher than for Ag based cells.

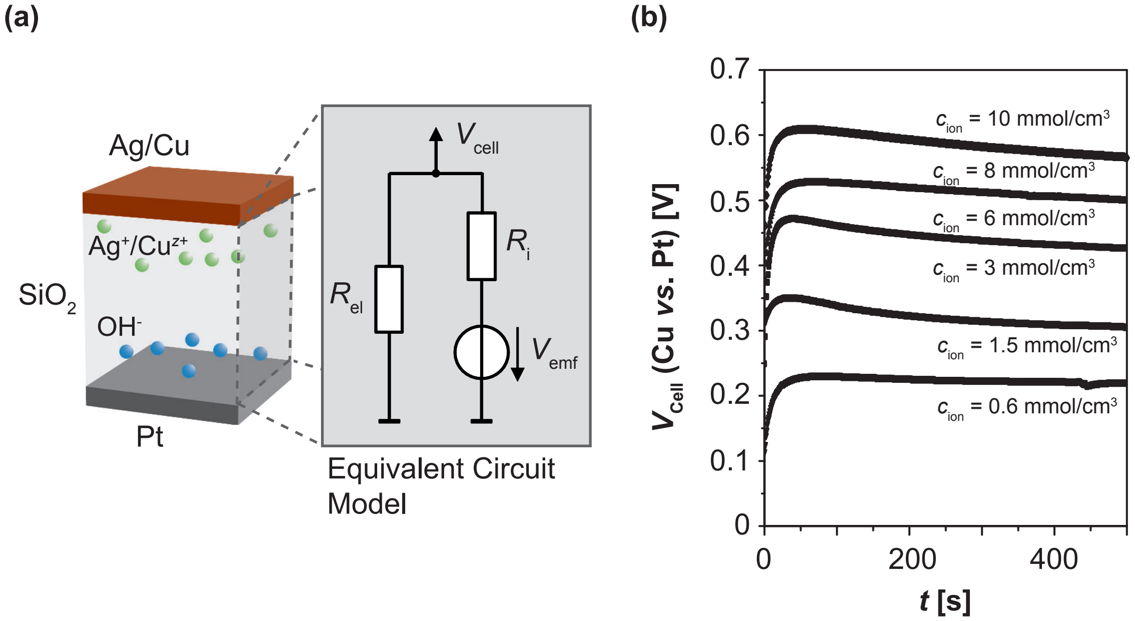

Figure 4.29. (a) Equivalent circuit model for Ag/SiO_2/Pt or Cu/SiO_2/Pt cells. The measurable cell voltage is determined by the nanobattery voltage V_{emf}, the ionic resistance R_{i} and the electronic resistance R_{el}. (b) Cell voltages of a Cu/SiO_2/Pt cell versus time for various ion concentrations. Redrawn from [72].

4.3.2. Impact of Water Partial Pressure

In section 4.1.3 the importance of counter charges for anodic oxidation has been discussed. The results of cyclic voltammetry in nitrogen atmosphere and different water partial pressures pH_2O indicate that hydroxide ions OH^- and not electrons are the dominating counter charges. OH^- is supplied by reduction of water from the ambient. The counter charge effect can be further analyzed by measuring the cell voltage by variation of pH_2O. Figure 4.30a depicts V_{Cell} versus pH_2O (in nitrogen atmosphere) for a Cu/SiO$_2$/Pt cell. The ion concentration of both cations and OH$^-$ is believed to be constant during the experiment. From equation 4.13 it is evident that the emf is influenced by $\left(a_{H_2O}\right)_{s"}$ (and thus, pH_2O) also when $(a_{Cu^{2+}})_{s'}$ and $\left(a_{OH^-}\right)_{s"}$ are constant. To ensure reproducible experimental conditions, the oxygen partial pressure pO_2 was monitored by an oxygen sensor simultaneously and was found to be constant during the measurements. The highest value for V_{Cell} is measured in anhydrous nitrogen atmosphere as expected from equ. 4.13. The system requires at least 60 min for relaxation as soon as quasi-equilibrium for each water partial pressure is reached. Figure 4.30b shows that V_{Cell} remains constant over days, in contrast to Ag/SiO$_2$/Pt cells where the relaxation is in the order of some hours. Cu/SiO$_2$/Pt cells are therefore more useful for electromotive force versus water partial pressure measurements. V_{Cell} can be reversibly tuned (increased or decreased) depending on the particular water partial pressure as depicted in figure 4.30c. Hence, pH_2O and therefore, the water molecules incorporated into SiO$_2$ do not significantly

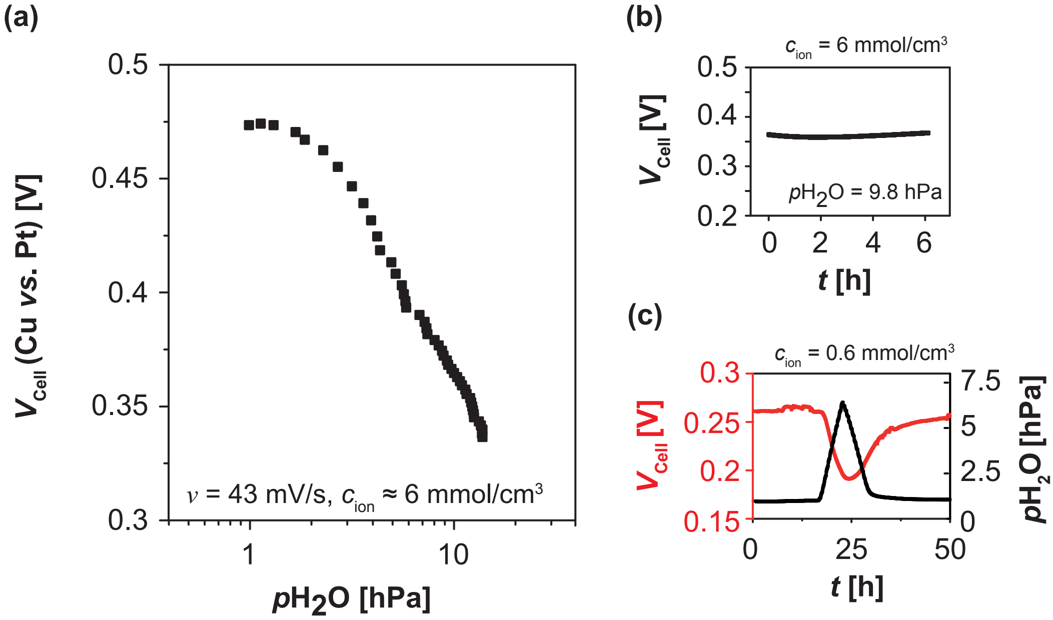

Figure 4.30. Electromotive force measurement at a constant ion concentration for a Cu/SiO$_2$/Pt cell. (a) V_{Cell} dependence on the water partial pressure in nitrogen atmosphere. Each point corresponds to a different pH_2O value. The initial ion concentration (indicated in the plot) was set prior to the measurements. (b) Transient measurement of V_{Cell} at constant c_{ion} and pH_2O. (c) V_{Cell} (red) response to the variation of pH_2O (black). The V_{Cell} response on pH_2O change is reversible. This indicates that the concentration gradient of Cu remains constant with time and pH_2O does not meaningfully increase the mobility of Cu ions in SiO$_2$. Redrawn from [72].

increase the ion mobility (due to solvent effects). As follows the Cu^{z+} and OH^- ion concentration gradients remain constant, and respectively, the actual origin of the emf is not changed.

In conclusion, the results presented above and in section 4.1.3 underline the importance of a counter charge/reaction. Without a counter charge/reaction anodic oxidation cannot take place, and thus, the resistive switching effect is not observed. These experiments evidently verified that water is mainly supplying the required counter charge(s) for anodic oxidation and hence resistive switching, rather than enhancing the cation mobility in SiO_2 thin films, which would result in an irreversible decrease of V_{Cell} by increase of $p\mathrm{H_2O}$. Electrons alone seem to play an inferior role as counter charges required for keeping the electroneutrality, because anodic oxidation is not observed in anhydrous atmosphere.

By XPS depth profiling (section 4.1.1) a pronounced increase of the Cu^{2+} concentration for the electrochemically treated sample in the immediate vicinity of the electrode is observed (section 4.1.1), whereas the concentration within the SiO_2 film is very small. Thus, the half cell potential at the working electrode interface (Cu/SiO_2) is most likely defined by the Cu^{2+} ion concentration, and at the counter electrode interface (SiO_2/Pt) the water redox reaction is determining the electrode potential and providing the counter charge needed for the Cu half cell reaction. Increasing the water partial pressure increases the half cell potential at the counter electrode, but lowers the absolute cell potential difference in accordance to equation 4.13. As soon as water is removed by decrease of $p\mathrm{H_2O}$, the cell voltage V_{Cell} will increase again in accordance to equation 4.13.

5. Resistive Switching Effect and Applications

This chapter deals with the resistive switching effect in electrochemical metallization memory cells based on silicon dioxide and silver iodide. It is shown that the resistance transition in ECM cells is strongly affected by redox processes (section 5.1) and nonequilibrium states (section 5.2) as described in the previous chapter. The feasibility of the fabricated ECM cells for practical applications is discussed in section 5.3. Furthermore, a nondestructive readout approach for passive crossbar arrays composed of complementary resistive switches (section 5.3.2) is introduced. This readout method can additionally be used for a fully parallel pattern recognition based on an associative capacitive network (section 5.3.3).

5.1. Switching Behavior in Silicon Dioxide and Silver Iodide

In this section the cation based resistive switching effect in silicon dioxide, as a widely used insulating material, and silver iodide, representing a typical solid electrolyte, is discussed. The switching effect is studied by both potentiodynamic current/voltage (I/V) sweep experiments as well as (ultra-) fast pulse experiments. Figure 5.1 depicts SEM images of micro crossbar (electrode area A between $2\,\mu\text{m} \times 2\,\mu\text{m}$ and $10\,\mu\text{m} \times 10\,\mu\text{m}$) and nano crossbar ($A = 100\,\text{nm} \times 100\,\text{nm}$) cells exemplarily for Ag/SiO_2/Pt based devices. For larger cell areas micro structured cells with a diameter between $100\,\mu\text{m}$ to $1\,\text{mm}$ were fabricated.

5.1.1. Current/Voltage Sweep Experiments

For many ECM devices (including SiO_2 [32; 53; 72] and GeS_x based cells [99; 100]) an initial *electroforming* step by applying a forming voltage V_F is required to be able to operate the memory cell. In this regard, the electroforming step is considered as

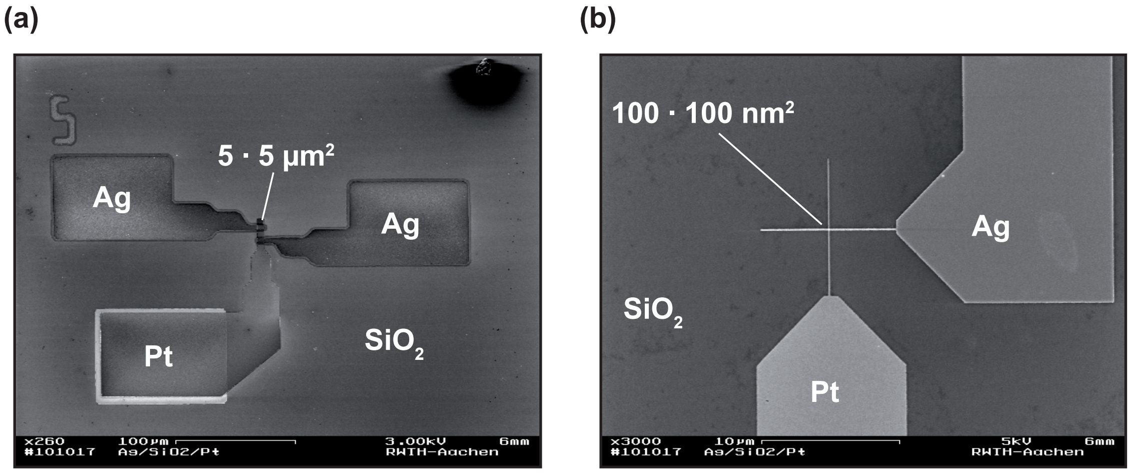
(a)
(b)
5 · 5 μm²
Ag
Ag
Pt
SiO₂
x260 100μm 3.00kV 6mm
#101017 Ag/SiO2/Pt RWTH-Aachen
100 · 100 nm²
Ag
SiO₂
Pt
x3000 10μm 5kV 6mm
#101017 Ag/SiO2/Pt RWTH-Aachen

Figure 5.1. Scanning Electron Microscopy of (a) micro crossbar, and (b) nano crossbar cells with a Ag/SiO_2/Pt layer stack [98].

a soft-break-down [101–104] and/or injection of mobile cations into the electronically insulating thin film [34; 71]. Here, the cell switches from a high resistive state to a low resistive state during electroforming. Either a current compliance I_{CC} or a series resistor is required to avoid damage of the cell after electroforming. The cell switches back to a high resistive state when a negative voltage is applied between the anode and cathode. In some ECM devices the resistance in the high resistive state is decreased by a few orders of magnitude after electroforming compared to the resistance of the pristine cell. In AgI based cells an electroforming process is not required [54]. This is contributed to the inherent high cation mobility in AgI and the presence of mobile cations within the electrolyte after fabrication.

Figure 5.2 Resistive switching behavior of Ag/SiO_2/Pt, Ag/AgI/Pt and Ag/GeS_x/Pt micro crossbars (μXBar) as well as a Ag/SiO_2/Pt nano crossbar (nXBar) [98]. Arrows indicate the direction of sweep.

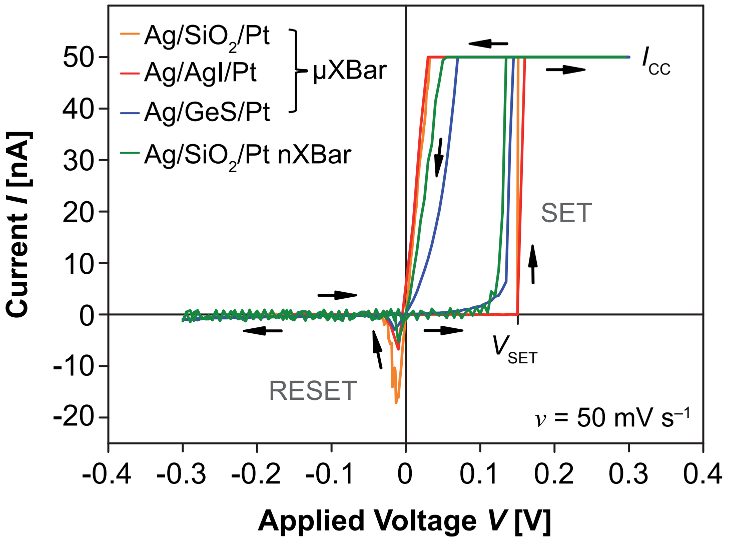

The subsequent I/V cycles, termed as *resistive switching* in the following, look similar to the electroforming process but the voltage for resistance transition (i.e. SET voltage, V_{SET}) is typically smaller compared to the electroforming voltage V_{F}. The resistive switching behavior for various ECM based cells including Ag/AgI/Pt micro crossbars (μXBar) as well as Ag/SiO_2/Pt micro and nano crossbars (nXBar) is shown in figure 5.2 (the electroforming step is not depicted). For comparison, a typical I/V curve for a Ag/GeS_x/Pt cell is also shown as well (details on fabrication and switching behavior can be found in [100]). A current compliance or series resistor is required during resistive switching as well to prevent damage of the cell in the low resistive state due to high currents.

Electroforming and Resistive Switching in Silicon Dioxide

Typical electroforming processes for Cu/SiO_2/Pt and Ag/SiO_2/Pt cells are shown in figure 5.3a and 5.3b, respectively. Regardless of the anode material a large statistical variation on both the forming voltage V_{F} as well as the SET voltages V_{SET} is observed. However, the forming voltage for silver based cells is typically smaller than for Cu based cells.

In ambient atmosphere and for an insulator thickness of 50 nm, the electroforming voltage for Cu/SiO_2/Pt cells varies from $V_{\mathrm{F}} = 2\,\mathrm{V}$ to $V_{\mathrm{F}} = 7\,\mathrm{V}$, and the SET voltage varies between $V_{\mathrm{SET}} = 0.25\,\mathrm{V}...2\,\mathrm{V}$. A similar behavior has been observed for Cu/SiO_2/Pt cells based on RF-sputtered silicon dioxide (see also [35; 105; 106]). For silver based cells the electroforming voltage varies from $V_{\mathrm{F}} = 1\,\mathrm{V}$ to $V_{\mathrm{F}} = 3\,\mathrm{V}$ (for a SiO_2 thickness of 50 nm). SET voltages between $V_{\mathrm{SET}} = 0.1\,\mathrm{V}...1.6\,\mathrm{V}$ were observed, which fits to SET voltages reported for Ag/SiO_2 based cells with various counter electrodes in literature [107–111].

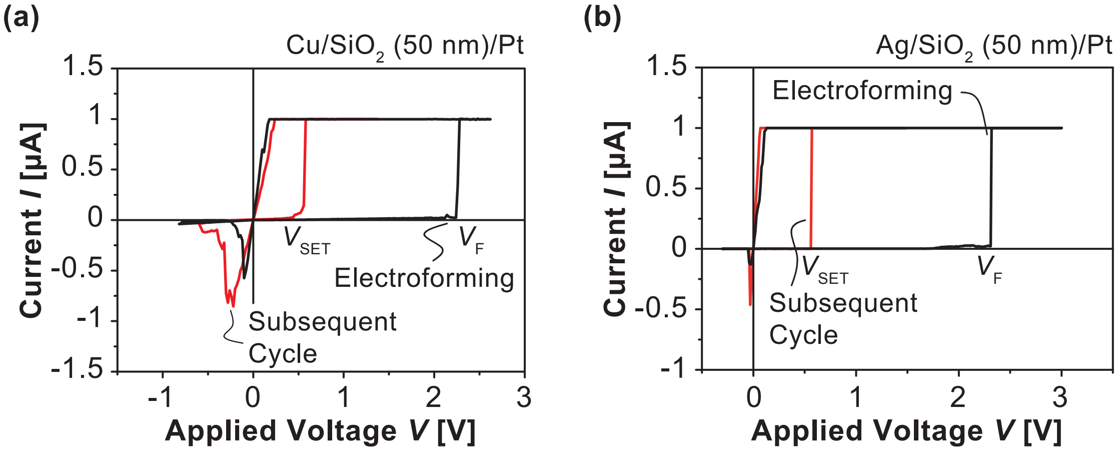

Figure 5.3. Electroforming and subsequent resistive switching of (a) a Cu/SiO_2/Pt [53] and (b) a Ag/SiO_2/Pt cell.

In general, the forming voltage increases by increase of the insulator thickness, while the SET voltages are nearly independent on the device geometry. This has been previously studied in detail for SiO_2 (e.g. [34; 35; 110]).

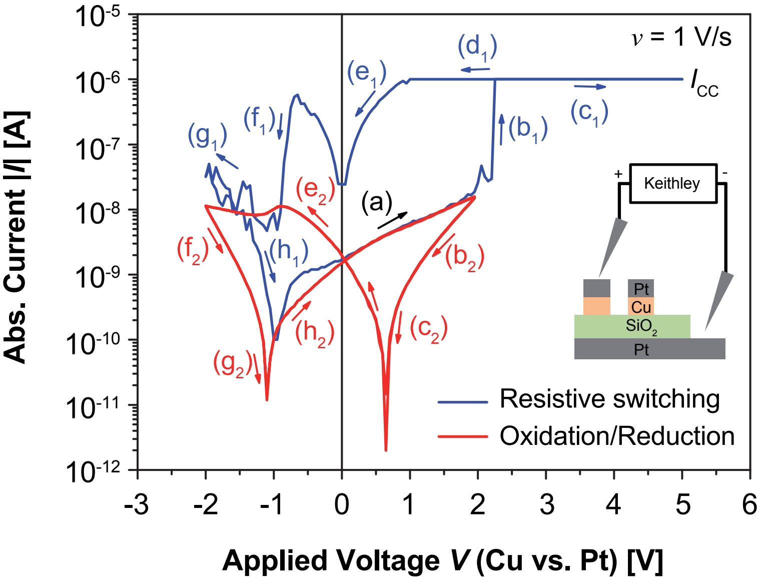

Figure 5.4 Electroforming step required to enable resistive switching of a $Cu/SiO_2/Pt$ cell (blue curve) [66]. By limitation of the vertex potential resistive switching is avoided and the oxidation/reduction reactions being the preceding processes of resistive switching can be analyzed (red curve) by cyclic voltammetry (CV).

The electroforming cycle is shown exemplarily for a $Cu/SiO_2/Pt$ cell in a logarithmic current scale in figure 5.4 and compared to the oxidation and reduction current measured during cyclic voltammetry (red curve). By limitation of the vertex potential to $\pm 2\,V$ resistive switching is avoided, and thus, oxidation and reduction of Cu and Cu^{z+} can be analyzed prior to the switching event by cyclic voltammetry (see chapter 4.1.1). Arrows indicate the sweeping direction (a) to (h). In case of (a) where Cu ions are formed the red curve and blue curve are overlaid. The case (b) to (h) for the red curve differs from the blue curve. The cell switches at an applied voltage of approximately $V = 2.4\,V$ (b_1). During switching to the low resistive state a current compliance I_{CC} is used to avoid damage of the cell ((c_1) and (d_1)). The cell switches back to the high resistive state by applying a negative voltage ((f_1) to (h_1)). Oxidation and reduction processes can be observed as shown by the red curve ((a) to (h_2)) when switching is avoided (see chapter 4.1). This implies that the current prior to the resistance transition represented by the blue curve is dominated by the ionic current as assumed in simulation models [25; 112; 113].

By controlling the current compliance the ON resistance R_{ON} in the LRS can be adjusted by orders of magnitude during voltage sweeping, which has been reported for various ECM material systems [53; 70; 114; 115] including SiO_2 [35; 106]. This *multilevel switching* by orders of magnitude cannot be solely explained by a simple change of the filament diameter (i.e. higher SET current results in an increase of the filament

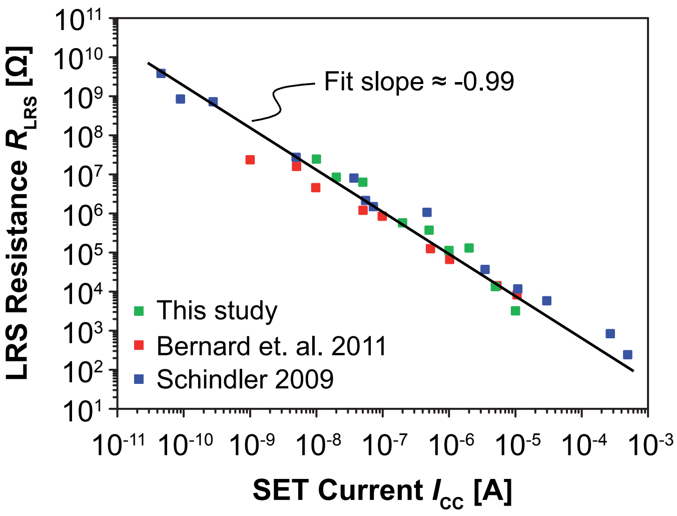

Figure 5.5 Multilevel switching for a Ag/SiO_2/Pt cell compared to results of Cu/SiO_2/Pt cells reported in literature (Bernard et. al. 2011 [106] and Schindler 2009 [35]).

diameter). For ON resistances above 13 kΩ tunneling between the filament and the active electrode is believed to be dominating the ON resistance [25]. This is further discussed in section 5.1.3. A comparison of multilevel switching results of typical Ag/SiO_2/Pt cells (this study) and results reported in literature for Cu/SiO_2/Pt cells (Bernard et. al. 2011 [106] and Schindler 2009 [35]) are shown in figure 5.5. The slope of ≈ -0.99 fits very well to simulation results [25]. In the context of multilevel switching the ON resistance is typically extracted from I/V curves. However, poor stability of high resistive ON states (R_{ON} above 13 kΩ) was observed, which has been also reported in literature [35; 40; 71; 116]. Only few reports indicate stable ON states above 13 kΩ for a reasonable long time [117–119].

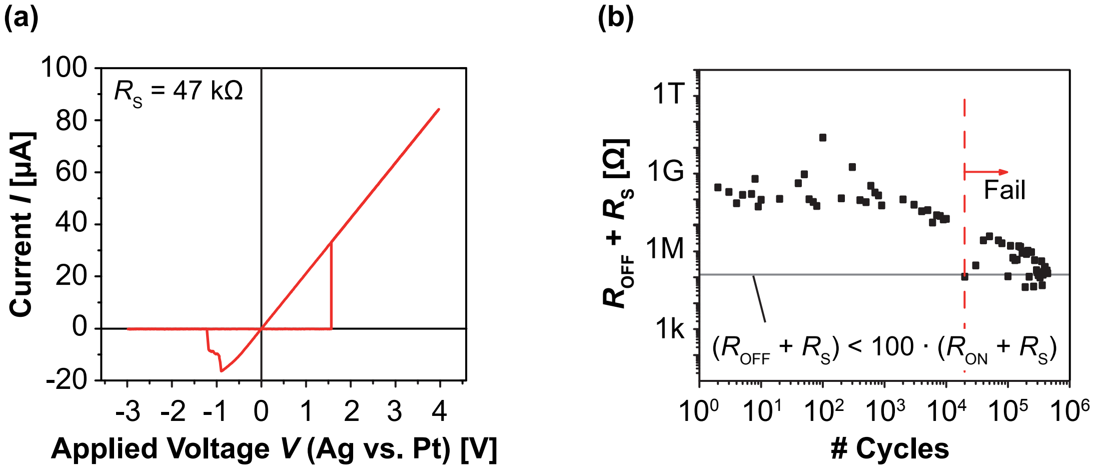

Figure 5.6. (a) Resistive switching of a Ag/SiO_2/Pt cell using a $R_{\mathrm{S}} = 47\,\mathrm{k}\Omega$ series resistor to limit the current in the low resistive ON state. (b) Endurance of the same cell. The device failure is here defined as soon as the cell exhibits a $R_{\mathrm{OFF}}/R_{\mathrm{ON}}$ ratio smaller than 100. The cell withstands more than 10^4 I/V cycles.

The finite response time of the current compliance is considered as a serious problem for resistive switching applications due to a current overshoot [120; 121]. The current compliance can have a significant impact on the device performance [122] and on the multilevel switching [123], if the current compliance is too slow and the current overshoot is too high. The response and tripping time for the *Keithley* 6430 source meter can be in the order of a few tens of milliseconds [124]. This seemed to be fast enough for multilevel switching as observed in this study. However, the endurance of cells measured using a current compliance was found to be poor (up to a few hundred cycles). A series resistor can be alternatively used to limit the current in the low resistive ON state. A typical I/V curve of a Ag/SiO$_2$/Pt cell in series to a shunt resistor $R_\mathrm{S} = 47\,\mathrm{k\Omega}$ is depicted in figure 5.6a. Using a series resistor, the cell withstands more than 10^4 I/V cycles (cf. 5.6b).

Resistive Switching in Silver Iodide

Typical resistive switching characteristics of a Ag/AgI/Pt micro crossbar are shown in figure 5.7a. In contrast to systems like SiO$_2$, an electroforming step is not required for AgI. This is contributed to a sufficient amount of mobile cations in the electrolyte in the as-deposited state. The comparatively small switching voltage V_SET is usually between 60 mV and 250 mV. For memory applications higher switching voltages (e.g. $V_\mathrm{SET} = 0.5\,\mathrm{V}$) are required to prevent unintentional SET of the cell. However, many ReRAMs including Ag/AgI/Pt cells show strongly nonlinear switching kinetics (see section 5.1.4), which fulfills the requirements for fast switching at moderate voltages and

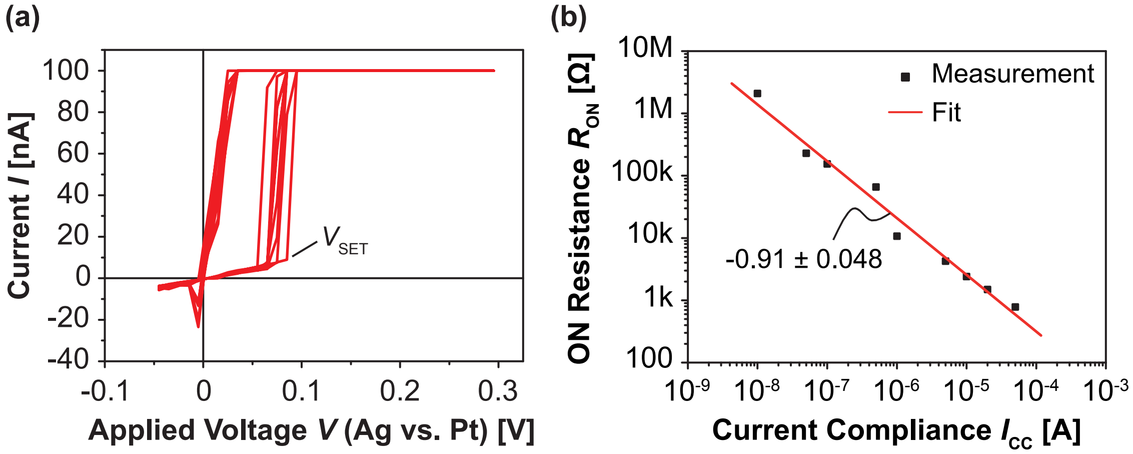

Figure 5.7. (a) Resistive switching characteristics of a Ag/AgI/Pt micro crossbar. In contrast to SiO$_2$ ReRAMs, an initial electroforming step to enable resistive switching is not required. (b) Multilevel switching by variation of the current compliance. The ON resistance was extracted from I/V curves. [54]

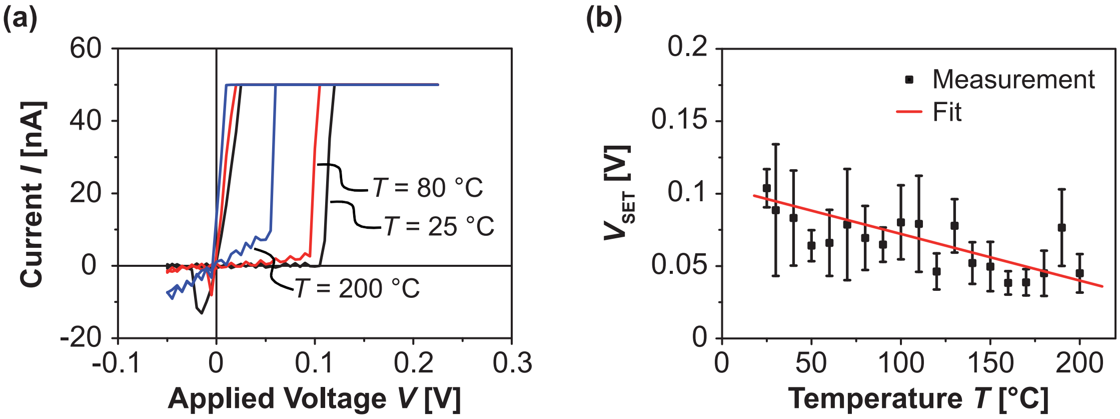

Figure 5.8. (a) Typical I/V curves for various temperatures $T = 25\,°\mathrm{C}$, $80\,°\mathrm{C}$ and $200\,°\mathrm{C}$, respectively. (b) SET voltage V_{SET} versus temperature.

prevention of unintended switching at low voltages for a reasonable voltage stress time. The maximum absolute current during RESET is typically smaller compared to SiO_2 cells. A potential reason could be that the electrochemical oxidation of the Ag filament is more feasible in AgI than in SiO_2. As depicted in figure 5.7b, the ON resistance can be adjusted by orders of magnitude by variation of the current compliance comparable to SiO_2 based ReRAMs (cf. 5.5).

Figure 5.8a shows the impact of elevated temperatures T on the resistive switching characteristics of AgI. The SET voltage is decreased by increase of the temperature. Additionally, the resistance in the OFF state is decreased, potentially due to an increase of the ion conductivity. The relation of V_{SET} versus T is shown in figure 5.8b. An abrupt decrease of the SET voltage after the γ-AgI to α-AgI phase transition ($T \approx 145\,°\mathrm{C}$) is not found. This is an indication that for slow sweep rates, in the order of some tens to hundred mV/s, the cation drift is not the limiting factor for resistive switching in

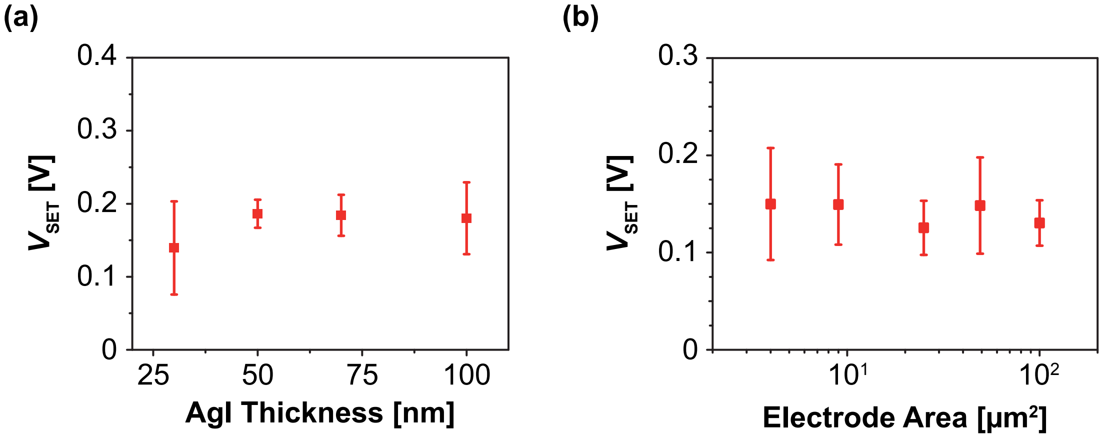

Figure 5.9. (a) Impact of AgI electrolyte thickness on the SET voltage. (b) SET voltage versus micro crossbar electrode area.

case of I/V sweeps. In contrast, as discussed in chapter 5.1.4, nucleation limitation and charge transfer can be the dominating factors.

Compared to SiO_2, the statistical variation (i.e. SET voltage, ON and OFF resistance) from cell to cell was found to be smaller. The SET voltages are similar even for cells with different AgI electrolyte thickness as depicted in figure 5.9a (similar results were reported for SiO_2 based ECM cells [35]). Additionally, a significant impact of the micro crossbar electrode area on the SET voltage has not been observed as shown in figure 5.9b.

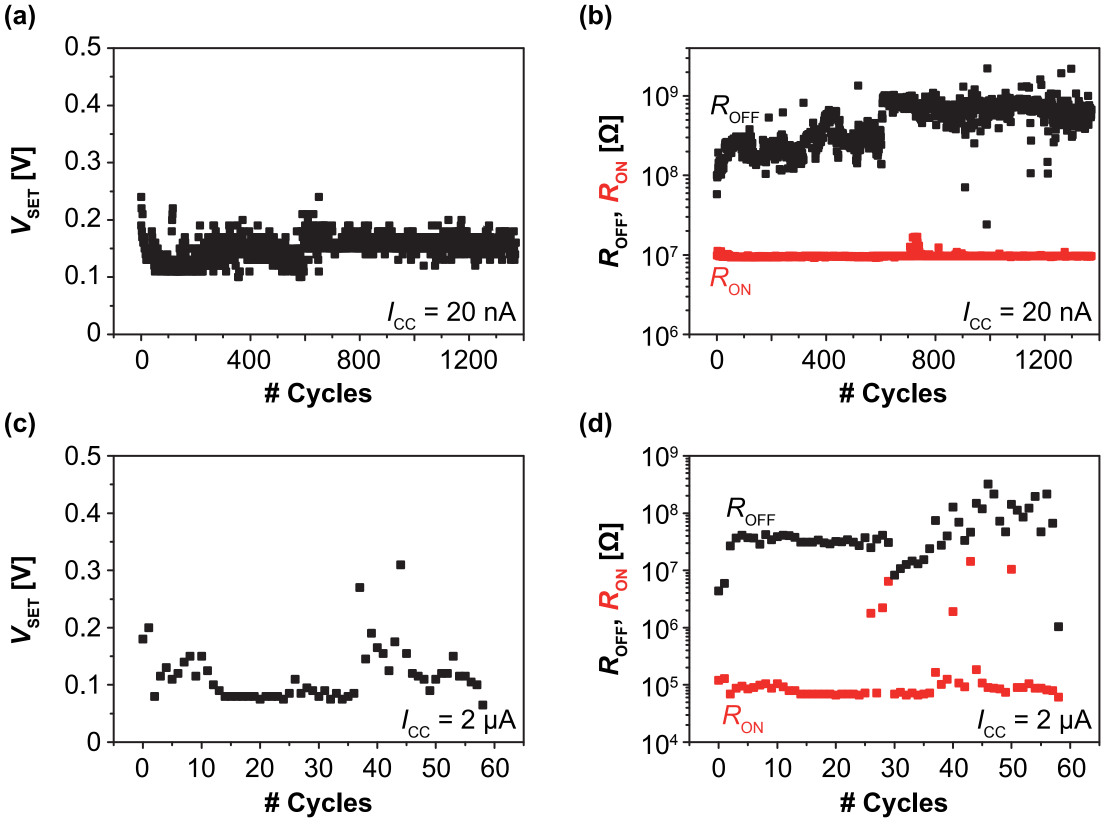

Figure 5.10. Endurance test for a Ag/AgI/Pt micro crossbar. (a) and (b) SET voltage, and ON and OFF resistance using a current compliance of 20 nA. (c) and (d) V_{SET}, and R_{ON} and R_{OFF} endurance using a current compliance of 2 μA.

Although the statistical variation in AgI is better than in SiO_2, the cells exhibit a poor device endurance depending on the current compliance level. For I_{CC} in the order of some μA to some tens of μA only few cycles can be performed. Afterwards, the cell cannot be RESET into the OFF state. For smaller current compliances the endurance is improved up to a few hundred cycles, but the ON resistance is comparatively high (above 1 MΩ). In figure 5.10 the endurance data of Ag/AgI/Pt micro crossbars are shown. The current compliance was set to 20 nA ((a) and (b)) and 2 μA ((c) and (d)), respectively. In some cases the ON state was not very stable after switching and the cell switched back to the OFF state as shown in Fig. 5.10d. For more than 1400 cycles in (a) and (b), and 58 cycles in (c) and (d) the cells were not able to RESET into the OFF state. For practical applications an ON resistance of $R_{\mathrm{ON}} \approx 50\,\mathrm{k}\Omega$ is required to reduce the voltage drop across the bit lines in a memory array [119; 125]. This is, however, not fulfilled by many ReRAM devices (e.g. [31; 35; 86; 126; 127], see also section 5.3.1).

5.1.2. Impact of Water Partial Pressure on Silicon Dioxide based Cells

The role of counter charge(s) and/or reactions at the counter electrode for anodic oxidation, and the impact of $p\mathrm{H_2O}$ on the electromotive force has been discussed in chapter 4.1.3 and 4.3.2 for $\mathrm{SiO_2}$ based cells. This section is focused on the impact of ambient moisture on the resistive switching behavior of $\mathrm{Ag/SiO_2/Pt}$ cells. The dielectric constant of $\mathrm{SiO_2}$ increases as the water partial pressure $p\mathrm{H_2O}$ increases as shown in figure 5.11a. Simultaneously, the dissipation factor tan δ increases by increase of $p\mathrm{H_2O}$. These effects are contributed to the penetration of water in the porous silicon dioxide thin film, and can practically be used for moisture sensors [128]. In figure 5.11b a pronounced dependence of $p\mathrm{H_2O}$ on the average forming voltage V_{F} is shown. High forming voltages have been observed for both anhydrous nitrogen and oxygen atmospheres. By further increase of the humidity a logarithmic decrease of the forming voltages has been observed.

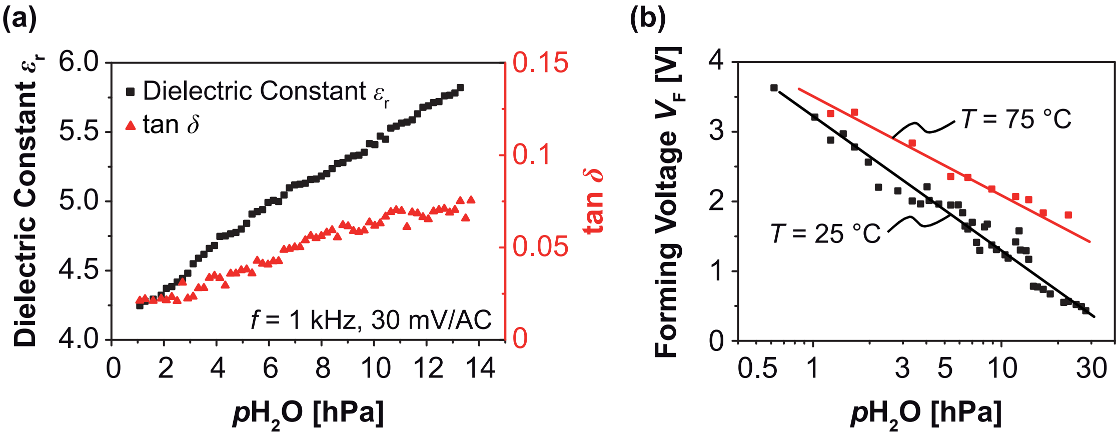

Figure 5.11. Impact of water partial pressure $p\mathrm{H_2O}$ on (a) the dielectric constant and dissipation factor tan δ, and (b) the forming voltage V_{F} of $\mathrm{Ag/SiO_2/Pt}$ cells in $\mathrm{N_2{:}H_2O}$ atmosphere [32].

As previously discussed in chapter 4.1.3, water from the ambient could be reduced at the $\mathrm{SiO_2/Pt}$ interface [72; 129], supplying the required counter charge, and hence, enabling resistive switching. Alternatively, hydration of $\mathrm{Ag^+}$ could enhance the metal cation drift across the insulator. Theoretical studies of hydrated Ag ions predict geometrically highly flexible hydrate structures with short lifetimes [130; 131], which could easily interact with SiO_2 during the drift across the insulator.

The same impact of moisture on the resistive switching effect of Cu/SiO_2/Pt cells has been reported in literature [73]. Here, the SET voltage increases in vacuum, which is also contributed to removal of previously incorporated water. Similar effects have been also reported for the Cu/poly(3-hexylthiophene)/Au system (P3HT) where the switching voltage decreases by increase of pH_2O [132].

5.1.3. Quantum Conductance Experiments

Multilevel switching has been reported for many material systems (e.g. [35; 70; 106; 114; 115]). A simple change of the filament geometry (i.e. filament radius) cannot properly describe this effect, since the ON resistance can be adjusted by many orders of magnitude [12]. In contrast, a tunnel gap between the filament and the active electrode can explain multilevel switching [25]. In case of low resistive ON states (i.e. $R_{\mathrm{ON}} < 13\,\mathrm{k}\Omega$) the device conductance is, however, equal or close to the single atomic point contact conductivity. In this case the device resistance can be dominated by a single or a few metal atoms between the filament and the active electrode.

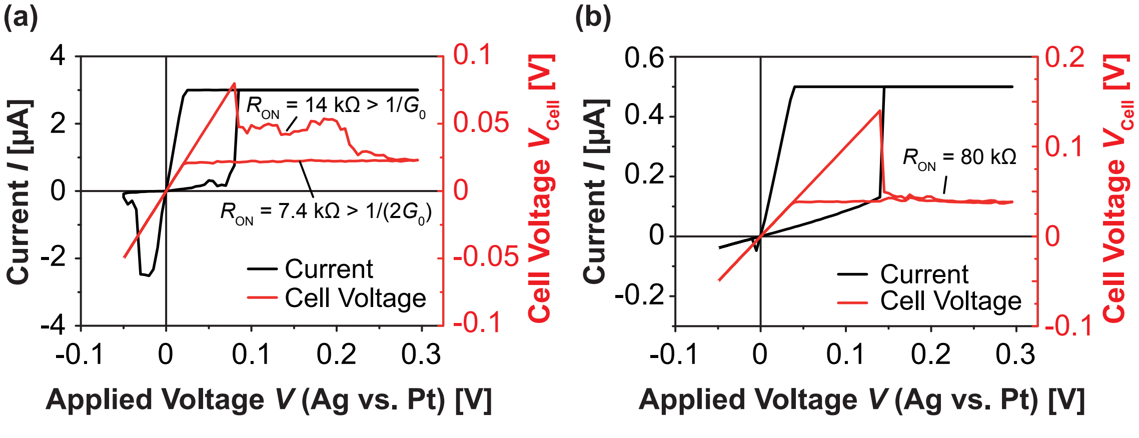

Figure 5.12. Analysis of filament formation by measuring the actual cell voltage drop simultaneously during an I/V sweep of a Ag/AgI/Pt cell [54]. (a) Although the cell already switched, a significant voltage drop of about 25 mV is observed during further sweeping, indicating a quantized change of the filament conductivity. (b) At lower current compliances a similar voltage drop is not observed.

After switching to the ON state, the effectively applied cell voltage is controlled (i.e. lowered) by the source meter to adjust the programmed current compliance. Typical cell voltages during I/V sweep are shown in figure 5.12. Although, the cell is switched to a specific ON resistance (depending on the current compliance), the effective cell voltage further decreases during the sweep (cf. 5.12a). This can be understood in a further (but slow) growth or strengthen of the metallic filament towards the active electrode, since the driving force (cell voltage) for electrochemical filament formation is reduced but still effective. However, for comparatively high $R_{\mathrm{ON}} >> 13\,\mathrm{k}\Omega$ the voltage decrease is rather continuous or nearly not detectable, which is exemplary shown in figure 5.12b. It is remarkable that only for low ON resistances $R_{\mathrm{ON}} < 13\,\mathrm{k}\Omega$ a nearly discrete voltage drop is observed.

In case of high R_{ON} the overall conductivity of the cell seems to be dominated by tunneling between the filament and the active electrode. By further growth of the filament the tunneling distance is reduced continuously resulting in a gradual change of the conductivity, and hence, gradual voltage drop. In contrast, in case of $R_{\mathrm{ON}} < 13\,\mathrm{k}\Omega$ the overall resistance is close to the resistance of a single atomic point contact $R_0 = 1/G_0 = \left(2e^2/h\right)^{-1} \approx 12.9\,\mathrm{k}\Omega \approx 1/\left(78\,\mu\mathrm{S}\right)$ [133]. Hence, a single metal atom of the filament seems to be dominating the device resistance. As the growth of the filament continues, a second atom can contribute to the conductivity resulting in a quantized decrease of the ON resistance, and as follows, a discrete cell voltage drop. This can explain the discrete voltage steps in figure 5.12a. In this respect, in both cases the filament resistance R_{f} of about $500\,\Omega$ to $1\,\mathrm{k}\Omega$ is in series either to the tunnel contact or to the atomic point contact. A proposed equivalent circuit of the overall cell resistance is depicted in figure 5.13. The contact resistance R_{c}, the filament resistance R_{f} as well as the resistance of the Ag and Pt electrodes R_{e} are contributing to the total cell resistance R_{ON} in the ON state. It should be noted that R_{f} and R_{c} may vary during measurement, and depend on the cell voltage due to further filament growth, whereas $R_{\mathrm{e}} << 100\,\Omega$ depends only on the device geometry and conductivity of Ag and Pt, and will be further neglected for simplification.

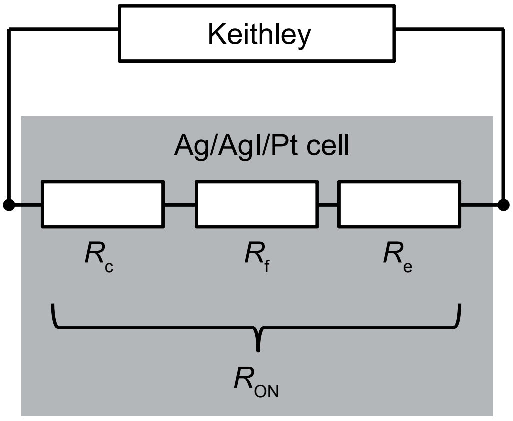

Figure 5.13 Equivalent circuit of a simple measurement setup consisting of the Ag/AgI/Pt cell and the *Keithley* source meter. The electrode resistance R_{e} is small compared to the contact resistance R_{c} and the filament resistance R_{f}. Hence, R_{e} will be further neglected. [54]

Quantized conductance values were only observed within a current window of $1\,\mu$A to $30\,\mu$A. By conventional I/V sweeps (cf. 5.12a) more than one or two discrete voltage drops were not detected. In contrast, several discrete conductance levels can be observed by a current sweep measurement as shown in figure 5.14a. At the beginning the cell is switched to the ON state using a current compliance of 100 nA. Subsequently, the current is increased stepwise from 100 nA to $20\,\mu$A by 100 nA and 2 s per step. The cell resistance/conductance is simultaneously measured. In figure 5.14a at least five quantized cell conductance levels can be observed, which fit well to integer multiple of the conductivity G_0 of an one atomic point contact. Here, a filament resistance $R_\mathrm{f} = 800\,\Omega$ was assumed. It should be noted that the current resulting in specific conductance level varies from cell to cell, and some levels (e.g. $1 \cdot G_0$ or $5 \cdot G_0$ in this example) can be skipped during measurement.

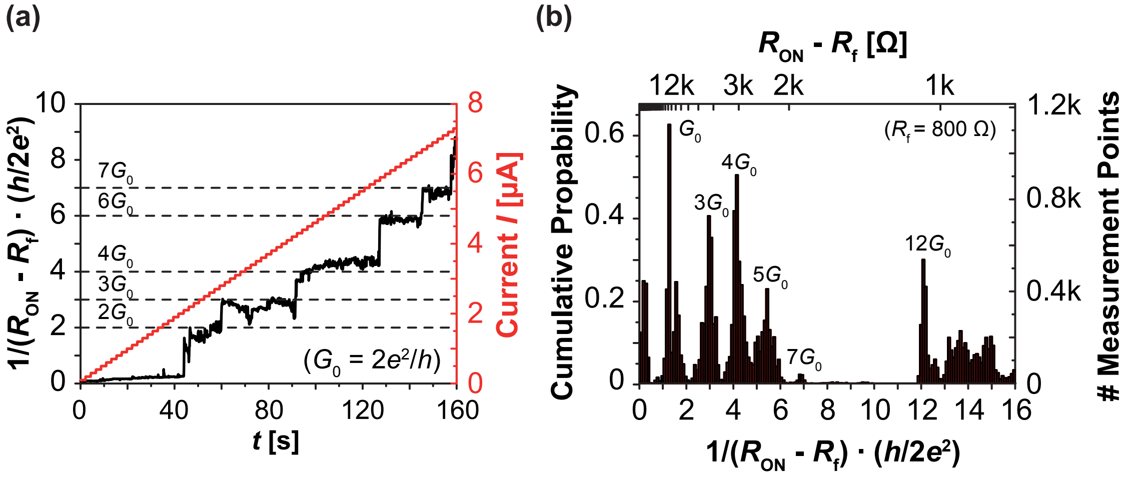

Figure 5.14. Analysis of quantized cell conductance by a current sweep using Ag/AgI/Pt cells. [54] (a) At least five quantized resistances have been observed in this example by current sweeping. (b) Cumulative statistics of measured cell conductivity.

Due to the statistical variation from cell to cell, 65 cells have been measured resulting in a total number of more than $2 \cdot 10^4$ conductivity measurement points. Based on these measurement points a cumulative statistics of cell conductivities has been calculated. $R_\mathrm{f} = 800\,\Omega$ is assumed because this value fits good to the resistance calculated by the conductivity of Ag (based on the Fuchs-Sondheimer theory [134]), a length of 30 nm and a diameter of $1 - 2$ nm [25]. The result is shown in figure 5.14b. It is remarkable, that maximum of the cumulative probability for specific conductivities $n \cdot G_0$ (with $n = 1, 2, 3, ...$) are observed. In particular, the maxima for $n = 1, 3, 4, 5$ are distinctive. Variation of the actual filament resistance from cell to cell and during measurement may result in deviation from the exact conductivity $n \cdot G_0$. However, the reason for the gap between $7 \cdot G_0$ and $12 \cdot G_0$ is unclear. It was found that for $R_\mathrm{ON} < 2\,\mathrm{k}\Omega$ the cell resistance drops fast below 1 kΩ. Hence, it is assumed that the measurement equipment is too slow to detect resistance levels between 2 kΩ and 1 kΩ in this experimental setup. Thus, in a cumulative statistics these resistances are potentially not contributing. Below 1 kΩ the cell resistance is nearly constant and may be dominated by the filament resistance. Therefore, this resistance is again contributing to the cumulative statistics. As the ON resistance decreases the LRS becomes more stable with less resistance fluctuation. Cell conductance values between $G = n \cdot G_0 = 1 \cdot G_0 ... 7 \cdot G_0$ are hardly stable at room temperature, since the relocation of a single atom has a strong impact on the device resistance. However, for lower temperatures the conductance values are stabilized as exemplarily shown for $T = 173\,\mathrm{K}$ in figure 5.15.

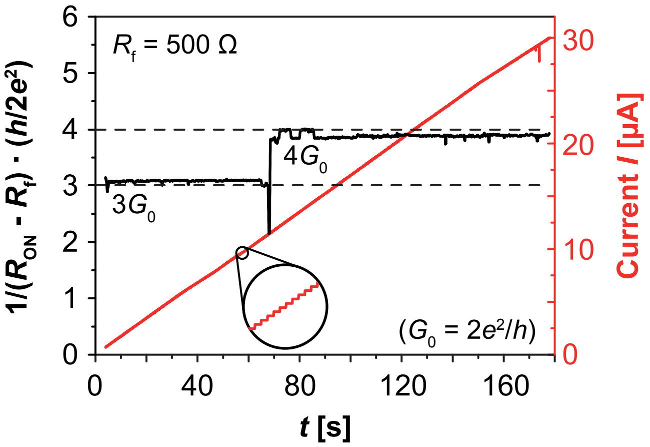

Figure 5.15 Quantum conductance experiment of a Ag/AgI/Pt cell at an ambient temperature of $T = 173\,\mathrm{K}$. Here, the conductance values fit very well to integer numbers of G_0 when a filament resistance of $R_f = 500\,\Omega$ is assumed.

Quantized conductance values are not only observed in AgI based resistive switches but also in silicon dioxide based ReRAMs. Figure 5.16 depicts various quantized conductance experiments for Ag/SiO_2/Pt micro crossbars analyzed by a current sweep similar to the experiment described above. The potential filament resistance R_f, which is in series to the contact resistance (cf. 5.13), seems to differ more from cell to cell compared to AgI based devices. In some cases the measurement results fit best to a comparatively high R_f in the order of a few kΩ, while for other cells a low $R_f \approx 100\,\Omega$ is more reasonable. The larger statistical spread of the generic resistive switching characteristics of silicon dioxide based cells, such as the switching voltage, is a potential reason for the variation of R_f.

In figure 5.17 the cumulative statistic of the measured cell conductivity levels of Ag/SiO_2/Pt micro crossbars is depicted. Here, the filament resistance R_f was first optimized so that the cell conductivity fits best to integer values of the atomic point contact conductivity. Afterwards, the cumulative statistic has been calculated. In contrast to AgI based ReRAMs, intermediate conductance steps (e.g. $1.5 \cdot G_0$, $2.5 \cdot G_0$ or $3.5 \cdot G_0$) are observed for Ag/SiO_2/Pt micro crossbars.

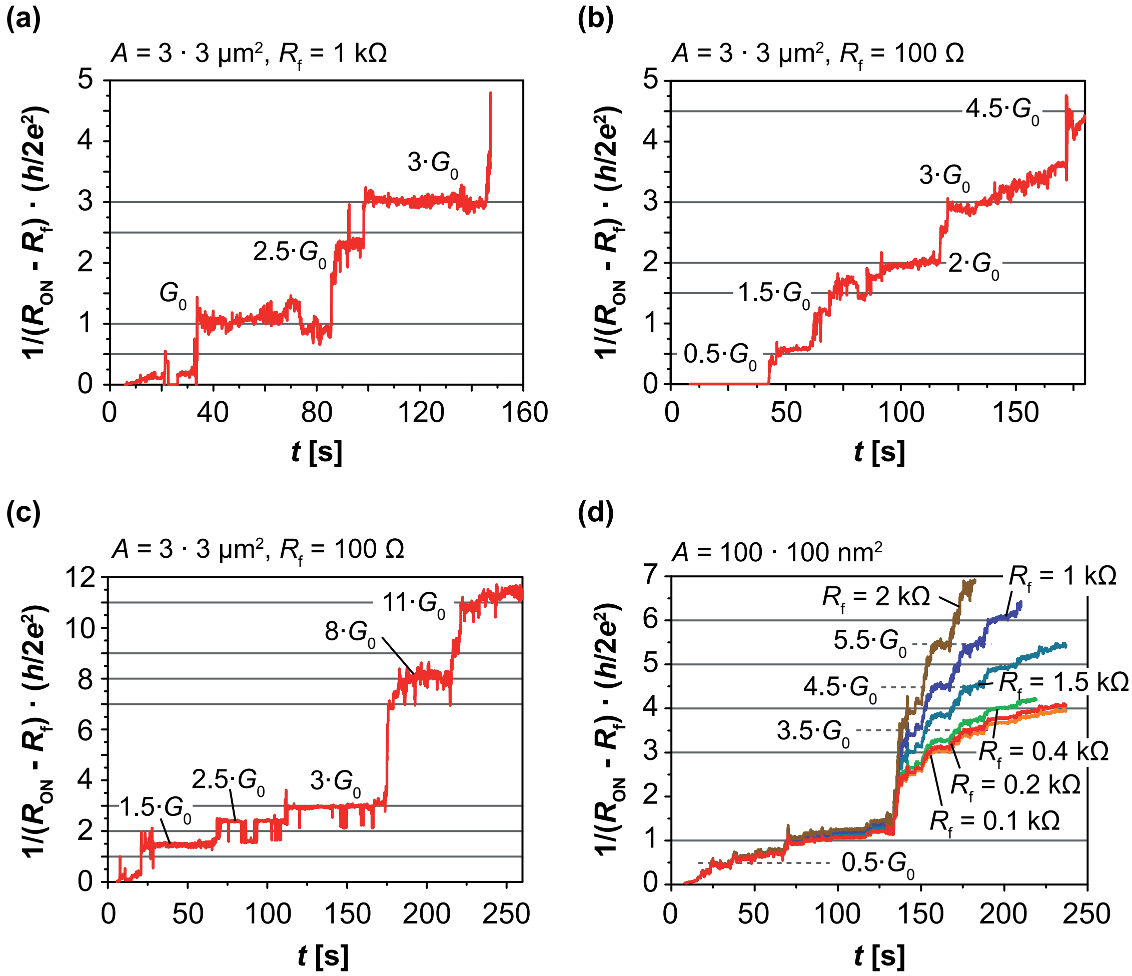

Figure 5.16. Analysis of quantized cell conductivities of Ag/SiO_2/Pt micro crossbars using current sweeps. The assumed filament resistance R_f differs more from cell to cell compared to AgI based devices: (a) $R_\mathrm{f} = 1\,\mathrm{k\Omega}$, (b) $R_\mathrm{f} = 100\,\Omega$ and (c) $R_\mathrm{f} = 200\,\Omega$. In (d) quantized cell conductivities of a of Ag/SiO_2/Pt nano crossbar are given. The current response is fitted by various filament resistances $R_\mathrm{f} = 100\,\Omega \ldots 1.5\,\mathrm{k\Omega}$.

At first glance, quantum size effects at room temperature seem to be questionable. Typically, quantum size effects are expected at cryogenic temperatures. However, as the dimensions of the filament are in the order or smaller than the phase coherence length of the electrons, quantum size effects become relevant [135]. The filament can be considered as a wave guide for electrons and the conductance can be expressed in terms of the Landauer theory. In this case the Landauer expression is applicable here as well since the Fermi wavelength of Ag or Cu is similar to the atomic diameter and the quantum mode splitting is in the order of $\approx 1\,\mathrm{eV}$ [119; 135].

Quantum size effects in resistively switching devices have been first reported for *gap type atomic switches* [136–138]. The atomic switch is an ECM cell where the active electrode (e.g. Ag) is covered by a mixed-conducting thin film (e.g. Ag_2S). In contrast to

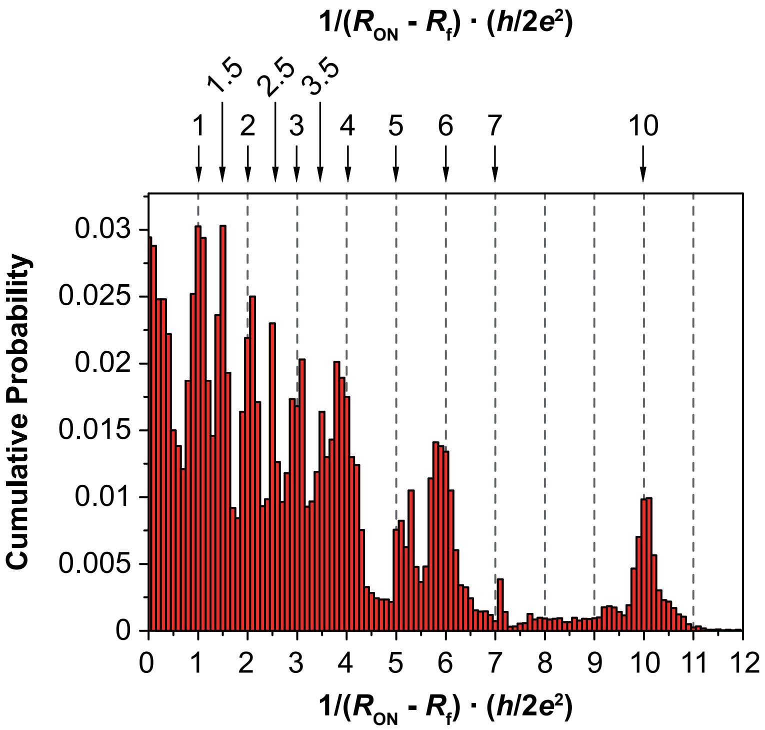

Figure 5.17. Cumulative statistic of the measured cell conductivity levels of Ag/SiO_2/Pt micro crossbars.

conventional ECM cells, a vacuum gap is separating the electrolyte and counter electrode. This can be easily achieved using a Pt STM tip (Scanning Tunneling Microscopy), or alternatively a special fabrication method based on sulfidation of the Ag electrode, and final electrochemical dissolution of a thin Ag layer separating the electrolyte and counter electrode [136]. Besides the prospect of high scalability to an almost atomic level, the atomic switch concept can be further used for neuromorphic applications [139], and spectroscopic and kinetic analysis of ion conductors on an atomic level [87].

In addition to conventional (*gapless*) ECM cells using AgI [54] or SiO_2 as electrolyte, quantized conductance effects have been observed for various ECM material systems including Ta_2O_5 [140], Ag_2S [141], GeS_2 [142], Ag/a-LSMO/Pt [143] and liquid systems [144], and even for VCM type devices like HfO_2 [145; 146]. Moreover, quantum size effects have been theoretically discussed in the context of memristors and memristive systems [147; 148].

5.1.4. Pulse Measurements and Switching Kinetics

As shown in figure 5.7a, AgI based cells switch at low SET voltage ($\approx 80\,\mathrm{mV}$) in case of potentiodynamic measurements, which seems to be disadvantageous for memory applications since it drastically reduces the read voltage margin. However, fast read- and write-pulses are preferably applied for memory applications. Therefore, it is important to analyze the switching behavior using short pulse voltages. Additionally, analysis of the switching kinetics over a large time scale can disclose electrochemical effects involved during resistive switching. This section deals with the analysis of the switching kinetics of Ag/AgI/Pt micro crossbars in a time scale of up to twelve orders of magnitude. The experimental data is compared to a simulation model, which accounts for three limitation factors: nucleation, charge transfer and cation drift limitation [87].

Pulse Measurements

In case of potentiodynamic experiments where the sweep rate was varied between 40 mV/s and 3 V/s, the SET voltage $V_{\mathrm{SET}} \approx 0.1\,\mathrm{V}$ was found to be nearly independent on the sweep rate [54]. In contrast, strong exponential relation between the pulse amplitude V_{Pulse} and the SET time t_{SET} is observed for pulse measurements as described below. This has been also demonstrated for various resistive switching materials [28].

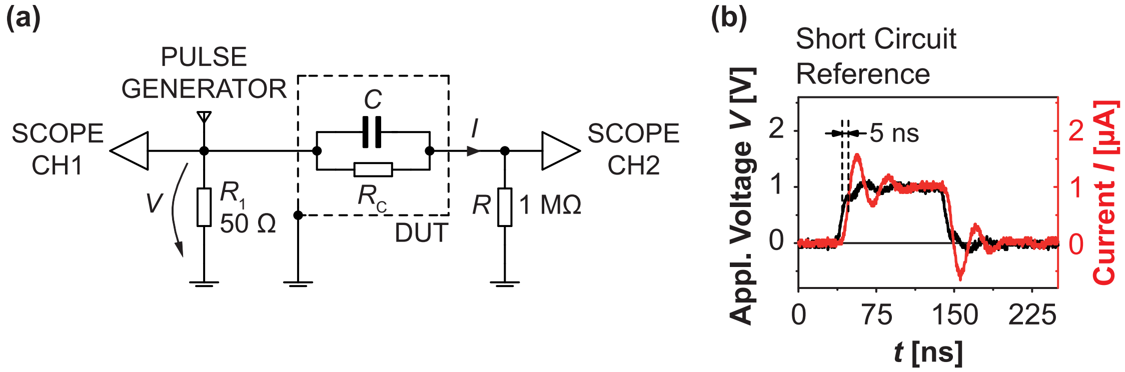

Figure 5.18. (a) Measurement setup for pulse experiments. The AgI micro crossbar cell (device under test, DUT) can be described by a $R_C C$ circuit. The voltage signal supplied by the pulse generator is recorded by an oscilloscope channel (SCOPE CH1) coupled by 50 Ω. The current response is recorded by a second oscilloscope channel (SCOPE CH2) coupled by 1 MΩ which acts as shunt resistor. (b) Short circuit reference measurement. The cable length in the RFI shielded measurement box was reduced in order to measure signals down to ≈ 10 ns.

The measurement setup for pulse experiments is shown in figure 5.18a. Two oscilloscope channels SCOPE CH1 and SCOPE CH2 are recording the voltage and current signal, respectively. SCOPE CH1 is connected to the Ag/AgI/Pt micro crossbar (device under test, DUT) and the pulse generator. The channel is coupled by 50 Ω to reduce high frequency reflexions. The input impedance (1 MΩ) of SCOPE CH2 acts as shunt resistor for the current/voltage conversion. The cable length was kept short in order to measure signals down to ≈ 10 ns as revised by a short circuit reference measurement (cf. 5.18b). The limiting factor in this measurement setup is the RC time given by the input impedance of SCOPE CH2 and the capacity of the DUT in the OFF state. In chapter 4.2.1 a capacitance of $\approx 250\,\mathrm{fF}$ was measured for $f = 1\,\mathrm{MHz}$ and a cross section area of $A = 10\,\mu\mathrm{m} \times 10\,\mu\mathrm{m}$. For pulse measurements, cells with a cross section area of up to $A = 3\,\mu\mathrm{m} \times 3\,\mu\mathrm{m}$ were used. This results in a cell capacity of about 10 fF...23 fF (which is below the measurement resolution of the LCR-Meter). Thus, the delay time of the measurement setup is given by $RC = 1\,\mathrm{M\Omega} \cdot 23\,\mathrm{fF} = 23\,\mathrm{ns}$. For a shorter delay time nano crossbar devices and a smaller shunt resistor should be used. However, the later results in a smaller current resolution. Alternatively, active amplifiers for I/V conversion could be used to reduce the RC time. For pulse measurements a pulse voltage between $V_{\mathrm{Pulse}} = 70\,\mathrm{mV}$ up to $V_{\mathrm{Pulse}} = 2\,\mathrm{V}$ was generated by the pulse generator, and the voltage and current signals were monitored using the oscilloscope. Recording long voltage pulses (above a pulse length of 1 s) is sophisticated using an oscilloscope. Therefore, a *Keithley* 6430 Source meter was used for long voltage pulses where the pulse voltage range is $V_{\mathrm{Pulse}} = 25\,\mathrm{mV} ... V_{\mathrm{Pulse}} = 100\,\mathrm{mV}$. In this context, the current in the ON state was limited by a current compliance of 100 nA instead of a series resistor. The voltage range for the source meter and pulse generator measurement setup are overlapping to ensure comparability.

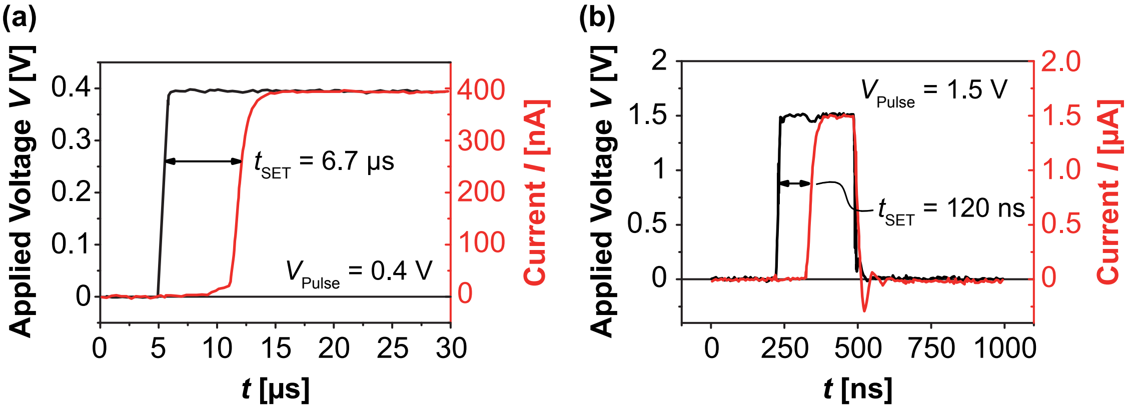

Figure 5.19. Short pulse measurements and current transients for (a) $V_{\mathrm{Pulse}} = 0.4\,\mathrm{V}$ and (b) $V_{\mathrm{Pulse}} = 1.5\,\mathrm{V}$ [54].

Typical voltage pulse measurements and the corresponding current response of the cells are depicted in figure 5.19. For small pulse voltages (e.g. $V_{\mathrm{Pulse}} = 0.4\,\mathrm{V}$, cf. 5.19a) the SET time t_{SET} is significantly larger than for high pulse voltages (e.g. $V_{\mathrm{Pulse}} = 1.5\,\mathrm{V}$) as shown in figure 5.19b. Here, the pulse length is $t_{\mathrm{Pulse}} = 250\,\mathrm{ns}$ with an applied voltage of $V_{\mathrm{Pulse}} = 1.5\,\mathrm{V}$. t_{SET} is defined as the time difference between the voltage signal rise and the current signal rise.

In figure 5.20 current transients for various pulse voltages over a large time scale (up to 12 orders of magnitude) are shown. For readability, only the current rise normalized with

Figure 5.20 Current transients for various pulse voltages over a large time scale of up to 12 orders of magnitude.

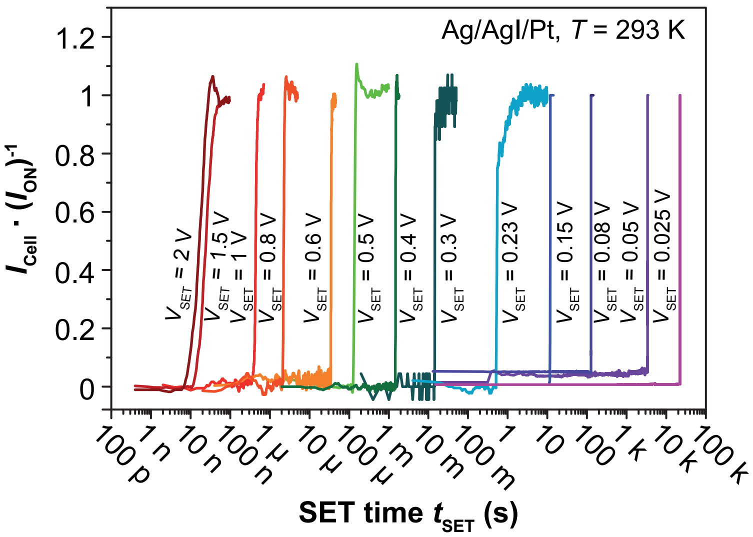

the maximum current in the low resistive ON state is shown. The maximum current is either given by the pulse voltage and the series resistor, or the current compliance depending on the measurement setup. From the current transients the average SET time for a specific pulse voltage can be extracted, which is depicted in figure 5.21a for $T = 298\,\mathrm{K}$ and in figure 5.24 for a sample temperature range between $T = 298\,\mathrm{K}$ and $T = 373\,\mathrm{K}$, respectively. The statistical probability for switching can be expressed by a Weibull distribution [149; 150]

$$F\left(t_{\mathrm{SET}}\right) = 1 - \exp\left(-\left(\frac{t_{\mathrm{SET}}}{\tau}\right)^{\beta}\right), \tag{5.1}$$

exemplarily shown for $V_{\mathrm{Pulse}} = 0.3\,\mathrm{V}, 0.4\,\mathrm{V}, 0.5\,\mathrm{V}, 1\,\mathrm{V}, 1.5\,\mathrm{V}$ and $2\,\mathrm{V}$ in figure 5.21. Here, F is the cumulative fraction of cells, which successfully switched to the ON state in a certain time t_{SET}. τ is a characteristic time where $F = 0.63$ [149]. The Weibull slope β defines the time-to-switch spreading degree and can provide information about the mechanism behind the switching event [149]. $\beta \approx 1...1.7$ increases slightly for $V_{\mathrm{Pulse}} \leq 0.5\,\mathrm{V}$. For higher pulse voltages $V_{\mathrm{Pulse}} \geq 1\,\mathrm{V}$ β increases from 2.2 to 5.1. This is an indication that between $V_{\mathrm{Pulse}} = 0.3\,\mathrm{V}$ and $2\,\mathrm{V}$ two different limiting factors are determining the switching time. For $V_{\mathrm{Pulse}} < 0.3\,\mathrm{V}$ less statistical information is available due to long pulse lengths of up to 10 h. The individual limiting factors are discussed in the next section.

Simulation Model

A simulation model for the strong nonlinearity of the switching kinetics of AgI was presented by S. Menzel et. al. [112]. The model accounts for three rate limiting steps,

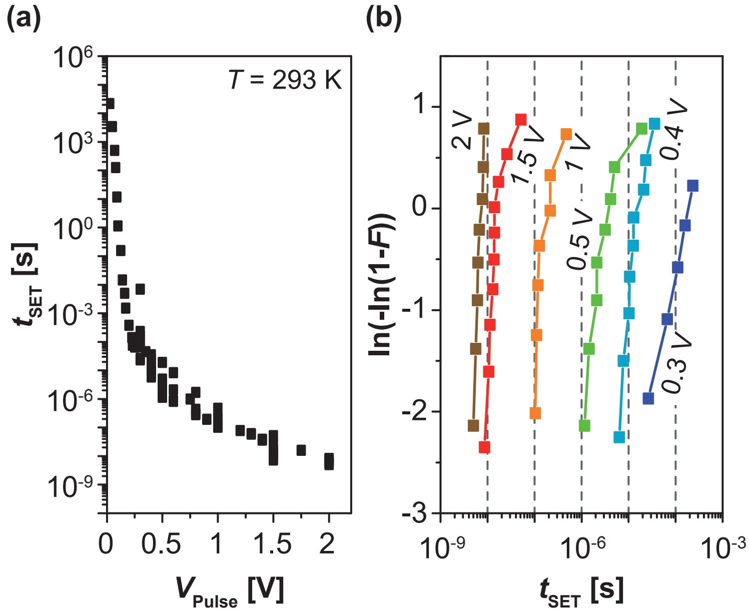

Figure 5.21 (a) Measurement data of switching kinetics at $T = 298\,\mathrm{K}$. (b) Weibull distribution of t_{SET} from (a), exemplarily for $V_{\mathrm{Pulse}} = 0.3\,\mathrm{V}, 0.4\,\mathrm{V}, 0.5\,\mathrm{V}, 1\,\mathrm{V}, 1.5\,\mathrm{V}$ and $2\,\mathrm{V}$.

which can be (i) a nucleation process to form a stable Ag nucleus on the Pt interface for the metal filament, (ii) the electron-transfer reaction, which occurs at the metal/electrolyte interfaces, and (iii) the cation transport within the electrolyte. These processes are schematically shown in figure 5.22. At first, oxidation of the active electrode takes place supplying a small number of cations (A). Further oxidation is initially limited until cations, which migrate across the electrolyte (B), are reduced at the counter electrode (C). A stable Ag nucleus is formed during the nucleation process (D). The nucleation time and the number of atoms required to form a stable nucleus generally depend on the cation species, the counter electrode and electrolyte material, and the nucleation overpotential. After the nucleation process, the filament growth (E) is both limited by the charge transfer reaction and/or migration process as soon as the filament approaches the active electrode (F), and the cell switches to the low resistive ON state. Depending

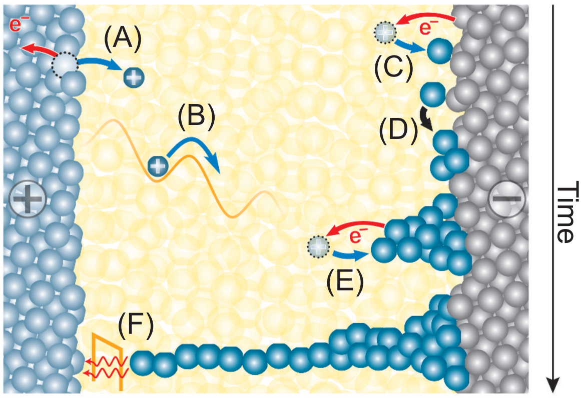

Figure 5.22 Schematic of the nucleation, charge transfer, and drift process during filament formation. Reproduced from [112].

on the experimental conditions and the material system at least one of these rate limiting steps is considered to dominate the switching time.

In figure 5.23 the equivalent circuit model for the switching simulation is shown. For simplicity a cylindrical filament is assumed to grow within the electrolyte, which is sandwiched between the active top and inert bottom electrode. The filament modulates the tunneling gap x. The 1D simulation model accounts both for electronic I_{Tu} and ionic current paths I_{ion}, respectively. The overpotentials η_{ac}, η_{nuc}, η_{hop}, and η_{fil} are introduced below. Details on the simulation can be found in [112]. The rate limiting steps (nucleation, charge transfer, and drift) are discussed in the following paragraphs in respect to the switching model.

Figure 5.23 Equivalent circuit model for 1D switching simulation. The switching layer of thickness L is sandwiched between the active top and inert bottom electrode. The filament grows within the electrolyte film and modulates the tunneling gap x. The model accounts both for ionic and electronic current paths. $R_{\mathrm{S}} = 1\,\mathrm{M\Omega}$ is the series resistor, $R_{\mathrm{el,ac}}$ and $R_{\mathrm{el,in}}$ are the active electrode and inert electrode resistances, respectively. R_{fil} is the filament resistance. Reproduced from [112].

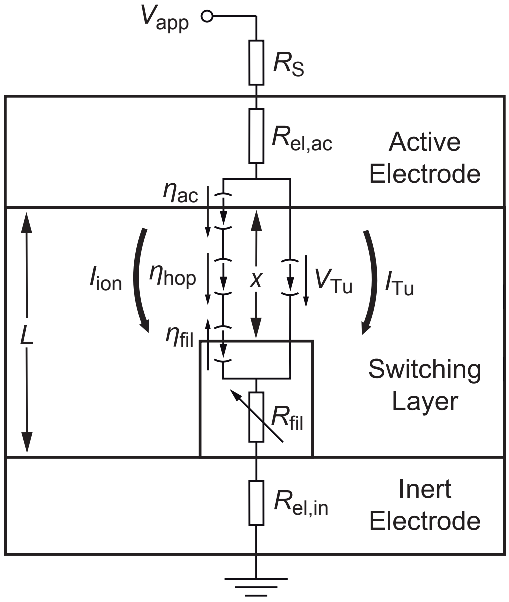

(i) Nucleation Process The nucleation process can be expressed by an activation energy $\Delta G^{\neq}_{\mathrm{nuc}}$, which should be added to the activation energy of the electrode reaction [87; 112]. During the nucleation process a stable Ag nucleus consisting of an integer number of atoms (further denoted as critical cluster size N_{c}) is formed. N_{c} depends on the applied voltage and in particular of the nucleation overpotential η_{nuc}. In special cases each vacancy acts as critical nucleus and $N_{\mathrm{c}} = 0$ holds [87]. During the nucleation time t_{nuc} the filament growth is significantly suppressed. The nucleation time is given by [87; 112]:

$$t_{\mathrm{nuc}} = t_{0,\mathrm{nuc}} \cdot \exp\left(\frac{\Delta G^{\neq}_{\mathrm{nuc}}}{k_{\mathrm{B}}T}\right) \cdot \exp\left(-\frac{(N_{\mathrm{c}} + \alpha)\, ze}{k_{\mathrm{B}}T}\eta_{\mathrm{nuc}}\right) \tag{5.2}$$

Beside N_c, η_nuc and $\Delta G^{\neq}_\mathrm{nuc}$, further parameters of equation 5.2 are the prefactor $t_{0,\mathrm{nuc}}$, the temperature T, the number z of electrons involved in the cation reduction, the charge transfer coefficient α, the Boltzmann constant k_B and the elementary charge e.

(ii) Charge Transfer Reaction The current density j_et of the electron transfer reaction is mathematically described by the Butler-Volmer equation [112], which has been introduced in chapter 2.2:

$$j_\mathrm{et} = j_{0,\mathrm{et}} \cdot \left[\exp\left(\frac{(1-\alpha)\, ze}{k_\mathrm{B}T}\eta_\mathrm{et}\right) - \exp\left(-\frac{\alpha ze}{k_\mathrm{B}T}\eta_\mathrm{et}\right)\right] \tag{5.3}$$

Parameters of the charge transfer reaction are the Butler-Volmer overpotential η_et and the exchange current density $j_{0,\mathrm{et}}$, which depends on the activation barrier $\Delta G^{\neq}_\mathrm{et}$ [112]:

$$j_{0,\mathrm{et}} = zec_{\mathrm{Ag}^+}k_{0,\mathrm{et}} \cdot \exp\left(-\frac{\Delta G^{\neq}_\mathrm{et}}{k_\mathrm{B}T}\right) \tag{5.4}$$

Here, $k_{0,\mathrm{et}}$ is a rate constant and c_{Ag^+} the cation concentration (i.e. Ag^+ ion concentration). The oxidation and reduction processes are described by the first and second exponential terms in equation 5.3, respectively. The oxidation process is dominating for a strong positive overpotential $\eta_\mathrm{et} > 0$ and $|\eta_\mathrm{et}| >> (k_\mathrm{B}T)/e$. In contrast, the reduction of cations predominates for $\eta_\mathrm{et} < 0$ and $|\eta_\mathrm{et}| >> (k_\mathrm{B}T)/e$.

(iii) Cation Drift The cation drift is expressed by a hopping transport, which is determined by the migration barrier enthalpy $H^{\neq}_\mathrm{hop}$, and calculated by the Mott-Gurney law [112]:

$$j_\mathrm{hop} = 2zec_{\mathrm{Ag}^+}af \cdot \exp\left(-\frac{\Delta H^{\neq}_\mathrm{hop}}{k_\mathrm{B}T}\right) \cdot \sinh\left(\frac{aze}{2k_\mathrm{B}T}E\right), \tag{5.5}$$

where a is the mean cation hopping distance, which is in the range of some inter atomic distances. Further parameters are f the attempt frequency, and E the externally applied electric field. The ion transport depends linearly on E for $E << (2k_\mathrm{B}T)/(aze)$. In contrast, the cations are exponentially accelerated for high electric fields where $E > (2k_\mathrm{B}T)/(aze)$.

The pulse voltage vs. SET time characteristic is simulated as follows: At first, the nucleation time t_nuc is calculated based on equation 5.2. During the nucleation the

Faradaic current is zero and the ECM cell is in the high resistive OFF state. Therefore, the nucleation overpotential is assumed to be equal to the pulse voltage $\eta_{\mathrm{nuc}} = V_{\mathrm{Pulse}}$. For considerable high electronic leakage current only a part of the pulse voltage drives the nucleation. The actual filamentary growth starts when $t = t_{\mathrm{nuc}}$, and is based on an extension of the dynamic switching model presented in [25]. The growth of the filament is modulated by the change of the tunneling gap x between the active electrode and the filament. The growth can be mathematically described by Faraday's law [151]:

$$\frac{\partial x}{\partial t} = -\frac{M_{\mathrm{Me}}}{ze\rho_{\mathrm{m,Me}}} j_{\mathrm{ion}}, \tag{5.6}$$

where M_{Me} and $\rho_{\mathrm{m,Me}}$ are the deposited metal atomic mass and density, respectively. j_{ion} is given either by the Butler-Volmer equation (see equation 5.3) or the hopping current (equation 5.5). For $\eta >> k_{\mathrm{B}}T/ze$ the Butler-Volmer equation can be approximated by the Tafel equation [37]. In general, the overpotentials at the filament/insulator interface η_{fil} and the active electrode/insulator interface η_{ac} are different. Thus, different equations apply for the description of the ionic currents across these two interfaces. The Tafel equation describing the ionic current at the filament/insulator interface reads [112]:

$$I_{\mathrm{fil,SET}} = j_{0,\mathrm{ct}} A_{\mathrm{fil}} \left(\exp\left(-\frac{\alpha ze}{k_{\mathrm{B}}T} \eta_{\mathrm{fil}} \right) - 1 \right), \tag{5.7}$$

with η_{fil} the electron transfer overpotential at the filament/electrolyte interface.

Analogous, the ionic current at the active electrode/insulator interface is given by [112]:

$$I_{\mathrm{ac,SET}} = j_{0,\mathrm{ct}} A_{\mathrm{ac}} \left(\exp\left(\frac{(1-\alpha)\, ze}{k_{\mathrm{B}}T} \eta_{\mathrm{ac}} \right) - 1 \right) \tag{5.8}$$

Here, η_{ac} is the electron transfer overpotential at the active electrode.

Moreover, the cation drift is expressed by the hopping current given in equation 5.5, the area A_{is} responsible for ionic conduction, and $E = \eta_{\mathrm{hop}}/x$ (with the hopping overpotential η_{hop}):

$$I_{\mathrm{hop}} = 2zec_{\mathrm{Ag^+}} A_{\mathrm{is}} af \cdot \exp\left(-\frac{\Delta G^{\neq}_{\mathrm{hop}}}{k_{\mathrm{B}}T} \right) \cdot \sinh\left(\frac{aze\eta_{\mathrm{hop}}}{2k_{\mathrm{B}}Tx} \right) \tag{5.9}$$

Due to the charge neutrality all ionic currents are equal, i.e. $I_{\mathrm{ion}} \equiv I_{\mathrm{fil,SET}} = I_{\mathrm{ac,SET}} = I_{\mathrm{hop}}$, and the overall current I is given by the tunneling and ionic current $I = I_{\mathrm{Tu}} + I_{\mathrm{ion}}$. It can be shown that I is only a function of the overpotential η_{fil} and the gap distance x [25]. During the simulation equation 5.6 is solved based on the equations derived above and Kirchhoff's law for the equivalent circuit model (cf. 5.23). Simulation parameters are given in table 5.1. Further details of the simulation can be found in [112].

Symbol	Value	Symbol	Value
M_{me}	$1.79 \cdot 10^{-22}\,\mathrm{g}$	$\Delta G^{\neq}_{\mathrm{nuc}}$	$0.8\,\mathrm{eV}$
z	1	$t_{0,\mathrm{nuc}}$	$2 \cdot 10^{-8}\,\mathrm{s}$
$\rho_{\mathrm{m,me}}$	$10.49\,\mathrm{g\,cm^{-3}}$	N_{c}	3
a	$0.25\,\mathrm{nm}$	A_{ac}	$804.25\,\mathrm{nm}^2$
α	0.3	A_{fil}	$12.57\,\mathrm{nm}^2$
$j_{0,\mathrm{ct}}$	$3.2 \cdot 10^{5}\,\mathrm{A\,m^{-2}}$	A_{is}	$12.57\,\mathrm{nm}^2$
$\Delta G^{\neq}_{\mathrm{ct}}$	$0.6\,\mathrm{eV}$	L	$20\,\mathrm{nm}$
$j_{0,\mathrm{hop}}$	$1.1 \cdot 10^{11}\,\mathrm{A\,m^{-2}}$	ρ_{fil}	$1.7 \cdot 10^{-8}\,\Omega\mathrm{m}$
R_{S}	$1\,\mathrm{M}\Omega$	R_{el}	$76.4\,\mathrm{m}\Omega$
$\Delta H^{\neq}_{\mathrm{hop}}$	$0.3\,\mathrm{eV}$		

Table 5.1. Simulation model parameters from [112].

The parameters in table 5.1 are based on literature values (e.g. M_{me} or $\rho_{\mathrm{m,me}}$), measurement results (e.g. $\Delta H^{\neq}_{\mathrm{hop}}$), or device geometry and the measurement setup (e.g. L and R_{S}). Further parameters such as N_{c} or α were chosen to fit to the pulse measurement data (cf. 5.24).

Comparison of Experimental Data and Simulation Results

Pulse experiments were performed for various temperatures, and SET times between $50\,\mathrm{ns} \leq t_{\mathrm{SET}} \leq 10^4\,\mathrm{s}$ were measured. The measurement results are shown in figure 5.24 and fit very well to the simulation model (solid lines). In regime I the nucleation seems to be the limitation for resistive switching. For simplification, all simulation parameters for the nucleation limitation (e.g. N_{c} or $\Delta G^{\neq}_{\mathrm{nuc}}$) are assumed to be constant. In a real device these parameters may depend on the applied voltage, and may also differ from cell to cell. In regime II resistive switching is limited by the electron transfer reaction, and regime III is a mixed controlled regime where the electron transfer reaction and ion drift are the limitation factors.

Both the simulation and pulse measurements show a very strong nonlinearity of the switching kinetics of Ag/AgI/Pt cells. This is advantageous from an application point of view: At low voltage stress (e.g. read access) switching of the cell is suppressed, while fast write access down to 50 ns and below is possible when higher voltages are applied. Based on the simulation it can be shown that the measurement setup, e.g. the pulse rise time, has a strong impact on the switching characteristics for high pulse voltages [112].

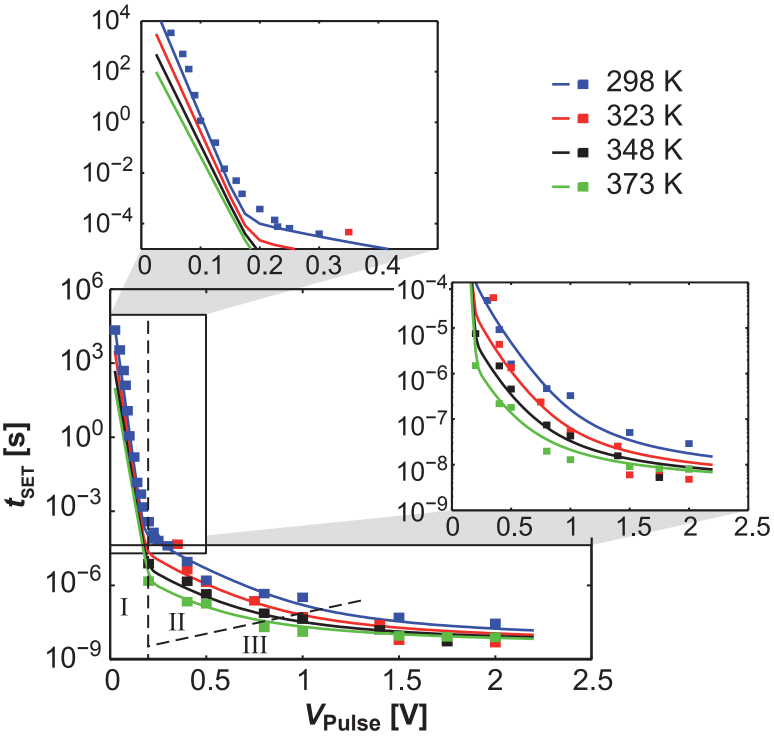

Figure 5.24. Pulse measurement data (squares) and simulation results (solid lines) for various ambient temperatures $T = 298\,\mathrm{K}$ (blue), $T = 323\,\mathrm{K}$ (red), $T = 348\,\mathrm{K}$ (black) and $T = 373\,\mathrm{K}$ (light green) [112]. I, II, III mark the nucleation limited, the electron transfer limited, and the mixed control regime, respectively. Details of statistical variation can be found in [54].

A SET time down to 50 ns at a comparatively moderate switching voltage of 2 V is fast compared to conventional Flash memory devices, where write-access is typically in the order of a few μs to ms [9]. Faster switching in the pico second range has been demonstrated for Nb_2O_5 VCM cells [152]. In case of AgI, switching below 10 ns may be in principle possible using an adequate high frequency measurement setup. However, by increase of the pulse voltage the risk of thin film decomposition is high, which would result in a significant device degradation.

5.2. Nanobatteries in Redox Based Resistive Switches

In chapter 4.3 nonequilibrium states originating from redox processes on the nanoscale that are responsible for resistive switching have been discussed. In open circuit conditions these nonequilibrium states result in an electromotive force, and based on the device characteristics a cell voltage can be measured, i.e. a *nanobattery*. In the following section the impact of this nanobattery effect on redox based resistive switches is discussed. In contrast to the cell voltage measurement before electroforming shown in chapter 4.3, here open circuit cell voltages and short circuit currents are analyzed after resistive switching (SET and subsequent RESET process). In some cases, in particular for VCM cells, a high conductive channel (both for ions and electrons) is potentially grown during the forming process. A similar effect is also discussed for ECM cells such as Cu/SiO_2/Pt [35]. Thus, the first switching cycle can have a strong impact on the nanobattery effect.

5.2.1. Electromotive Force Measurements under Open Circuit and Short Circuit Conditions

In figure 5.25a the cell voltage of a Ag/SiO_2/Pt cell in open circuit condition after switching and RESET is shown. For comparison, the cell voltages for cells without a previous electroforming and switching step are depicted as well (see chapter 4.3). The cell shows an open circuit voltage similar to the cell with $c_{\mathrm{ion}} = 1.4 \cdot 10^{-4}\,\mathrm{M\,cm^{-3}}$. Note, during the RESET process cations are reduced depending on the negative voltage amplitude.

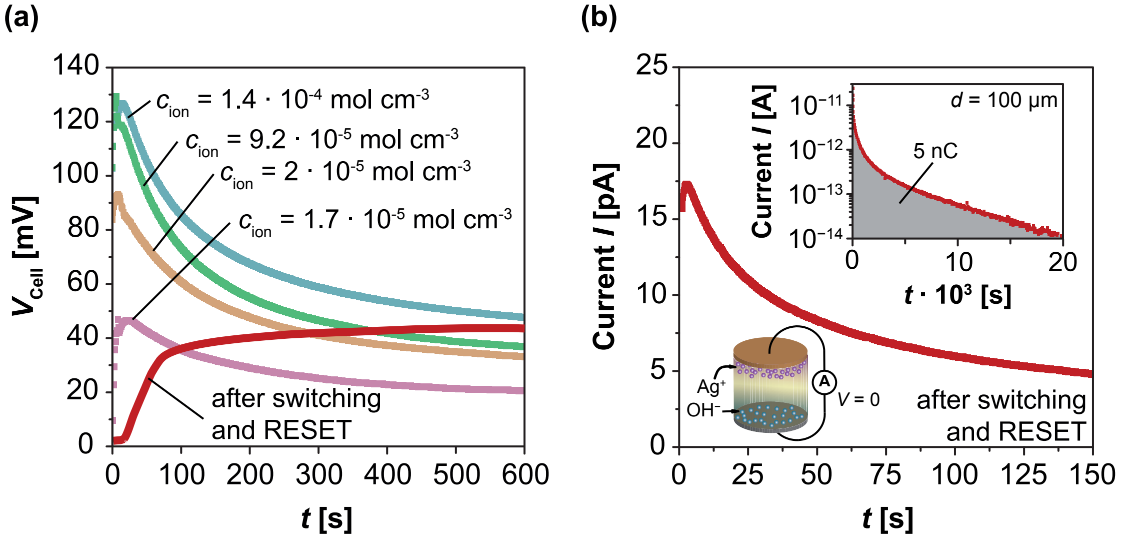

Figure 5.25. Nanobattery effect in Ag/SiO_2/Pt resistive switching devices [40]. (a) Open circuit cell voltage for a cell after SET and RESET operation (red curve) compared to cell voltages without a previous electroforming step (blue, green, brown and purple curves). (b) Short circuit discharge current density ($V_{\mathrm{Cell}} = 0$) of the same cell with similar ion concentration. The inset depicts the discharge current over a long time scale. The measurement limitation is about 0.01 pA.

Since the cell is characterized by a measurable cell voltage in open circuit conditions, a short circuit discharge current density is measured when $V_{\mathrm{Cell}} = 0$ is applied (cf. 5.25b).

In the inset the discharge current is shown until it is close to the measurement limitation of about 0.01 pA. The cell current scales with the electrode area as depicted in figure 5.26. This is an indication that the nanobattery effect is not dominated by a filament in this particular ECM system but by the whole electrode area. In general, both the cell voltage and the short circuit current may depend on the device characteristics, and in some cases they may scale in a non trivial manner according to equation 2.19. However, the electromotive force voltage itself and effects, which can be caused by nonequilibrium states, are still persistent.

Figure 5.26 Short circuit discharge current density ($V_{\mathrm{Cell}} = 0$) after SET and RESET of a Ag/SiO_2/Pt cell [40]. The discharge current (recorded after a discharge time of $t = 150\,\mathrm{s}$, see inset) scales with the electrode diameter indicating that the nanobattery effect is dominated by the whole electrode area.

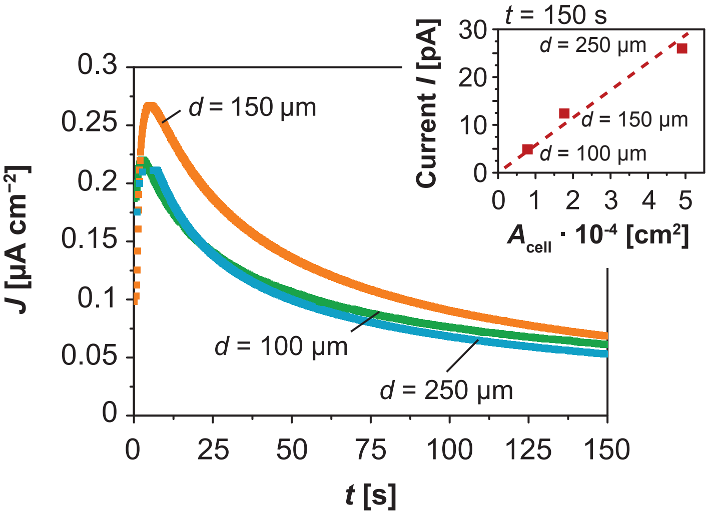

In general, during device operation the RESET process can be incomplete and further ions are generated in the following SET cycle. This results in an ion accumulation at the electrode interfaces (or depletion in case of a strong RESET, see section 5.2.2), and therefore, in a non-zero crossing I/V curve. Figure 5.27a depicts a typical I/V curve of a Cu/SiO_2/Pt cell. The non-zero crossing characteristic (also termed as *non-pinched* characteristics at the origin of the I–V plane) is clearly observed in the inset. Note, the absolute voltage value for the axis crossing at $I = 0$ is not equal to the open circuit cell voltage, since the emf voltage is a static thermodynamic value and I/V sweeps are potentiodynamic measurements.

Moreover, this non-zero crossing effect is pronounced for relatively large micro scale cells, since the ionic current generally scales with the electrode diameter depending on the ReRAM system. In some VCM type cells the ionic current is believed to be of filamentary nature and in this case the non-zero crossing effect does not scale with the device geometry [40].

For Ag/SiO_2/Pt cells a similar non-zero crossing effect is observed (cf. 5.27b). Here, the RESET process is analyzed with respect to further ion reduction after dissolution of the filament. At first, the cell is switched to the ON state. Afterwards, the cell is RESET to

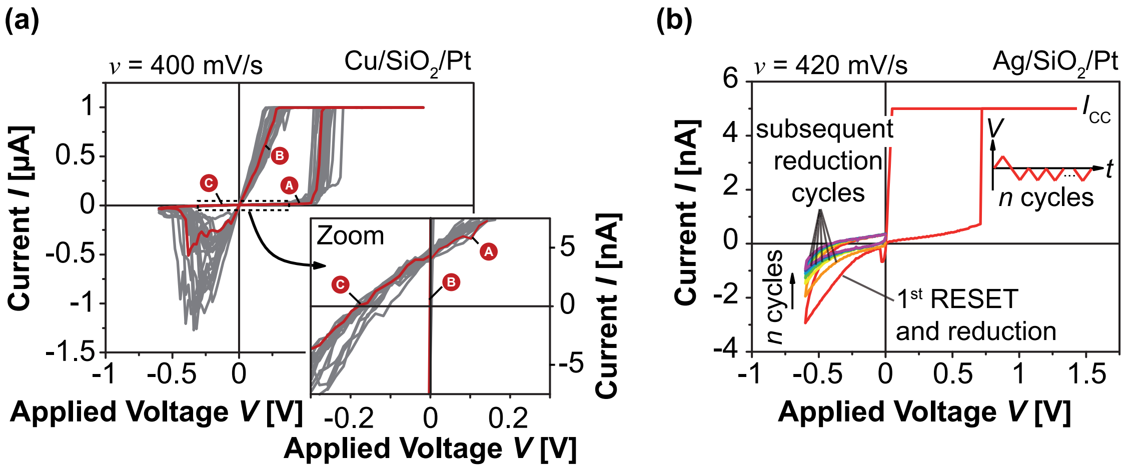

Figure 5.27. Non-zero crossing effect in ECM type resistive switching cells [40]. (a) Cu/SiO$_2$/Pt cells with a pronounced non-zero crossing behavior for $V = 0$. (b) Non-zero crossing of a Ag/SiO$_2$/Pt cell with special attention to subsequent reduction cycles. The RESET process appears to be incomplete resulting in an ion accumulation at the interfaces.

the OFF state, and further cycling in the negative voltage regime is performed. The first RESET cycle appears to be incomplete since further ion reduction is observed during the subsequent reduction cycles. Thus, although the cell is switched back to the OFF state an ion accumulation at the interfaces can still remain, which affects the device performance as discussed in section 5.2.2.

Both VCM type and ECM type memory cells are based on redox reactions on the nanoscale. Hence, nonequilibrium states are inherently induced during device operation. In figure 5.28 open circuit cell voltages of several material systems are summarized. The particular cell voltage depends on the device operation history such as voltage amplitude or sweep rate. The cell voltages of VCM type cells are smaller, which is due to a higher electronic partial conductivity (i.e. $t_{\mathrm{el}} \approx 10^3 \cdot t_{\mathrm{i}}$) [40].

In 1971, L. Chua introduced the *memristor* as the missing fourth basic circuit element [153] and further developed the theory of *memristive devices* [154; 155]. By definition, the memristor or memristive device is a passive device, which resistance depends on the previous device operation. The resistance of the device is linked to inner *state variable(s)*. The zero-crossing hysteresis loop is an important *fingerprint* of memristors and memristive devices [153; 156–158]. For example, Lissajous curves do not show a zero-crossing hysteresis loop, and are thus, not termed as memristors. In 2008, the serendipitous discovery of the link between redox based nano ionic resistive memory cells, and memristors and memristive devices has further intensified the research in the field of resistive switches [40; 127; 159]. In this context, at least one state variable describing a structural change of the filament is needed, e.g. the gap distance between the filament

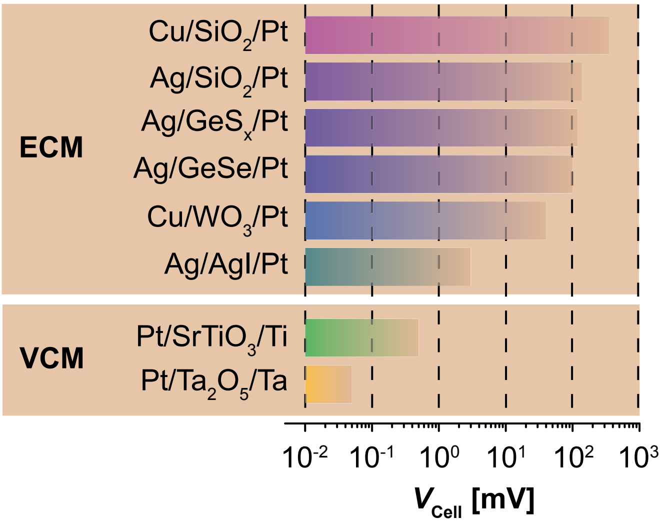

Figure 5.28 Open circuit cell voltages for several VCM and ECM type memory cells [40]. The cell voltage of VCM material systems is potentially smaller due to a higher electronic partial conductivity.

and active electrode [28; 160]. Recently, the question of the scientific legitimacy of a physical memristor has been raised in literature [161–163].

Moreover, the inherent non-zero crossing effect of VCM and ECM type cells is in conflict with the fingerprint of the existing memristor theory. Thus, a modified theory termed as *extended memristive devices* has been developed, which accounts for the nanobattery effect [40]. In contrast to the existing memristor model, the ionic resistance and the filament (controlled resistance) are separated. This is closer to the device physics since the state variable (filament/electrode gap distance) depends only on the total charge flow through the ionic resistance.

In the original paper by L. Chua the device resistance is not separated in an electronic and ionic partial resistance. Thus, the state variable also depends on the charge flow

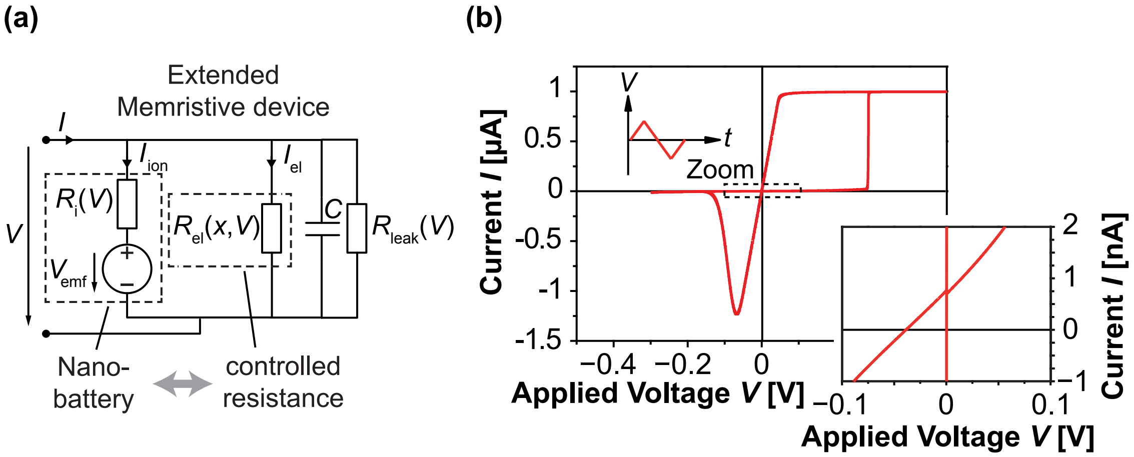
(a)
Extended Memristive device
I
I_{ion}
I_{el}
$R_i(V)$
$R_{el}(x,V)$
C
$R_{leak}(V)$
V
V_{emf}
Nano-battery
controlled resistance
(b)
V
t
Zoom
1
0.5
0
-0.5
-1
-1.5
−0.4 −0.2 0
Current I [µA]
Applied Voltage V [V]
2
1
0
−1
−0.1 0 0.1
Current I [nA]
Applied Voltage V [V]

Figure 5.29. Extended memristive device model [40]. (a) Equivalent circuit of the extended memristive device accounting for the nanobattery effect and ionic resistance. (b) The SPICE simulation results fit very well to the measurement data shown in figure 5.27.

towards the filament. However, only the ionic current contributes to the redox reactions and mass transport, and thus, the change of the device resistance. In the extended memristive device model the nanobattery is in series to the ionic resistance. Discharging effects of the nanobattery in the ON or OFF state can explain retention and endurance problems as discussed in the following section.

5.2.2. Influence on Device Endurance and Retention

The violation of the zero-crossing axiom may seem to be a side note in the context of the memristor theory. However, the impact of the discovered nonequilibrium states on the switching, endurance, and the retention of ReRAM devices is of high practical interest. The relaxation of the electromotive force voltage for example leads to a shift of

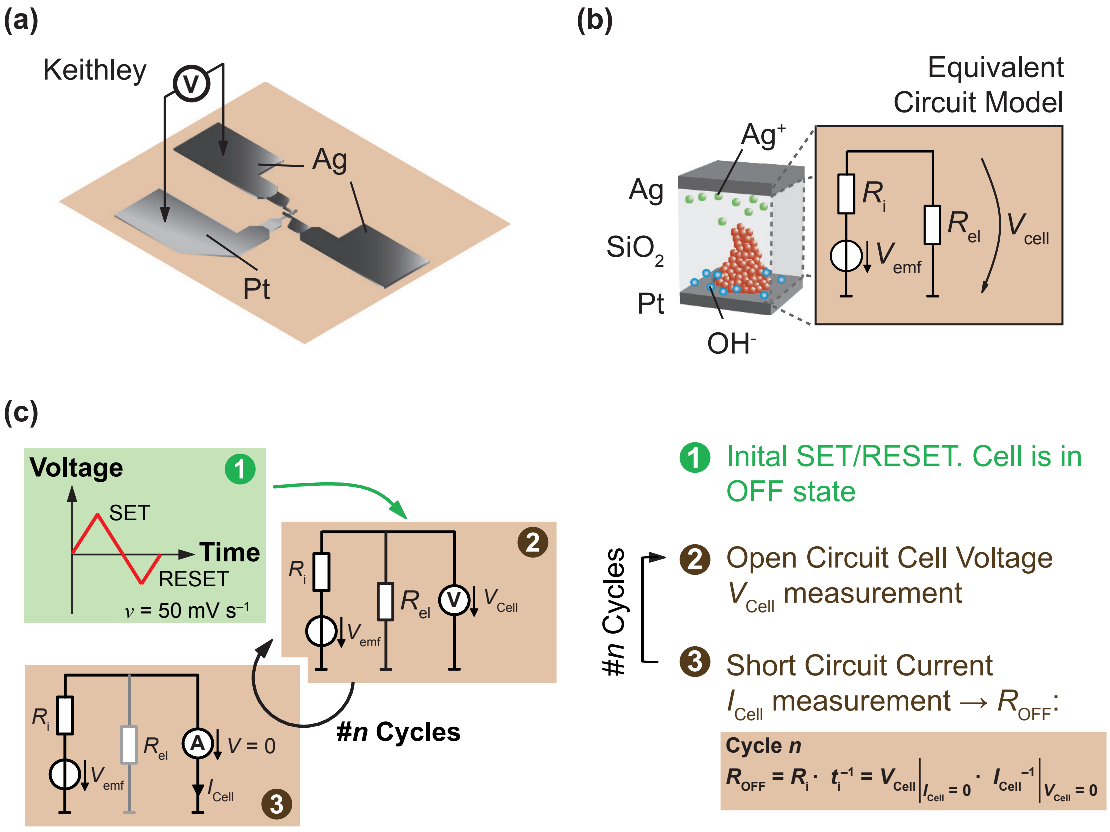
(a)
Keithley
V
Ag
Pt
(b)
Equivalent Circuit Model
Ag⁺
Ag
SiO₂
Pt
OH⁻
Rᵢ
Rₑₗ
V_cell
V_emf
(c)
Voltage
1
SET
Time
RESET
ν = 50 mV s⁻¹
2
Rᵢ
Rₑₗ
V
V_Cell
V_emf
Rᵢ
Rₑₗ
A
V = 0
V_emf
I_Cell
3
#n Cycles
#n Cycles
1 Inital SET/RESET. Cell is in OFF state
2 Open Circuit Cell Voltage V_Cell measurement
3 Short Circuit Current I_Cell measurement → R_OFF:
Cycle n
R_OFF = Rᵢ · tᵢ⁻¹ = V_Cell|I_Cell = 0 · I_Cell⁻¹|V_Cell = 0

Figure 5.30. (a) Schematic and measurement setup for endurance and retention experiments shown for a ECM micro crossbar. (b) Nanobattery effect exemplarily shown for a Ag/SiO_2/Pt cell. The ion concentration gradients of Ag^+ and OH^- result in the formation of a nanobattery voltage V_{emf}, which is measurable as a cell voltage V_{Cell} in the OFF state of the cell. R_{i} is the ionic and R_{el} the electronic (i.e. leakage current in the OFF state, and filament/tunnel gap in the ON state) resistance. (c) Schematic of the measurement procedure. The ionic resistance R_{i}, and thus, the OFF state resistance R_{OFF} is increased during time. Redrawn from Ref. [98]

the resistance level (both for the ON and OFF resistance). Therefore, the impact of the nanobattery effect on the device endurance and state retention both for micro and nano crossbars was analyzed.

OFF state resistance R_{OFF} retention and SET voltage variability measurements were performed to study the impact of nonequilibrium states on the device characteristics [98]. The equivalent circuit model of redox based resistive switches (e.g. a Ag/SiO$_2$/Pt based ECM cell, cf. 5.30a) inherently consists of a nanobattery V_{emf}, an ionic resistance R_{i}, and an electronic (leakage) resistance R_{el} as shown in Fig. 5.30b [40]. V_{emf} results from chemical asymmetry of the electrode materials and/or nonequilibrium states due to nano ionic effects, such as ion concentration gradients of Ag$^+$ and OH$^-$ in case of SiO$_2$. Both R_{el} and R_{i} are determining the OFF state resistance as shown in Fig. 5.30b. While R_{el} depends on the materials parameters and device geometry, and remains constant after the forming process, the drift of R_{OFF} is determined only by R_{i}.

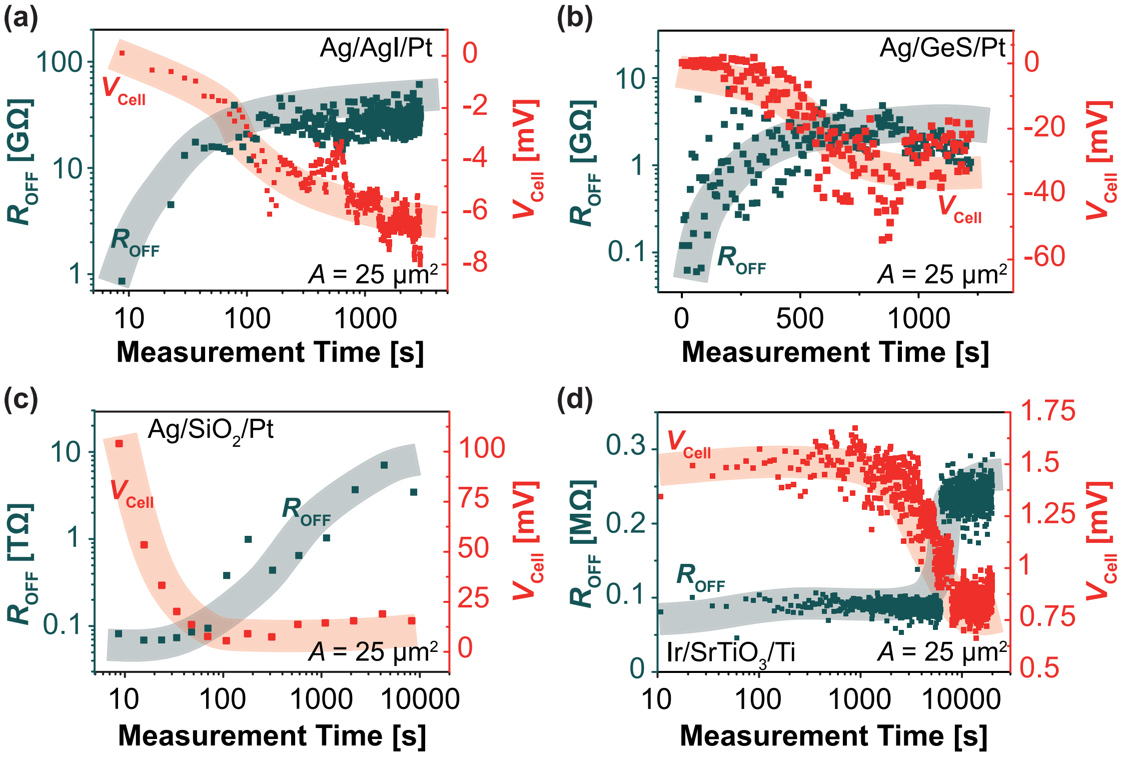

Figure 5.31. OFF state retention and V_{Cell} relaxation versus time for (a) AgI, (b) GeS$_x$ and (c) SiO$_2$ ECM cells, and a (d) SrTiO$_3$ VCM cell. [98]

A scheme of the OFF state retention measurement is shown in Fig. 5.30c. The cells are first SET and RESET. Afterwards, R_{OFF} is repeatedly calculated by measuring the cell voltage V_{Cell} (which is determined by V_{emf}, R_{i} and R_{el}) and subsequently the short circuit current. R_{OFF} can be expressed by the ionic transference number t_{i} [40] of the individual materials system and R_{i}. The measurement results for V_{Cell} and R_{OFF} versus time are shown in Fig. 5.31a-d both for ECM and VCM type cells [98]. In all cases a relaxation of the cell voltage (and in such a way, V_{emf}) is observed. Simultaneously, R_{i}, and thus, the OFF resistance shifts to higher values during emf relaxation. Hence, the OFF resistance becomes more stable in these cases. While the relaxation of R_{i}, and as follows R_{OFF}, is due to discharging of the nanobattery (see equivalent circuit model in Fig. 5.30b), the relaxation time depends on the local ion distribution and movement, as well as the chemical and electrochemical potential gradient of charged or neutral species of the particular material system. Moreover, this resistance shift has to be taken into account for the retention of high resistive multilevel states [164; 165].

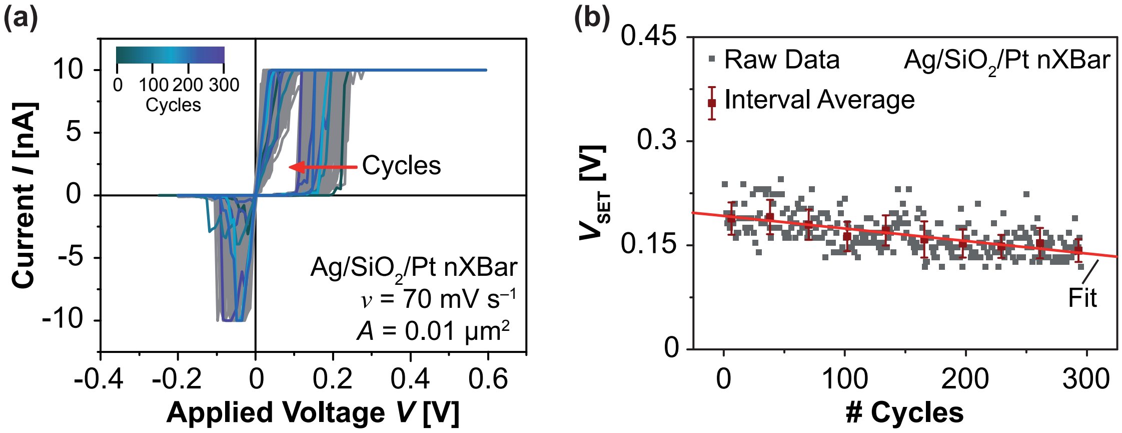

Figure 5.32. Resistive switching endurance for Ag/SiO$_2$/Pt nano crossbar cells [98]. (a) I/V curves with highlighted cycles indicating a shift of the SET voltage (where the cell switches from the high resistive state to the low resistive state) to smaller values. (b) Extracted SET voltage V_{SET} for the cell in (a). A clear decrease of V_{SET} is observed.

Besides OFF state retention the SET voltage variability, and in this way, the device endurance is of high practical importance. Therefore, the SET voltage shift of Ag/SiO$_2$/Pt nano crossbars has been analyzed [98]. The current/voltage curves are depicted in Fig. 5.32a. The SET voltages for each cycle have been extracted from these I-V curves and are shown in Fig. 5.32b. A clear trend of a SET voltage decrease by 30 % is observed. By further cycling the SET voltage will further decrease to zero and the cell is stuck in ON state.

Several failure mechanisms have been proposed in literature mainly for VCM type systems. For example, B. Chen et. al. [166; 167] suggest that during RESET cycles the recombination rate of the oxygen vacancies is reduced, which further reduces R_{OFF}. For ECM type systems, very little has been published on endurance failure mechanisms [12]. In the section above an extended memristor model [40] is presented, which accounts for the nanobattery effect for both ECM and VCM devices. Simulation results for several SET and RESET cycles based on the extended memristor model are shown in Fig. 5.33.

During RESET operation a considerable number of ions are remaining resulting in an ion accumulation at the interfaces, which can drastically affect the SET voltage variation. The simulation results for an incomplete RESET shown in Fig. 5.33a fit very well to the measurement data from Fig. 5.32a. After several cycles the cell is stuck in ON state.

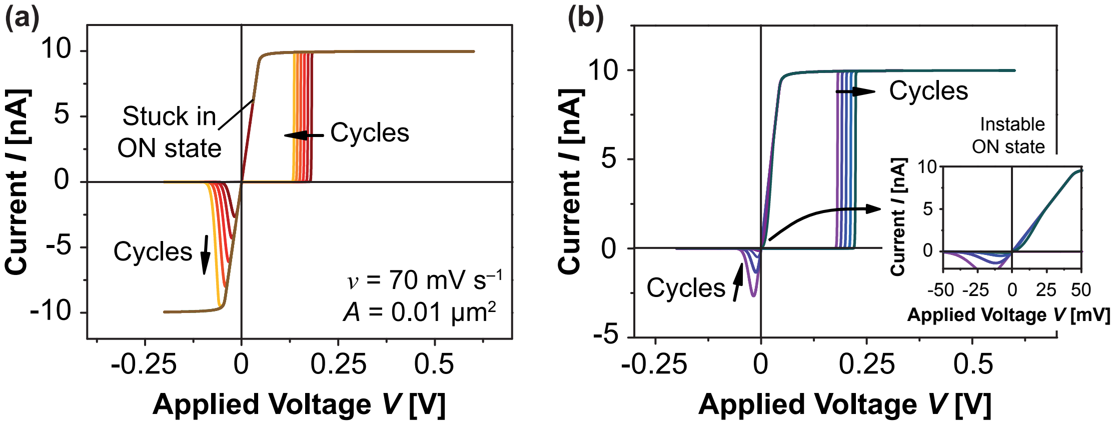

Figure 5.33. Simulation results based on the extended memristor model [40; 98]. Arrows indicate the trend of the SET voltage and absolute maximum RESET current by further cycling. (a) The cell is stuck in ON state due to incomplete RESET operations. (b) Unstable ON states are observed for emf voltages in the range of the RESET voltage.

Besides V_{SET} degradation ON state retention problems have been published especially for comparatively high resistive ON states [119; 164; 165]. Using the extended memristor model, ON state retention problems in ECM cells (as depicted in Fig. 5.33b) can also be explained [98]: Since RESET voltages of ECM cells are typically small, an emf voltage in the range of the RESET voltage (and the same polarity) can induce self-dissolution of the filament. This emf voltage can exemplarily originate from the formation of counter charges (e.g. OH^- [72]) at the active electrode, and can be a driving force for oxidation of the filament tip. In case of high resistive ON states this oxidation results in a spontaneous and unintended filament dissolution. For low resistive ON states the filament remains stable after the nanobattery is discharged.

5.3. Resistive Switching Applications

5.3.1. Electrochemical Metallization Cells for Memory Applications

In this section, the applicability of SiO_2 and AgI based ECM cells for memory applications is discussed. The performance of state of the art memories, and in particular of Flash cells, and requirements for future memory technology are given in the International Technology Roadmap for Semiconductors (ITRS) [2]. To compete with Flash technology, the ECM cells fabricated in this study have to fulfill the IRTS requirements.

Both AgI and SiO_2 based cells can be operated using smaller programming voltages than NAND Flash ($17\,V - 19\,V$) and NOR Flash ($7\,V - 9\,V$). For example, Ag/AgI/Pt cells can be switched within 50 ns when a pulse voltage of only 2 V is applied. The switching kinetics of SiO_2 based cells need to be further investigated, but some reports in literature indicate that a SET time below 200 ns is achievable when moderate voltages (below 5 V) are applied [168]. In contrast, the time for write access of Flash memories is typically in the order of some tens of micro seconds to milli seconds. Thus, the ECM cells discussed in this study have the potential to outperform current Flash technology in respect to high speed write access using moderate voltages.

The energy to write a bit is directly linked to the operation voltage regime and the programming time. The write energy for Ag/AgI/Pt micro crossbars is about 10^{-13} J/bit. In many Flash memories the write operation is based on hot electron injection and requires a write energy of about 10^{-10} J/bit [9]. Thus, AgI based ECM cells offer the benefit of a significant decrease of the power consumption compared to Flash.

Of high importance for practical use is the device endurance. The requirements for NOR Flash are 10^5 write and erase cycles, and for NAND Flash 10^4 write and erase cycles are needed, respectively [2]. The ECM cells fabricated in this study and the measurement setup were not optimized to achieve a high endurance. However, using a series resistor Ag/SiO_2/Pt cells can withstand more than 10^4 potentiodynamic switching cycles. The endurance may be further improved when voltage pulses and a transistor close to the memory cell as selector device and current limiter are used. Similar results have been also reported for Cu/SiO_2/Pt cells [35]. In contrast to SiO_2, the endurance of AgI based cells is yet insufficient, and no significant improvement has been observed when a series resistor is used as current limiter instead of the source meter current compliance. Nevertheless, an endurance of 10^4 does not fulfill the requirements of the ITRS for ReRAMs (at least 10^5 write and erase cycles are needed [2]). Hence, further research should be focused on the improvement of the device endurance of these material systems.

The resistive switching effect is contributed to a very localized change of the device resistance. In fact, quantized conductance values observed both for SiO_2 and AgI based ECM cells reveal that the device resistance can be dominated by the conductance values of a few atoms. This implies an ultimate scalability of ECM cells to an almost atomic level, which overcomes the scaling limitation of conventional Flash technology.

A serious problem for passive crossbar arrays is the asymmetry between the SET and RESET voltage (shown for example in figure 5.2). Depending on the write and read scheme [169], a memory cell can lose its stored information by unintended RESET, when the absolute RESET voltage is very small [170]. In CRS (Complementary Resistive Switch, [16]) based arrays a series resistor can be used to overcome this drawback [171].

A major disadvantage of the fabricated ECM cells is the poor retention of the logic states. The retention requirement for nonvolatile memories is 10 years [2]. While the fabricated cells remain in the high resistive OFF state for years, the ON state retention is a serious problem. When the ON state resistance R_{ON} is above $\approx 13\,\mathrm{k\Omega}$ the retention is in the order of only several minutes. When R_{ON} is below $13\,\mathrm{k\Omega}$ a retention time of several hours can be achieved. However, for memory array applications an ON state resistance in the order of $50\,\mathrm{k\Omega}$ is required due to the voltage drop across the bitlines. In literature most of the retention studies were performed when comparatively low resistive ON states were programmed ($R_{\mathrm{ON}} << 13\,\mathrm{k\Omega}$, e.g. [31; 35; 86; 126; 127]). A detailed study of the ON state retention has not been done in this study but reports in the literature indicate that achieving a high ON state retention for $R_{\mathrm{ON}} > 13\,\mathrm{k\Omega}$ is difficult [119]. A potential reason could be the influence of nonequilibrium states. In this context, further research is required to solve the ON state retention problem.

5.3.2. Nondestructive Readout of Complementary Resistive Switches

One of the major benefits of resistive switches is the feasibility to fabricate large and dense passive crossbar memory arrays. However, the current sneak path problem (crosstalk of neighboring cells) is a major challenge of a purely passive architecture. E. Linn et. al. suggested to use a complementary setup of two bipolar resistive switching cells called Complementary Resistive Switch (CRS) [16; 49; 160; 171–173], which drastically reduces the sneak path problem. However, a drawback of the CRS concept is the destructive current based readout, where the CRS cell is switched and the current response is analyzed in order to identify the stored information. Hence, the conventional destructive CRS readout is limited by the switching speed. Furthermore, the CRS device requires a high switching endurance to perform up to 10^{16} destructive readout operations (which is the endurance requirement for DRAM [2]).

This problem is solved by a nondestructive capacity based readout (NDRO) [174]. The basic idea of the NDRO approach is an asymmetric setup of a CRS device, where both resistive switching cells have similar switching characteristics, but are distinguishable by different capacities. Figure 5.34a illustrates the equivalent circuit model of the alternative

CRS cell setup shown in figure 5.34b. Here, the CRS cell is fabricated in a lateral setup for process simplification. Using the lateral setup up to 50 % of the process steps required for patterning can be saved [171].

The two resistive switching elements A and B can be described by their device resistance R_A and R_B, as well as their inherent capacity C_A and C_B. During normal CRS operation either R_A or R_B is in the low resistive state, and thus, short circuiting the respective element capacity (cf. 5.34c,d). In redox based resistive switches the switching is due to formation and dissolution of a nanoscale filament, whose area is practically insignificant compared to the electrode area [174; 175]. The capacity of each element is given by the element geometry (electrode distance and area) and the permittivity of the switching material. Here, different electrode areas are used. In practical applications different element capacities can be prepared by different electrode distances and/or the use of materials with different permittivity of each element to decrease the lateral feature size of the CRS device.

If the resistance levels for HRS and LRS of both elements are similar but the cell capacities are different, one can distinguish by measuring the time constant of the overall device whether element A or element B is in the LRS or HRS without switching. Alternatively, the stored information can be analyzed by a capacitive voltage divider. For state 1 (see figure 5.34c) and fast read access ($\omega \to \infty$) the output voltage of the capacitive voltage divider is given by [174]:

$$V_\mathrm{out,1} = V_\mathrm{in} \frac{C_\mathrm{A}}{C_\mathrm{A} + C_\mathrm{out}} \tag{5.10}$$

Here, V_in is the read pulse voltage and C_out is a reference capacity of the capacitive voltage divider. Typically, the inherent bit line capacity is used in memory applications as reference capacity [174]. Analogous to equation 5.10 the output voltage for state 0 (figure 5.34d) is given by (for $\omega \to \infty$):

$$V_\mathrm{out,0} = V_\mathrm{in} \frac{C_\mathrm{B}}{C_\mathrm{B} + C_\mathrm{out}} \tag{5.11}$$

In figure 5.35a the voltage response for $V_\mathrm{in} = 0.5\,\mathrm{V}$ is shown both for state 1 and 0. One can clearly distinguish between both logic states. When TiO_2 is used instead of SiO_2, the normalized voltage margin is increased up to 8.1 % due to the higher dielectric constant of TiO_2 [174]. Note that a discrete reference capacity is used here ($C_\mathrm{out} = 24\,\mathrm{pF}$) given

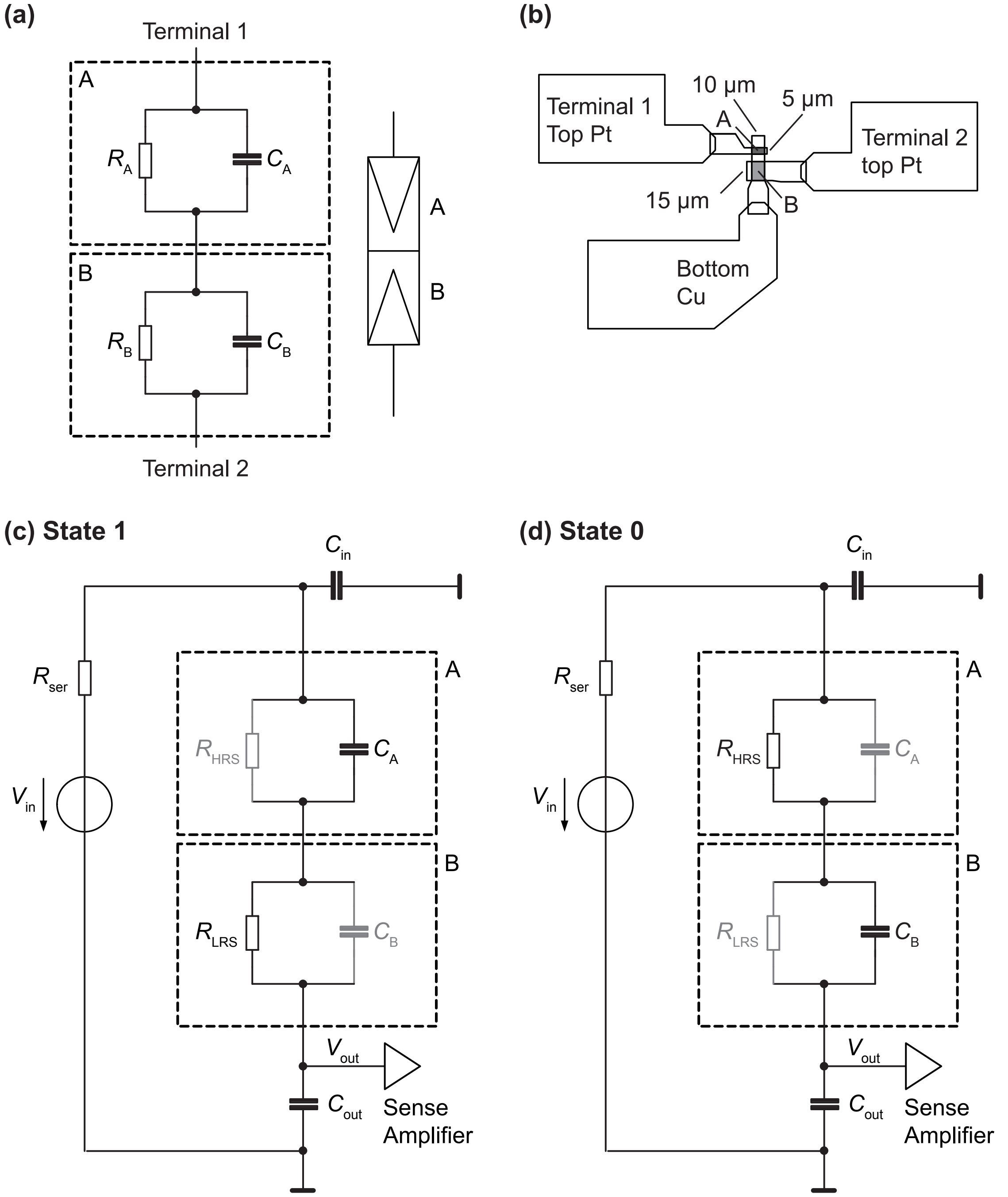
(a)
Terminal 1
A
R_A
C_A
B
R_B
C_B
Terminal 2
A
B
(b)
Terminal 1
Top Pt
10 µm
A
5 µm
Terminal 2
top Pt
15 µm
B
Bottom
Cu
(c) State 1
C_{in}
R_{ser}
V_{in}
A
R_{HRS}
C_A
B
R_{LRS}
C_B
V_{out}
C_{out}
Sense
Amplifier
(d) State 0
C_{in}
R_{ser}
V_{in}
A
R_{HRS}
C_A
B
R_{LRS}
C_B
V_{out}
C_{out}
Sense
Amplifier

Figure 5.34. Capacity based nondestructive readout for CRS cells redrawn from [174]. (a) Equivalent network for a CRS device. In state LRS/HRS (state 0) $R_{\mathrm{A}} = R_{\mathrm{LRS}}$ and $R_{\mathrm{B}} = R_{\mathrm{HRS}}$ holds, while in state HRS/LRS (state 1) $R_{\mathrm{A}} = R_{\mathrm{HRS}}$ and $R_{\mathrm{B}} = R_{\mathrm{LRS}}$ holds. C_{A} and C_{B} are independent of the device state, and depend only on device geometry and material permittivity. In (b) an exemplary device geometry is shown. The area of element A is $A_{\mathrm{A}} = 50\,\mu\mathrm{m}^2$ and area of element B is $A_{\mathrm{B}} = 150\,\mu\mathrm{m}^2$, hence $C_{\mathrm{A}}/C_{\mathrm{B}} = 1/3$. (c) and (d) depict the equivalent circuit of a CRS device and circuitry for capacitive voltage divider evaluation. The behavior of element A and B is either dominated by a low resistance or capacitance depending on the particular element state.

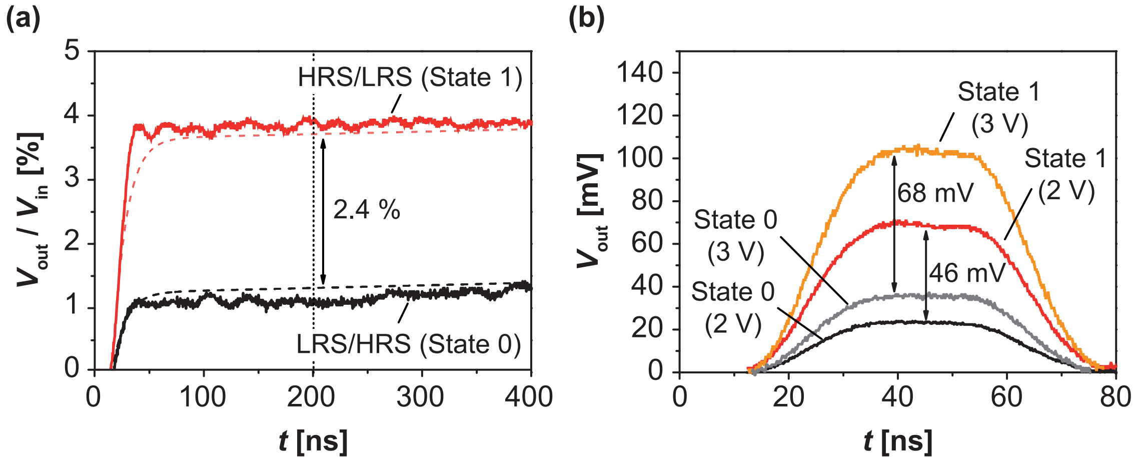

Figure 5.35. (a) Capacitive readout of SiO_2 based CRS cells [174]. The film thickness for both elements A and B is $d = 8\,\text{nm}$ (area size see figure 5.34). The ON state resistance is $R_{\text{LRS}} = 130\,\Omega$ and the OFF state resistance is $R_{\text{HRS}} = 10\,\text{M}\Omega$. $C_{\text{A}} = 0.9\,\text{pF}$ and $C_{\text{B}} = 0.3\,\text{pF}$ resulting in a normalized voltage margin of 2.4 %. (b) The nonlinear switching kinetics can be used to increase the input voltage for short pulse lengths (here 50 ns) [174], exemplarily shown for $V_{\text{in}} = 2\,\text{V}$ and $V_{\text{in}} = 3\,\text{V}$, respectively. Voltage margins are about 46 mV for a 2 V input pulse and 68 mV for a 3 V input pulse, respectively.

by the amplifier input capacity. To increase the voltage margin an optimized reference capacity $C_{\text{out,opt}}$ can be found for a $m \times m$ array [174]:

$$C_{\text{out,opt}} = m \cdot \sqrt{C_{\text{A}} \cdot C_{\text{B}}} \tag{5.12}$$

In this case the voltage margin in a 8×8 ($m = 8$) SiO_2 based array is 6.5 % with $C_{\text{A}}/C_{\text{B}} = 10$.

It should be emphasized that the preparation of a fast sense amplifier with a desirable small input capacity as well as high input resistance, and optimized for a small voltage margin reported above is challenging. The circuit of the noninverting sense amplifier used in Ref. [174] for the nondestructive readout is shown in Fig. 5.36a. A wideband unity gain amplifier (OPA 656N) with a voltage amplification of $A_V = 10$ was used. The layout of the circuit is depicted in Fig. 5.36b. The cable and wire lengths were kept small to measure ultra short pulses down to some tens of nanoseconds. The absolute voltage margin for $V_{\text{in}} = 0.5\,\text{V}$ is $\Delta V_{\text{out}} = 12\,\text{mV}$. The input voltage $V_{\text{in}} = 0.5\,\text{V}$ was chosen because it is below the potentiodynamic switching voltage of the tested devices. In this context, the strong nonlinear switching kinetics of redox based resistive switches (compare section 5.1.4) can be used to increase the absolute voltage margin. Figure 5.35b depicts the voltage response for $V_{\text{in}} = 2\,\text{V}$ and $V_{\text{in}} = 3\,\text{V}$, respectively. The output voltage margin is increased of up to $\Delta V_{\text{out}} = 48\,\text{mV}$ and $\Delta V_{\text{out}} = 68\,\text{mV}$, respectively.

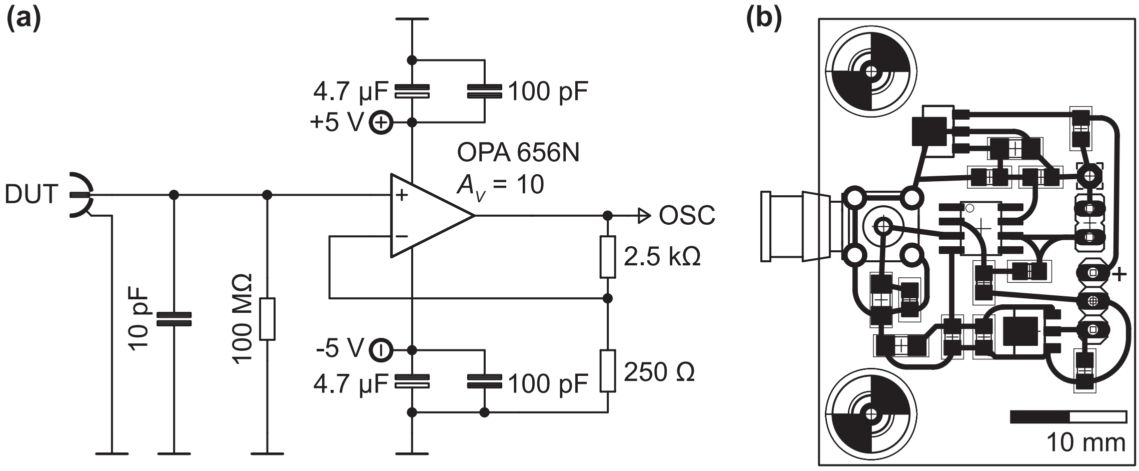

Figure 5.36. (a) Fast noninverting sense amplifier circuit for nondestructive readout of CRS cells. (b) Layout of the sense amplifier. The cable and wire lengths were kept small to measure ultra short pulses.

The presented nondestructive readout approach for CRS cells can be used for small to medium sized purely passive crossbar arrays [174]. It offers the potential of an ultra fast and low power read access. However, the read voltage margin of the nondestructive readout depends on the array size. For large crossbar arrays the voltage margin is potentially too small for sense amplifiers.

5.3.3. Logic and Neuromorphic Applications

Besides memory applications resistive switches can be also used for logic and neuromorphic applications. In case of the implementation of logic functions, several approaches are reported in literature, including programmable interconnects (i.e. programmable logic arrays, PLA) [17; 176], passive crossbar memory arrays acting as look-up tables (LUT) [177], and a sequential logic concept [18; 178; 179]. In general, resistive switches and CRS cells can be considered as *Moore machines* [171], which are able to perform the *implication* (*IMP*) operation. By sequential execution of the negate *IMP* operation (*NIMP*) or the reserve implication (*RIMP*), 14 out of 16 Boolean logic functions (e.g. *NOR* or *AND* operation) can be realized with a single memory cell [180]. The remaining two Boolean logic functions (*XOR* and *XNOR* operation) require two memory cells.

Neuromorphic applications using resistive switches are typically based on the ON state retention and nonlinear switching kinetics [20; 139]. In this respect, the ON state retention is either increased or decreased by input pulses (e.g. amplitude or pulse count). In this context, the resistive switching cell can be characterized by a *learning ability* represented by the ON state retention.

A complete different approach for neuromorphic applications was suggested in Ref. [125], which utilizes the nondestructive readout discussed in section 5.3.2. Here, an associative capacitive network (ACN) is formed using CRS cells where the logic information is stored in a capacitive manner. The CRS cells are capable of providing a weighted synaptic-like contribution on a shared line, which is called match-line. In contrast to previous ACN concepts [181], the information is here represented as different nonvolatile capacity values instead of volatile charge stored in fixed memory capacities. The basic principle of ACNs is a bit-by-bit *XNOR* operation between the input (search pattern) and stored capacity value (template). A single match-line for an one bit j matching operation of template i (array row) is depicted in Fig. 5.37. The output voltage V_{out} of the amplifier is related to the Hamming distance (HD), i.e. similarity, of the input x_j and template pattern. The template pattern is stored in CRS cells as the capacity value $C_{\mathrm{T}(i,j)}$ and its negate $C_{\mathrm{N}(i,j)}$. A negate is required to avoid different output voltages for the same HD [125]. The red equivalent circuit symbols for CRS cells in state 0 and 1 (cf. 5.37), respectively, are an example of a stored pattern. When the input pattern is $x_j = 1$ (and its negate is $\bar{x}_j = 0$, indicated by a red 1 and 0, respectively) the resulting Hamming distance is HD $= 1$, for example.

Φ_1 and Φ_2 are operation modes to precharge the cells and start the measurement, respectively. The switches S_1, S_2 and S_3 are closed during reset operation Φ_1 (RST). The Hamming distance evaluation (EVAL) is performed during operation Φ_2 when the switches S_4 and S_5 are closed. Each match-line i consists of a match-line reference capacity $C_{\mathrm{M},i}$. The match-line voltage is compared to a threshold voltage V_{TH}. The output voltage is low when the match-line voltage is below the threshold voltage and high when match-line voltage is above V_{TH}. The higher the match-line voltage the less similar are the search and template pattern (i.e. high HD). When a ramp voltage (from a low voltage to a high voltage level) is used as threshold voltage signal, the output voltage of each comparator in line i can be used for a fully parallel search of the

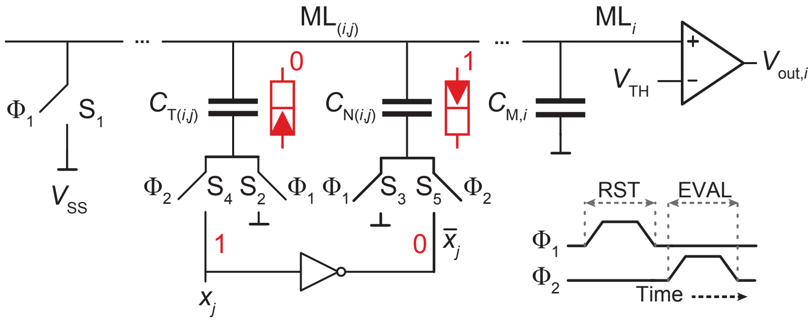

Figure 5.37. A single match-line ML_i consisting of two CRS cells, a threshold voltage, and an analog comparator for an one bit matching operation. Redrawn from [125].

minimum Hamming distance of an input pattern and various stored pattern. In this case comparators of match-lines with a more similar stored and input pattern switch faster to a high voltage level than those, where the stored and input pattern are less similar. This time difference can be used for a parallel analog calculation of the Hamming distance between the input and each stored pattern. Additionally, a Winner-Take-All (WTA) circuit [182] can be used to search for the template with the highest similarity.

Typical applications of these ACNs include internet and network switches and routers as binary and ternary Content Addressable Memories (CAMs), cognitive computing, and intelligent data processing [125]. The advantages of this approach are a fully parallel memory-intense search operation, high scalability (compared to CMOS based CAMs), and improved retention due to nonvolatile information storage. A disadvantage is the conditional probability of up to a few percent to detect HD > 1 as the minimum Hamming distance (HD $= 0$) by mistake [125].

Due to feasibility a read-only-memory (ROM) array consisting of $8 \times (8 + 8)$ fixed capacities and appropriated readout circuits were fabricated in the context of this work. The basic circuit of each match-line comparator amplifier is shown in Fig. 5.38a. In accordance to the nondestructive readout circuit a fast wideband unity gain amplifier (OPA 656N) is used as voltage follower, located as close as possible to the memory array. High frequency reflexion are reduced by curved wires as shown in the circuit layout in Fig. 5.38b for up to eight match-lines. The input pattern $y_{1\ldots8}$ and its negate $\bar{y}_{1\ldots8}$ is programmed by switches, and supplied by a pulse voltage V_{Pulse}. Each voltage follower output voltage is compared to the threshold ramp voltage V_{TH} using a fast comparator (MAX99E).

In Fig. 5.38c comparator output voltages $V_{\mathrm{out},1\ldots8}$ (for specific test input and template pattern) and the pulse voltage signal are shown. Initially, the output voltages are reset from $V_{\mathrm{out},i} = 5\,\mathrm{V}$ to $V_{\mathrm{out},i} = 0\,\mathrm{V}$. Afterwards, the threshold voltage is increased according to the applied ramp voltage. In this example the match-line voltages of template $i = 1$ has the smallest HD, and thus, the output voltage $V_{\mathrm{out},1}$ switches at first to 5 V. Subsequently, the other comparator output voltages are switching to 5 V depending on the specific Hamming distance. These voltage transients vary when different input and template patterns are used.

Each comparator output voltage can be further analyzed. In the context of this work an analog adder circuit was designed, which acts as a Winner-Take-All circuitry. At first, each comparator output voltage is buffered until an ENABLE signal starts the WTA measurement ($V_{\mathrm{out},i} = \mathrm{WL}_i$). Each output voltage is then weighted by a unique amplification $A_{V,i}$. In the example of Fig. 5.38c output $i = 1$ is first set to the high voltage level while the other outputs are 0 V. Thus, output $i = 1$ is weighted by

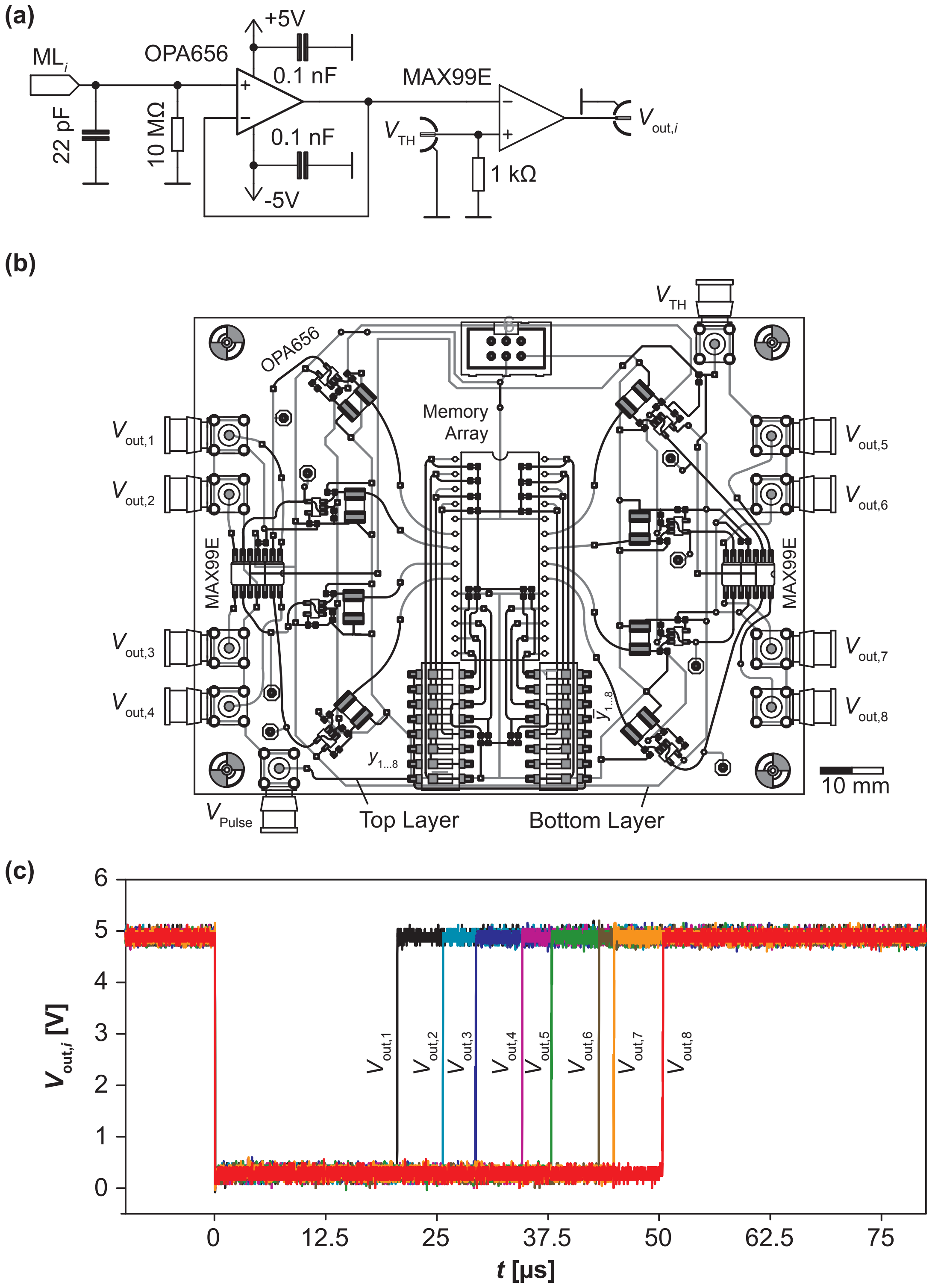
(a)
ML$_i$
22 pF
10 MΩ
OPA656
+5V
0.1 nF
0.1 nF
-5V
MAX99E
V_{TH}
1 kΩ
$V_{out,i}$
(b)
V_{TH}
OPA656
Memory
Array
$V_{out,1}$
$V_{out,2}$
$V_{out,3}$
$V_{out,4}$
$V_{out,5}$
$V_{out,6}$
$V_{out,7}$
$V_{out,8}$
MAX99E
MAX99E
$y_{1...8}$
$\bar{y}_{1...8}$
V_{Pulse}
Top Layer
Bottom Layer
10 mm
(c)
$V_{out,i}$ [V]
0
1
2
3
4
5
6
$V_{out,1}$
$V_{out,2}$
$V_{out,3}$
$V_{out,4}$
$V_{out,5}$
$V_{out,6}$
$V_{out,7}$
$V_{out,8}$
0
12.5
25
37.5
50
62.5
75
t [μs]

Figure 5.38. Demonstration of an ACN based on a 8×16 capacity array. (a) Voltage follower and match-line comparator amplifier for each match-line $i = 1...8$. (b) Layout of the 8×16 ACN circuit. (c) Example of comparator output voltages $V_{\text{out}1...8}$ using test input and template patterns.

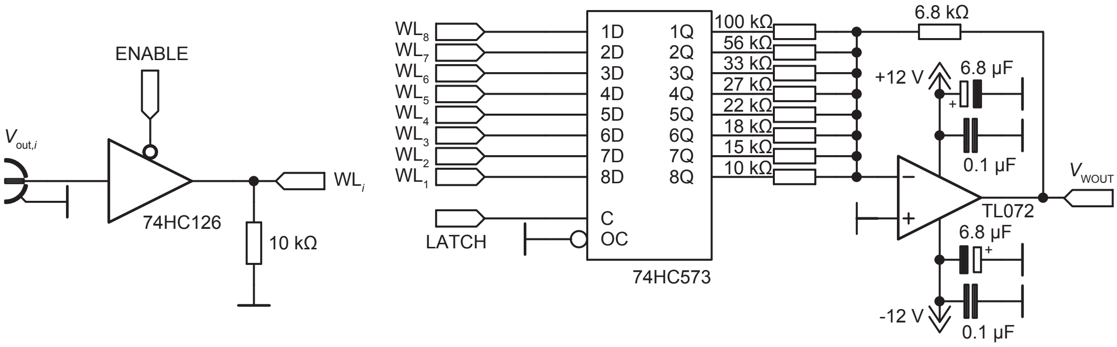
ENABLE
$V_{\text{out},i}$
74HC126
10 kΩ
WL_i
WL_8
WL_7
WL_6
WL_5
WL_4
WL_3
WL_2
WL_1
LATCH
1D
2D
3D
4D
5D
6D
7D
8D
C
OC
1Q
2Q
3Q
4Q
5Q
6Q
7Q
8Q
74HC573
100 kΩ
56 kΩ
33 kΩ
27 kΩ
22 kΩ
18 kΩ
15 kΩ
10 kΩ
6.8 kΩ
+12 V
6.8 µF
0.1 µF
TL072
6.8 µF
-12 V
0.1 µF
V_{WOUT}

Figure 5.39. Simple analog adder with LATCH functionality acting as Winner-Take-All circuitry.

$A_{V,1} = -6.8\,\text{k}\Omega/10\,\text{k}\Omega \approx -0.68$. The WTA output voltage V_{WOUT} is then the summation of all weighted output voltages: $V_{\text{WOUT}} = \sum_i^8 A_{V,i} \cdot V_{\text{out},i}$. A LATCH functionality is able to stop the WTA evaluation and the WTA output voltage remains constant. If the LATCH functionality is not used, the WTA output voltage is a staircase like signal, where each step depends on the input and template patterns, and the specific match-line weight as shown in Fig. 5.40.

Figure 5.40 Example of the staircase like output voltage of the analog adder (LATCH functionality is disabled) based on the input signal in Fig. 5.38c. The first step corresponds to the match-line with lowest HD.

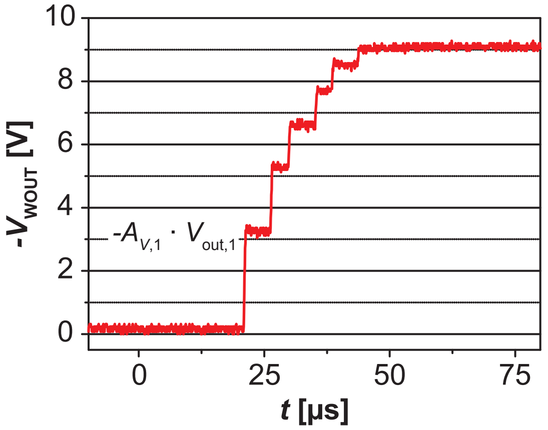

The search speed of the discussed ACN circuits can be significantly increased. For example, the circuit in Fig. 5.38a,b is able to analyze the match-line voltages within some tens of nanoseconds. However, the analog adder based on a TL072 general-purpose operational amplifier in Fig. 5.39 has a unity gain bandwidth of only 3 MHz, which drastically limits the evaluation speed. The search speed can be increased using wideband amplifiers for the WTA circuit. Alternatively, conventional CMOS based WTA circuits can be used [182] for further acceleration of the Hamming distance evaluation.

The discussed associative capacitive network is able to perform a fully parallel search for the smallest Hamming distance of an input pattern and up to eight stored template patterns. Monte-Carlo simulations revealed that the array can be increased of up to

$41 \times (40 + 40)$ template bits [125]. If HD $= 0$ the match-line output is high with a probability of $p = 0.95$. For HD $= 3$ the match-line output is high with $p = 0.05$. Hence, the ACN approach is able to detect HD $= 0$ with a high probability.

6. Conclusions

6.1. Summary

In this thesis, redox processes and cation mass transport in two model materials, SiO_2 and AgI, have been investigated. Special attention has been paid to the resistive switching effect. Silicon dioxide represents the class of insulating materials while silver iodide is a well-known stoichiometric ion conductor. On the nanoscale, both materials show ionic or mixed ionic–electronic characteristics as confirmed by various experimental results of this study. The aim of this work was to identify physical and electrochemical processes, which are involved prior and during the resistive switching effect of cation based ECM cells.

In silicon dioxide, mobile cations need to be injected in order to operate the memory cell. By cyclic voltammetry (CV) redox reactions of Ag/Ag^+ as well as Cu/Cu^{z+} at the interface with SiO_2 were observed. Spectroscopic analysis including X-ray Absorption Spectroscopy (XAS) and X-ray Photo Electron Spectroscopy (XPS) complemented the electrical measurements. While in Ag based silicon dioxide cells the charge number is $z = 1$ for cations, CV measurements reveal the evidence of partial redox reactions in Cu based SiO_2 cells. From potentiodynamic experiments Cu^+ and Cu^{2+} are both observed and Cu^{2+} ions are found using depth-profile XPS. According to XAS experiments, Cu^{2+} appears to be the more mobile cation species in $Cu/SiO_2/Pt$ ECM cells, and may be thus, the dominating cation species for resistive switching in SiO_2. The mobility of Ag^+ and Cu^{z+} cations in the fabricated SiO_2 thin films was found to be orders of magnitudes higher compared to the extrapolated values in bulk SiO_2 at room temperature. The dissolved cation concentration in silicon dioxide thin films depends on the sweep rate and may therefore vary during memory operation depending on the pulse length, pulse voltage rise time and amplitude. Moreover, the ion mobility shows a strong dependence on the ion concentration indicating ion–ion interactions typical for concentrated solution conditions. Potentiodynamic and open circuit measurements demonstrate the formation of cations proceeds in parallel to reduction of moisture supplied by the ambient. As follows, counter charges and/or counter reactions at the inert electrode play a crucial role for resistive switching.

Contrary to SiO_2, silver iodide contains mobile cations and is known to be a cation conductor even at room temperature. α-AgI becomes *superionic* above a transition temperature of $T \approx 150\,^\circ\mathrm{C}$. Since an electroforming voltage is not required to enable resistive switching in AgI based cells and the switching voltages are comparatively low, the voltage amplitude is too small for cyclic voltammetry experiments. However, impedance spectroscopy of Ag/AgI/Pt ECM cells and open circuit measurements of Ag/AgI/C(I_2) cells were used to analyze the electronic and ionic partial conductivity of the fabricated AgI thin films. A high ion mobility close to the bulk value was found in the AgI thin films. Being a stoichiometric material, the ion concentration in AgI should be constant during device operation in contrast to SiO_2 based cells. Despite X-ray Absorption Spectroscopy complemented by X-ray Diffraction (XRD) reveal that the Ag/AgI interface is chemically inactive, nanoscale Ag metal crystallites can penetrate in the AgI thin film. This results in a loss of electric contact in case of thin Ag electrodes and can impact the retention of the low resistive ON state.

Based on the analysis of redox and transport phenomena in solid thin films, resistive switching of SiO_2 and AgI based ECM cells was investigated. In both material systems the resistive switching effect is similar compared to other ECM memory cells including Ag/GeS_x/Pt and Ag/$GeSe_x$/Pt. However, in SiO_2 an electroforming voltage is required to enable resistive switching and the switching voltages are typically larger compared to AgI. Multilevel switching was observed both in AgI and SiO_2 based memory cells. In this context, current sweeps reveal the existence of quantized cell conductance steps in AgI and SiO_2 based ECM cells, which can be attributed to a multiple of the one atomic point contact conductivity. Furthermore, the nonlinear switching kinetics were studied over 12 orders of magnitude in time using Ag/AgI/Pt cells. Switching below 50 ns at moderate pulse amplitudes ($\leq 2\,\mathrm{V}$) has been demonstrated. The experimental switching results are consistent with an advanced 1D simulation model accounting for nucleation effects, charge transfer and cation drift.

The existence of nonequilibrium states, which are inherently induced during device operation in redox based resistive switches, was highlighted in this thesis. These nonequilibrium states result in a nanobattery effect leading to non-zero crossing I–V characteristics. The relaxation of the nanobattery voltage affects the device stability and endurance, which is consistent with the *extended memristor model*.

Applications based on the specific characteristics of resistive switches are complementing this thesis. An asymmetric setup of a complementary resistive switching cell can be alternatively considered as switchable capacity. The presented nondestructive readout approach for CRS cells makes use of this asymmetric setup. Further development of the asymmetric CRS approach resulted in the concept of associative capacitive networks allowing fully parallel pattern recognition.

6.2. Outlook

While the electrochemical metallization effect is observed in various material systems, only SiO_2 has been yet systematically analyzed by cyclic voltammetry experiments. CV could be established as a generic measurement tool to analyze the cation concentration and mobility as well as redox reactions prior to the switching event. In this respect, the measurement problems of cyclic voltammetry for analyzing resistively switching thin films of conventional bulk ion conductors, such as AgI, needs to be solved. Additionally, further research should be focused on resistively switching memory cells based on cation redox reactions in various amorphous oxide material systems such as Ta_2O_5 [101] and Al_2O_3 [118]. An open question in this context is the reason for the high cation mobility observed in nanoscale solid films, which is essential for resistive switching. The impact of the thin film morphology and chemical composition on the cation diffusion behavior may gain deeper insight into the processes determining the resistive switching characteristics. Additionally, the relevance and nature of potential counter charges and/or counter reactions in material systems other than SiO_2 were not yet studied in detail.

The scalability of ECM cells is of high importance to compete with conventional Flash technology. Using Conductive Atomic Force Microscopy, filaments with a diameter of 20 nm have been observed [27]. Conductance experiments showing quantum size effects revealed that even a single metal atom can determine the memory cell resistance. This implies an ultimate scalability of ECM cells to an almost atomic level, which needs to be thoroughly investigated. Besides scalability, the research on device endurance and retention problems should be further intensified. In terms of proper device modeling, a single simulation model for ECM cells is advantageous. Such a comprehensive model should account for the mechanisms responsible for the nonlinear switching kinetics, quantum-size effects and the impact of nonequilibrium states on the resistive switching characteristics. Based on this simulation model, strategies to improve the device endurance or to eliminate retention problems due to the nanobattery effect may be derived. From an application point of view further device engineering is mandatory to comply with the requirements of large and dense passive memory arrays (such as ON state resistance and SET and RESET voltage window).

Finally, new logic concepts, like the sequential logic approach [18; 171; 178; 179] and neuromorphic applications including CRS based associative capacitive networks [125; 181], should be in the focus of future investigations. Further research on resistive switches could therefore lead to a paradigm shift in information technology.

List of Figures

2.1. Categories of resistive switches (based on [11]). Special attention is paid to two-terminal redox related electrochemical metallization cells. 6
2.2. Categories of resistive switches classified by the operating voltage regime. Blue and red color indicate the current/voltage characteristic in the HRS and LRS, respectively. The RESET process is highlighted by green colored lines (redrawn from [26]). (a) Unipolar switching (only one voltage polarity is shown for simplification) and (b) bipolar switching. 7
2.3. Basic principle of the resistive switching effect during a current-voltage (I/V) sweep in electrochemical metallization cells [28]. 8
2.4. Graphical representation of the current density j described by the Butler-Volmer equation. (a) Anodic and cathodic fraction to the net current density, (b) net current density depending on the asymmetry parameter α. 10
2.5. Linear voltage sweep while simultaneously measuring the current density response. (a) Transient voltage signals for two different sweep rates $\nu_1 > \nu_2$. (b) Current density response of the electrochemical system. . . 11
2.6. Oxidation and reduction measured by applying triangular voltage sweeps. (a) Transient measurement of the current during oxidation, (b) cyclic voltammetry (adapted from [36]). 12
2.7. Graphical representation of the dimensionless current density function χ (adapted from [36; 37]). 14
2.8. Cyclic voltammograms for different sweep rates $\nu_1 < \nu_2 < \nu_3$ in case of (a) a reversible redox reaction, (b) a quasi reversible reaction and (c) an irreversible redox reaction (adapted from [38]). 16
2.9. Multistep charge transfer reaction of an oxidation process $\mathrm{S} \longrightarrow \mathrm{S}^{z+} + z\mathrm{e}^-$ and $\mathrm{P} \longrightarrow \mathrm{P}^{z+} + z\mathrm{e}^-$. The blue curve is the current density j response of the electrochemical system consisting of the superimposition of both partial reactions (adapted from [37]). 17

2.10. Origins of nonequilibrium states in redox based resistive switches resulting in an electromotive force voltage V_{emf} (redrawn from [40]). $e\varphi$ describes the electrostatic potential. (a) Nernst potential V_{N} given by electrochemical activity gradient of atomic silver μ_{Ag}, (b) concentration gradient of Ag^+ and OH^- ions resulting in a diffusion potential voltage V_{d}, (c) the chemical potential of silver must be extended by an additional surface energy term in case of a nanosized filament, resulting in the Gibbs-Thomson potential V_{GT}, and (d) the emf voltage cannot be measured in case of a metallic short circuit. The interfaces electrode/electrolyte (insulator) and electrolyte (insulator)/electrode are labeled by s' and s". 18
2.11. Schematic of a H_2 partial pressure concentration cell with a concentration gradient determined by the hydrogen partial pressure in both half cells $p{H_2}^{\mathrm{I}} > p{H_2}^{\mathrm{II}}$. 19
2.12. Example of the origin of a diffusion potential for two theoretical systems. (a) Concentration profile for Na^+ and OH^- ions in case of a 1 mol:NaOH/10^{-5} mol:NaOH solution system. The concentration of both ions is equal. The red and green arrows indicate the diffusion direction of each species. Both anions and cations diffuse in the same direction. (b) Concentration profile for Ag^+ and OH^- in case of a Ag/SiO_2/Pt ReRAM cell. Now, the concentration profiles are not in the same direction, and thus, the directions of diffusion are opposed. 21

3.1. Schematic of the Cluster Tool 500 ES by *von Ardenne*. The 6" high vacuum process tool is equipped with an e-beam evaporation chamber, a sputter chamber and a transfer chamber. The Inverse Sputter Etching (ISE) position is not used in this work. 24
3.2. Vapor pressure results for SiO_2 (Yaws et. al. [47]) and AgI (Stull et. al. [48]). The evaporation temperature T_{B} is plotted versus the absolute ambient pressure p. 25
3.3. (a) Principle of X-ray Diffraction. The interference spectrum depends on the crystallographic characteristic of the thin film and the incident angle Θ. (b) Crystalline response of a platinum thin film on (100) orientated silicon. 27
3.4. (a) Schematic of a X-ray Reflectivity measurement setup and (b) XRR scans of wet-thermally oxidized SiO_2 and e-beam evaporated SiO_2. . . . 28

3.5. Resistive switching of a Ag/AgI/Pt micro crossbar cell. The current is given as black curve, while the effectively applied voltage to the cell is shown as red curve. As soon as the cell switches to the ON state, the source meter switches from voltage to current driven mode. 30
3.6. Current compliance overshoot experiment. A current compliance of $I_{\mathrm{CC}} = 50\,\mathrm{nA}$ is applied and a current overshoot of up to 105 nA is recorded. . 30
3.7. Cyclic voltammetry of a Cu/SiO_2/Pt cell using sputtered silicon dioxide (Cu electrode diameter $d = 100\,\mu\mathrm{m}$). The sweep rate is set to 10 mV/s. (a) Voltage and current transients during cycling. (b) Corresponding cyclo voltammogram. 31
3.8. Rutherford Backscattering Spectroscopy of (a) 120 nm e-beam evaporated silicon dioxide and (b) 215 nm rf sputtered SiO_2. In both cases the measurements fit to simulations of stoichiometric SiO_2. 33
3.9. X-ray Reflectivity of (a) wet-thermal oxidized, e-beam evaporated and sputtered SiO_2, and (b) e-beam evaporated SiO_2 after temperature annealing. The thickness of the wet-thermal oxidized SiO_2 layer is 450 nm and of the e-beam and sputtered thin films between 15 nm and 30 nm, respectively. 33
3.10. Atomic Force Microscopy of a 30 nm thick e-beam evaporated SiO_2 thin film on (a) a SiO_2/Si substrate and (b) a Pt/TiO_2/SiO_2/Si substrate. . 34
3.11. XRD profiles of a AgI thin film deposited on a silicon wafer simultaneously measured during increase of the sample temperature indicating a phase transition at $T \approx 145\,^\circ\mathrm{C}$. 35
3.12. AgI thin film morphology and density analysis. (a) Atomic Force Microscopy scan of a deposited AgI thin film on Si revealing a high roughness of $r_{\mathrm{RMS}} \approx 5.3\,\mathrm{nm}$ ($r_{\mathrm{RMS}} \approx 4.6\,\mathrm{nm}$ based on the XRR measurement). (b) XRR measurement of a AgI thin film (intended thickness 20 nm) on a silicon substrate. The measurement is compared to a simulation of a 23.8 nm thick AgI layer. The thin film density ρ_{AgI} can be calculated by measuring the critical angle (see section 3.2.1). 36
3.13. Flow chart of the pattern transfer for AgI based micro crossbars [54]. . 37

4.1. Cyclic voltammetry of a Cu/SiO_2/Pt cell (Cu top electrode diameter $d = 150\,\mu\mathrm{m}$) [53]. By limitation of the voltage amplitude to avoid resistive switching, redox processes prior to the switching event can be analyzed. Arrows and labels indicate the direction of the sweep. 40
4.2. Kinetics of anodic Cu oxidation [53]. (a) Cyclic voltammorgrams by variation of the sweep rate ν. (b) Reduction peak j_{p} vs. $\nu^{1/2}$. 41

4.3. Cyclic voltammetry of a Ag/SiO_2/Pt cell (Ag top electrode diameter $d = 150\,\mu$m). Analogous to Cu/SiO_2/Pt cells, Ag based cells also show redox reactions during cyclic voltammetry. However, the voltage amplitude is reduced since the electroforming and SET voltages for resistive switching of Ag/SiO_2/Pt cells are typically smaller than for Cu/SiO_2/Pt cells. . . 41

4.4. Ion concentration for a Cu/SiO_2/Pt cell. [66] (a) The ion concentration c_{ion} is calculated by the total charge Q and cell geometry. Q is given by the integration of the current during anodic oxidation. (b) Ion concentration depending on the sweep rate. At high sweep rates less time is available for anodic oxidation resulting in a lower ion concentration. 42

4.5. (a) Ion concentration c_{ion} for a Ag/SiO_2/Pt cell versus sweep rate ν. c_{ion} is smaller for Ag than for Cu based cells. (b) Diffusion coefficient D for Ag^+ ions in SiO_2. D is significantly smaller compared to Cu based cells (cf. 4.6a). 43

4.6. Diffusion behavior of cations in SiO_2 [66]. (a) Diffusion coefficient D of Cu^{z+} ions depending on the ion concentration c_{ion}. (b) Diffusion coefficient D for both Cu^{z+} and Ag^+ ions as a function of the sweep rate ν. The ion concentration, and thus, the diffusion coefficient can be adjusted by variation of ν. 44

4.7. Temperature dependence of diffusion coefficient D (a) and *solid solubility* c (b) of singly ionized Ag and Cu atoms in SiO_2 derived from Ref. [67] (labeled by (1)) and compared to values measured in this study (labeled by (2) with $\nu = 0.1\,\mathrm{V/s}$). The extrapolation to room temperature for D is indicated by dotted lines. 45

4.8. Cation distribution in a Cu/SiO_2/Pt cell. (a) For simplification only the signal response around the binding energy of Cu $2p_{3/2}$ at the Cu/SiO_2 interface is shown (see zoom). Depth profile XPS analysis of (b) a pristine Cu/SiO_2/Pt cell and (c) a cell after anodic oxidation. The distribution of Cu^{2+} ions underneath the Cu electrode can be clearly observed. Redrawn from [72]. 46

4.9. Partial redox reactions observed at a low sweep rate $\nu = 15\,\mathrm{mV/s}$ [66]. Various peaks are observed, which are contributed to Cu^+ and Cu^{2+} redox reactions. 47

4.10. O K-edge XAS spectra in TEY mode of pure SiO_2 and SiO_2 thin films, covered by 5 nm Cu or Ag thin films, respectively. The Ag/SiO_2 and pure SiO_2 spectra are similar (except for a small Ag M_3-edge absorption) indicating the absence of any chemical interaction of Ag and SiO_2. Reproduced from Ref. [74]. 49

4.11. Analysis of oxidation state of Cu on top of SiO_2 [74]. Magnified view of the O K-edge XAS spectra in (a) TEY and (b) FY mode. In (c) the contributions from Pt/SiO_2 and Pt are subtracted, respectively. (d) Cu $L_{2,3}$-edge XAS of Cu/SiO_2/Pt and Cu/Pt samples (TEY mode). The spectra look very similar and the sharp features reflect the coexistence of Cu^{2+} and Cu^+ ions with considerable higher-energy backgrounds for both samples [74]. Additionally, a high Cu^0 background is observed in both samples indicating that only a few percent of Cu atoms are oxidized. (e) Hybridization strengths of Cu (3d/4sp)-O (2p) orbitals in the Cu^+ and Cu^{2+} ions. The features for Cu^{2+} (3d) and (4sp) in brown, Cu^+ (3d-4sp) in gray, and Cu^{2+} and Cu^+ (4sp) in yellow of O K-edge XAS spectra are decomposed exemplary for clarity, respectively. These signals contribute to the total spectra (green) which is very similar to the measured O K-edge XAS spectra. 50

4.12. Schematic of the bond structures of (a) fourfold-coordinated Cu^{2+} and (b) twofold-coordinated Cu^+ ions in association with SiO_4 networks in the SiO_2 matrix [74]. 51

4.13. Role of water supplying counter charges during anodic oxidation [72]. (a) Impact of water partial pressure pH_2O on redox reactions studied by cyclic voltammetry. (b) Potential water penetration in SiO_2. 53

4.14. (a) Impact of pH_2O on the ion concentration c_{ion} for various sweep rates $\nu = 0.2\,\text{V/s}$ to $1.7\,\text{V/s}$. (b) Diffusion coefficient D as a function of the water partial pressure. As pH_2O increases the ion concentration increases as well, and ion-ion interactions become dominating. This results in a decrease of D at high water partial pressures. Redrawn from [72]. . . . 54

4.15. Impact of counter electrode material on the redox reactions prior to resistive switching. (a) CV of Cu/SiO_2/CE cells with various counter electrodes CE = Pt, Ir, Ti and Ru, and (b) of a Cu/SiO_2/Al cell. Redrawn from [76]. 55

4.16. (a) c_{ion} depending on the counter and active electrode material. (b) c_{ion} for various CE materials as a function of the sweep rate ν for Cu based cells. Redrawn from [76]. 55

4.17. Hydrogen evolution potential (vs. SCE) for various electrode materials vs. work function. A general trend can be observed: the hydrogen evolution potential decreases as the work function increases. Small hydrogen evolution potentials are found for noble metals such as Pt and Ir but also Ni. Materials in italic are used as active electrode material, and those in bold red font are used as counter electrode material in this study. Variation of the hydrogen evolution potential can be explained by the measurement conditions such as temperature, current density, and sweep rate. Details are given in Miles et. al 1976 [77], Morse et. al. 1967 [78], Hickling et. al. [79], J. Bockris 1947 [80] and Shibutani et. al. 1998 [81]. The work function is based on measurement data given in [82; 83]. Redrawn from [76]. 56

4.18. c_{ion} from figure 4.16b as a function of the hydrogen evolution potential (measured vs. SCE) [77], exemplary for $\nu = 3\,\text{V/s}$ and $\nu = 20\,\text{mV/s}$ for selected counter electrode materials. Data points labeled with asterisk are extrapolated values from figure 4.16b. Redrawn from [76]. 57

4.19. Redox reactions and ion concentration for Cu/SiO_2 based cells with various counter electrode materials. (a) Cyclic voltammetry for counter electrode materials CE = Yb, Sa and La. (b) Corresponding ion concentration versus sweep rate. (c) Cyclic voltammetry for counter electrode materials CE = ITO and TiN. (d) Corresponding ion concentration versus sweep rate. Redrawn from [76]. 58

4.20. (a) Measurement setup for evaluating the electronic and ionic partial conductivity. (b) The ionic transference number is derived from the ratio of measured cell voltage V_{Cell} and theoretically expected emf voltage. . 60

4.21. Impedance spectroscopy of a Ag/AgI/Pt micro crossbar cell. The measurement of the complex impedance Z fits well to a simulation based on the equivalent circuit shown in the inset. From the fit parameters a total conductivity of $\sigma \approx 1.9 \cdot 10^{-6}\,\Omega^{-1}\text{cm}^{-1}$ was calculated. 61

4.22. Temperature dependence of the ion conductivity σ_{ion} of Ag/AgI/Pt micro crossbars measured by impedance spectroscopy. A phase transition is observed for $T \approx 130\,°\text{C} - 150\,°\text{C}$. 61

4.23. Capacity, dielectric constant and dissipation factor tan δ measurement of a Ag/AgI/Pt micro crossbar cell versus frequency f. At small frequencies a high dissipation factor is observed, because AgI is a good ion conductor. This results in a high dielectric constant. At high frequencies the dissipation factor is drastically reduced, and the dielectric constant of about $\epsilon_\mathrm{r} \approx 10$ is similar to values reported for bulk AgI in the microwave range [93]. 62

4.24. XAS of bare AgI thin films and AgI thin films covered by Ag layers (thickness 10 nm, 20 nm and 50 nm) [64]. (a) Ag L_3-edge XAS and (b) their derivative spectra of the AgI films after Ag deposition. For comparison the signal of a Ag foil is added. 63

4.25. (a) Difference spectra derived from the XAS spectra in figure 4.24a. (b) Schematic description to account for the difference analysis in (a) [64]. . 64

4.26. (a) I L_3-edge XAS spectra and (b) XRD profiles of the AgI thin films with and without additional Ag evaporation [64]. The I L_3-edge XAS spectra reveal no change in the local structure of AgI by evaporation of Ag. However, adding Ag can take effect in the scale of some tens of atoms as revealed by the inset in (b). The full-width-at-half-maximum (FWHM) of the (111) γ-AgI peak for each sample is also tabulated. (c) XRD pattern close to the (400) Si peak indicating no decrease of signal intensity as observed for the γ-AgI (111) peak in the inset of (b). . . . 65

4.27. Measurement setup for emf measurements of a Ag/SiO_2/Pt cell [40]. A similar procedure is used for emf measurements of Cu/SiO_2/Pt cells. The cell voltage V_Cell was measured (as depicted in the inset) using a high impedance voltage mode of the source meter after anodic oxidation. For Cu based cells the voltage amplitude can be increased due to higher forming voltages. 67

4.28. Electromotive force measurements for a Ag/SiO_2/Pt cell [40]. (a) Cell voltage V_Cell versus time for various ion concentrations c_ion adjusted by the sweep rate during anodic oxidation. (b) V_Cell versus c_ion. The ionic transference number can be determined by the slope of the regression line. The inset depicts a schematic of the concentration gradients of cations and counter charges (e.g. OH^- ions) both contributing to the emf. . . . 68

4.29. (a) Equivalent circuit model for $Ag/SiO_2/Pt$ or $Cu/SiO_2/Pt$ cells. The measurable cell voltage is determined by the nanobattery voltage V_{emf}, the ionic resistance R_{i} and the electronic resistance R_{el}. (b) Cell voltages of a $Cu/SiO_2/Pt$ cell versus time for various ion concentrations. Redrawn from [72]. 69

4.30. Electromotive force measurement at a constant ion concentration for a $Cu/SiO_2/Pt$ cell. (a) V_{Cell} dependence on the water partial pressure in nitrogen atmosphere. Each point corresponds to a different pH_2O value. The initial ion concentration (indicated in the plot) was set prior to the measurements. (b) Transient measurement of V_{Cell} at constant c_{ion} and pH_2O. (c) V_{Cell} (red) response to the variation of pH_2O (black). The V_{Cell} response on pH_2O change is reversible. This indicates that the concentration gradient of Cu remains constant with time and pH_2O does not meaningfully increase the mobility of Cu ions in SiO_2. Redrawn from [72]. 70

5.1. Scanning Electron Microscopy of (a) micro crossbar, and (b) nano crossbar cells with a $Ag/SiO_2/Pt$ layer stack [98]. 74

5.2. Resistive switching behavior of $Ag/SiO_2/Pt$, Ag/AgI/Pt and $Ag/GeS_x/Pt$ micro crossbars (μXBar) as well as a $Ag/SiO_2/Pt$ nano crossbar (nXBar) [98]. Arrows indicate the direction of sweep. 74

5.3. Electroforming and subsequent resistive switching of (a) a $Cu/SiO_2/Pt$ [53] and (b) a $Ag/SiO_2/Pt$ cell. 75

5.4. Electroforming step required to enable resistive switching of a $Cu/SiO_2/Pt$ cell (blue curve) [66]. By limitation of the vertex potential resistive switching is avoided and the oxidation/reduction reactions being the preceding processes of resistive switching can be analyzed (red curve) by cyclic voltammetry (CV). 76

5.5. Multilevel switching for a $Ag/SiO_2/Pt$ cell compared to results of $Cu/SiO_2/Pt$ cells reported in literature (Bernard et. al. 2011 [106] and Schindler 2009 [35]). 77

5.6. (a) Resistive switching of a $Ag/SiO_2/Pt$ cell using a $R_{\mathrm{S}} = 47\,\mathrm{k}\Omega$ series resistor to limit the current in the low resistive ON state. (b) Endurance of the same cell. The device failure is here defined as soon as the cell exhibits a $R_{\mathrm{OFF}}/R_{\mathrm{ON}}$ ratio smaller than 100. The cell withstands more than 10^4 I/V cycles. 77

5.7. (a) Resistive switching characteristics of a Ag/AgI/Pt micro crossbar. In contrast to SiO_2 ReRAMs, an initial electroforming step to enable resistive switching is not required. (b) Multilevel switching by variation of the current compliance. The ON resistance was extracted from I/V curves. [54] . . . 78

5.8. (a) Typical I/V curves for various temperatures $T = 25\,°\mathrm{C}$, $80\,°\mathrm{C}$ and $200\,°\mathrm{C}$, respectively. (b) SET voltage V_{SET} versus temperature. . . . 79

5.9. (a) Impact of AgI electrolyte thickness on the SET voltage. (b) SET voltage versus micro crossbar electrode area. . . . 79

5.10. Endurance test for a Ag/AgI/Pt micro crossbar. (a) and (b) SET voltage, and ON and OFF resistance using a current compliance of 20 nA. (c) and (d) V_{SET}, and R_{ON} and R_{OFF} endurance using a current compliance of $2\,\mu\mathrm{A}$. . . . 80

5.11. Impact of water partial pressure $p\mathrm{H_2O}$ on (a) the dielectric constant and dissipation factor tan δ, and (b) the forming voltage V_{F} of Ag/SiO_2/Pt cells in N_2:H_2O atmosphere [32]. . . . 81

5.12. Analysis of filament formation by measuring the actual cell voltage drop simultaneously during an I/V sweep of a Ag/AgI/Pt cell [54]. (a) Although the cell already switched, a significant voltage drop of about 25 mV is observed during further sweeping, indicating a quantized change of the filament conductivity. (b) At lower current compliances a similar voltage drop is not observed. . . . 82

5.13. Equivalent circuit of a simple measurement setup consisting of the Ag/AgI/Pt cell and the *Keithley* source meter. The electrode resistance R_{e} is small compared to the contact resistance R_{c} and the filament resistance R_{f}. Hence, R_{e} will be further neglected. [54] . . . 83

5.14. Analysis of quantized cell conductance by a current sweep using Ag/AgI/Pt cells. [54] (a) At least five quantized resistances have been observed in this example by current sweeping. (b) Cumulative statistics of measured cell conductivity. . . . 84

5.15. Quantum conductance experiment of a Ag/AgI/Pt cell at an ambient temperature of $T = 173\,\mathrm{K}$. Here, the conductance values fit very well to integer numbers of G_0 when a filament resistance of $R_{\mathrm{f}} = 500\,\Omega$ is assumed. 85

5.16. Analysis of quantized cell conductivities of Ag/SiO_2/Pt micro crossbars using current sweeps. The assumed filament resistance R_f differs more from cell to cell compared to AgI based devices: (a) $R_\mathrm{f} = 1\,\mathrm{k\Omega}$, (b) $R_\mathrm{f} = 100\,\Omega$ and (c) $R_\mathrm{f} = 200\,\Omega$. In (d) quantized cell conductivities of a of Ag/SiO_2/Pt nano crossbar are given. The current response is fitted by various filament resistances $R_\mathrm{f} = 100\,\Omega ... 1.5\,\mathrm{k\Omega}$. 86

5.17. Cumulative statistic of the measured cell conductivity levels of Ag/SiO_2/Pt micro crossbars. 87

5.18. (a) Measurement setup for pulse experiments. The AgI micro crossbar cell (device under test, DUT) can be described by a $R_\mathrm{C}C$ circuit. The voltage signal supplied by the pulse generator is recorded by an oscilloscope channel (SCOPE CH1) coupled by $50\,\Omega$. The current response is recorded by a second oscilloscope channel (SCOPE CH2) coupled by $1\,\mathrm{M\Omega}$ which acts as shunt resistor. (b) Short circuit reference measurement. The cable length in the RFI shielded measurement box was reduced in order to measure signals down to $\approx 10\,\mathrm{ns}$. 88

5.19. Short pulse measurements and current transients for (a) $V_\mathrm{Pulse} = 0.4\,\mathrm{V}$ and (b) $V_\mathrm{Pulse} = 1.5\,\mathrm{V}$ [54]. 89

5.20. Current transients for various pulse voltages over a large time scale of up to 12 orders of magnitude. 90

5.21. (a) Measurement data of switching kinetics at $T = 298\,\mathrm{K}$. (b) Weibull distribution of t_SET from (a), exemplarily for $V_\mathrm{Pulse} = 0.3\,\mathrm{V}, 0.4\,\mathrm{V}, 0.5\,\mathrm{V}, 1\,\mathrm{V}, 1.5\,\mathrm{V}$ and $2\,\mathrm{V}$. 91

5.22. Schematic of the nucleation, charge transfer, and drift process during filament formation. Reproduced from [112]. 91

5.23. Equivalent circuit model for 1D switching simulation. The switching layer of thickness L is sandwiched between the active top and inert bottom electrode. The filament grows within the electrolyte film and modulates the tunneling gap x. The model accounts both for ionic and electronic current paths. $R_\mathrm{S} = 1\,\mathrm{M\Omega}$ is the series resistor, $R_\mathrm{el,ac}$ and $R_\mathrm{el,in}$ are the active electrode and inert electrode resistances, respectively. R_fil is the filament resistance. Reproduced from [112]. 92

5.24. Pulse measurement data (squares) and simulation results (solid lines) for various ambient temperatures $T = 298\,\mathrm{K}$ (blue), $T = 323\,\mathrm{K}$ (red), $T = 348\,\mathrm{K}$ (black) and $T = 373\,\mathrm{K}$ (light green) [112]. I, II, III mark the nucleation limited, the electron transfer limited, and the mixed control regime, respectively. Details of statistical variation can be found in [54]. 96

5.25. Nanobattery effect in Ag/SiO_2/Pt resistive switching devices [40]. (a) Open circuit cell voltage for a cell after SET and RESET operation (red curve) compared to cell voltages without a previous electroforming step (blue, green, brown and purple curves). (b) Short circuit discharge current density ($V_{\mathrm{Cell}} = 0$) of the same cell with similar ion concentration. The inset depicts the discharge current over a long time scale. The measurement limitation is about 0.01 pA. 97
5.26. Short circuit discharge current density ($V_{\mathrm{Cell}} = 0$) after SET and RESET of a Ag/SiO_2/Pt cell [40]. The discharge current (recorded after a discharge time of $t = 150\,\mathrm{s}$, see inset) scales with the electrode diameter indicating that the nanobattery effect is do-minated by the whole electrode area. . 98
5.27. Non-zero crossing effect in ECM type resistive switching cells [40]. (a) Cu/SiO_2/Pt cells with a pronounced non-zero crossing behavior for $V = 0$. (b) Non-zero crossing of a Ag/SiO_2/Pt cell with special attention to subsequent reduction cycles. The RESET process appears to be incomplete resulting in an ion accumulation at the interfaces. 99
5.28. Open circuit cell voltages for several VCM and ECM type memory cells [40]. The cell voltage of VCM material systems is potentially smaller due to a higher electronic partial conductivity. 99
5.29. Extended memristive device model [40]. (a) Equivalent circuit of the extended memristive device accounting for the nanobattery effect and ionic resistance. (b) The SPICE simulation results fit very well to the measurement data shown in figure 5.27. 100
5.30. (a) Schematic and measurement setup for endurance and retention experiments shown for a ECM micro crossbar. (b) Nanobattery effect exemplarily shown for a Ag/SiO_2/Pt cell. The ion concentration gradients of Ag^+ and OH^- result in the formation of a nanobattery voltage V_{emf}, which is measurable as a cell voltage V_{Cell} in the OFF state of the cell. R_{i} is the ionic and R_{el} the electronic (i.e. leakage current in the OFF state, and filament/tunnel gap in the ON state) resistance. (c) Schematic of the measurement procedure. The ionic resistance R_{i}, and thus, the OFF state resistance R_{OFF} is increased during time. Redrawn from Ref. [98] 101
5.31. OFF state retention and V_{Cell} relaxation versus time for (a) AgI, (b) GeS_x and (c) SiO_2 ECM cells, and a (d) $SrTiO_3$ VCM cell. [98] 102

5.32. Resistive switching endurance for Ag/SiO_2/Pt nano crossbar cells [98]. (a) I/V curves with highlighted cycles indicating a shift of the SET voltage (where the cell switches from the high resistive state to the low resistive state) to smaller values. (b) Extracted SET voltage V_{SET} for the cell in (a). A clear decrease of V_{SET} is observed. 103

5.33. Simulation results based on the extended memristor model [40; 98]. Arrows indicate the trend of the SET voltage and absolute maximum RESET current by further cycling. (a) The cell is stuck in ON state due to incomplete RESET operations. (b) Unstable ON states are observed for emf voltages in the range of the RESET voltage. 104

5.34. Capacity based nondestructive readout for CRS cells redrawn from [174]. (a) Equivalent network for a CRS device. In state LRS/HRS (state 0) $R_{\mathrm{A}} = R_{\mathrm{LRS}}$ and $R_{\mathrm{B}} = R_{\mathrm{HRS}}$ holds, while in state HRS/LRS (state 1) $R_{\mathrm{A}} = R_{\mathrm{HRS}}$ and $R_{\mathrm{B}} = R_{\mathrm{LRS}}$ holds. C_{A} and C_{B} are independent of the device state, and depend only on device geometry and material permittivity. In (b) an exemplary device geometry is shown. The area of element A is $A_{\mathrm{A}} = 50\,\mu\mathrm{m}^2$ and area of element B is $A_{\mathrm{B}} = 150\,\mu\mathrm{m}^2$, hence $C_{\mathrm{A}}/C_{\mathrm{B}} = 1/3$. (c) and (d) depict the equivalent circuit of a CRS device and circuitry for capacitive voltage divider evaluation. The behavior of element A and B is either dominated by a low resistance or capacitance depending on the particular element state. 107

5.35. (a) Capacitive readout of SiO_2 based CRS cells [174]. The film thickness for both elements A and B is $d = 8\,\mathrm{nm}$ (area size see figure 5.34). The ON state resistance is $R_{\mathrm{LRS}} = 130\,\Omega$ and the OFF state resistance is $R_{\mathrm{HRS}} = 10\,\mathrm{M}\Omega$. $C_{\mathrm{A}} = 0.9\,\mathrm{pF}$ and $C_{\mathrm{B}} = 0.3\,\mathrm{pF}$ resulting in a normalized voltage margin of 2.4 %. (b) The nonlinear switching kinetics can be used to increase the input voltage for short pulse lengths (here 50 ns) [174], exemplarily shown for $V_{\mathrm{in}} = 2\,\mathrm{V}$ and $V_{\mathrm{in}} = 3\,\mathrm{V}$, respectively. Voltage margins are about 46 mV for a 2 V input pulse and 68 mV for a 3 V input pulse, respectively. 108

5.36. (a) Fast noninverting sense amplifier circuit for nondestructive readout of CRS cells. (b) Layout of the sense amplifier. The cable and wire lengths were kept small to measure ultra short pulses. 110

5.37. A single match-line ML_i consisting of two CRS cells, a threshold voltage, and an analog comparator for an one bit matching operation. Redrawn from [125]. 111

5.38. Demonstration of an ACN based on a 8 × 16 capacity array. (a) Voltage follower and match-line comparator amplifier for each match-line $i = 1...8$. (b) Layout of the 8 × 16 ACN circuit. (c) Example of comparator output voltages $V_{\mathrm{out}1...8}$ using test input and template patterns. 113
5.39. Simple analog adder with LATCH functionality acting as Winner-Take-All circuitry. 114
5.40. Example of the staircase like output voltage of the analog adder (LATCH functionality is disabled) based on the input signal in Fig. 5.38c. The first step corresponds to the match-line with lowest HD. 114

List of Tables

5.1. Simulation model parameters from [112]. 95

Bibliography

[1] G. E. Moore, Cramming more components onto integrated circuits *Electronics*, vol. 38, no. 8, pp. 114–117, 1965.

[2] International Technology Roadmap for Semiconductors, Edition 2012 *http://www.itrs.net/*.

[3] Y. Fujisaki, Current Status of Nonvolatile Semiconductor Memory Technology *Japanese Journal of Applied Physics*, vol. 49, no. 10, pp. 1–14, 2010.

[4] Y. Fujisaki, Review of Emerging New Solid-State Non-Volatile Memories *Japanese Journal of Applied Physics*, vol. 52, p. 40001, 2013.

[5] T. Endoh, K. Kinoshita, T. Tanigami, Y. Wada, K. Sato, K. Yamada, T. Yokoyama, N. Takeuchi, K. Tanaka, N. Awaya, K. Sakiyama, and F. Masuoka, Novel ultrahigh-density flash memory with a stacked-surrounding gate transistor (S-SGT) structured cell *IEEE Transactions on Electron Devices*, vol. 50, no. 4, pp. 945–951, 2001.

[6] H. T. Lue, T. H. Hsu, Y. H. Hsiao, S. P. Hong, M. T. Wu, F. H. Hsu, N. Z. Lien, S. Y. Wang, J. Y. Hsieh, L. W. Yang, T. Yang, K. C. Chen, K. Y. Hsieh, and C. Y. Lu, A Highly Scalable 8-Layer 3D Vertical-Gate (VG) TFT NAND Flash Using Junction-Free Buried Channel BE-SONOS Device *Symposium On VLSI Technology Systems and Application (VLSI)*, pp. 131–132, 2010.

[7] A. V. Khvalkovskiy, D. Apalkov, S. Watts, R. Chepulskii, R. S. Beach, A. Ong, X. Tang, A. Driskill-Smith, W. H. Butler, P. B. Visscher, D. Lottis, E. Chen, V. Nikitin, and M. Krounbi, Basic principles of STT-MRAM cell operation in memory arrays *Journal of Physics D: Applied Physics*, vol. 46, no. 13, p. 139601, 2013.

[8] R. Waser and M. Aono, Nanoionics-based resistive switching memories *Nature Materials*, vol. 6, no. 11, pp. 833–840, 2007.

[9] R. Waser, *Nanoelectronics and Information Technology.* Wiley-VCH, 3 ed., 2012.

[10] D. Ielmini, R. Bruchhaus, and R. Waser, Thermochemical resistive switching: materials, mechanisms, and scaling projections *Phase Transitions*, vol. 84, no. 7, pp. 570–602, 2011.

[11] R. Waser, R. Dittmann, G. Staikov, and K. Szot, Redox-Based Resistive Switching Memories - Nanoionic Mechanisms, Prospects, and Challenges *Advanced Materials*, vol. 21, no. 25-26, pp. 2632–2663, 2009.

[12] I. Valov and M. N. Kozicki, Cation-based resistance change memory *Journal of Physics D*, vol. 46, p. 074005, 2013.

[13] A. Sawa, Resistive switching in transition metal oxides *Materials Today*, vol. 11, no. 6, pp. 28–36, 2008.

[14] K. Kim, D. S. Jeong, and C. S. Hwang, Nanofilamentary resistive switching in binary oxide system; A review on the present status and outlook *Nanotechnology*, vol. 22, no. 25, 2011.

[15] W. Lu, D. S. Jeong, M. Kozicki, and R. Waser, Electrochemical metallization cells-blending nanoionics into nanoelectronics? *MRS Bulletin*, vol. 37, no. 2, pp. 124–130, 2012.

[16] E. Linn, R. Rosezin, C. Kügeler, and R. Waser, Complementary Resistive Switches for Passive Nanocrossbar Memories *Nature Materials*, vol. 9, no. 5, pp. 403–406, 2010.

[17] J. R. Heath, P. J. Kuekes, G. S. Snider, and R. S. Williams, A Defect-Tolerant Computer Architecture: Opportunities for Nanotechnology *Science*, vol. 280, no. 5370, pp. 1716–1721, 1998.

[18] E. Lehtonen and M. Laiho, Stateful Implication Logic with Memristors *2009 IEEE/ACM International Symposium on Nanoscale Architectures*, pp. 33–36, 2009.

[19] S. H. Jo, T. Chang, I. Ebong, B. B. Bhadviya, P. Mazumder, and W. Lu, Nanoscale Memristor Device as Synapse in Neuromorphic Systems *Nano Letters*, vol. 10, no. 4, pp. 1297–1301, 2010.

[20] T. Ohno, T. Hasegawa, T. Tsuruoka, K. Terabe, J. K. Gimzewski, and M. Aono, Short-term plasticity and long-term potentiation mimicked in single inorganic synapses *Nature Materials*, vol. 10, pp. 591–595, 2011.

[21] C. Schindler, S. C. P. Thermadam, R. Waser, and M. N. Kozicki, Bipolar and unipolar resistive switching in Cu-doped SiO_2 *IEEE Transactions on Electron Devices*, vol. 54, no. 10, pp. 2762–2768, 2007.

[22] X. F. Liang, Y. Chen, L. Shi, J. Lin, J. Yin, and Z. G. Liu, Resistive switching and memory effects of AgI thin film *Journal of Physics D: Applied Physics*, vol. 40, no. 16, pp. 4767–4770, 2007.

[23] D. Ielmini, Reliability issues and modeling of Flash and post-Flash memory *Microelectronic Engineering*, vol. 86, no. 7-9, pp. 1870–1875, 2009.

[24] R. Waser, Emerging Non-Volatile Memories by Exploiting Redox Reactions on the Nanoscale *ECS Transactions*, vol. 25, no. 7, pp. 441–446, 2009.

[25] S. Menzel, U. Böttger, and R. Waser, Simulation of multilevel switching in electrochemical metallization memory cells *Journal of Applied Physics*, vol. 111, no. 1, p. 14501, 2012.

[26] R. Waser, Resistive non-volatile memory devices *Microelectronic Engineering*, vol. 86, no. 7-9, pp. 1925–1928, 2009.

[27] C. Schindler, K. Szot, S. K. anduser, and R. Waser, Controlled local filament growth and dissolution in Ag-Ge-Se *physica status solidi - Rapid Research Letters*, vol. 2, no. 3, pp. 129–131, 2008.

[28] I. Valov, R. Waser, J. R. Jameson, and M. N. Kozicki, Electrochemical metallization memories-fundamentals, applications, prospects *Nanotechnology*, vol. 22, no. 25, pp. 254003/1–22, 2011.

[29] R. Waser, R. Dittmann, M. Salinga, and M. Wuttig, Function by defects at the atomic scale - New concepts for non-volatile memories *Solid-State Electronics*, vol. 54, no. 9, pp. 830–840, 2010.

[30] D. Ielmini, C. Cagli, and F. Nardi, Resistance transition in metal oxides induced by electronic threshold switching *Applied Physics Letters*, vol. 94, no. 6, p. 063511, 2009.

[31] M. N. Kozicki, M. Park, and M. Mitkova, Nanoscale memory elements based on solid-state electrolytes *IEEE Transactions on Nanotechnology*, vol. 4, no. 3, pp. 331–338, 2005.

[32] S. Tappertzhofen, M. Hempel, I. Valov, and R. Waser, Proton Mobility in SiO_2 Thin Films and Impact of Hydrogen and Humidity on the Resistive Switching Effect *Materials Research Society Symposium Proceedings*, vol. 1330, 2011.

[33] L. Yang, C. Kügeler, K. Szot, A. Rüdiger, and R. Waser, The influence of copper top electrodes on the resistive switching effect in TiO_2 thin films studied by conductive atomic force microscopy *Applied Physics Letters*, vol. 95, no. 1, p. 13109, 2009.

[34] C. Schindler, G. Staikov, and R. Waser, Electrode kinetics of Cu-SiO_2-based resistive switching cells: Overcoming the voltage-time dilemma of electrochemical metallization memories *Applied Physics Letters*, vol. 94, no. 7, p. 072109, 2009.

[35] C. Schindler, *Resistive switching in electrochemical metallization memory cells.* PhD thesis, RWTH Aachen University, Aachen, 2009.

[36] C. H. Hamann, A. Hamnett, and W. Vielstich, *Electrochemistry.* Wiley-VCH, 2 ed., 2007.

[37] A. Bard and L. Faulkner, *Electrochemical Methods: Fundamentals and Applications.* Wiley-VCH, 2001.

[38] J. Heinze, Cyclovoltammetrie - die Spektroskopie des Elektrochemikers *Angewandte Chemie*, vol. 96, no. 11, pp. 823–840, 1984.

[39] R. Nicholson and I. Shain, Theory of Stationary Electrode Polarography. Single Scan and Cyclic Methods Applied to Reversible, Irreversible, and Kinetic Systems *Analytical Chemistry*, vol. 36, no. 4, pp. 706–723, 1964.

[40] I. Valov, E. Linn, S. Tappertzhofen, S. Schmelzer, J. v. d. Hurk, F. Lentz, and R. Waser, Nanobatteries in redox-based resistive switches require extension of memristor theory *Nature Communications*, vol. 4, p. 1771, 2013.

[41] K. Vetter, *Electrochemical Kinetics.* Springer, 1961.

[42] J. F. Watts and J. Wolstenholme, *An Introduction to Surface Analysis by XPS and AES.* Wiley-VCH, 2003.

[43] M. Setou, *Imaging Mass Spectrometry.* Springer, 2008.

[44] P. M. Vilarinho, Y. Rosenwaks, and A. I. Kingon, *Scanning Probe Microscopy: Characterization, Nanofabrication And Device Application Of Functional Materials.* Springer, 2005.

[45] J. M. Walls, *Methods of surface analysis: techniques and applications.* Cambridge University Press, 1990.

[46] M. Röscher, *Lead-free Piezoelectric Transducers for Vibration-based Energy Harvesting Devices.* PhD thesis, RWTH Aachen University, Aachen, 2011.

[47] C. L. Yaws, *Handbook of Vapor Pressure: Inorganic Compunds and Elements*, vol. 4. Gulf Publishing, 1995.

[48] D. Stull, Vapor Pressure of Pure Substances. Organic and Inorganic Compounds *Industrial and Engineering Chemistry*, vol. 39, no. 4, pp. 517–540, 1947.

[49] R. Rosezin, *Stacked device structures for resistive memory and logic.* PhD thesis, RWTH Aachen University, Aachen, 2012.

[50] U. Hilleringmann, *Silizium-Halbleitertechnologie.* Teubner B.G., 2004.

[51] M. Meier, C. Nauenheim, S. Gilles, D. Mayer, C. Kügeler, and R. Waser, Nanoimprint for future non-volatile memory and logic devices *Microelectronic Engineering*, vol. 85, pp. 870–872, 2008.

[52] M. Birkholz, *Thin Film Analysis by X-Ray Scattering. Techniques for Structural Characterization.* Wiley-VCH, 2005.

[53] S. Tappertzhofen, S. Menzel, I. Valov, and R. Waser, Redox Processes in Silicon Dioxide Thin Films using Copper Microelectrodes *Applied Physics Letters*, vol. 99, no. 20, p. 203103, 2011.

[54] S. Tappertzhofen, I. Valov, and R. Waser, Quantum conductance and switching kinetics of AgI based microcrossbar cells *Nanotechnology*, vol. 23, no. 14, pp. 145703/1–6, 2012.

[55] *Model 6430 Sub-Femtoamp Remote SourceMeter Instruction Manual.* Keithley Instruments Inc., Cleveland, USA, 1999.

[56] J. Rutman and I. Riess, Reference electrodes for thin-film solid-state ionic devices *Solid State Ionics*, vol. 179, no. 1-6, pp. 108–112, 2008.

[57] J. Winkler, P. Hendriksen, N. Bonanos, and M. Mogensen, Geometric requirements of solid electrolyte cells with a reference electrode *Journal of the Electrochemical Society*, vol. 145, no. 4, pp. 1184–1192, 1998.

[58] V. Brichzin, J. Fleig, H. Habermeier, G. Cristiani, and J. Maier, The geometry dependence of the polarization resistance of Sr-doped $LaMnO_3$ microelectrodes on yttria-stabilized zirconia *Solid State Ionics*, vol. 152, pp. 499–507, 2002.

[59] A. Hashibon, S. Raz, and I. Riess, Preferred position for the reference electrode in solid state electrochemistry *Solid State Ionics*, vol. 149, no. 3-4, pp. 167–176, 2002.

[60] H. R. Philipp, Optical properties of non-crystalline Si, SiO, SiO_x and SiO_2 *Journal of Physics and Chemistry of Solids*, vol. 32, no. 8, pp. 1935–1945, 1971.

[61] S. Kondo, T. Itoh, and T. Saito, Strongly enhanced optical absorption in quench-deposited amorphous AgI films *Physical Review B*, vol. 57, no. 20, pp. 13235–13240, 1998.

[62] T. Ida and K. Kimura, Ionic conductivity of small-grain polycrystals of silver iodide *Solid State Ionics*, vol. 107, no. 3-4, pp. 313–318, 1998.

[63] P. S. Kumar and C. S. Sunandana, γ-AgI films by iodization at ambient temperature *Thin Solid Films*, vol. 323, pp. 110–114, 1998.

[64] D. Y. Cho, S. Tappertzhofen, R. Waser, and I. Valov, Chemically-inactive interfaces in thin film Ag/AgI systems for resistive switching memories *Scientific Reports*, vol. 3, p. 1169, 2013.

[65] G. Burley, Structure of Hexagonal Silver Iodide *Journal of Chemical Physics*, vol. 38, no. 12, pp. 2807–2812, 1963.

[66] S. Tappertzhofen, H. Mündelein, I. Valov, and R. Waser, Nanoionic transport and electrochemical reactions in resistively switching silicon dioxide *Nanoscale*, vol. 4, no. 10, pp. 3040–3043, 2012.

[67] J. D. McBrayer, R. M. Swanson, and Y. W. Sigmon, Diffusion of metals in silicon dioxide *Journal of the Electrochemical Society*, vol. 133, no. 6, pp. 1242–6, 1986.

[68] Y. Shacham-Diamand, A. Dedhia, D. Hoffstetter, and W. G. Oldham, Copper Transport in Thermal SiO_2 *Journal of the Electrochemical Society*, vol. 140, no. 8,

pp. 2427–2432, 1993.

[69] D. B. Strukov and R. S. Williams, Exponential ionic drift: fast switching and low volatility of thin-film memristors *Applied Physics A*, vol. 94, no. 3, pp. 515–519, 2009.

[70] C. Schindler, M. Meier, R. Waser, and M. N. Kozicki, Resistive switching in Ag-Ge-Se with extremely low write currents *Non-Volatile Memory Technology Symposium (NVMTS)*, pp. 82–85, 2007.

[71] C. Schindler, M. Weides, M. N. Kozicki, and R. Waser, Low current resistive switching in Cu-SiO_2 cells *Applied Physics Letters*, vol. 92, no. 12, p. 122910, 2008.

[72] S. Tappertzhofen, I. Valov, T. Tsuruoka, T. Hasegawa, R. Waser, and M. Aono, Generic Relevance of Counter Charges for Cation-Based Nanoscale Resistive Switching Memories *ACS Nano*, vol. 7, no. 7, p. 6396–6402, 2013.

[73] T. Tsuruoka, K. Terabe, T. Hasegawa, I. Valov, R. Waser, and M. Aono, Effects of Moisture on the Switching Characteristics of Oxide-Based, Gapless-Type Atomic Switches *Advanced Functional Materials*, vol. 22, no. 1, pp. 70–77, 2011.

[74] D. Y. Cho, S. Tappertzhofen, R. Waser, and I. Valov, Bond Nature of Active Metal Ions in SiO_2-based Electrochemical Metallization Memory Cells *Nanoscale*, vol. 5, no. 5, pp. 1781–1784, 2013.

[75] J. Yano and V. K. Yachandra, X-ray absorption spectroscopy *Photosynthesis Research*, vol. 102, no. 2-3, pp. 241–254, 2009.

[76] S. Tappertzhofen, R. Waser, and I. Valov, Impact of Counter Electrode Material on the Redox Processes in Resistive Switching Memories *ChemElectroChem*, vol. 1, no. 8, p. 1287–1292, 2014.

[77] M. H. Miles and M. A. Thomason, Periodic Variations of Overvoltages for Water Electrolysis in Acid Solutions from Cyclic Voltammetric Studies *Journal of the Electrochemical Society*, vol. 123, no. 10, pp. 1459–1461, 1976.

[78] S. Morse and N. Greene, Hydrogen Overpotential on Rare Earth Metals *Electrochimica Acta*, vol. 12, no. 2, pp. 179–189, 1967.

[79] A. Hickling and F. Salt, Studies in hydrogen overvoltage at high current densities. Part VI. The mechanism of hydrogen overvoltage *Transactions of the Faraday Society*, vol. 38, pp. 474–489, 1942.

[80] J. Bockris, Electrolytic polarisation - I. The overpotential of hydrogen on some less common metals at high current densities. Influence of current density and time *Transactions of the Faraday Society*, vol. 43, no. 7, pp. 417–429, 1947.

[81] H. Shibutani, T. Higashijima, H. Ezaki, M. Morinaga, and K. Kikuchi, An electronic approach to the hydrogen overpotential for Zr alloys *Electrochimica Acta*, vol. 43,

pp. 3235–3239, 1998.

[82] H. B. Michaelson, Work Functions of the Elements *Journal of Applied Physics*, vol. 21, no. 6, pp. 536–540, 1950.

[83] W. Martienssen and H. Warlimont, *Springer Handbook of Condensed Matter and Materials Data.* Springer, 2005.

[84] G. D. Sharma, A. K. . Tripathi, D. C. Dube, and S. C. Mathur, Electrical conduction mechanism in crystal violet dye sensitised with AgI *Journal of Physics D*, vol. 16, no. 10, pp. 1977–1983, 1983.

[85] J. Garbarczyk, M. Wasiucionek, B. Wnetrzewski, and W. Jakubowski, Mixed electronic-ionic conduction in glasses of the AgI-Ag_2O-V_2O_5-P_2O_5 system *Physica Status Solidi*, vol. 156, no. 2, pp. 441–449, 1996.

[86] X. F. Liang, Y. Chen, L. Chen, J. Yin, and Z. G. Liu, Electric switching and memory devices made from $RbAg_4I_5$ films *Applied Physics Letters*, vol. 90, no. 2, p. 022508, 2006.

[87] I. Valov, I. Sapezanskaia, A. Nayak, T. Tsuruoka, T. Bredow, T. Hasegawa, G. Staikov, M. Aono, and R. Waser, Atomically controlled electrochemical nucleation at superionic solid electrolyte surfaces *Nature Materials*, vol. 11, no. 6, pp. 530–535, 2012.

[88] K. Shahi and S. Chandra, Electrical-Conductivity and Thermoelectric-Power of $Ag_6I_4WO_4$ Solid Electrolyte *Physica Status Solidi A*, vol. 28, no. 2, pp. 653–661, 1975.

[89] M. Tatsumisago, K. Okuda, N. Itakura, and T. Minami, Crystallization of α-AgI from AgI-Ag_2O-M_xO_y ($M_xO_y = B_2O_3$, GeO_2, WO_3) melts and glasses *Solid State Ionics*, vol. 121, pp. 193–200, 1999.

[90] K. Shahi and J. Wagner, Ionic Conductivity and Thermoelectric Power of Pure and Al_2O_3-Dispersed AgI *Journal of the Electrochemical Society*, vol. 128, no. 1, pp. 6–13, 1981.

[91] H. Hoshino and M. Shimoji, Electrical Properties of Silver Iodide *Journal of Physics and Chemistry of Solids*, vol. 35, no. 3, pp. 321–326, 1974.

[92] P. C. Allen and D. Lazarus, Effect of pressure on ionic conductivity in rubidium silver iodide and silver iodide *Physical Review B*, vol. 17, no. 4, pp. 1913–1927, 1978.

[93] H. Roemer and G. Luther, Conductivity and dielectric constant of superionic AgI in the microwave region *Ferroelectrics*, vol. 38, no. 1-4, pp. 919–922, 1981.

[94] S. P. Sankaranarayanan, *Synthesis of Nanoparticles of certain materials and their characterization.* PhD thesis, Mahatma Gandhi University, Kottayam, 2001.

[95] B. Deb and A. Ghosh, Dielectric and conductivity relaxation in AgI doped silver selenite superionic glasses *Journal of Applied Physics*, vol. 108, no. 7, p. 74104, 2010.

[96] D.-Y. Cho, I. Valov, J. van den Hurk, S. Tappertzhofen, and R. Waser, Direct Observation of Charge Transfer in Solid Electrolyte for Electrochemical Metallization Memory *Advanced Materials*, vol. 24, no. 33, pp. 4552–4556, 2012.

[97] I. Valov, S. Tappertzhofen, E. Linn, and R. Waser, The Role of Electrochemical Interfaces in ReRAM Memory Cells *ECS Transactions*, vol. 58, no. 7, pp. 189–196, 2013.

[98] S. Tappertzhofen, E. Linn, U. Böttger, R. Waser, and I. Valov, Nanobattery Effect in RRAMs - Implications on Device Stability and Endurance *IEEE Electron Device Letters*, vol. 35, no. 2, pp. 208–210, 2014.

[99] S. Lin, L. Zhao, J. Zhang, H. Wu, Y. Wang, H. Qian, and Z. Yu, Electrochemical Simulation of Filament Growth and Dissolution in Conductive-Bridging RAM (CBRAM) with Cylindrical Coordinates *IEEE Electron Devices Meeting (IEDM)*, 2012.

[100] J. van den Hurk, I. Valov, and R. Waser, Preparation and characterization of GeS_x thin-films for resistive switching memories *Thin Solid Films*, vol. 527, pp. 299–302, 2012.

[101] T. Tsuruoka, K. Terabe, T. Hasegawa, and M. Aono, Forming and switching mechanisms of a cation-migration-based oxide resistive memory *Nanotechnology*, vol. 21, no. 42, pp. 425205/1–8, 2010.

[102] J. Suñé, E. Miranda, D. Jiménez, S. Long, and M. Liu, From dielectric failure to memory function *Non-Volatile Memory Technology Symposium (NVMTS)*, 2011.

[103] P. C. Yang, T. C. Chang, S. C. Chen, Y. S. Lin, H. C. Huang, and D. S. Gan, Influence of Bias-Induced Copper Diffusion on the Resistive Switching Characteristics of a SiON Thin Film *Electrochemical and Solid State Letters*, vol. 14, no. 2, pp. H93–H95, 2011.

[104] S. Lombardo, J. H. Stathis, B. P. Linder, K. L. Pey, F. Palumbo, and C. H. Tung, Dielectric breakdown mechanisms in gate oxides *Journal of Applied Physics*, vol. 98, no. 12, p. 121301, 2005.

[105] S. P. Thermadam, S. K. Bhagat, T. L. Alford, Y. Sakaguchi, M. N. Kozicki, and M. Mitkova, Influence of Cu diffusion conditions on the switching of Cu-SiO_2-based resistive memory devices *Thin Solid Films*, vol. 518, no. 12, pp. 3293–3298, 2010.

[106] Y. Bernard, V. T. Renard, P. Gonon, and V. Jousseaume, Back-end-of-line compatible Conductive Bridging RAM based on Cu and SiO_2 *Microelectronic Engineering*,

vol. 88, no. 5, pp. 814–816, 2011.

[107] M. Meier, S. Gilles, R. Rosezin, C. Schindler, S. Trellenkamp, A. Rüdiger, D. Mayer, C. Kügeler, and R. Waser, Resistively switching Pt/spin-on glass/Ag nanocells for non-volatile memories fabricated with UV nanoimprint lithography *Microelectronic Engineering*, vol. 86, no. 4-6, pp. 1060–1062, 2009.

[108] M. Meier, C. Schindler, S. Gilles, R. Rosezin, A. Rüdiger, C. Kügeler, and R. Waser, A Nonvolatile Memory With Resistively Switching Methyl-Silsesquioxane *IEEE Electron Device Letters*, vol. 30, no. 1, pp. 8–10, 2009.

[109] R. Rosezin, M. Meier, S. Trellenkamp, C. Kügeler, and R. Waser, Observation of unipolar resistance switching in silver doped methyl-silsesquioxane *Microelectronic Engineering*, vol. 87, no. 5-8, pp. 1531–1533, 2010.

[110] R. Rosezin, M. Meier, U. Breuer, C. Kügeler, and R. Waser, Electroforming and Resistance Switching Characteristics of Silver-Doped MSQ With Inert Electrodes *IEEE Transactions on Nanotechnology*, vol. 10, no. 2, pp. 338–343, 2011.

[111] D. Yu, L. F. Liu, B. Chen, F. F. Zhang, B. Gao, Y. H. Fu, X. Y. Liu, J. F. Kang, and X. Zhang, Multilevel resistive switching characteristics in Ag/SiO_2/Pt RRAM devices *International Conference of Electron Devices and Solid-State Circuits (EDSSC)*, pp. 1–2, 2011.

[112] S. Menzel, S. Tappertzhofen, R. Waser, and I. Valov, Switching Kinetics of Electrochemical Metallization Memory Cells *Physical Chemistry Chemical Physics*, vol. 15, no. 18, pp. 6945–6952, 2013.

[113] S. Menzel and R. Waser, Analytical Analysis of the Generic SET and RESET Characterisitics of Electrochemical Metallization Memory Cells *Nanoscale*, vol. 22, no. 5, pp. 11003–11010, 2013.

[114] K. Tsunoda, Y. Fukuzumi, J. R. Jameson, Z. Wang, P. B. Griffin, and Y. Nishi, Bipolar resistive switching in polycrystalline TiO_2 films *Applied Physics Letters*, vol. 90, no. 11, p. 113501, 2007.

[115] M. N. Kozicki, C. Gopalan, M. Balakrishnan, M. Park, and M. Mitkova, Nonvolatile memory based on solid electrolytes *Non-Volatile Memory Technology Symposium (NVMTS)*, pp. 10–17, 2004.

[116] C. P. Hsiung, H. W. Liao, J. Y. Gan, T. B. Wu, J. C. Hwang, F. Chen, and M. J. Tsai, Formation and Instability of Silver Nanofilament in Ag-Based Programmable Metallization Cells *ACS Nano*, vol. 4, no. 9, pp. 5414–5420, 2010.

[117] M. Kund, G. Beitel, C. U. Pinnow, T. Röhr, J. Schumann, R. Symanczyk, K. D. Ufert, and G. Müller, Conductive bridging RAM (CBRAM): an emerging non-volatile memory technology scalable to sub 20nm *IEEE Electron Devices Meeting*

(IEDM), pp. 754–757, 2005.

[118] A. Belmonte, W. Kim, B. Chan, N. Heylen, A. Fantini, M. Houssa, M. Jurczak, and L. Goux, 90nm W/Al_2O_3/TiW/Cu 1T1R CBRAM cell showing low-power, fast and disturb-free operation *IEEE International Memory Workshop (IMW)*, 2013.

[119] J. Jameson, P. Blanchard, C. Cheng, J. Dinh, A. Gallo, V. Gopalakrishnan, C. Gopalan, B. Guichet, S. Hsu, D. Kamalanathan, D. Kim, F. Koushan, M. Kwan, K. Law, D. Lewis, Y. Ma, V. McCaffrey, S. Park, S. Puthenthermadam, E. Runnion, J. Sanchez, J. Shields, K. Tsai, A. Tysdal, D. Wang, R. Williams, M. Kozicki, J. Wang, V. Gopinath, S. Hollmer, and M. V. Buskirk, Conductive-bridge memory (CBRAM) with excellent high-temperature retention *IEEE Electron Devices Meeting (IEDM)*, pp. 30.1.1–30.1.4, 2013.

[120] B. Sun, L. Liu, N. Xu, B. Gao, Y. Wang, D. Han, X. Liu, R. Han, and J. Kang, The effect of the current compliance on the resistive switching behaviors in TiN/ZrO_2/Pt memory device *Japanese Journal of Applied Physics*, vol. 48, p. 04C061, 2009.

[121] B. Gao, W. Y. Chang, B. Sun, H. W. Zhang, L. F. Liu, X. Y. Liu, R. Q. Han, T. B. Wu, and J. F.Kang, Identification and application of current compliance failure phenomenon in RRAM device *Symposium On VLSI Technology, Systems and Applications (VLSI)*, pp. 144–145, 2010.

[122] Y.-S. Chen, W.-H. Liu, H.-Y. Lee, P.-S. Chen, S.-M. Wang, C.-H. Tsai, Y.-Y. Hsu, P.-Y. Gu, W.-S. Chen, F. Chen, C.-H. Lien, and M.-J. Tsai, Impact of compliance current overshoot on high resistance state, memory performance, and device yield of HfO_x based resistive memory and its solution *Symposium On VLSI Technology Systems and Application (VLSI)*, 2011.

[123] D. Ielmini, Filamentary-switching model in RRAM for time, energy and scaling projections *IEEE Electron Devices Meeting (IEDM)*, pp. 17.2.1–17.2.4, 2011.

[124] K. Saxe, Assembly of a measurement station for the characterization of resistive switching memory cells *Student thesis, RWTH Aachen University, Aachen*, 2012.

[125] O. Kavehei, E. Linn, L. Nielen, S. Tappertzhofen, S. Skafidas, I. Valov, and R. Waser, Associative Capacitive Network based on Nanoscale Complementary Resistive Switches for Memory-Intensive Computing *Nanoscale*, vol. 5, no. 11, pp. 5119–5128, 2013.

[126] X. B. Yan, J. Yin, H. X. Guo, Y. Su, B. Xu, H. T. Li, D. W. Yan, Y. D. Xia, and Z. G. Liu, Bipolar resistive switching performance of the nonvolatile memory cells based on $(AgI)_{0.2}(Ag_2MoO_4)_{0.8}$ solid electrolyte films *Journal of Applied Physics*,

vol. 106, no. 5, p. 54501, 2009.

[127] D. B. Strukov, G. S. Snider, D. R. Stewart, and R. S. Williams, The missing memristor found *Nature*, vol. 453, no. 7191, pp. 80–83, 2008.

[128] Z. Chen and C. Lu, Humidity sensors: A review of materials and mechanisms *Sensor Letters*, vol. 3, no. 4, pp. 274–295, 2005.

[129] C. Cao, Y. He, J. Torras, E. Deumens, S. B. Trickey, and H. P. Cheng, Fracture, water dissociation, and proton conduction in SiO_2 nanochains *Journal of Chemical Physics*, vol. 126, no. 21, p. 211101, 2007.

[130] R. Armunanto, C. Schwenk, and B. Rode, Structure and dynamics of hydrated Ag (I): Ab initio quantum mechanical-molecular mechanical molecular dynamics simulation *Journal of Physical Chemistry A*, vol. 107, no. 17, pp. 3132–3138, 2003.

[131] J. L. Fulton, S. M. Kathmann, G. K. Schenter, and M. Balasubramanian, Hydrated Structure of Ag(I) Ion from Symmetry-Dependent, K- and L-Edge XAFS Multiple Scattering and Molecular Dynamics Simulations *Journal of Physical Chemistry A*, vol. 113, no. 50, pp. 13976–13984, 2009.

[132] N. Knorr, R. Wirtz, S. Rosselli, and G. Nelles, Field-Absorbed Water Induced Electrochemical Processes in Organic Thin Film Junctions *Journal of Physical Chemistry C*, vol. 114, no. 37, pp. 15791–15796, 2010.

[133] J. Krans, C. Muller, I. Yanson, T. Govaert, R. Hesper, and J. M. van Ruitenbeek, One-Atom Point Contacts *Physical Review B*, vol. 48, no. 19, pp. 14721–14724, 1993.

[134] E. H. Sondheimer, The mean free path of electrons in metals *Advanced Physics*, vol. 1, no. 1, pp. 1–42, 1952.

[135] N. Agrait, A. L. Yeyati, and J. M. v. Ruitenbeek, Quantum properties of atomic-sized conductors *Physics Reports*, vol. 377, pp. 81–279, 2003.

[136] K. Terabe, T. Hasegawa, T. Nakayama, and M. Aono, Quantized conductance atomic switch *Nature*, vol. 433, no. 6, pp. 47–50, 2005.

[137] M. Aono and T. Hasegawa, The Atomic Switch *Proceedings of the IEEE*, vol. 98, no. 12, pp. 2228–2236, 2010.

[138] T. Hasegawa, A. Nayak, T. Ohno, K. Terabe, T. Tsuruoka, J. K. Gimzewski, and M. Aono, Memristive operations demonstrated by gap-type atomic switches *Applied Physics A*, vol. 102, no. 4, p. 811–815, 2011.

[139] T. Hasegawa, T. Ohno, K. Terabe, T. Tsuruoka, T. Nakayama, J. K. Gimzewski, and M. Aono, Learning Abilities Achieved by a Single Solid-State Atomic Switch *Advanced Materials*, vol. 22, pp. 1831–1834, 2010.

[140] T. Tsuruoka, T. Hasegawa, K. Terabe, M, and Aono, Conductance quantization and synaptic behavior in a Ta_2O_5-based atomic switch *Nanotechnology*, vol. 23, no. 43, p. 435705, 2012.

[141] J. J. T. Wagenaar, M. Morales-Masis, and J. M. van Ruitenbeek, Observing quantized conductance steps in silver sulfide: Two parallel resistive switching mechanisms *Journal of Applied Physics*, vol. 111, no. 1, p. 14302, 2012.

[142] J. R. Jameson, N. Gilbert, F. Koushan, J. Saenz, J. Wang, S. Hollmer, M. Kozicki, and N. Derhacobian, Quantized Conductance in Ag/GeS_2/W Conductive-Bridge Memory Cells *IEEE Electron Device Letters*, vol. 33, no. 2, pp. 257–259, 2012.

[143] D. Liu, H. Cheng, X. Zhu, G. Wang, and N. Wang, Analog Memristors Based on Thickening/Thinning of Ag Nanofilaments in Amorphous Manganite Thin Films *ACS Applied Materials and Interfaces*, vol. 5, no. 21, pp. 11258–11265, 2013.

[144] F. Q. Xie, L. Nittler, C. Obermair, and T. Schimmel, Gate-controlled atomic quantum switch *Physical Review Letters*, vol. 93, no. 12, p. 128303, 2004.

[145] S. Long, X. Lian, C. Cagli, X. Cartoixà, R. Rurali, E. Miranda, D. Jiménez, L. Perniola, M. Liu, and J. Suñé, Quantum-size effects in hafnium-oxide resistive switching *Applied Physics Letters*, vol. 102, p. 183505, 2013.

[146] Y.-E. Syu, T.-C. Chang, J.-H. Lou, T.-M. Tsai, K.-C. Chang, M.-J. Tsai, Y.-L. Wang, M. Liu, and S. M. Sze, Atomic-level quantized reaction of HfO_x memristor *Applied Physics Letters*, vol. 102, p. 172903, 2013.

[147] E. Miranda, D. Jiménez, and J. Suñé, The Quantum Point-Contact Memristor *IEEE Electron Device Letters*, vol. 33, no. 10, pp. 1474–1476, 2012.

[148] Y. V. Pershin and M. D. Ventra, Neuromorphic, Digital, and Quantum Computation With Memory Circuit Elements *Proceedings of the IEEE*, vol. 100, no. 6, pp. 2071–2080, 2012.

[149] W. Weibull, A Statistical Distribution Function of Wide Applicability *Journal of Applied Mechanics*, vol. 18, no. 3, pp. 293–297, 1951.

[150] R. Hill and L. Dissado, Theoretical basis for the statistics of dielectric breakdown *Journal of Physics C*, vol. 16, no. 11, pp. 2145–2156, 1983.

[151] M. Faraday, Experimental researches in electricity *Philosophical Transactions of the Royal Society*, vol. 124, pp. 77–122, 1834.

[152] M. D. Pickett and R. S. Williams, Sub-100 fJ and sub-nanosecond thermally driven threshold switching in niobium oxide crosspoint nanodevices *Nanotechnology*, vol. 23, no. 21, p. 215202, 2012.

[153] L. Chua, Memristor - the missing circuit element *IEEE Transactions on Circuit Theory*, vol. CT-18, no. 5, pp. 507–519, 1971.

[154] L. Chua and S. M. Kang, Memristive devices and systems *Proceedings of the IEEE*, vol. 64, no. 2, pp. 209–223, 1976.

[155] L. Chua, Device Modeling via Basic Non-Linear Circuit Elements *IEEE Transactions on Circuits and Systems*, vol. 27, no. 11, pp. 1014–1044, 1980.

[156] L. Chua, The Fourth Element *Proceedings of the IEEE*, vol. 100, no. 6, pp. 1920–1927, 2012.

[157] L. Chua, V. Sbitnev, and H. Kim, Hodgkin-Huxley Axon is Made of Memristors *International Journal of Bifurcation and Chaos*, vol. 22, no. 3, p. 1230011, 2012.

[158] A. Ascoli, F. Corinto, V. Senger, and R. Tetzlaff, Memristor Model Comparison *IEEE Circuits and Systems Magazine*, vol. 13, no. 2, pp. 89–105, 2013.

[159] L. Chua, Resistance switching memories are memristors *Applied Physics A*, vol. 102, no. 4, pp. 765–783, 2011.

[160] E. Linn, S. Menzel, S. Ferch, and R. Waser, Compact modeling of CRS devices based on ECM cells for memory, logic and neuromorphic applications *Nanotechnology*, vol. 24, no. 38, p. 384008, 2013.

[161] P. Meuffels and H. Schröder, Comment on Exponential ionic drift: fast switching and low volatility of thin-film memristors by D.B. Strukov and R.S. Williams in Applied Physics A (2009) 94: 515-519 *Applied Physics A*, vol. 105, no. 1, pp. 65–67, 2011.

[162] H. Kim and S. P. Adhikari, Memistor Is Not Memristor *IEEE Solid-State Circuits Magazine*, vol. 12, no. 1, pp. 75–78, 2012.

[163] S. Vongehr, Missing the Memristor *Advanced Science Letters*, vol. 17, pp. 285–290, 2012.

[164] M. Wu, Y. Lin, W. Jang, C. Lin, and T. Tseng, Low-power and highly reliable multilevel operation in ZrO_2 1T1R RRAM *IEEE Electron Device Letters*, vol. 32, no. 8, pp. 1026–1028, 2011.

[165] C. Cagli, F. Nardi, and D. Ielmini, Modeling of Set/Reset Operations in NiO-Based Resistive Switching Memory devices *IEEE Transactions on Electron Devices*, vol. 56, no. 8, p. 1712, 2009.

[166] B. Chen, Y. Lu, B. Gao, Y. H. Fu, F. F. Zhang, P. Huang, Y. S. Chen, L. F. Liu, X. Y. Liu, J. F. Kang, Y. Y. Wang, Z. Fang, H. Y. Yu, X. Li, X. P. Wang, N. Singh, G. Q. Lo, and D. L. Kwong, Physical Mechanisms of Endurance Degradation in TMO-RRAM *IEEE Electron Devices Meeting (IEDM)*, 2011.

[167] Y. Lu, B. Chen, B. Gao, Z. Fang, Y. H. Fu, J. Q. Yang, L. F. Liu, X. Y. Liu, H. Y. Yu, and J. F. Kang, Improvement of endurance degradation for oxide based resistive switching memory devices correlated with oxygen vacancy accumulation

effect *IEEE Reliability Physics Symposium (IRPS)*, pp. MY.4.1–4, 2012.

[168] R. Rosezin, E. Linn, C. Kügeler, R. Bruchhaus, and R. Waser, Crossbar Logic Using Bipolar and Complementary Resistive Switches *IEEE Electron Device Letters*, vol. 32, no. 6, pp. 710–712, 2011.

[169] J. Mustafa and R. Waser, A novel reference scheme for reading passive resistive crossbar memories *IEEE Transactions on Nanotechnoly*, vol. 5, no. 6, pp. 687–691, 2006.

[170] C. Liaw, Integrated semiconductor memory with an arrangement of nonvolatile memory cells, and method *United States Patent 7277312*, 2007.

[171] E. Linn, *Complementary Resistive Switches.* PhD thesis, RWTH Aachen University, Aachen, 2012.

[172] R. Rosezin, E. Linn, L. Nielen, C. Kügeler, R. Bruchhaus, and R. Waser, Integrated Complementary Resistive Switches for Passive High-Density Nanocrossbar Arrays *IEEE Electron Device Letters*, vol. 32, no. 2, pp. 191–193, 2011.

[173] E. Linn, S. Menzel, R. Rosezin, U. Böttger, R. Bruchhaus, and R. Waser, *Nanoelectronic Device Applications Handbook: Modeling of Complementary Resistive Switches.* CRC Press, 2013.

[174] S. Tappertzhofen, E. Linn, L. Nielen, R. Rosezin, F. Lentz, R. Bruchhaus, I. Valov, U. Böttger, and R. Waser, Capacity based Nondestructive Readout for Complementary Resistive Switches *Nanotechnology*, vol. 22, no. 39, p. 395203, 2011.

[175] Y. Yang, P. Gao, L. Li, X. Pan, S. Tappertzhofen, S. Choi, R. Waser, I. Valov, and W. D. Lu, Electrochemical dynamics of nanoscale metallic inclusions in dielectrics *Nature Communications*, vol. 5, p. 4232, 2014.

[176] M. M. Ziegler and M. R. Stan, CMOS/Nano Co-Design for Crossbar-Based Molecular Electronic Systems *IEEE Transactions on Nanotechnology*, vol. 2, no. 4, pp. 217–230, 2003.

[177] S. Paul and S. Bhunia, A Scalable Memory-Based Reconfigurable Computing Framework for Nanoscale Crossbar *IEEE Transactions on Nanotechnology*, vol. 11, pp. 451–42, 2011.

[178] E. Lehtonen, J. H. Poikonen, and M. Laiho, Two memristors suffice to compute all Boolean functions *Electronics Letters*, vol. 46, no. 3, pp. 239–240, 2010.

[179] J. Borghetti, G. S. Snider, P. J. Kuekes, J. J. Yang, D. R. Stewart, and R. S. Williams, 'Memristive' switches enable 'stateful' logic operations via material implication *Nature*, vol. 464, no. 7290, pp. 873–876, 2010.

[180] E. Linn, R. Rosezin, S. Tappertzhofen, U. Böttger, and R. Waser, Beyond von Neumann-logic operations in passive crossbar arrays alongside memory operations

Nanotechnology, vol. 23, pp. 305205/1–6, 2012.

[181] A. S. Chawla and H. C. Lin, A cross-point MNOS capacitor memory *IEEE Electron Devices Meeting (IEDM)*, vol. 22, pp. 181–184, 1979.

[182] M. Robinson, H. Yoneda, and E. Sánchez-Sinencio, A modular CMOS design of a Hamming network *IEEE Transactions on Neural Networks*, vol. 3, no. 3, pp. 444–456, 1992.

A. Appendix

PVD Parameters

Various device fabrication parameters based on sputtering and evaporation technologies (see chapter 3) are given here.

RF-Sputtering Silicon Dioxide

Target Size and Material:	6 inch SiO_2
Power:	300 W
Max. DC-Bias:	1000 V
Pressure:	$5.4 \cdot 10^{-3}$ hPa
Sputter Time (50 nm):	300 s
Gas Flow:	30 sccm Ar

RF-Sputtering ITO

Target Size and Material:	6 inch ITO
Power:	300 W
Max. DC-Bias:	1000 V
Pressure:	$5.4 \cdot 10^{-3}$ hPa
Sputter Time (100 nm):	120 s
Gas Flow:	30 sccm Ar

DC-Sputtering TiN (on Si Wafer)

Target Size and Material:	6 inch Ti
Power:	200 W
Pressure:	$5.8 \cdot 10^{-3}$ hPa
Sputter Time (20 nm):	150 s
Gas Flow:	27 sccm Ar, 2 sccm N_2

DC-Sputtering Silicon

Target Size and Material:	6 inch Si
Power:	200 W
Pressure:	$7.7 \cdot 10^{-3}$ hPa
Sputter Time (50 nm):	500 s
Gas Flow:	40 sccm Ar

DC-Sputtering Platinum

Target Size and Material:	6 inch Pt
Power:	300 W (DC)
Pressure:	$5.4 \cdot 10^{-3}$ hPa
Sputter Time (100 nm):	86 s
Gas Flow:	30 sccm Ar

Electron Beam Evaporation Silicon Dioxide

Crucible Material:	SiO_2
High Voltage:	8.4 kV
Current:	$\approx$ 12 mA (Circulating Beam)
Evaporation Speed:	0.01 nm/s
Pressure:	$\approx 10^{-6}$ hPa

Electron Beam Evaporation Silver and Copper

Crucible Material:	Ag/Cu
High Voltage:	8.4 kV
Current:	$\approx$ 145 mA/160 mA (Circulating Beam)
Evaporation Speed:	0.02 nm/s
Pressure:	$\approx 10^{-6}$ hPa

Thermal Evaporation Silver Iodide

Crucible Material:	AgI
Evaporation Speed:	0.1 nm/s
Pressure:	$\approx 10^{-5}$ hPa

Curriculum Vitae

Stefan Tappertzhofen

Geburtsdatum: 25.06.1984

Geburtsort: Düsseldorf

Familienstand: ledig

Staatsangehörigkeit: deutsch

Bildungsweg

1990 - 1994	Katholische Grundschule Florensstraße, Düsseldorf
1994 - 1996	Realschule Florastraße, Düsseldorf
1996 - 2003	St. Ursula Gymnasium, Düsseldorf Abschluss: Abitur
2004 - 2009	Studium der Elektrotechnik und Informationstechnik an der RWTH Aachen Abschluss: Diplom-Ingenieur
2009 - 2014	Wissenschaftlicher Angestellter am Institut für Werkstoffe der Elektrotechnik, Lehrstuhl 2, der RWTH Aachen

Publication List

Peer Review Journals

S. Tappertzhofen, R. Waser, I. Valov. *Impact of Counter Electrode Material on the Redox Processes in Resistive Switching Memories*. ChemElectroChem (2014), 1, 8, p. 1287–1292

S. Yang, P. Gao, X. Pan, S. Tappertzhofen, S. Choi, R. Waser, I. Valov, W. Lu. *Electrochemical dynamics of nanoscale metallic inclusions in dielectrics*. Nature Communications (2014), 5, 4232

S. Tappertzhofen, E. Linn, U. Böttger, R. Waser, I. Valov. *Nanobattery Effect in RRAMs - Implications on Device Stability and Endurance*. IEEE Electron Device Letters (2014), 35, 2, p. 208-210

I. Valov, S. Tappertzhofen, E. Linn, R. Waser. *The Role of Electrochemical Interfaces in ReRAM Memory Cells*. ECS Transactions (2013), 58, 7, p. 189-196

S. Tappertzhofen, I. Valov, T. Tsuruoka, T. Hasegawa, R. Waser, M. Aono. *Generic Relevance of Counter Charges for Cation-Based Nanoscale Resistive Switching Memories*. ACS Nano (2013), 7, 7, p. 6396–6402

D.-Y. Cho, S. Tappertzhofen, R. Waser, I. Valov. *Bond Nature of Active Metal Ions in SiO_2-based Electrochemical Metallization Memory Cells*. Nanoscale (2013), 5, 5, p. 1781-1784

D.-Y. Cho, S. Tappertzhofen, R. Waser, I. Valov. *Chemically-inactive interfaces in thin film Ag/AgI system for resistive switching memories*. Scientific Reports (2013), 3, 1169, p. 1-5

O. Kavehei, E. Linn, L. Nielen, S. Tappertzhofen, S. Skafidas, I. Valov, R. Waser. *Associative Capacitive Network based on Nanoscale Complementary Resistive Switches for Memory-Intensive Computing*. Nanoscale (2013), 5, 11, p. 5119-5128

S. Menzel, S. Tappertzhofen, R. Waser, I. Valov. *Switching Kinetics of Electrochemical Metallization Memory Cells*. Physical Chemistry Chemical Physics (2013), 15, 18, p. 6945-6952

I. Valov, E. Linn, S. Tappertzhofen, S. Schmelzer, J. van den Hurk, F. Lentz, R. Waser. *Nanobatteries in redox-based resistive switches require extension of memristor theory.* Nature Communications (2013), 4, 1771

S. Tappertzhofen, H. Mündelein, I. Valov, R. Waser. *Nanoionic transport and electrochemical reactions in resistively switching silicon dioxide.* Nanoscale (2012), 4, 10, p. 3040-3043

D.-Y. Cho, I. Valov, J. van den Hurk, S. Tappertzhofen, R. Waser. *Direct Observation of Charge Transfer in Solid Electrolyte for Electrochemical Metallization Memory.* Advanced Materials (2012), 24, 33, p. 4552-4556

S. Tappertzhofen, I. Valov, R. Waser. *Quantum conductance and switching kinetics of AgI based microcrossbar cells.* Nanotechnology (2012), 23, 14, 145703

E. Linn, R. Rosezin, S. Tappertzhofen and U. Böttger, R. Waser. *Beyond von Neumann-logic operations in passive crossbar arrays alongside memory operations.* Nanotechnology (2012), 23, 305205 p. 1-6

S. Tappertzhofen, S. Menzel and I. Valov and R. Waser. *Redox Processes in Silicon Dioxide Thin Films using Copper Microelectrodes.* Applied Physics Letters (2011), 99, 20, 203103 p. 1-3

S. Tappertzhofen, E. Linn, L. Nielen, R. Rosezin, F. Lentz, R. Bruchhaus, I. Valov, U. Böttger, R. Waser. *Capacity based Nondestructive Readout for Complementary Resistive Switches.* Nanotechnology (2011), 22, 39, 395203 p. 1-7

S. Tappertzhofen, M. Hempel, I. Valov, R. Waser. *Proton Mobility in* SiO_2 *Thin Films and Impact of Hydrogen and Humidity on the Resistive Switching Effect.* Materials Research Society Symposium Proceedings (2011), 1330

M. Röscher, S. Tappertzhofen, T. Schneller. *Precursor Homogeneity and Crystallization Effects in Chemical Solution Deposition-Derived Alkaline Niobate Thin Films.* Journal American Ceramic Society (2011), 94, 7, p. 2193 - 2199

Conference Talks

S. Tappertzhofen, I. Valov, R. Waser. *New Insights into Redox Based Resistive Switches.* Non-Volatile Memory Technology Symposium 2013 (Invited Talk), Minneapolis, USA

S. Tappertzhofen, I. Valov, R. Waser. *Controllable Quantum Point Contacts in Nanoscale Resistive Switches*. Materials Research Spring Meeting 2013, San Francisco, USA

S. Tappertzhofen, I. Valov, R. Waser. *Nanoionic Redox Processes in Silicon Dioxide*. Materials Research Spring Meeting 2013, San Francisco, USA

S. Tappertzhofen, I. Valov, R. Waser *Quantum Conductance of AgI based Resistive Switches: Towards an Atomic Scale Memory*. Nature Conference 2012, Aachen, Germany

S. Tappertzhofen, M. Hempel, I. Valov, R. Waser. *Proton mobility in* SiO_2 *thin films and impact of hydrogen and humidity on the resistive switching effect*. Materials Research Spring Meeting 2011, San Francisco, USA

Posters

S. Tappertzhofen, E. Linn, L. Nielen, R. Rosezin, F. Lentz, R. Bruchhaus, I. Valov, U. Böttger, R. Waser. *Capacity based Nondestructive Readout for Complementary Resistive Switches*. International RRAM Workshop IMEC 2011, Leuven, Belgium

S. Tappertzhofen, I. Valov, R. Waser. *Impedance Spectroscopy on Electrochemical Metallization Cells (ECM) based on Silicon Dioxide*. Nanodays 2010, Aachen, Germany

Patents

R. Rosezin, F. Lentz, R. Bruchhaus, E. Linn, I. Valov, R. Waser, S. Tappertzhofen, L. Nielen *Verfahren zum nichtdestruktiven Auslesen resistiver Speicherelemente*. German Patent DE102011012738 (2012)

Copyright Information

Parts of this thesis have been published in the context of this research in Refs. [28; 32; 53; 54; 66; 72; 76; 98; 112; 125; 174].

Fig. 2.3: Permission from [28] to reproduce grant by IOP Publishing.

Fig. 2.10, 4.27, 4.28, 5.25, 5.27, 5.29: Reprinted with permission from [40]. Copyright 2013 Nature Publishing Group.

Fig. 3.4, 5.11: Reprinted with permission from [32]. Copyright Materials Research Society.

Fig. 3.13, 5.12, 5.14, 5.19, 5.7: Reprinted with permission from [54]. Copyright IOP Publishing.

Fig. 4.15, 4.16, 4.17, 4.18, 4.19: Reproduced [76] from with permission from Wiley-VCH Publishing.

Fig. 4.2: Reprinted with permission from [53]. Copyright American Institute of Physics.

Fig. 4.4, 4.6, 4.11, 4.12, 4.26, 5.3: Reproduced [66] from with permission from The Royal Society of Chemistry.

Fig. 4.8, 4.13, 4.14, 4.29, 4.30: Reprinted with permission from [72]. Copyright 2014 American Chemical Society.

Fig. 5.1, 5.30, 5.31, 5.32, 5.33: Reprinted with permission from [98]. IEEE Copyright 2014.

Fig. 5.24: Reproduced from [112] with permission from the PCCP Owner Societies.

Fig. 5.34, 5.35: Reprinted with permission from [174]. Copyright IOP Publishing.

Fig. 5.37: Reproduced [125] from with permission from The Royal Society of Chemistry.